Tidal currents and vertical mixing processes beneath Filchner-Ronne ice shelf

Thesis

TIDAL CURRENTS AND VERTICAL MIXING PROCESSES BENEATH FILCHNER-RONNE ICE SHELF

Keith Makinson
BEng (Hons)

A thesis submitted in partial fulfilment of the requirements of the Open University for the degree of Doctor of Philosophy

March 2002

British Antarctic Survey, Natural Environment Research Council,
Cambridge, United Kingdom

DATE OF SUBMISSION: 31 JANUARY 2002
DATE OF AWARD: 23 SEPTEMBER 2002

Abstract

Oceanographic measurements have been undertaken at sites on Filchner-Ronne Ice Shelf using hot-water drilled holes allowing conductivity-temperature-depth profiling and the deployment of instrument moorings. The data show that Western Shelf Water enters the sub-ice shelf cavity and occupies the lower portion of the water column. This is the water that provides the external heat necessary for melting within the sub-ice shelf cavity. A depth–averaged tidal model of the region has been used to show that in areas with shallow water and large topographic gradients, tidal oscillations with peak velocities up to 1 m s^{-1} play a significant role in the vertical mixing and transport of water masses. The estimated energy dissipation beneath Filchner-Ronne Ice Shelf resulting from surface friction is 25 GW, approximately 1% of the world's total tidal dissipation. The model indicates that Lagrangian tidal residual currents have fluxes of up to 250,000 m^3 s^{-1}, and speeds of over 5 cm s^{-1} along the ice front, with over 350,000 m^3 s^{-1} being exchanged between the sub–ice shelf cavity and adjacent continental shelf. These currents are particularly efficient in ventilating the sub–ice shelf cavity within 150 km of Ronne Ice Front. Furthermore, a one-dimensional turbulence closure ocean model has been applied to this sub-ice shelf environment which significantly lies near the critical latitude for the semi-diurnal tide. Here, the Coriolis frequency equals the tidal frequency, resulting in a strong depth dependent tidal current and thick boundary layers. Both the model and observations show that stratification significantly affects how the shape of the tidal current ellipse varies with depth. The model also shows that vertical mixing and basal melting are sensitive to tidal ellipse polarization with anticlockwise rotating tidal currents maintaining the highest melt rates. This sensitivity is due, in large part, to the proximity of the critical latitude.

Table of Contents

Table of Figures

Table of tables

Acronyms and Abbreviations

AABW	Antarctic Bottom Water
ACC	Antarctic Circumpolar Current
AWI	Alfred-Wegener-Institute
BAS	British Antarctic Survey
CFL	Courant-Friedrichs-Lewy
CMR	Christian Michelsen Research
CTD	Conductivity-Temperature-Depth
CTP	Conductivity-Temperature-Pressure
DBDB5	Digital Bathymetric Data Base 5
ESW	Eastern Shelf Water
FRIS	Filchner-Ronne Ice Shelf
GEBCO	General Bathymetric Chart of the Oceans
HSSW	High Salinity Shelf Water
HWD	Hot Water Drill
ISW	Ice Shelf Water
IW	Internal Wave
KPP	K-Profile Parameterization
MICOM	Miami Iso-Pycnic Coordinate Model
MWDW	Modified Weddell Deep Water
MY	Mellor-Yamada
SI	Shear Instability
SPRT	Standard Platinum Resistance Thermometer
TKE	Turbulent Kinetic Energy
WDW	Weddell Deep Water / Warm Deep Water
WSBW	Weddell Sea Bottom Water
WSDW	Weddell Sea Deep Water
WSW	Western Shelf Water
WW	Winter Water

List of accompanying material

Makinson, K. and K. W. Nicholls. Modeling tidal currents beneath Filchner-Ronne Ice Shelf and on the adjacent continental shelf: their effect on mixing and transport. *Journal of Geophysical Research,* 104(C6): 13449-13465, 1999. (Reprint)

Makinson, K. Modeling tidal current profiles and vertical mixing beneath Filchner-Ronne Ice Shelf, Antarctica. *Journal of Physical Oceanography*, 32(1), 202-215, 2002. (Reprint)

Acknowledgements

I would like to thank the many colleagues who have offered help and encouragement throughout the course of the work presented in this thesis and I wish to thank the following:

My supervisors Dr Keith Nicholls and Dr Grant Bigg who provided friendly and expert guidance whenever it was required. I would particularly like to thank Keith Nicholls who initially encouraged me into the world of tides and numerical modelling.

The members of the group: Chris Doake, Adrian Jenkins, Lars Semdsrud, David Vaughan and Andy Wood who have reviewed and commented on various chapters or papers associated with this thesis.

The fieldwork described in this thesis was very much a team effort and was successfully carried out with the assistance of Steve Hinde, Mark Johnson, Dr Keith Nicholls and Dr Svein Østerhus. Also, to the support staff at Halley and Rothera stations, especially the Air Unit for all their efforts in deploying the team members and vast amounts of equipment and fuel.

The work presented in this thesis has been undertaken whilst I have been an employee of British Antarctic Survey. I am grateful to BAS for providing the facilities and funding for my research.

Finally I must thank my family for their support throughout the course of this work.

Declaration

I declare that no material contained in this thesis has been used in any other submission for an academic award and that the work is entirely my own, except where specifically stated to the contrary. Some of the results have already been published and reprints of two papers which have resulted from the work are included at the back of this thesis.

Keith Makinson

CHAPTER 1

Introduction

1.1 Aims and scope of the thesis

1.1.1 Problems to be addressed

Ice shelves are the floating portion of the continental ice sheet. As they are in direct contact with both the ocean and atmosphere, they are the most sensitive parts of the ice sheet to a changing environment. Processes within the sub-ice shelf cavity between the ocean and overlying ice shelf are exceptionally difficult to study by direct observation, yet they play a key role in the mass balance of the ice sheet and convection within the world's deep oceans. Therefore, sub-ice shelf oceanographic processes represent an important element of the global ocean system and form the main focus of this thesis.

The work described in this thesis attempts to address a number of oceanographic questions relating to the effects of tides beneath Filchner-Ronne Ice Shelf.

1) *What is the regional distribution and magnitude of oscillatory and residual tidal currents?*
2) *How do tidal currents influence the vertical mixing and ultimately basal melting beneath the ice shelf?*
3) *How do the processes of mixing and melting effect the sub-ice shelf oceanography, the ice shelf morphology and the ocean beyond?*

The approach has been to apply numerical models to these questions, provide field data for model validation and to relate the results to the overall understanding of sub-ice shelf oceanography.

1.1.2 Outline of thesis

The first part of this thesis presents oceanographic fieldwork conducted at three sites on Filchner-Ronne Ice Shelf where oceanographic moorings were deployed. Details of the equipment and methods employed to obtain oceanographic data from beneath the ice shelf are given in Chapter 2, together with a broad description of the data that will be used later in this thesis to help validate a two-dimensional barotropic tidal model and assess a one-dimensional vertical mixing model. The barotropic tidal model and a description of the domain used in this study are outlined in Chapter 3 including its validation using tidal elevations. The output from the model also includes tidal currents and a comparison with the available tidal current measurements is given in Chapter 4. The average tidal currents and mixing energies are then used to discuss how the pattern of basal melting is influenced by tidally induced vertical heat fluxes. Chapter 5 presents the modelled Eulerian and Lagrangian residual currents that result from tidally generated mean flows and Stokes drift. These data are used to explain some of the features found in hydrographic observations from the shore lead and the morphology to the ice shelf close to the ice front. The results presented in chapters 4 and 5 have been published in *Makinson and Nicholls* [1999] and a copy of this paper is included at the back of this thesis.

The latter part of the thesis addresses the mechanisms of tidal vertical mixing and its influence on basal melting. Chapter 6 presents, a one-dimensional vertical mixing model coupled thermodynamically to the ice shelf. Chapter 7 describes the application of the mixing model to Filchner-Ronne Ice Shelf (FRIS) in general and also at specific locations. The broader implications for FRIS of the results from the mixing model are then discussed, including explanations of the observations close to or beneath the ice shelf. The model and many of the results presented in chapters 6 and 7 have been published in *Makinson* [2002] and a copy of this paper is included at the back of this thesis. Finally Chapter 8 summarises the main results of this thesis and considers their implications for the future modelling of

sub-ice shelf circulation. As an introduction to the work described in this thesis the remainder of this chapter is devoted to a brief review of other work in this field.

1.2 Ice shelves

Ice shelves are the floating extension of the Antarctic Ice Sheet and intimately couple ice sheet and ocean. They are fed by fast flowing ice streams and receive 60% of the continent's present day accumulation [*Giovinetto and Bentley*, 1985]. They can range in thickness from 2000 m at the grounding lines where the ice first goes afloat, to 100 m at the ice front and can extend over several hundred kilometres. They comprise 11% of the ice sheet area [*Lythe et al.*, 2000], fringe almost half the Antarctic coast and cover 40% (1.56×10^6 km^2) of the Antarctic Continental Shelf (Figure 1.1). Mass loss occurs by both iceberg calving from the seaward margins and melting at the ice shelf base. Uniquely, water masses in the sub-ice shelf cavities are isolated from direct interaction with the atmosphere and the ocean forcing is linked to the exchange of heat, freshwater and momentum at the ice shelf base. The interaction between water masses and ice shelf base result in: regions of strong basal melting particularly near deep grounding lines; the formation of marine ice bodies through the accumulation of ice crystals at the ice shelf base; and the production of seawater at temperatures below the surface freezing point, which have been identified as a component of global bottom water masses [*Schlosser et al.*, 1990; *Toggweiler and Samuels*, 1995].

1.3 Oceanography of the Southern Ocean

The Southern Ocean encircles the entire Antarctic continent and its associated ice shelves, and is bounded by the Antarctic continent to the south and the polar front to the north. This ocean has profound effects on many large scale oceanographic processes, and these effects are evident throughout the world's oceans. The ocean basins of the Southern Ocean have depths exceeding 4500 m while the relatively deep continental shelves typically have depths

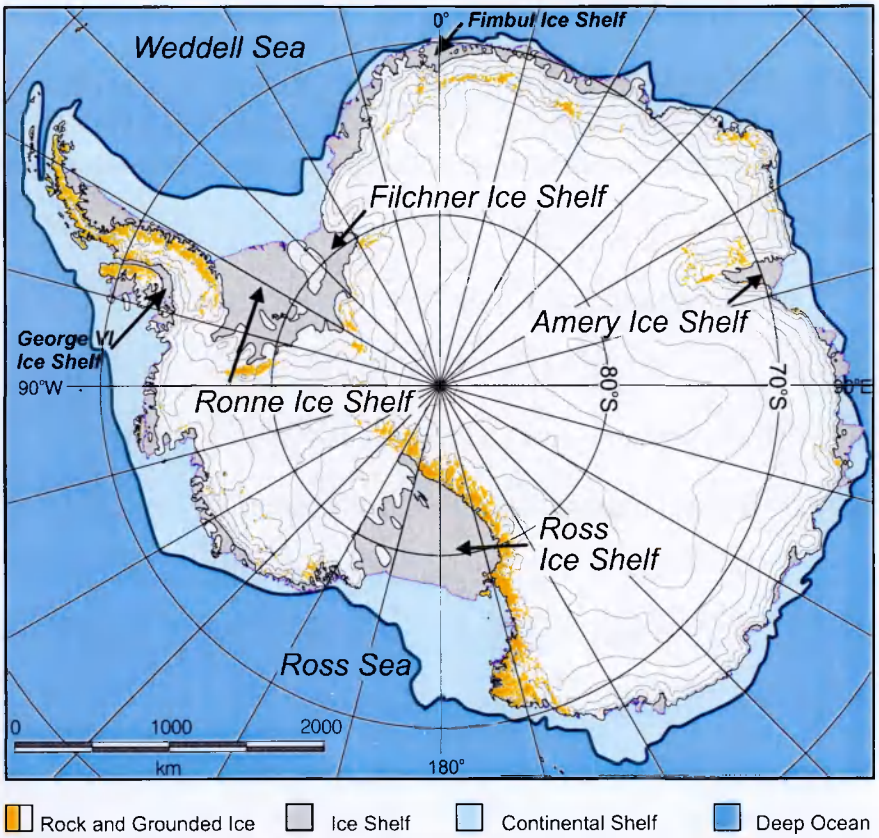

Figure 1.1 Map of Antarctica with surface elevation contours every 500 m reaching a maximum exceeding 4000 m in East Antarctica. The ice shelves (grey) cover 40% of the continental shelf (light blue).

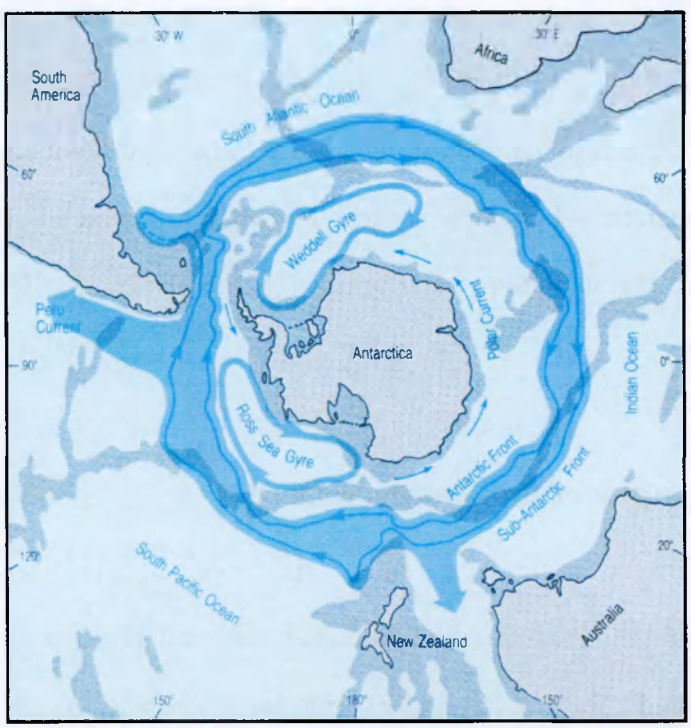

Figure 1.2 Taken from *Bearman* [1989]. Schematic map showing the circulation in the Southern Ocean. The path of the Antarctic Circumpolar Current (ACC) is shown by the dark blue with the darker lines indicating the average positions of the Antarctic Front and Sub-Antarctic Front. The approximate positions of the gyres in the Weddell Sea and Ross Sea are also shown, as is the path of the Antarctic Coastal Current or Polar Current.

of 300-500 m. Around East Antarctica these shelves are generally narrow (< 200 km) but around West Antarctica they are much broader, and, in the cases of the Weddell and Ross seas, they extend more than 1000 km from the shelf break.

The current structure around the continent is dominated by the Antarctic Circumpolar Current (ACC) that flows in an eastward direction (Figure 1.2) driven by the mean wind stress. Observations show that as the ACC passes through the relatively narrow Drake Passage between South America and the Antarctic Peninsula the transport averages 134 x 10^6 m^3 s^{-1} [*Nowlin and Klinck*, 1986]. However, along much of the continental margin there is a narrow westward current, the Antarctic coastal current. This current is not completely circumpolar, but becomes incorporated in the clockwise gyres in the Weddell and Ross seas.

Another feature of the Southern Ocean is the large fluctuations in sea ice extent (Figure 1.3), which varies between 4 x 10^6 km^2 in the austral summer and 21 x 10^6 km^2 in the austral winter when it covers about 60 % of the Southern Ocean. Its formation process is aided by the effect of strong katabatic winds that blow from the continent, forcing the sea ice northward thus forming and maintaining polynyas and allowing further sea ice production over the continental shelf [*Bromwich and Kurtz*, 1984]. Within these polynyas vigorous cooling and salinisation of surface waters occurs in winter months, particularly in the shore leads around the Antarctic coastline. The process of brine rejection is critical to the ultimate formation of bottom water masses as it densifies surface water masses. These surface water masses decrease the vertical stability of the ocean and enhance mixing via convection down into the water column [e.g. *Martinson*, 1990; *Ushio et al.*, 1999; *Bindoff et al.*, 2001]. The prevailing offshore movement of the sea-ice creates an export of fresh water ensuring a net brine production in these regions. After modification by shelf break processes or interaction with ice shelves these dense saline waters result in deep and

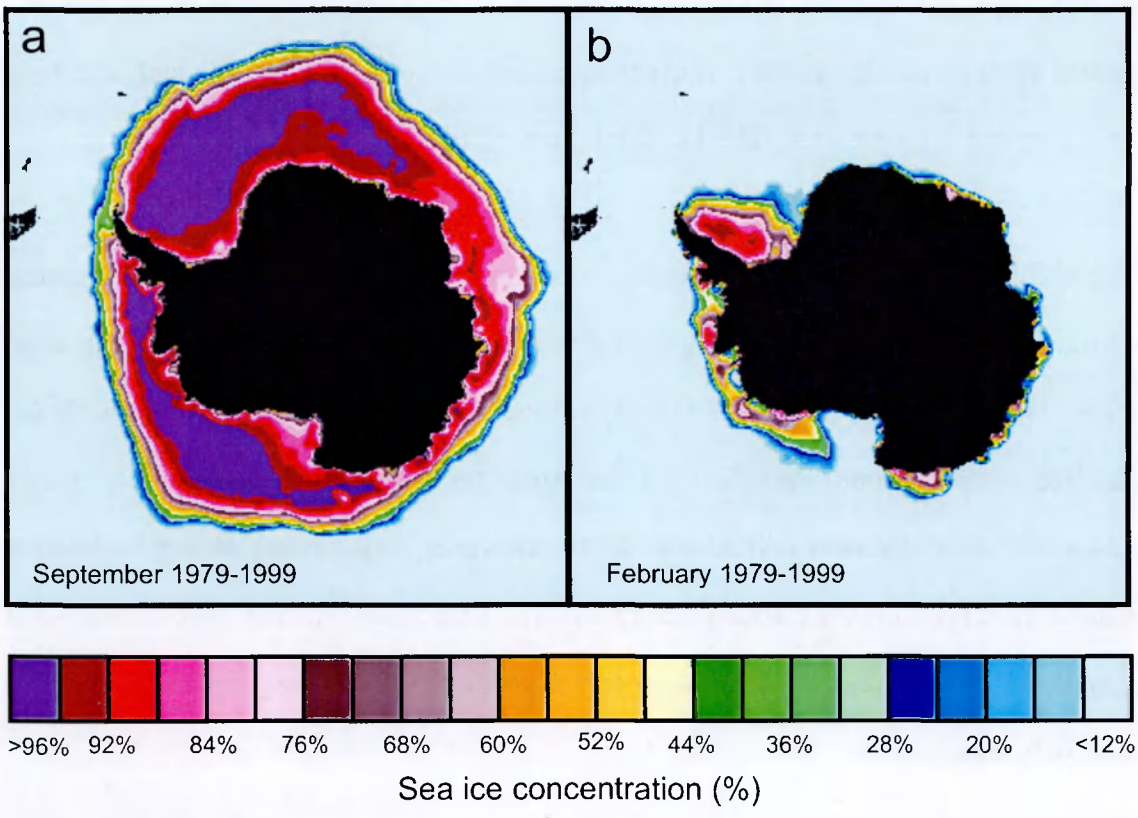

Figure 1.3 Seasonal changes in ice cover around Antarctica, as determined using passive microwave satellite measurements. Both images show the average monthly sea ice concentrations spanning the years 1979 to 1999 for **(a)** September (sea ice maximum) and **(b)** February (sea ice minimum). The different colours represent the percentage of sea-surface covered by ice. The data was provided by the EOS Distributed Active Archive Center at the National Snow and Ice Data Center, University of Colorado, Boulder, CO, USA.

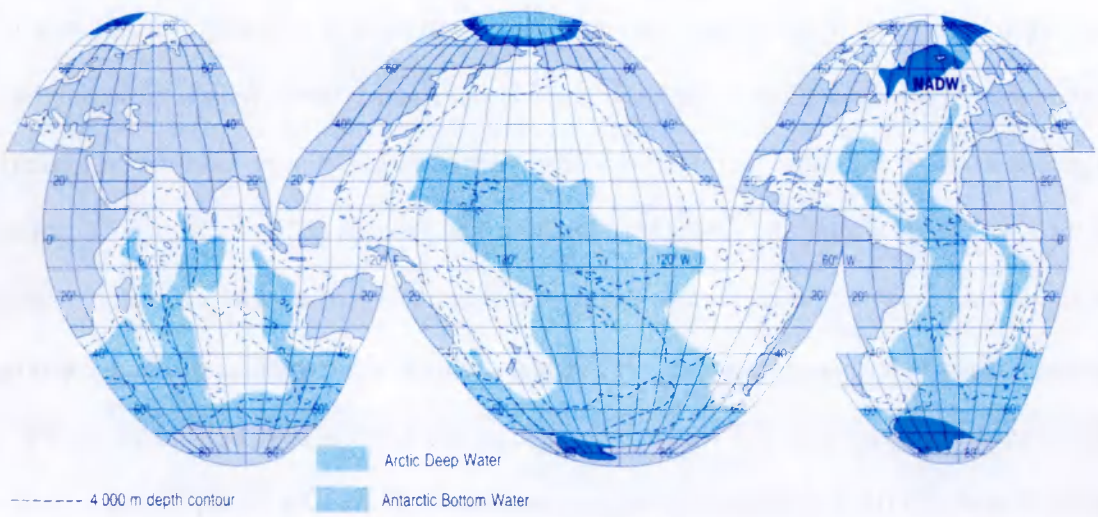

Figure 1.4 Taken from *Bearman* [1989]. The global distribution of deep water and bottom water masses with the source regions shown as dark blue. Antarctic Bottom Water (AABW) is the most widespread water mass in the world and is found in all three ocean basins, particularly in their southern parts.

bottom water formation [*Foster and Carmack*, 1976a; *Foldvik et al.*, 1985b; *Foster et al.*, 1987].

The net bottom water production rate in the Southern Ocean amounts to 21 ±6 Sv (1 Sv = 10^6 m^3 s^{-1}) [*Ganachaud and Wunsch*, 2000]. Spreading out from its source regions Antarctic Bottom Water (AABW) can be traced as far north as 50°N in the abyssal plains of north Atlantic basins (Figure 1.4) by its thermohaline characteristics and other chemical constituents [*Mantyla and Reid*, 1983]. It is this bottom water formation that helps drive part of the descending arm of the large-scale thermohaline circulation of the world's oceans through the sinking of cold, dense water masses, particularly in the Weddell Sea.

1.4 Oceanography of the Weddell Sea

The dense water masses formed within the Weddell Gyre are commonly referred to as two separate water masses, namely, Weddell Sea Deep Water (WSDW) with a potential temperature range of -0.7°C to 0.0°C and Weddell Sea Bottom Water (WSBW) with a potential temperature < -0.7°C. These are the major source of the bottom water for the world ocean [*Foldvik and Gammelsrød*, 1988; *Gordon et al.*, 1993; *Ganachaud and Wunsch*, 2000], and represent the densest of the major oceanic water masses [*Mantyla and Reid*, 1983]. Formation of these dense water masses in the Weddell Sea is favoured by the large-scale Weddell Gyre circulation. Here relatively warm saline water masses from the ACC are transported southward where they loose heat and gain density before turning northward along the Antarctic Peninsula to reach the northern periphery of the Weddell Gyre [*Fahrbach et al.*, 1995]. The formation of deep and bottom waters is believed to occur in specific sites in the western and southwestern Weddell Sea in the regions of FRIS and Larsen Ice Shelf [*Schlosser et al.*, 1990; *Fahrbach et al.*, 1994; *Weppernig et al.*, 1996].

The broad continental shelf in the southwestern part of the Weddell Sea is a primary region where the production of dense shelf water occurs. During a slow (~5 year) westward traverse across the shelf [*Gill*, 1973; *Foldvik et al.*, 1985b; *Jacobs et al.*, 1985], shelf waters are cooled towards their freezing point by contact with the atmosphere and increase their salinity because of the accumulation of brine during the production of sea ice. Much of the sea-ice forms in winter months in coastal polynyas kept open by katabatic winds draining from the continental interior. Close to ice shelves, tidal currents help to maintain open water [*Foldvik and Gammelsrød*, 1988], as does tidal divergence along the edge of the continental shelf [*Padman and Kottmeier*, 2000]. Water masses can attain salinities of over 34.8 psu adjacent to the Antarctic Peninsula and with temperatures approaching or at the surface freezing point (-1.91°C), it is the densest water mass in Antarctic waters and is referred to as Western Shelf Water (WSW) or generically as High Salinity Shelf Water (HSSW). In contrast, water in the east of the region has had insufficient time for brine to accumulate and is called Eastern Shelf Water (ESW). Over the deep Weddell Sea in summer, melting sea ice and solar heating cause a freshening and warming of only the very surface waters, the characteristics of the winter mixed layer being preserved in a sub-surface water mass known as Winter Water (WW) that remains close to the surface freezing point. Where Weddell Deep Water or Warm Deep Water (WDW) with a potential temperature above 0°C mixes with WW it forms modified Weddell Deep Water (MWDW) [*Foster and Carmack*, 1976b] which can find its way onto the continental shelf and intrude as far as the front of FRIS [*Foldvik et al.*, 1985a; *Gammelsrød et al.*, 1994]. Ice Shelf Water (ISW) is found close to the front of FRIS and within the Filchner Depression out to the continental shelf break. ISW is characterised by potential temperatures below the surface freezing point of seawater, and is formed by the interaction of WSW with ice at the base of FRIS. The upper layers of the ISW emerging from beneath Filchner Ice Shelf flow out of Filchner Depression and overflow at a depth of 600 m down the continental slope. Current meters at the top of the continental slope show an average yearly overflow of

0.8 ±0.2 Sv with an average temperature of -2.0°C [*Foldvik et al.*, 1985d; *Foldvik et al.*, 2001]. Because ISW is particularly cold, its downslope movement may be aided by a thermobaric effect where, as it descends the slope, it becomes increasingly more dense than its surroundings [*Killworth*, 1977]. Observations show that the plume is an intense thin bottom boundary current that can be traced to depth of 2500 m while maintaining its characteristics [*Foldvik et al.*, 1985c].

A schematic of the different water masses found in the Weddell Sea is shown in the potential temperature(Θ) - salinity (S) diagram in Figure 1.5. A principal component of AABW, defined as a deep bottom water mass with potential temperature < 2°C outside the Weddell Gyre, is WSBW. In the southern Weddell Sea, WSBW is formed by mixing water

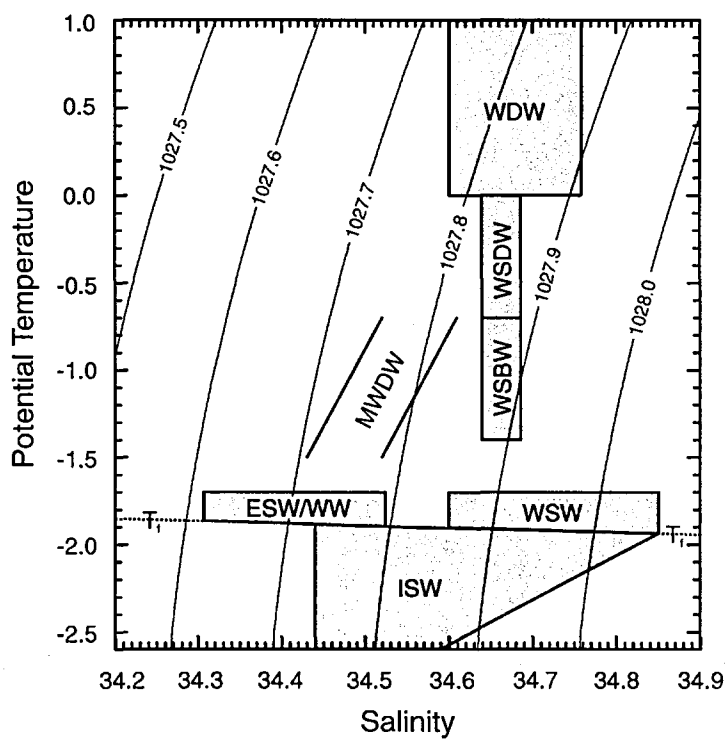

Figure 1.5 Modified from *Foldvik et al.* [1985b]. Schematic showing the water mass characteristics (in potential temperature-salinity space) of Weddell Sea Bottom Water (WSBW) and Weddell Sea Deep Water (WSDW). Other water masses are Warm Deep Water or Weddell Deep Water (WDW), Modified Warm Deep Water (MWDW), Winter Water (WW), Eastern Shelf Water (ESW), Western Shelf Water (WSW) and Ice Shelf Water (ISW). Also shown is the surface freezing point (T_f) and lines of constant potential density (kg m^{-3}) referenced to the sea surface.

masses with temperatures close to the freezing point at the continental shelf break. There are thought to be two specific modes of WSBW formation:

1. Through mixing near the shelf break of WDW with WW and WSW to form dense WSBW that flows down the continental slope, entraining the surrounding water as it descends into the deep ocean [*Foster and Carmack*, 1976a; *Foster et al.*, 1987].

2. As ISW spills over the continental shelf break and descends the slope it entrains and mixes with WDW and WSDW to form WSBW [*Foldvik et al.*, 1985b].

Using isotopes of Helium and Oxygen as tracers, *Weppernig et al.* [1996] found that ISW contributed significantly to the formation of WSDW and WSBW. Taking the estimated flow of ISW over the shelf break north of the Filchner Depression of 1 Sv together with the ratios of WSW, WW and ISW, they calculated a formation rate of about 5 Sv of WSBW. Many studies have estimated the total production for deep water formation in the Weddell Sea. They have used various parameters such as currents, temperature and salinity [*Foldvik et al.*, 1985b; *Gordon et al.*, 1993; *Muench and Gordon*, 1995; *Fahrbach et al.*, 2001], Helium and Oxygen isotopes [*Weppernig et al.*, 1996], chlorofluorocarbon concentrations [*Meredith et al.*, 2001] and phosphate-oxygen concentrations [*Broecker et al.*, 1998]. These estimates for the production of WSBW range form 1 to 5 Sv depending upon water type definitions, geographical locations and parameters measured. Considerable uncertainty still surrounds the overall production rate of bottom water masses in the Weddell Sea. However, the Weddell Sea remains a primary region for the formation of bottom water masses and is becoming progressively better known.

1.5 Filchner-Ronne Ice Shelf

The largest mass of floating ice on Earth is located in the southern Weddell Sea at the margin of the Antarctic Ice Sheet. The Filchner-Ronne system of ice shelves (Figure 1.6) is fed by ten major ice streams, draining 24% of the area of the continent's grounded ice

[*Giovinetto and Bentley*, 1985]. As the ice moves seaward further accumulation results from snow fall and the deposition of ice crystals at the ice shelf base. Ice is lost either by melting at the ice shelf base or by calving of icebergs at the ice front. FRIS covers an area of almost 450,000 km^2 [*Fox and Cooper*, 1994] and its ice thickness ranges from around 300 m at the ice front to a maximum of 2000 m at its deep grounding lines. Within the ice shelf there are three major ice rises, the largest of which, Berkner Island, extends more than 350 km south of the ice front, dividing the ice shelf into Ronne Ice Shelf (western portion) and Filchner Ice Shelf (eastern portion). In the southern portion of Ronne Ice Shelf lie Korff and Henry ice rises, with Doake Ice Rumples between them forming an additional major obstacle to the flow of ice. Between the ice rises and rumples three gaps allow the passage of water. There are two further small distinct points of grounding, Kershaw Ice Rumples close to the mouth of Rutford Ice Stream and Hemmen Ice Rise off the north west corner of Berkner Island.

Extending 400 km to the northeast of FRIS is a broad continental shelf with typical seabed depths of 400 m. The dominant feature of the seabed is the Filchner Depression that extends south from the continental shelf break, under Filchner Ice Shelf and along the east coast of Berkner Island towards the grounding line of Foundation Ice Stream (Figure 1.7). To the west of the region lies Ronne Depression which does not extend far beyond the ice front and is not as deep as Filchner Depression. Beneath the ice shelf Ronne Depression is bounded by the Antarctic Peninsula to the west and a ridge to the east and, farther south, Korff Ice Rise. Beneath FRIS the topography of the seabed is dominated by a downward slope towards the continental interior, where seabed depths can be over 1000 m greater than along the ice front. The seabed is deepest at the grounding lines of ice streams such as Rutford and Foundation (>1500 m). Typically the sub-ice shelf cavity dips downwards towards the grounding line as the seabed deepens and the ice shelf thickens. This geometry has important consequences for the ocean circulation within the cavity.

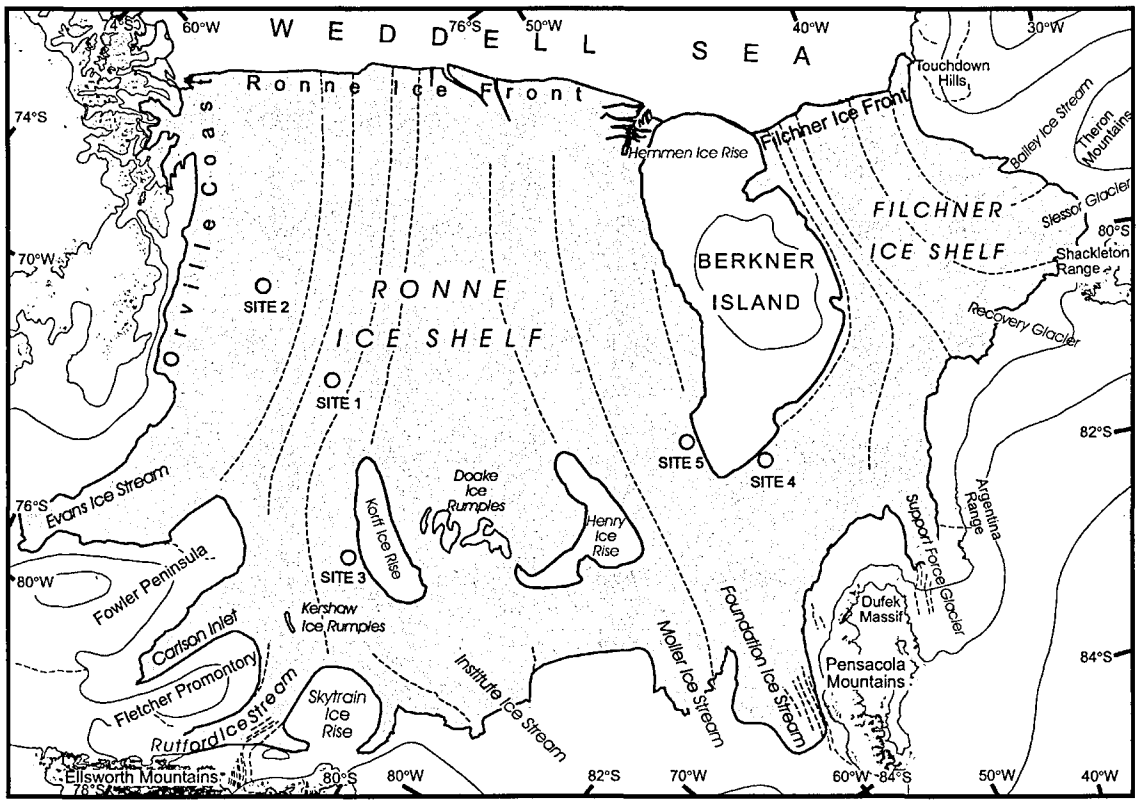

Figure 1.6 Map showing Filchner-Ronne Ice Shelf and the flow lines that delineate the discharge from the ten major ice streams that flow into the ice shelf. Geographical locations and drill sites (red dots) cited in the text are also shown.

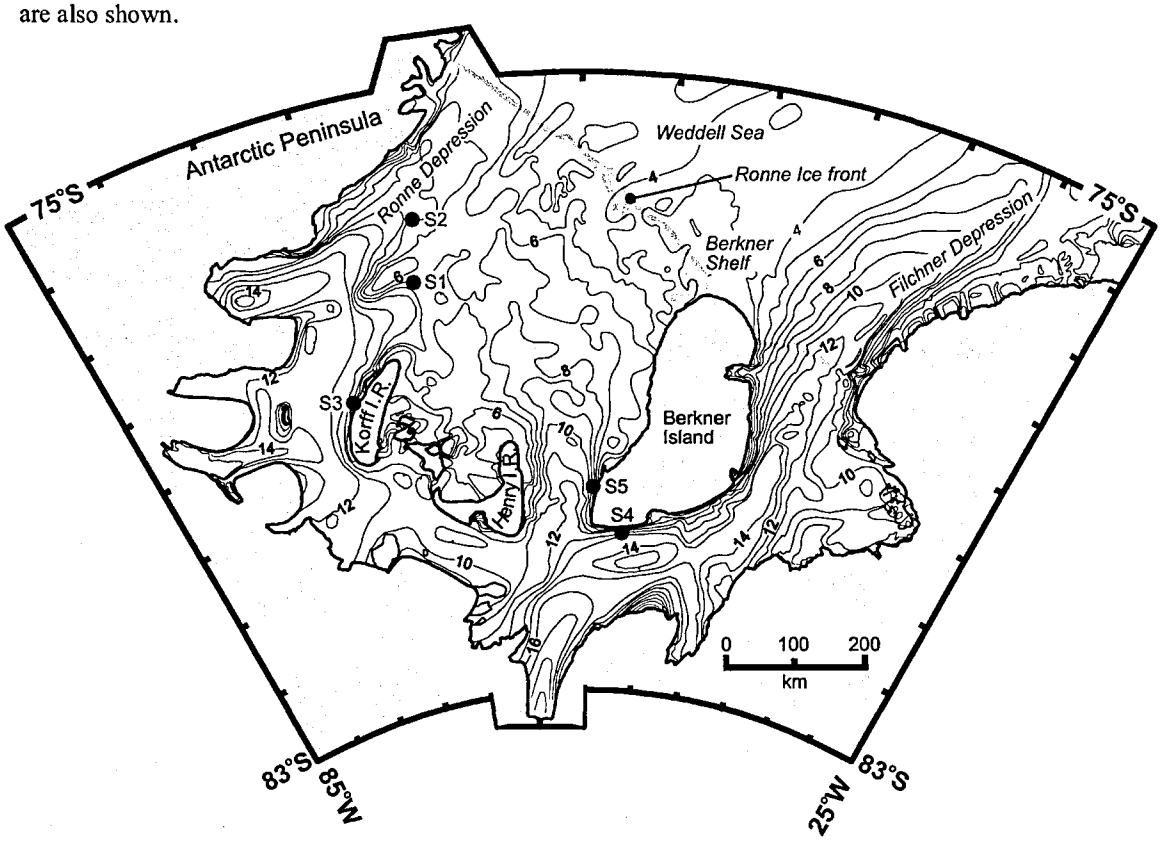

Figure 1.7 Modified from *Nicholls and Makinson* [1998]. Map showing the bathymetry in the area of Filchner-Ronne Ice Shelf. The contours give bathymetry in 100's of metres below sea level [*Johnson and Smith*, 1997] and S1, S2, S3, S4 and S5 show the positions of the five drill sites.

1.6 Ice-ocean interactions

The Antarctic Ice Sheet annually supplies an average 2.6 x 10^{15} kg of freshwater to the Southern Ocean via melting of the ice, either from icebergs or from under ice shelves [*Jacobs et al.*, 1992]. The circulation and associated meltwater input beneath ice shelves have a considerable impact on shelf water masses [e.g. *Foldvik et al.*, 1985b], and up to 75% of the ocean's deep waters may retain a signature of this meltwater input from beneath FRIS [*Toggweiler and Samuels*, 1995].

Melting beneath ice shelves relies on seawater having a temperature above the in situ freezing point, which is dependent on the concentration of dissolved salts and the pressure. Both increasing salt content and increasing pressure depresses the freezing point of the seawater. WSW with a salinity of 34.7 psu has a freezing point of -1.9°C. However, it is the depression of the freezing point with pressure that has important implications for ice-ocean interaction, with the freezing point being depressed by 0.00075°C for every decibar increase in pressure. Close to deep grounding lines the freezing point can be up to 1.5°C lower than the surface freezing point, resulting in high melt rates when WSW within the sub-ice shelf cavity comes into contact with the ice shelf base.

Cooling and freshening of seawater caused by melting, forces potential temperature and salinity along a straight line trajectory in Θ-S space. For an ice shelf with a temperature profile close to the freezing point, ice/ocean interactions result in water column properties that follow a line with a gradient close to 2.4°C psu^{-1}, whereas for an ice shelf with surface temperatures of -30°C the gradient increases to 2.8°C psu^{-1} [*Gade*, 1979]. Because of this relationship, the melt water signature strongly constrains the properties of waters modified beneath ice shelves.

The introduction of glacial melt water into seawater not only modifies its Θ-S properties but introduces two tracers important to Antarctic oceanography. Because of the preferential evaporation of ^{16}O over the oceans, snow fall that makes up the glacial ice is low in ^{18}O compared with seawater [*Morgan*, 1982]. Consequently, glacial melt water is low in ^{18}O, and, by comparing the $^{18}O/^{16}O$ ratio for inflowing and outflowing water, the concentration of melt water can be calculated, provided the ratio is known for the glacial ice. A second tracer is Helium, which is trapped in air bubbles in the ice and is also released into the water during melting. Because of the low solubility of helium in water, pure glacial meltwater is supersaturated and contains 14 times more Helium than ambient seawater, which has equilibrated with the atmosphere at surface pressure [*Schlosser*, 1986]. This provides a clear melt water signature, provided that the meltwater-rich outflow has not had the opportunity to re-equilibrate with the atmosphere.

1.7 Sub-ice shelf circulation

1.7.1 Observations

The density of the cold water masses found over the continental shelves is determined almost exclusively by salinity. When dense HSSW flows beneath an ice shelf and comes into contact with the ice shelf base it is cooled, but more importantly freshened, leading to buoyant plume of ISW rising up the inclined base of the ice shelf [*MacAyeal*, 1984b; *MacAyeal*, 1985a; *Jenkins*, 1999]. Turbulence within the plume entrains warmer water from below, sustaining melting and maintaining the ISW density below that of the surrounding waters. However, with decreasing depth the freezing point increases and where insufficient heat is entrained, the water becomes supercooled. Under these conditions disc-shaped frazil ice crystals can form and grow, before rising up to be deposited on the ice shelf base and forming marine ice bodies. *Robin* [1979] suggested that this process could lead to large areas of freezing and using ice-penetrating radar surveys [*Robin et al.*, 1983] mapped the marine ice bodies beneath FRIS (a meteoric ice/ocean interface gives strong radar returns

and meteoric ice/marine ice gives weak returns). Using ice core drilling, *Oerter et al.*, [1992] confirmed the presence of a large marine ice body beneath FRIS. Where marine ice deposits survive to reach the front of ice shelves, calved icebergs that roll over reveal green ice that result from the impurities in the marine ice (Figure 1.8) [*Warren et al.*, 1993]. The water modified beneath the ice shelf by these episodes of melting and freezing ultimately emerges at the ice front as ISW. Within such a core of outflowing ISW on the western side of Filchner Depression, frazil ice platelets of centimetre size have also been observed at a depth of 250 m [*Dieckmann et al.*, 1986].

Most oceanographic work in the southern Weddell Sea has been confined by perennial sea ice to the shore lead along the Filchner-Ronne Ice Front [*Foldvik et al.*, 1985a; *Gammelsrød et al.*, 1994] (Figure 1.9) and in the central part of the Weddell Sea [*Gill*, 1973; *Foster and Carmack*, 1976b; *Fahrbach et al.*, 1994]. Ship-borne oceanographic measurements close to the front of ice shelves identify the properties of water masses flowing in and out of the cavity, providing further clues about the sub-ice shelf oceanographic conditions, although they are confined to the short austral summer. However, instrument moorings can also be deployed and, despite the dangers from ice front advance, iceberg calving and the need for

Figure 1.8 An ice berg in the Weddell Sea with bands of green and white marine ice (under sunny conditions). The variation in the green colour depends upon the amount of marine-derived organic matter trapped within the ice [*Warren et al.*, 1993] during its formation from ice crystals that precipitate up from the ocean beneath the ice shelf. (Photo : Keith Makinson).

repeat cruises to recover instruments, a few year-round measurements close to ice fronts have been made [*Woodgate et al.*, 1998; *Foldvik et al.*, 2001].

Observations of the environment beneath Antarctic ice shelves are limited by the presence of the ice shelf itself. Only a small number of direct observations have been made through rifts or access holes drilled through ice shelves, because this usually requires an expensive air-supported operation to transport personnel, equipment and fuel to the drilling sites. Before 1986 there had been no direct observations from beneath FRIS, but using a hot water drill to penetrate the ice shelf, access was gained to the sub-ice shelf cavity [*Engelhardt and Determann*, 1987]. Using the difference between the depth of the radar reflection and the depth of ice drilled through, *Engelhardt and Determann* [1987] determined the presence of a 300 m thick layer of marine ice, as well as a 35 m layer of unconsolidated frazil ice at the ice shelf base. *Oerter et al.*, [1992] later obtained a 320 m ice core, about 50 km closer to the ice front, and confirmed the presence of marine ice below a depth of 150 m. Other hot water drilled holes where used to determine basal melt rates and obtain water samples [*Grosfeld*, 1990]. In the early 1990's groups from the British Antarctic Survey (BAS) and Alfred-Wegener-Institute (AWI) used hot water drills [*Makinson*, 1993; *Nixdorf et al.*, 1996] to penetrate the ice shelf at several locations on Ronne Ice Shelf. The first sub-ice shelf Conductivity-Temperature-Depth (CTD) profiles were obtained via hot water drilled holes in 1990/91 and 1991/92 [*Nicholls et al.*, 1991; *Robinson et al.*, 1994] and long term thermistor cable moorings to measure temperature were also deployed.

1.7.2 Numerical models

Because of the lack of observational data, numerical models have been developed to complement the sparse observations. These range from one-dimensional sub-ice shelf plume models to three-dimensional circulation models that extend out across the

continental shelf and into the deep ocean [*Williams et al.*, 1998]. In turn these models can be used to identify key locations where observational resources should be directed.

Modelling of the thermohaline circulation described above was initially undertaken using one-dimensional plume models that follow the development of the turbulent buoyant plume from grounding line to ice front. The plume of ISW was driven by the density difference between it and the WSW that filled the rest of the cavity. The vertical heat flux required to melt ice and maintain the buoyancy of the plume was obtained by entrainment of the underlying WSW (Figure 1.10). Mixing within the plume resulted from its motion, and the rate of entrainment was determined from the plume velocity and the bulk Richardson number. Where the density contrast fell to zero it was assumed that the plume detached itself from the ice shelf base and exited the cavity at depth (Figure1.10). The first models were applied to Ross Ice Shelf and had some success in simulating the properties of ISW outflows observed at the front of the ice shelf [*MacAyeal*, 1984b; *MacAyeal*, 1985a]. Further developments were made by *Jenkins* [1991] and *Nicholls and Jenkins* [1993] when a plume model was applied to Ronne Ice Shelf. Good agreement between observed and modelled melt/freeze rates was found along most of the flow line, except near the grounding line and ice front. In these areas tidal effects are likely to be important factors, however these were not included in the model.

More recently, the process of growth and deposition under supercooled conditions of frazil ice crystals, which rise up through the water column and accrete at the ice shelf base has been included in plume models [*Bombosch and Jenkins*, 1995; *Jenkins and Bombosch*, 1995]. The frazil ice crystals reduce the bulk density and cause the plume to accelerate, encouraging the growth of more crystals while deposition onto the ice shelf base causes it to decelerate and allow yet more crystals to settle out. As the flow regime usually depends on the basal topography, frazil ice deposition is often intense and highly localized

[*Bombosch and Jenkins*, 1995]. *Bombosch and Jenkins* [1995] identified several regions beneath FRIS were their model predicted high basal accumulation rates. These areas agreed reasonably well with the upstream extremity of the marine ice bodies beneath the ice shelf.

A two-dimensional circulation model has been used to attempt to calculate the likely circulations beneath FRIS [*Hellmer and Olbers*, 1989; *Hellmer and Olbers*, 1991]. The circulation was assumed to follow the ice thickness gradient and, as with the plume models, lateral variations in ice shelf gradients and the effects of Coriolis and tides were ignored. The circulation pattern between the interconnected cavities of Filchner Ice Shelf and Ronne Ice Shelf were examined using three differing geometries. In all cases each cavity was dominated by a single overturning cell with regions of melting and freezing. Two of the geometries used a shallow water column at the front of Ronne Ice Shelf. In these cases outflowing ISW occupied the whole water column at Ronne Ice Front, so both cavities were supplied with WSW from the inflow at Filchner Ice Front. Within the cavity beneath Ronne Ice Shelf the model indicated that water may recirculate several times before leaving the cavity as ISW. For the third geometry, a thicker water column at Ronne Ice Front allowed WSW to inflow. A stronger circulation developed beneath Ronne Ice Shelf because of the large density gradients between the inflow and outflow. Some of the inflow from Ronne Ice Front also supported the weaker circulation beneath Filchner Ice Shelf.

Determann and Gerdes [1994] applied the first three-dimensional circulation model to the sub-ice shelf domain. It incorporated the effects of the Earth's rotation on the ocean dynamics which had been neglected in previous sub-ice shelf modelling efforts. The model results highlighted that the circulation was constrained to follow the f/H contours, where f is the Coriolis parameter and H is the water column depth. The ice front consequently presented a considerable barrier to water mass exchange between the cavity and open ocean. Also, internal recirculation was indicated with regions of intense melting and

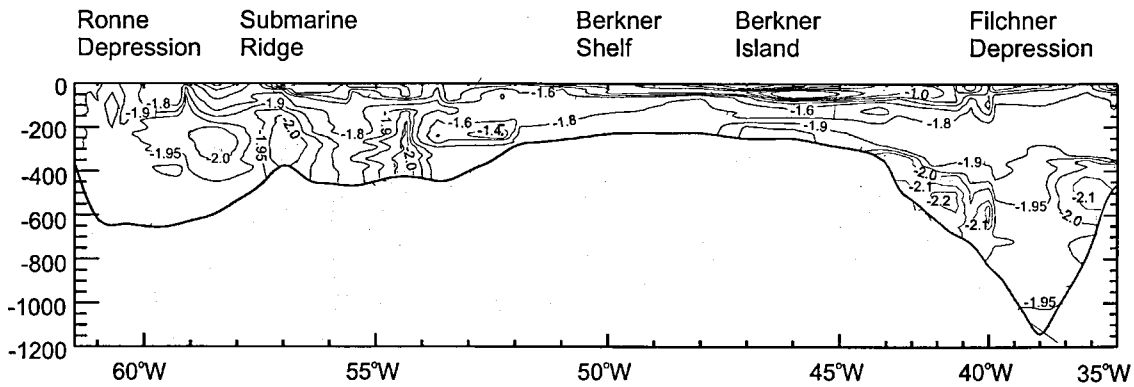

Figure 1.9 Section of potential temperature along the ice front from Ronne depression to the Filchner Depression [after *Foldvik et al.*, 1985c]. ISW colder than -2.0°C is shown in blue and MWDW above -1.6°C is shown in red. The bathymetry is represented by the dark shading.

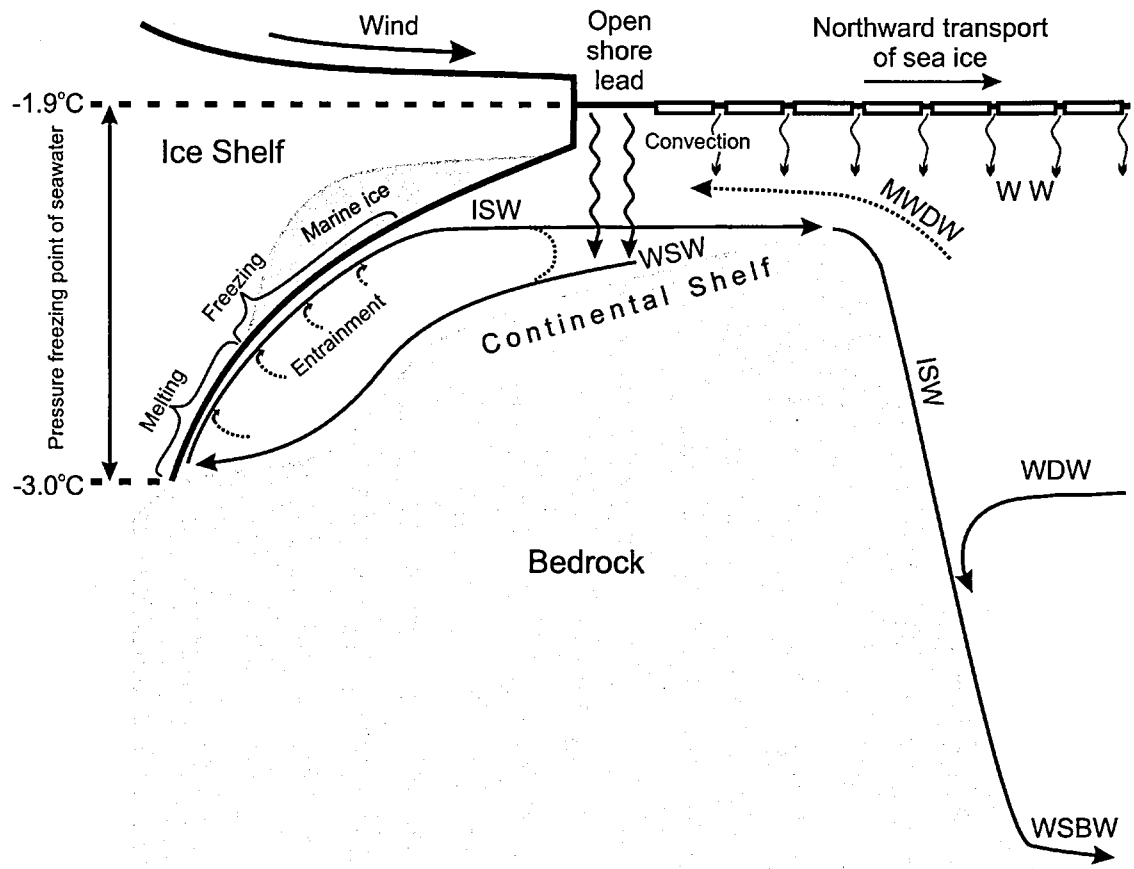

Figure 1.10 Schematic of the circulation over the continental shelf and beneath Filchner-Ronne Ice Shelf. At the continental shelf break Weddell Deep Water (WDW) mixes with Winter Water (WW) to form Modified Weddell Deep Water (MWDW) that intrudes across the continental shelf. Close to the ice front, Western Shelf Water (WSW) is formed by salt release during sea ice formation, particularly in the shore lead which is maintained through the winter by offshore winds and tidal currents. Where the WSW comes into contact with the ice shelf base at depth melting takes place due to the depression of the freezing point. This process forms buoyant Ice Shelf Water (ISW) which rises up the ice shelf base, further melting takes place until the ISW becomes super cooled and freezing takes place. The ISW exits the cavity at depth, crossing the continental shelf before descending the continental slope to form Weddell Sea Bottom Water (WSBW) and ultimately Antarctic Bottom Water (AABW).

freezing driving the flow. Extending the model to include the open ocean and atmospheric forcing, *Grosfeld et al.* [1997] found that the slopes of the Ronne and Filchner depressions were important. Here, the *f*/H contours cross the ice front with only a small lateral displacement, thus allowing the flow to cross the ice front, while elsewhere the ice front remained a barrier (Figure 1.11).

A drawback with all the sub-ice shelf thermohaline models outlined above is that they do not consider the impact of tidal forcing. In an environment isolated from atmospheric forcing, oscillatory tidal currents can generate residual circulations and provide a significant source of turbulent kinetic energy. These processes may be important to ice front exchanges and the vertical heat flux through the water column, both of which might lead to modification of the sub-ice shelf thermohaline circulation.

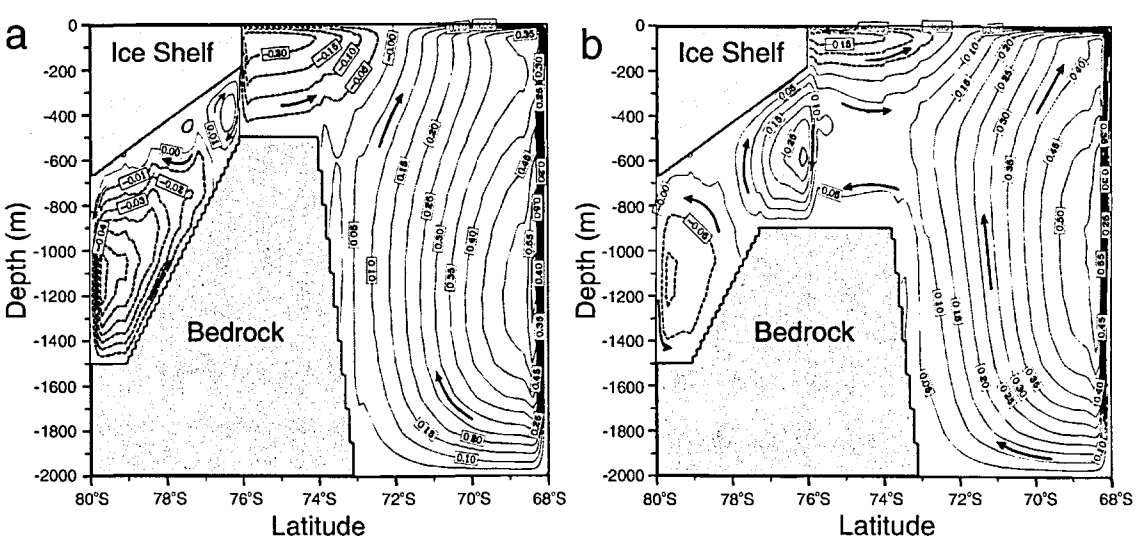

Figure 1.11 Taken from *Grosfeld et al.* [1997]. Stream function of the zonally integrated mass transport for two versions of the three-dimensional model using idealised geometry patterned on that found in the southern Weddell Sea. **(a)** Contains an ice shelf cavity, open continental shelf and open deep ocean. The contour interval beneath the ice shelf is 0.01 Sv and 0.05 Sv in the open ocean. **(b)** Same as **(a)** but two 900 m deep depressions cross either side of the continental shelf. The contour interval 0.05 Sv (1 Sv = 10^6 m^3 s^{-1}).

1.8 Ocean tides

Tidal energy is propagated from astronomical forcing of the oceans to the continental shelves, and is eventually dissipated by bottom friction in shallow water through the generation of turbulence. The most recent estimates of the rate of global energy input into the worlds ocean from astronomical forcing determined from satellite observations is 2.4 TW, with estimates through analysis of orbit perturbations, satellite altimetry and hydrodynamic models yielding similar dissipation rates [*Le Provost and Lyard*, 1997; *Munk*, 1997]. Isolated from direct atmospheric forcing, tides may represent the most energetic currents within a sub-ice shelf cavity.

The presence of an ice shelf provides a solid boundary at the top of the water column with effectively no horizontal motions, so its dynamical influence is to exert drag on the motion of the water, much like that exerted by the seabed. For vertical motions the ice shelf can be considered a free surface with no flexural rigidity, so it rises and falls passively with the tides. Only within a few kilometres of the grounding lines is this a poor assumption [*MacAyeal*, 1984a; *Vaughan*, 1995]. The draft of the ice shelf effectively reduces the water column thickness, with a step change in water column thickness occurring at the ice front.

Tides play a role in the atmosphere-ice-ocean system. Tidal currents help maintain shore leads along the front of ice shelves [*Foldvik and Gammelsrød*, 1988] and divergence in the current field maintains further leads, particularly near the continental shelf break [*Padman and Kottmeier*, 2000]. The generation of mean tidal currents or residual currents through the interaction of tidal oscillations with topography will advect water masses, particularly along ice fronts [*MacAyeal*, 1985b]. Vertical mixing can help modify water masses through turbulent mixing at the seabed and ice shelf base, and beneath ice shelves vertical mixing can enhance basal melting.

In the seas around the Antarctic continent the largest observed tidal range is in the southwest corner of Ronne Ice Shelf. Near the grounding line of Rutford Ice Stream a gravimeter record, dominated by semi-diurnal tides, showed peak-to-peak displacements of about 6 m [*Doake*, 1992]. Recently, *Padman et al.* [2002] used a circum-Antarctic tidal model to confirm that the largest tides occur in the Southern Weddell Sea and that in the channel south of Henry and Korff ice rises the tidal range can exceed 7 m during spring tides. In the Ross Sea, which is dominated by diurnal tides, the range does not exceed 2 m except close to the southern Siple Coast [*Padman et al.*, 2002].

Tidal models that include the cavity beneath FRIS within their domains such as *Genco et al.* [1994] and *Smithson et al.* [1996] have only investigated tidal elevations. Beneath Ross Ice Shelf it has been suggested that tidal currents and their associated mixing maybe one of the primary controls on the strength of the thermohaline circulation and that tidal rectification may help drive water masses in and out of the cavity [*MacAyeal*, 1984b; *MacAyeal*, 1985b]. *Scheduikat and Olbers* [1990] made a more detailed study of tidally induced vertical mixing and its effect on melting and freezing at the ice-ocean interface beneath Ross Ice Shelf with moderate success. When compared with Ross Ice Shelf, FRIS has greater levels of tidal activity. Clearly, to understand how the sub-ice shelf system works in detail, tidal activity beneath FRIS needs to be considered [*Williams et al.*, 1998].

1.9 References

Bearman, G., *Ocean Circulation*, Open University and Pergamon Press, 1989.

Bindoff, N.L., G.D. Williams, and I. Allison, Sea-ice growth and water-mass modification in the Mertz Glacier polynya, East Antarctica, during winter, in *Annals of Glaciology, Vol 33*, pp. 399-406, 2001.

Bombosch, A., and A. Jenkins, Modeling the Formation and Deposition of Frazil Ice beneath Filchner-Ronne Ice Shelf, *Journal of Geophysical Research, 100* (C4), 6983-6992, 1995.

Broecker, W.S., S.L. Peacock, S. Walker, R. Weiss, E. Fahrbach, M. Schroeder, U. Mikolajewicz, C. Heinze, R. Key, T.H. Peng, and S. Rubin, How much deep water is formed in the Southern Ocean?, *Journal of Geophysical Research-Oceans, 103* (C8), 15833-15843, 1998.

Bromwich, D.H., and D.D. Kurtz, Katabatic Wind Forcing of the Terra-Nova Bay Polynya, *Journal of Geophysical Research-Oceans, 89* (C3), 3561-3572, 1984.

Determann, J., and R. Gerdes, Melting and freezing beneath ice shelves: implications from a three-dimensional ocean-circulation model, *Annals of Glaciology, 20*, 413-419, 1994.

Dieckmann, G., G. Rohardt, H. Hellmer, and J. Kipfstuhl, The occurrence of ice platelets at 250 m depth near the Filchner Ice Shelf and its significance for sea ice biology, *Deep-Sea Research, 33* (2), 141-148, 1986.

Doake, C.S.M., Gravimetric tidal measurements on Filchner-Ronne Ice Shelf, in *Filchner Ronne Ice Shelf Programme Report*, pp. 34-39, Alfred-Wegener-Institute, Bremerhaven, Germany, 1992.

Engelhardt, H., and J. Determann, Borehole Evidence for a Thick Layer of Basal Ice in the Central Ronne Ice Shelf, *Nature, 327* (6120), 318-319, 1987.

Fahrbach, E., S. Harms, G. Rohardt, M. Schröder, and R.A. Woodgate, Flow of bottom water in the northwestern Weddell Sea, *Journal of Geophysical Research-Oceans, 106* (C2), 2761-2778, 2001.

Fahrbach, E., G. Rohardt, N. Scheele, M. Schröder, V. Strass, and A. Wisotzki, Formation and Discharge of Deep and Bottom Water in the Northwestern Weddell Sea, *Journal of Marine Research, 53* (4), 515-538, 1995.

Fahrbach, E., G. Rohardt, M. Schröder, and V. Strass, Transport and structure of the Weddell Gyre, *Annales Geophysicae, 12*, 840-855, 1994.

Foldvik, A., and T. Gammelsrød, Notes on Southern Ocean hydrography, sea-ice and bottom water formation, *Palaeogeography, Palaeoclimatology, Palaeoecology, 67*, 3-17, 1988.

Foldvik, A., T. Gammelsrød, E. Nygaard, and S. Østerhus, Current meter measurements near Ronne Ice Shelf, Weddell Sea: Implications for circulation and melting underneath the Filchner-Ronne ice shelves, *Journal of Geophysical Research*, 2001.

Foldvik, A., T. Gammelsrød, N. Slotsvik, and T. Tørresen, Oceanographic conditions on the Weddell Sea Shelf during the German Antarctic Expedition 1979/80, *Polar Research, 3* (2), 209-226, 1985a.

Foldvik, A., T. Gammelsrød, and T. Tørresen, Circulation and water masses on the Southern Weddell Sea Shelf, in *Oceanology of the Antarctic Continental Shelf*, edited by S.S. Jacobs, pp. 5-20, American Geophysical Union, Washington DC, 1985b.

Foldvik, A., T. Gammelsrød, and T. Tørresen, Hydrographic observations from the Weddell Sea during the Norwegian Antarctic Research Expedition 1976/77, *Polar Research, 3* (2), 177-193, 1985c.

Foldvik, A., T. Gammelsrød, and T. Tørresen, Physical oceanography studies in the Weddell Sea during the Norwegian Antarctic Research Expedition 1978/79, *Polar Research, 3* (2), 195-207, 1985d.

Foster, T.D., and E.C. Carmack, Frontal zone mixing and Antarctic Bottom Water formation in the southern Weddell Sea, *Deep-Sea Research, 23*, 301-317, 1976a.

Foster, T.D., and E.C. Carmack, Temperature and salinity structure in the Weddell Sea, *Journal of Physical Oceanography, 6*, 36-44, 1976b.

Foster, T.D., A. Foldvik, and J.H. Middleton, Mixing and Bottom Water Formation in the Shelf Break Region of the Southern Weddell Sea, *Deep-Sea Research Part a-Oceanographic Research Papers, 34* (11), 1771-1794, 1987.

Fox, A.J., and A.P.R. Cooper, Measured properties of the Antarctic ice sheet derived from the SCAR Antarctic digital database, *Polar Record, 30*, 201-206, 1994.

Gade, H.G., Melting of Ice in Sea Water: A Primitive Model with Application to the Antarctic Ice Shelf and Icebergs, *Journal of Physical Oceanography, 9* (1), 189-198, 1979.

Gammelsrød, T., A. Foldvik, O.A. Nøst, Ø. Skagseth, L.G. Anderson, E. Fogelqvist, K. Olsson, T. Tanhua, E.P. Jones, and S. Østerhus, Distribution of water masses on the continental shelf in the Southern Weddell Sea, in *The polar oceans and their role in shaping the global environment*, edited by O.M. Johannesen, R.D. Muench, and J.E. Overland, pp. 159-176, AGU, Washington DC, 1994.

Ganachaud, A., and C. Wunsch, Improved estimates of global ocean circulation, heat transport and mixing from hydrographic data, *Nature, 408* (6811), 453-457, 2000.

Genco, M.L., F. Lyard, and C. Le Provost, The Oceanic Tides in the South-Atlantic Ocean, *Annales Geophysicae, 12* (9), 868-886, 1994.

Gill, A.E., Circulation and bottom water production in the Weddell Sea, *Deep-Sea Research, 20*, 111-140, 1973.

Giovinetto, M.B., and C.R. Bentley, Surface balance in ice drainage systems in Antarctica, *Antarctic Journal of the US, 20* (4), 6-13, 1985.

Gordon, A.L., B.A. Huber, H.H. Hellmer, and A. Ffield, Deep and Bottom Water of the Weddell Seas Western Rim, *Science, 262* (5130), 95-97, 1993.

Grosfeld, K., Temperature profiles and investigation of the ice-shelf/ocean boundary using hot water drilled holes: report of field work on FRIS 1989/90, in *Filchner Ronne Ice Shelf Programme Report No 4*, edited by H. Oerter, pp. 109-111, Alfred-Wegener-Institute for Polar and Marine Research, Bremerhaven, Germany, 1990.

Grosfeld, K., N. Blindow, and F. Thyssen, Bottom melting on the Filchner-Ronne Ice Shelf, Antarctica, using different measuring techniques, *Polarforschung, 62*, 71-76, 1992.

Grosfeld, K., R. Gerdes, and J. Determann, Thermohaline circulation and interaction between ice shelf cavities and the adjacent open ocean, *Journal of Geophysical Research, 102* (C7), 15595-15610, 1997.

Hellmer, H.H., and D.J. Olbers, A two-dimensional model for the thermohaline circulation under an ice shelf, *Antarctic Science, 1*, 325-336, 1989.

Hellmer, H.H., and D.J. Olbers, On the Thermohaline Circulation beneath the Filchner-Ronne Ice Shelves, *Antarctic Science, 3* (4), 433-442, 1991.

Jacobs, S.S., R.G. Fairbanks, and Y. Horibe, Origin and evolution of water masses near the Antarctic Continental Margin: Evidence from $H_2{}^{18}O/H_2{}^{16}O$ ratios in seawater, in *Oceanology of the Antarctic Continental Shelf*, edited by S.S. Jacobs, pp. 59-85, American Geophysical Union, Washington DC, 1985.

Jacobs, S.S., H.H. Helmer, C.S.M. Doake, A. Jenkins, and R.M. Frolich, Melting of Ice Shelves and the Mass Balance of Antarctica, *Journal of Glaciology, 38* (130), 375-387, 1992.

Jenkins, A., A One-Dimensional Model of Ice Shelf-Ocean Interaction, *Journal of Geophysical Research, 96* (C11), 20671-20677, 1991.

Jenkins, A., The impact of melting ice on ocean waters, *Journal of Physical Oceanography, 29* (9), 2370-2381, 1999.

Jenkins, A., and A. Bombosch, Modeling the Effects of Frazil Ice Crystals on the Dynamics and Thermodynamics of Ice Shelf Water Plumes, *Journal of Geophysical Research, 100* (C4), 6967-6981, 1995.

Johnson, M.R., and A.M. Smith, Seabed topography under the southern and western Ronne Ice Shelf, derived from seismic surveys, *Antarctic Science, 9* (2), 201-208, 1997.

Killworth, P.D., Mixing in the Weddell Sea continental slope, *Deep Sea Res, 24*, 427-448, 1977.

Le Provost, C., and F. Lyard, Energetics of the M-2 barotropic ocean tides: an estimate of bottom friction dissipation from a hydrodynamic model, *Progress in Oceanography, 40* (1-4), 37-52, 1997.

Lythe, M.B., D.G. Vaughan, and the BEDMAP consortium, BEDMAP - bed topography of the Antarctic, 1:10 000 000 scale map., British Antarctic Survey, Cambridge, 2000.

MacAyeal, D.R., Numerical Simulations of the Ross Sea Tides, *Journal of Geophysical Research, 89* (C1), 607-615, 1984a.

MacAyeal, D.R., Thermohaline Circulation Below the Ross Ice Shelf - a Consequence of Tidally Induced Vertical Mixing and Basal Melting, *Journal of Geophysical Research, 89* (C1), 597-606, 1984b.

MacAyeal, D.R., Evolution of tidally triggered meltwater plumes below ice shelves, in *Oceanology of the Antarctic Continental Shelf*, edited by S.S. Jacobs, pp. 133-143, American Geophysical Union, Washington DC, 1985a.

MacAyeal, D.R., Tidal rectification below the Ross Ice Shelf, Antarctica, in *Oceanology of the Antarctic Continental Shelf*, edited by S.S. Jacobs, pp. 109-132, American Geophysical Union, Washington DC, 1985b.

Makinson, K., The Bas Hot-Water Drill - Development and Current Design, *Cold Regions Science and Technology, 22* (1), 121-132, 1993.

Makinson, K., Modeling tidal current profiles and vertical mixing beneath Filchner-Ronne Ice Shelf, Antarctica, *Journal of Physical Oceanography, 32*(1), 202-215, 2002.

Makinson, K., and K.W. Nicholls, Modeling tidal currents beneath Filchner-Ronne Ice Shelf and on the adjacent continental shelf: their effect on mixing and transport, *Journal of Geophysical Research, 104* (C6), 13449-13465, 1999.

Mantyla, A.W., and J.L. Reid, Abyssal Characteristics of the World Ocean Waters, *Deep-Sea Research Part A-Oceanographic Research Papers, 30* (8), 805-&, 1983.

Martinson, D.G., Evolution of the Southern-Ocean Winter Mixed Layer and Sea Ice - Open Ocean Deep-Water Formation and Ventilation, *Journal of Geophysical Research-Oceans, 95* (C7), 11641-11654, 1990.

Meredith, M.P., A.J. Watson, and K.A. Van Scoy, Chlorofluorocarbon-derived formation rates of the deep and bottom waters of the Weddell Sea, *Journal of Geophysical Research-Oceans, 106* (C2), 2899-2919, 2001.

Morgan, V.I., Antarctic Ice-Sheet Surface Oxygen Isotope Values, *Journal of Glaciology, 28* (99), 315-323, 1982.

Muench, R.D., and A.L. Gordon, Circulation and Transport of Water Along the Western Weddell Sea Margin, *Journal of Geophysical Research-Oceans, 100* (C9), 18503-18515, 1995.

Munk, W., Once again: Once again - tidal friction, *Progress in Oceanography, 40* (1-4), 7-35, 1997.

Nicholls, K.W., and A. Jenkins, Temperature and Salinity beneath Ronne Ice Shelf, Antarctica, *Journal of Geophysical Research, 98* (C12), 22553-22568, 1993.

Nicholls, K.W., and K. Makinson, Ocean circulation beneath the western Ronne Ice Shelf, as derived from in situ measurements of water currents and properties, in *Ocean, Ice, and Atmosphere: Interactions at the Antarctic Continental Margin*, edited by S.S. Jacobs, and R.F. Weiss, pp. 301-318, American Geophysical Union, Washingtion DC, 1998.

Nicholls, K.W., K. Makinson, and A.V. Robinson, Direct oceanographic observations from under the Rutford flowline, Ronne Ice Shelf., in *Filchner Ronne Ice Shelf Programme Report No 5*, edited by H. Oerter, pp. 27-31, Alfred-Wegener-Institute for Polar and Marine Research, Bremerhaven, Germany, 1991.

Nixdorf, U., H. Oerter, and H. Miller, The Hot-Water Drilling System of the Alfred Wegener Institute fur Polar und Meeresforschung (AWI), in *Proceedings of the 7th SCALOP symposium on Antarctic logistics and operations*, pp. 203, Cambridge, UK, 1996.

Nowlin, W.D., and J.M. Klinck, The Physics of the Antarctic Circumpolar Current, *Reviews of Geophysics*, *24* (3), 469-491, 1986.

Oerter, H., J. Kipfstuhl, J. Determann, H. Miller, D. Wagenbach, A. Minikin, and W. Graf, Evidence for Basal Marine Ice in the Filchner-Ronne Ice Shelf, *Nature*, *358* (6385), 399-401, 1992.

Padman, L., H.a. Fricker, R. Coleman, S. Howard, and L. Erofeeva, A New Tidal Model for the Antarctic Ice Shelves and Seas, *Annals of Glaciology*, *In Press*, 2002.

Padman, L., and C. Kottmeier, High-frequency ice motion and divergence in the Weddell Sea, *Journal of Geophysical Research*, *105* (C2), 3379-3400, 2000.

Robin, G.D., C.S.M. Doake, H. Kohnen, R.D. Crabtree, S.R. Jordan, and D. Moller, Regime of the Filchner-Ronne Ice Shelves, Antarctica, *Nature*, *302* (5909), 582-586, 1983.

Robin, G.d.Q., Formation, flow, and disintegration of ice shelves, *Journal of Glaciology*, *24*, 259-271, 1979.

Robinson, A., K. Makinson, and K. Nicholls, The oceanic environment beneath the north-west Ronne Ice Shelf, Antarctica, *Annals of Glaciology*, *20*, 386-390, 1994.

Scheduikat, M., and D.J. Olbers, A one-dimensional mixed layer model beneath the Ross Ice Shelf with tidally induced vertical mixing, *Antarctic Science*, *2*, 29-42, 1990.

Schlosser, P., Helium: a new tracer in Antarctic oceanography, *Nature*, *321*, 233-235, 1986.

Schlosser, P., R. Bayer, A. Foldvik, T. Gammelsrød, G. Rohardt, and K.O. Munnich, O-18 and Helium as Tracers of Ice Shelf Water and Water Ice Interaction in the Weddel Sea, *Journal of Geophysical Research*, *95* (C3), 3253-3263, 1990.

Smithson, M.J., A.V. Robinson, and R.A. Flather, Ocean tides under the Filchner-Ronne Ice Shelf, Antarctica, *Annals of Glaciology*, *23*, 217-225, 1996.

Toggweiler, J.R., and B. Samuels, Effect of Sea-Ice on the Salinity of Antarctic Bottom Waters, *Journal of Physical Oceanography*, *25* (9), 1980-1997, 1995.

Ushio, S., T. Takizawa, K.I. Ohshima, and T. Kawamura, Ice production and deep-water entrainment in shelf break polynya off Enderby Land, Antarctica, *Journal of Geophysical Research-Oceans*, *104* (C12), 29771-29780, 1999.

Vaughan, D.G., Tidal Flexure at Ice Shell Margins, *Journal of Geophysical Research*, *100* (B4), 6213-6224, 1995.

Warren, S.G., C.S. Roesler, V.I. Morgan, R.E. Brandt, I.D. Goodwin, and I. Allison, Green icebergs formed by freezing of organic-rich seawater to the base of Antarctic ice shelves, *Journal of Geophysical Research*, *98*, 6921-6928, 1993.

Weppernig, R., P. Schlosser, S. Khatiwala, and R.G. Fairbanks, Isotope data from Ice Station Weddell: Implications for deep water formation in the Weddell Sea, *Journal of Geophysical Research-Oceans*, *101* (C11), 25723-25739, 1996.

Williams, M.J.M., A. Jenkins, and J. Determann, Physical controls on ocean circulation beneath ice shelves revealed by numerical models, in *Ocean, Ice, and Atmosphere: Interactions at the Antarctic Continental Margin*, edited by S.S. Jacobs, and R. Weiss, pp. 285-299, AGU, Washington DC, 1998.

Woodgate, R.A., M. Schrøder, and S. Østerhus, Moorings from the Filchner Trough and the Ronne Ice Shelf Front: Preliminary Results, in *Filchner Ronne Ice Shelf Programme Report No 12*, edited by H. Oerter, pp. 85-90, Alfred-Wegener-Institute for Polar and Marine Research, Bremerhaven, Germany, 1998.

CHAPTER 2

Field Work on Filchner-Ronne Ice Shelf

2.1 Introduction

2.1.1 History of sub-ice shelf oceanography

Prior to direct observations, sub-ice shelf circulation has generally been inferred from ship-borne ice front measurements [e.g. *Foldvik et al.,* 1985; *Nøst and Foldvik,* 1994; *Nøst and Østerhus,* 1998]. Direct oceanographic observations beneath ice shelves are limited by the presence of the ice shelf itself, which varies in thickness from a few hundred metres to 2 km. Furthermore, the remoteness of the sites selected for direct observations require an expensive logistical operation to transport personnel, equipment and fuel to field locations using ski-equipped aircraft. At present the only way of gaining direct oceanographic measurements from beneath ice shelves is by drilling access holes and using oceanographic instruments modified for borehole deployment.

In 1977, as part of the Ross Ice Shelf Project, an access hole was drilled using a flame-jet drill through 420 m of ice at Site J-9 (82°22.5'S 168°37.5'W) [*Clough and Hansen*, 1979] allowing oceanographic profiles of the 240 m thick water column to be obtained over a six-day period [*Foster*, 1983]. Such access holes to the underlying seawater allow CTD profiles of the water column to be obtained together with water samples that can be analysed for oceanographic tracers such as $\delta^{18}O$ and δD. The salinity, temperature and tracers collectively provide a "signature" of the water masses that can be used to identify the origins of the water and their subsequent interactions with the ice shelf. Once oceanographic profiling has been completed, it is possible to deploy a range of

instrumentation to monitor temperature, conductivity, and current speed and direction. These instruments can be regularly logged to provide long term measurements from within the ice shelf, the water column and across the ice/ocean interface. Such data sets can reveal changes in ice shelf temperatures [*Paren and Cooper*, 1988], basal melt rates [*Grosfeld and Blindow*, 1993] and fluctuations in the characteristics of the water column [*Nicholls et al.*, 1991]. Knowledge of these directly observed parameters beneath ice shelves aids mass balance studies, the understanding of the dynamics of ice shelf and ocean, and the ice/ocean interaction. Besides Ross Ice Shelf, a small number of CTD observations have also been made beneath George VI Ice Shelf [*Cooper et al.*, 1988], Fimbul Ice Shelf [*Østerhus and Orheim*, 1992], Ronne Ice Shelf [*Nicholls and Makinson*, 1998; *Nicholls et al.*, 2001] and most recently Amery Ice Shelf [*Mike Craven, Pers. com.*, 2001].

On FRIS the first CTD profiles from beneath the ice shelf were obtained in January 1991. A hot water drill was used to penetrate ice 562 m thick at Site 1 about 300 km from the ice front in the western area of Ronne Ice shelf (Figure 2.1). A borehole deployable CTD and water sampling system was used to obtain the first in situ information from the 364-m deep water column [*Nicholls et al.*, 1991]. In the following year, an access hole at Site 2 yielded more in situ data from the eastern flank of Ronne Depression [*Robinson et al.*, 1994; *Robinson and Makinson*, 1994], 200 km from the ice front. Here ice 541 m thick overlies a 400 m water column. At both these sites, CTD sections and water samples were obtained and long term thermistor cables deployed with data initially transmitted via satellite link. Site 3 was occupied in January 1996 and was located 500 km from the ice front and 17 km west of Korff Ice Rise where 825 m of ice overlies a 485-m deep water column [*Nicholls et al.*, 1997]. CTD sections and water samples were obtained. An oceanographic mooring was deployed for long term measurements that consisted of two current meters and five Conductivity-Temperature-Pressure (CTP) units. A thermistor cable was also deployed that extended down to the first current meter, about 20 m below the ice base. All data were

recorded locally in a data logger with data from mooring also being transmitted via satellite link.

2.1.2 Aims of fieldwork

The aim of the field work was to acquire further unique oceanographic data in the ocean cavity beneath FRIS that could address some of the unresolved oceanographic questions. The work described here is a continuation of an investigation into the oceanographic regime beneath FRIS that began in the early 1990's. The focus is away from the western Ronne Ice Shelf of sites 1, 2 and 3, to the south eastern corner of Ronne Ice Shelf and westernmost Filchner Ice Shelf. The aim was to provide data on water column structure and circulation, estimated rates of melting and/or freezing, water mass residence times and source locations as well as seasonal variations, tidal currents and vertical energy fluxes. These data will be used to validate the tidal model in Chapter 4, evaluate residual tidal currents in Chapter 5 and the contribution of tides to the vertical heat flux in Chapter 7. The data sets will also be used by others to help control the large scale circulation models that are applied to the sub-ice shelf cavity. The remainder of this chapter describes the techniques and instruments employed in gathering sub-ice shelf oceanographic data.

2.2 Gaining access - Hot water drilling 1998/99

2.2.1 Logistical constrains and site locations

Both Antarctica itself and the BAS logistics infrastructure place limitations on the hot water drilling/oceanographic work. The use of Twin Otter aircraft to establish field camps limits the maximum size of single items of equipment such as drill winches, oceanographic moorings and snowmobiles (skidoos), with some items having to be broken down and reassembled in the field. Each item must also be light enough to be hand-manageable by four or fewer personnel, working on soft snow. With Twin Otter payloads of around 2000 lbs, deployment of equipment, fuel and personnel requires many input flights. The

Figure 2.1 Location map showing the logistical routes (red) to the drill sites on Filchner-Ronne Ice Shelf via various permanent stations and field fuel depots using both ships and aircraft. The ice shelves are shaded in grey.

large distance to the nearest station requires the aircraft to refuel at least once or twice, therefore the flying hours required to service both the fuel depots and the field site increase rapidly with distance from a station. Consequently, the number of instrumented sites across FRIS is limited because of the expense of this type of work. Sites are chosen on the basis of testing as many sub-ice shelf circulation models as possible, the aim being to disprove models as clearly as possible. Ideally, the observational data should identify the model(s) that most closely match the physical processes occurring beneath FRIS, rather than provide only partial agreement for several models.

Previous hot water drilling work on Ronne Ice Shelf (sites 1, 2 and 3) has been supported from Rothera Station using Twin Otter aircraft. The aircraft refuel at permanent fuel depots at Fossil Bluff on the east coast of Alexander Island, and at Sky-Hi in the Sweeney Mountains, southern Palmer Land (Figure 2.1). These depots are also supported from Rothera Station. After the completion of drilling at Site 3, a depot of drilling equipment was established at Site 4 (80°59.1' S 51°36.4' W) in January 1996 between Berkner Island and the Dufek Coast, 12 km south of Berkner Island. Fuel depots were placed at both Site 4 and Site 5 (80°20.0' S 54°46.4) in the following years, with Site 5 located between Berkner Island and Henry Ice Rise, 17 km west of the southwestern coast of Berkner Island. The 1998/99 fieldwork at sites 4 and 5 was primarily supported from Halley Station on the Brunt Ice Shelf because of its proximity, only 800 km distant, as opposed to Rothera Station, more than 1500 km to the north. The remaining drilling and oceanographic equipment was in place by the end of December 1998, having been flown by Twin Otter from Halley Station via a fuel depot at Touchdown Hills (Figure 2.1)

2.2.2 Local seismic surveys

Bathymetric and ice thickness data had previously been obtained in the vicinity of Site 4 [*Johnson and Smith*, 1997] and were used to identify the best location for the drill site. In

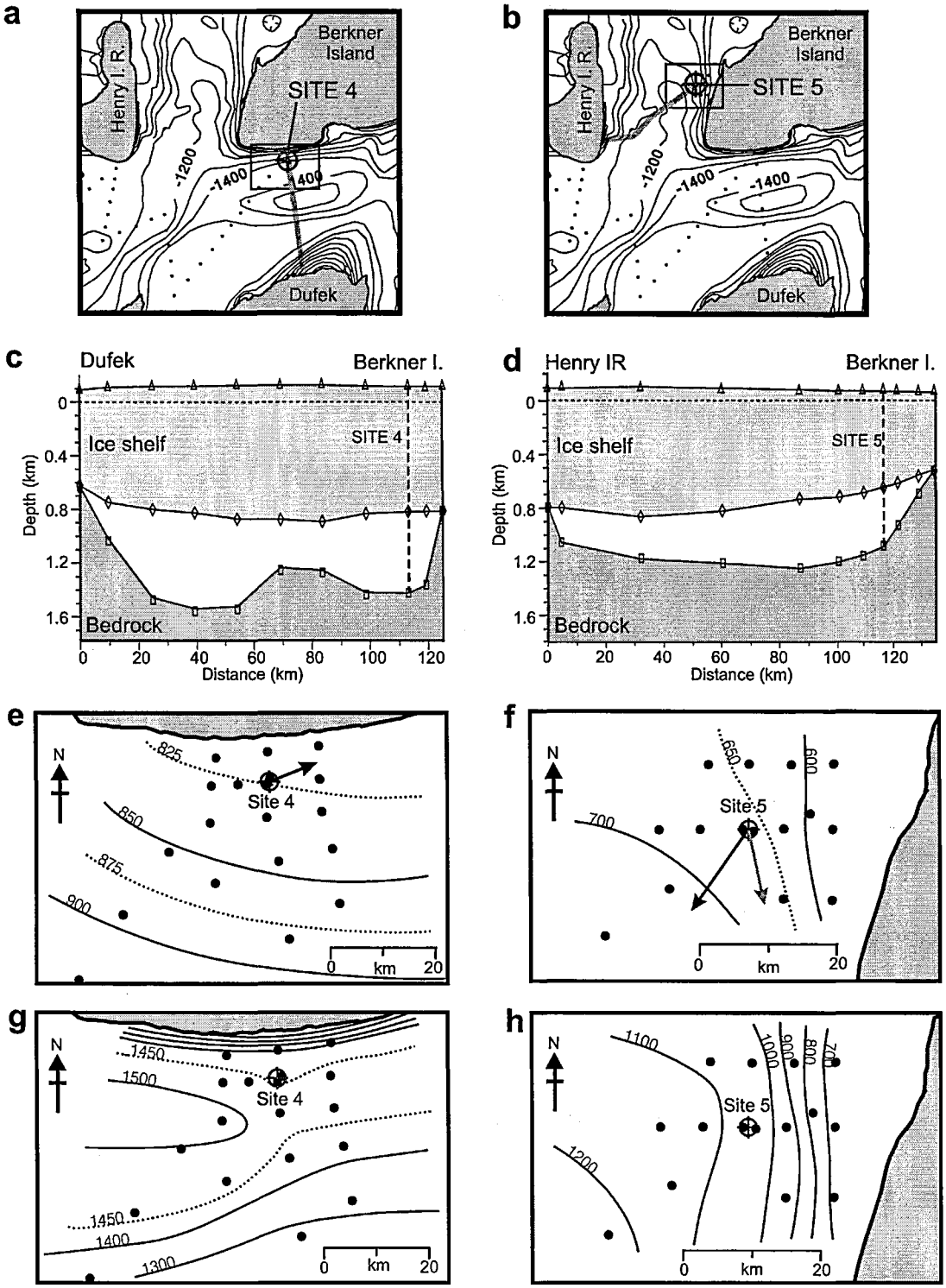

Figure 2.2 Modified from *Nicholls et al.* [2001]. Topography in the vicinity of sites 4 and 5, as determined by local seismic surveys. The areas covered by the survey are indicated by the highlighted boxes in **(a)** and **(b)** together with the path of the cross sections shown in **(c)** and **(d)**. The cross sections show the thickness of ice shelf and water column with the vertical dashed lines indicating the location of the drill sites. Markers on the ice and bedrock surfaces indicate the location of seismic stations along the section. Contours of ice shelf draft in metres around Sites 4 and 5 are shown in **(e)** and **(f)** with the dots showing the locations of seismic measurements The shaded area is grounded ice (the coast) and the arrows indicate the velocity of the mean flow. **(g)** and **(h)** show the contours of bedrock depth from the local survey around the drill sites.

the vicinity of Site 5, previously existing bathymetric maps [*Vaughan et al.*, 1994] were based on only a few scattered data points. Local seismic surveys were performed by a two-man travelling party (Mark Johnson and Steve Hinde) around each of the drill sites at a grid spacing of 5 to 10 km to both refine the selection of the drill sites and to aid in the interpretation of the data [*Nicholls et al.*, 2001]. Maps showing contours of ice shelf draft and bedrock topography are given in Figure 2.2 together with cross sections running out from the coast of Berkner Island to the Dufek Massif coast and Henry Ice Rise. Both bedrock and ice base topography are smooth at this resolution with the Site 4 section showing a mid-channel ridge, flat ice base and steep slope towards the Berkner Island Coast. The Site 5 section shows a relatively gentle rise in the bedrock towards the Berkner Island coast that is accompanied by a similar rise in the ice base.

2.2.3 Drilling system description

The BAS hot water drill was initially developed to obtain direct oceanographic observations from beneath George VI Ice Shelf and more recently Ronne Ice Shelf. The original Hot Water Drill (HWD) provided a means of rapidly gaining access to the sea water beneath George VI Ice Shelf for a period of hours or days [*Cooper et al.*, 1988]. Through the 1990's the work on Ronne Ice Shelf placed more demands on the HWD, and I adapted ideas from other drilling projects such as the Ross Ice Shelf Project at J-9, Antarctica [*Koci*, 1984], Jakobshavns Glacier, Greenland [*Iken et al.*, 1989], Ice Stream B, Antarctica [*Humphrey and Echelmeyer*, 1990]. I successfully incorporated these ideas into the BAS hot water drilling system [*Makinson*, 1993] and a programme of hot water drilling on Ronne Ice Shelf began in the 1990/91 austral summer at Site 1.

The hot water drilling system used at sites 4 and 5 is a significantly enhanced version of the system described by [*Makinson*, 1993; *Makinson*, 1994] that had been used at sites 1, 2 and 3. The description here outlines the present drill configuration and a schematic is given in

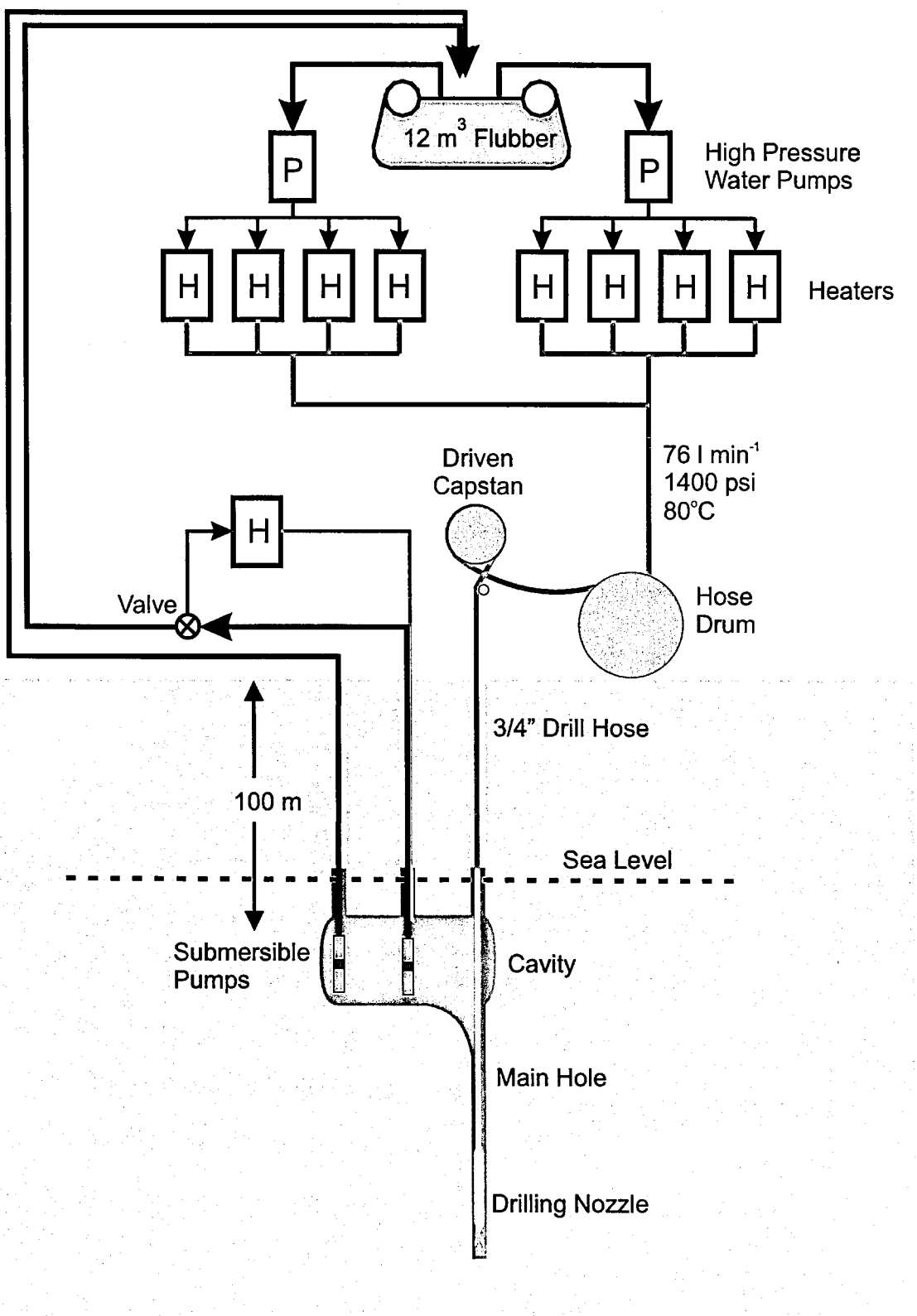

Figure 2.3 Block diagram of the hot water drilling system used on Filchner-Ronne Ice Shelf at Sites 3, 4 and 5 to drill through ice up to 941 m thick.

Figure 2.3. At the heart of the system is a pair of diesel-driven, positive-displacement, high pressure CAT pumps, each rated at 38 l min^{-1} flow rate at a maximum pressure of 2000 psi. The water is heated by a rank of up to eight oil-burners with horizontal, double coiled heat exchangers. The nominal power for each burner is 80 kW with an estimated efficiency of about 60% for the whole heating system.

Two submersible borehole pumps, powered by 2 hp single phase electric motors, retrieve water from the borehole cavity and return it to a 12 m^3 storage flubber via a 1" bore thermoplastic hose. The flubber is made from a plastic covered fabric and packs into a small volume. The 60 m immediately above the nozzle was ¾" steel braided hose, the remainder consisting of 350 m lengths of ¾" thermoplastic hose with a polyester fibre braid. The steel hose is used to provide weight to keep the drill hose vertical. The drill hose is lowered and raised using a hydraulically-powered capstan and stored at low tension on the winch drum, which is also hydraulically powered (Figure 2.4). Electrical power for the drilling system is primarily provided by a pair of diesel-driven, 8 KVA, single phase generators, with smaller petrol-driven generators also available.

Initial drilling of the hole uses a nozzle with a forward pointing, full cone water jet. The reaming nozzles use a backward pointing cone jet that washes over the larger nozzle of either 0.13 m or 0.17 m diameter, guaranteeing a minimum hole diameter. At the front of the reaming nozzle there is a long nose section to follow the existing hole. Several drill parameters are monitored by a data logger and PC: water temperature and pressure at the surface, tension in the hose, speed and depth of the nozzle. In addition, a small data logger fitted inside the reaming nozzles records the temperature of the water arriving at the nozzle.

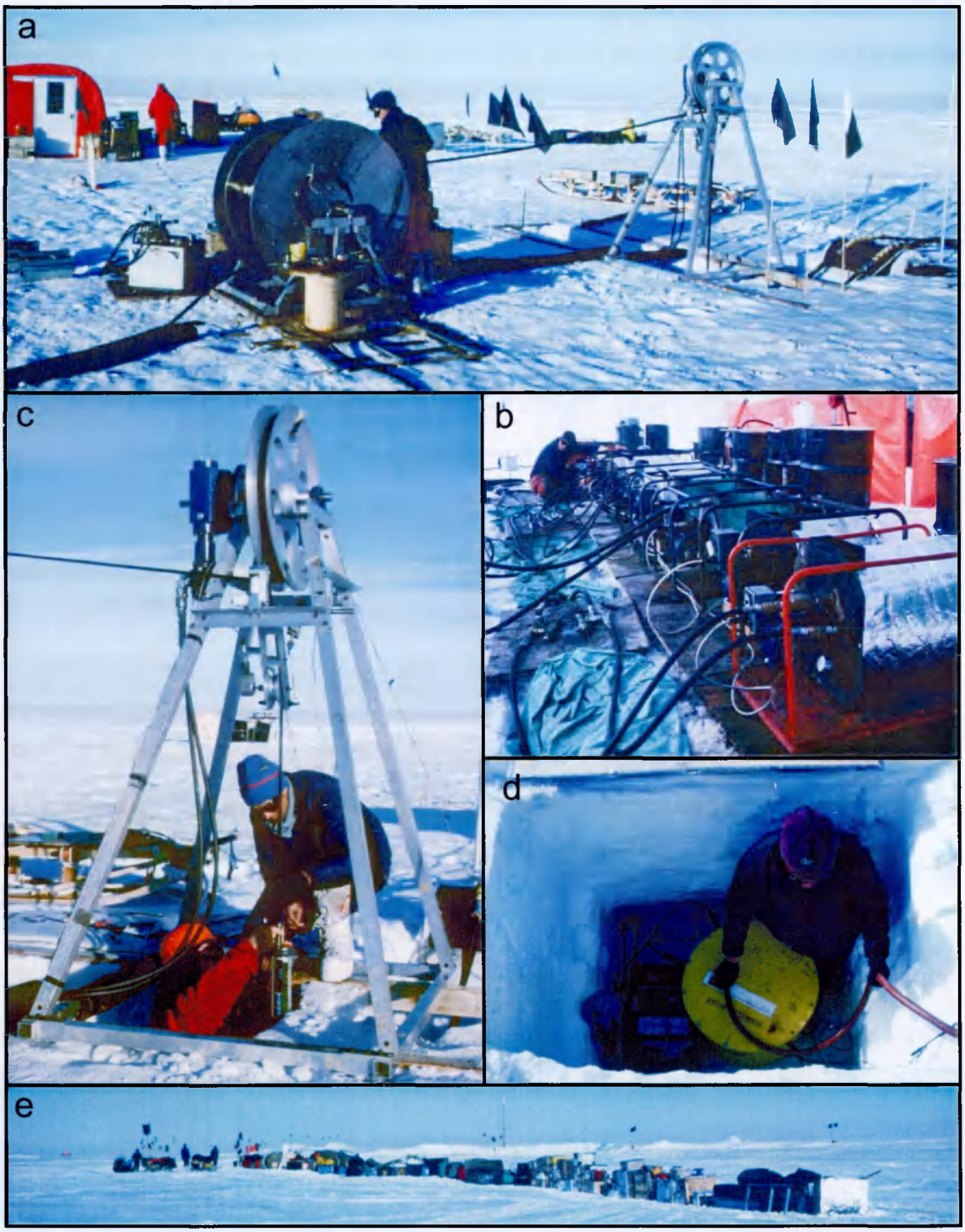

Figure 2.4 The BAS hot water drill and members of the drilling team on Ronne Ice Shelf at Site 4. **(a)** In the foreground, Steve Hinde re-lays the drilling hose on the winch drum which can store over 1000 m of 3/4" bore hose with the work tent in the background. To the right is the 2 m circumference capstan wheel used to power the drilling hose up and down the hole and on the far right are the two 1" bore hoses from the submersible pumps 105 m below the surface. **(b)** Shows the rank of eight heat exchangers used to heat the water with wind breaks behind to provide shelter for the equipment and drillers. **(c)** Svein Østerhus and Keith Nicholls attaching a Conductivity-Temperature unit to the cable during the deployment of the oceanographic mooring. **(d)** Mark Johnson (also in **(b)**) prepares the mooring data logger unit in a pit which will be covered in snow to protect the unit from the worst of the winter cold. **(e)** Cargo ready to be flown to Site 5, with the Site 4 Argos transmitter in the middle background. (Photo's : Keith Makinson)

2.2.4 Mode of operation

The initial method of operation of the drill system has remained virtually unchanged for the course of drilling programme on Ronne Ice Shelf. The method provides a drilling strategy that best utilises the available fuel and satisfies the needs of the oceanographic work. Firstly, water from the storage tank is used to drill two parallel holes, approximately one metre apart, 0.25 m in diameter to a depth that is below sea level (115 m at Site 4 and 95 m at Site 5). To establish the water recirculation system an interconnecting cavity is formed (Figure 2.3) and the drilling of the main hole can begin using the smaller nozzle. The hole is drilled to a depth of 420 m before it is reamed using the 0.13 m nozzle to ensure the required minimum hole diameter. Drilling and reaming continues in 350 m sections until the base of the ice shelf is reached. The primary indication that the ice shelf has been penetrated comes from a sudden change in the water level when the hydraulic connection is made with the sea. The hole is reamed up to a diameter of 0.30 m using the reaming nozzles, the diameter of the hole can be checked using a borehole caliper before any oceanographic work begins. To combat the constant refreezing of the water filled hole, periodic reaming is essential to maintain the required diameter. The work then settles into a cycle of oceanographic and reaming work periods, this continues until fuel supplies dictate that the CTD profiling work must stop and, after a final ream, a range of instrumentation is deployed to monitor temperature, conductivity and current speed and direction. At Site 4 the access hole was drilled over 3.2 days through 941 m of ice that was underlain by 621 m of water. A total of 6500 l of fuel was used to drill and maintain the hole for just over 4 days. At Site 5, 4500 l of fuel was used to create and maintain the access hole over a three-day period. The ice at Site 5 was 763 m thick and underlain by 402 m of water. At both sites, once the CTD work had been completed, the hole was re-widened and an instrument mooring deployed.

Five people were available during the drilling at sites 4 and 5 with four personnel being regarded as the minimum required for the drilling and oceanographic work, which can continue 24 hours-a-day for up to a week or more. During the shift work people were allocated a core 12-hour work period and a 6-hour core sleep period. The three hours either side of the work period were used for either work or rest depending on the status of the drilling or CTD work.

2.2.5 Determination of drilling speeds

A hole drilled through an ice shelf should ideally be of constant diameter to allow the most efficient use of the hole for oceanographic work. As the water temperature at the nozzle decreases because of heat losses through the hose wall, the amount of energy available for drilling is reduced. To compensate for this loss, the drilling speed is reduced with increasing depth. During the field season at Site 3, a miniature data logger was used to measure directly the temperature of the water arriving at the nozzle. The 120 m immediately above the nozzle was ¾″ steel braided hose, the remainder consisting of 350 m of ¾″ polyester fibre braid hose. During drilling and reaming of the hole, the water level remained at 90 m below surface and water pumped down the hose took approximately 6 minutes to reach the nozzle. In that time the water cools as the hose conducts heat away to the cold water surrounding the hose. Since the surface water temperature (T_{in}), flow rate (Q_d) and depth of the nozzle (y) are known, the thermal resistance (Z) of the hose can be determined from [*Humphrey and Echelmeyer*, 1990]:

$$T_d(y) - T_w = T_{in} e^{-y/\lambda} \tag{2.1}$$

where

$$\lambda = \rho_d c_d Q_d Z \tag{2.2}$$

where T_d is the nozzle water temperature at depth y, T_w is the water temperature outside the hose ($\approx 0°C$), λ is a characteristic decay length, and ρ_d and c_d are water density and specific

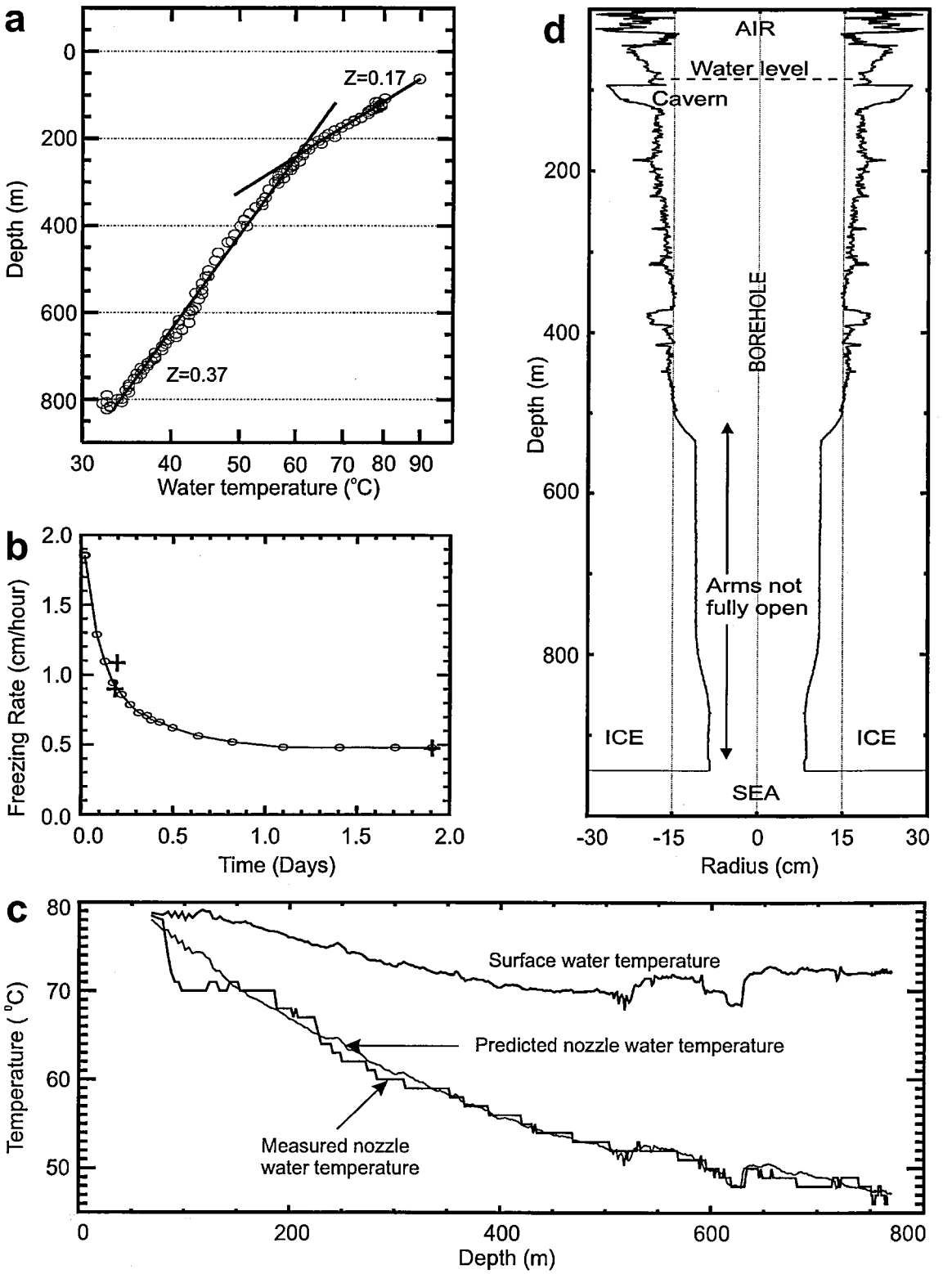

Figure 2.5 **(a)** Nozzle water temperature ($\log_{10}$ scale) versus depth below surface at Site 3. The solid lines represent the best least squares fit to the observed temperatures with the gradients providing the thermal resistance of the two types of hose used. **(b)** Measured freezing rate (change in hole diameter) in a test well versus time for a water filled hole in ice at -28°C [*Srikanta Jois*, 1993]. The crosses show the freezing rates measured at Site 1 using successive caliper profiles [*Makinson*, 1993]. **(c)** Results from logging water temperature at the surface and at the drilling nozzle at Site 5. Also shown is the nozzle water temperature predicted using the thermal properties of the two types of hose that were deduced using data from Site 3. **(d)** A measured caliper profile of the hole drilled at Site 5 soon after the reaming of the hole had finished.

heat capacity per unit volume. The values of Z for the steel braid and polyester fibre braid hoses were determined to be 0.17 m °C W^{-1} and 0.37 m °C W^{-1} respectively, from the best least squares fit to the data (Figure. 2.5a) [*Makinson*, 1996]. Knowledge of these values allows the prediction of the nozzle water temperature for future work. This enables a more accurate determination of the necessary drilling speeds for the production of holes of a uniform diameter.

At sites 4 and 5 the same hoses were used as at Site 3, but there was only 60 m steel braid hose and the flow rate was increased by almost a factor of two. Using the thermal properties of the hoses, Figure 2.5c shows that the predicted nozzle temperatures closely match the measured temperatures.

Using successive caliper profiles at Site 1, a few hours after the hole had been drilled in ice at -26°C, showed borehole closure rates (by refreezing) of 9 to 11 mm hr^{-1} that decreased to 5 mm hr^{-1} once the hole had been open for almost two days [*Makinson*, 1994]. *Srikanta Jois* [1993] undertook a comprehensive hole refreezing study in a test well with ice at -28°C, similar to the ice temperatures on Ronne Ice Shelf. The results confirmed the field observations, with initial refreezing rates of almost 20 mm hr^{-1} that fell to 5 mm hr^{-1} after the hole had been open over 24 hours (Figure 2.5b). Using a simple model that uses the thermal characteristics of the hoses and rates of borehole refreezing, optimum drilling speeds were determined to provide a hole approximately 0.3 m in diameter at Site 4 (Figure 2.5d).

2.3 Sub-ice shelf oceanographic instruments

2.3.1 CTD profiler

The slim-line (60 mm diameter) and light weight (4 kg) CTD units were designed and built by Meerestechnik-Elektronic GmbH in Germany. The three instruments were specially

designed to be borehole deployable under polar conditions and to take 150 ml water samples. The water sampler was based on the *Richards and Melling* [1987] design, and is pressure compensated to avoid the introduction of errors as potentially supercooled water samples are raised to the surface [*Nicholls and Jenkins*, 1993]. The water samples can then be analysed for salinity and oceanographic tracers such as $\delta^{18}O$ and δD. The instrument is connected to the surface via a single conductor armoured cable that is used for power and signal output.

Temperature accuracy is quoted at 0.01 °C with a resolution of 0.001 °C and the conductivity has a quoted accuracy of 0.01 mS cm^{-1} and resolution of 0.001 mS cm^{-1}. With careful calibration an accuracy of ±0.003°C and ±0.003 mS cm^{-1} could be achieved. The pressure is accurate to 0.1%. Signals from the sensors are digitised in the probe and transmitted to the surface unit at a measurement frequency of 3 Hz and logged by a laptop PC.

2.3.2 Thermistor cable

The Betatherm thermistors were the glass bead type with a nominal resistance of 3 kΩ at 25°C. In an attempt to remove the measurement inaccuracies that had plagued previous deployments which were assumed to result from the water pressure at depth, the thermistors for the Site 3 deployment were enclosed in a small metal tube and soldered into the cable wires. At the lower end, the wires were soldered together and two remaining wires without thermistors are used as a common return. A polyurethane jacket was then extruded over the whole assembly and the resulting time constant for the thermistors was about 3 minutes. Once deployed a Campbell 21X data logger is used to measure the thermistors and record the data with a resolution of 0.002°C.

For both field measurements and during calibration of thermistors the Steinhart-Hart equation is required for the resistance-temperature relationship. The Steinhart-Hart equation

is an empirically developed third degree polynomial that best represents the resistance-temperature relationship of NTC thermistors. When resistance is known the form of the equation is

$$\frac{1}{T} = A + B\ln R + C(\ln R)^3, \tag{2.3}$$

where T is temperature in degrees Kelvin and R is the resistance in Ohms. The coefficients; A, B and C can be solved simultaneously using three temperatures spanning the temperature range of interest.

2.3.3 Conductivity-temperature-pressure units and current meters

The sub-ice shelf oceanographic moorings were developed by Christian Michelsen Research (CMR) in Norway. Their IFIX inductive instrument systems [*Lothe*, 2000] have successfully been deployed beneath Fimbul Ice Shelf, FRIS and beneath drifters in the Weddell Sea. The system consists of three main parts, the cable, the instruments and the surface unit. The two-way length of cable is made up of a kevlar strength member, braided nylon cover and teflon-insulated copper wire and is designed to withstand mechanical stresses and high water pressures and be relatively inexpensive. The instruments communicate using an inductive link (Figure 2.6). Often, the geometry of the ice shelf and cavity are poorly known and the oceanography is certainly unknown. Having inductive communications allows sensors to be easily placed anywhere on the cable without the need to install connectors. The instruments are set to make a measurement each hour, with the current meters vector averaging over an interval of 10 minutes. Each instrument unit has its own set of batteries and data is digitised locally before transmission to the surface. Because of this type of inductive communications through the pressure housing, the main body is made of glass and the ends are of titanium. The surface unit contains a data logger and Argos satellite transmitters, which allow near real time data to be transmitted to the user, who is also able to monitor the health of the system. There is a dropout rate of about

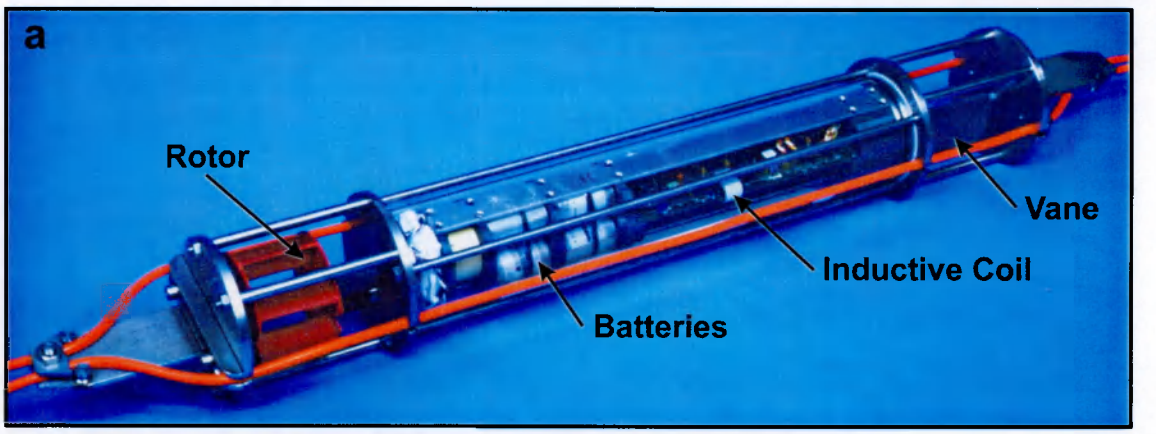

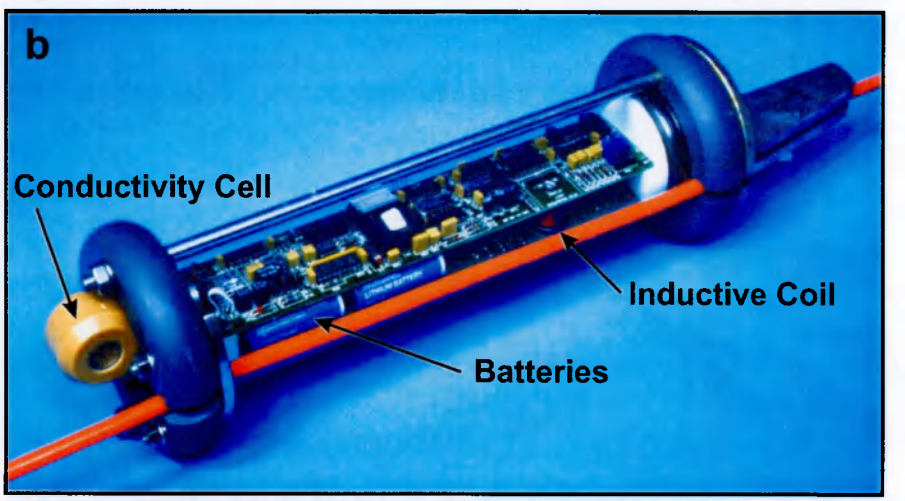

Figure 2.6 Photographs of the sub-ice shelf oceanographic mooring instruments used at Site 3, 4 and 5.
(a) Vane and rotor current meter with glass pressure housing. (Photo: from BAS)
(b) Conductivity-Temperature-Pressure unit with glass pressure housing. (Photo: from BAS)
(c) Doppler current meter unit being deployed at Site 5. (Photo: Keith Makinson)

15% using the satellite link but the full data set is also backed up locally on a data logger. Once operational, the surface data logger and lithium battery pack are buried at least 1 m below the snow surface to insulate the unit during the winter. The whole system has sufficient battery capacity to remain operational for more than three years.

The vane and rotor current meters have an estimated accuracy of 0.01 m s^{-1} and rotor has a speed threshold of about 0.003 m s^{-1}. The direction is accurate to 5°. The acoustic current meters based on the Aanderra RCM9 sensor have an accuracy of ±0.5 cm s^{-1} and a resolution of 0.3 cm s^{-1}. These sensors integrate over a region up to about 1 m from the instrument and the direction is accurate to 5°. Temperature and conductivity sensors have a resolution of 0.02°C and 0.02 mS cm^{-1}.

2.3.4 Instrument calibrations (temperature and salinity)

All oceanographic instruments need to be calibrated pre and post deployment, although post deployment calibration is not always possible for many instruments used beneath ice shelves. I set up an in-house calibration facility has been set up at BAS to calibrate the sub-ice shelf oceanographic instruments (CTD's, thermistor cables and mooring instruments) and better understand their characteristics over the relatively narrow range of temperatures and salinities found beneath FRIS. The facility consists of a well-stirred 250 l bath, enclosed with up to 30 cm of polystyrene insulation (Figure 2.7). For low temperature calibrations salt is added to depress the freezing point, typically -5°C for CTD calibrations and as low as -12°C for thermistor cables. Calibration data are taken at several points over the conductivity range of 25 mS cm^{-1} to 30 mS cm^{-1} and over the temperature range of -5°C to +5°C. During the conductivity calibration the salinity of the bath remains constant and the water is cooled by a primary cooler and a smaller heat exchanger in a secondary water bath. If constant temperatures are required for instruments with large time constant, the secondary bath is used to stabilise the calibration bath temperature to within ±0.0005°C

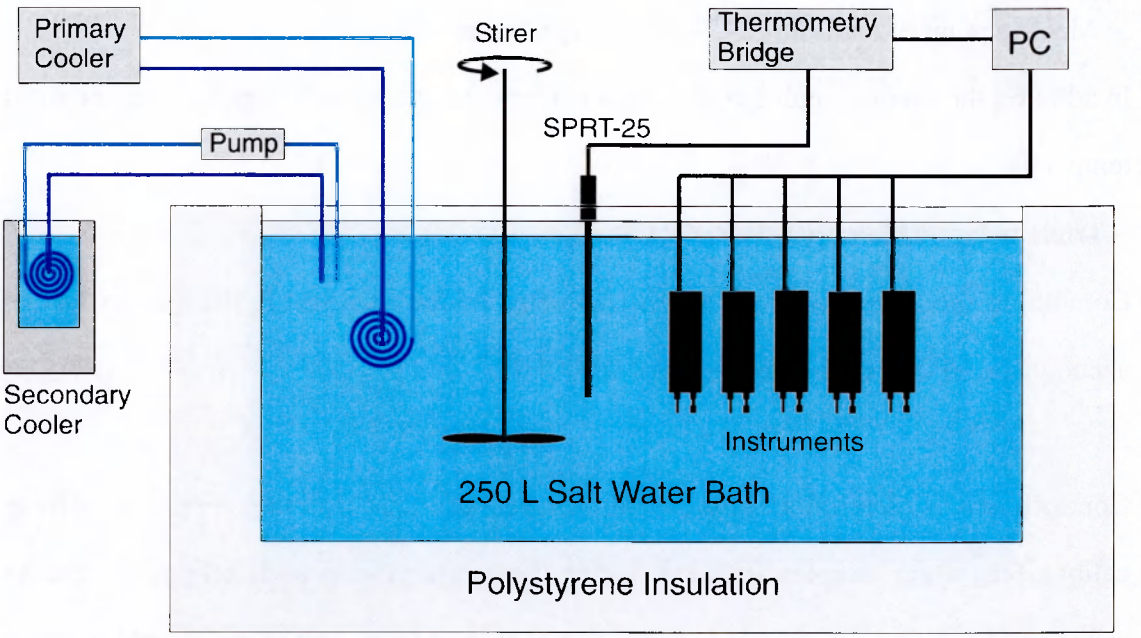

Figure 2.7 Schematic of the facility used to calibrate the sub-ice shelf oceanographic instruments.

over several minutes, providing a more accurate calibration. During the calibration of instruments with conductivity cells, the cell is gently cleaned before each set of measurements using a small bottle brush with a detergent/alcohol mixture. The instrument is then rinsed and returned to the bath.

Water temperature in the bath is measured using an Automatic Systems Laboratories Ltd. F300 Mk2 thermometry bridge with a Tinsley Model 5187SA Primary Standard Platinum Resistance Thermometer (SPRT). The nominal resistance of the SPRT is 25 Ω ±0.5 Ω at 0.0000°C. The thermometry bridge is calibrated against a standard resistor of nominal resistance 25 Ω and calculated resistance of 24.998967 Ω. All temperatures use the reference T90 temperature scale and the thermometer is regularly calibrated using the following fixed points:

- Triple point of water (0.01000°C), type 16 cell ±0.001°C
- Triple point of diphenylether (26.865°C), type 16 cell ±0.005°C

- Melting point of Gallium (29.7646°C), type 16 cell ±0.001°C

In addition the thermometer has also been calibrated commercially against a lower fixed temperature

- Triple point of Mercury (-38.8344°C)

Combining the calibrations of the thermometry bridge and SPRT, the system has an accuracy of ±0.001°C and resolution of 0.0001°C.

Conductivity is determined from both temperature and salinity. For conductivity calibrations, water samples are taken during the measurements to determine the correct salinity of the bath. The sample bottle is rinsed at least twice before the sample is taken. The samples are then analysed commercially using a Guildline Autosal salinometer with an accuracy of better than ±0.002 psu and resolution of better than ±0.0002 psu. Salinity calculations remain on the T68 temperature scale, therefore temperatures (T90) are multiplied by a factor of 1.00024 before calculating the actual water bath conductivity.

2.4 Field data

A brief description of the data obtained from sites 4 and 5 is given in this section together with data from Site 3. These data are used as input or validation data for the numerical models presented in later chapters.

2.4.1 CTD profiles

All the CTD profiles given in this section were cleaned to remove obviously erroneous spikes, filtered using a 5-point Hanning filter, binned at 1 dbar intervals and then the profiles from each site were averaged [*Nicholls et al.*, 1997; *Nicholls et al.*, 2001]. The average profiles for potential temperature (θ) and salinity (S) are shown in Figure 2.8 for sites 3, 4 and 5. At Site 3 the profiler was used to obtain 8 CTD profiles and 4 water samples over a 24 hour period from the 485 m water column. From the CTD profiles, the

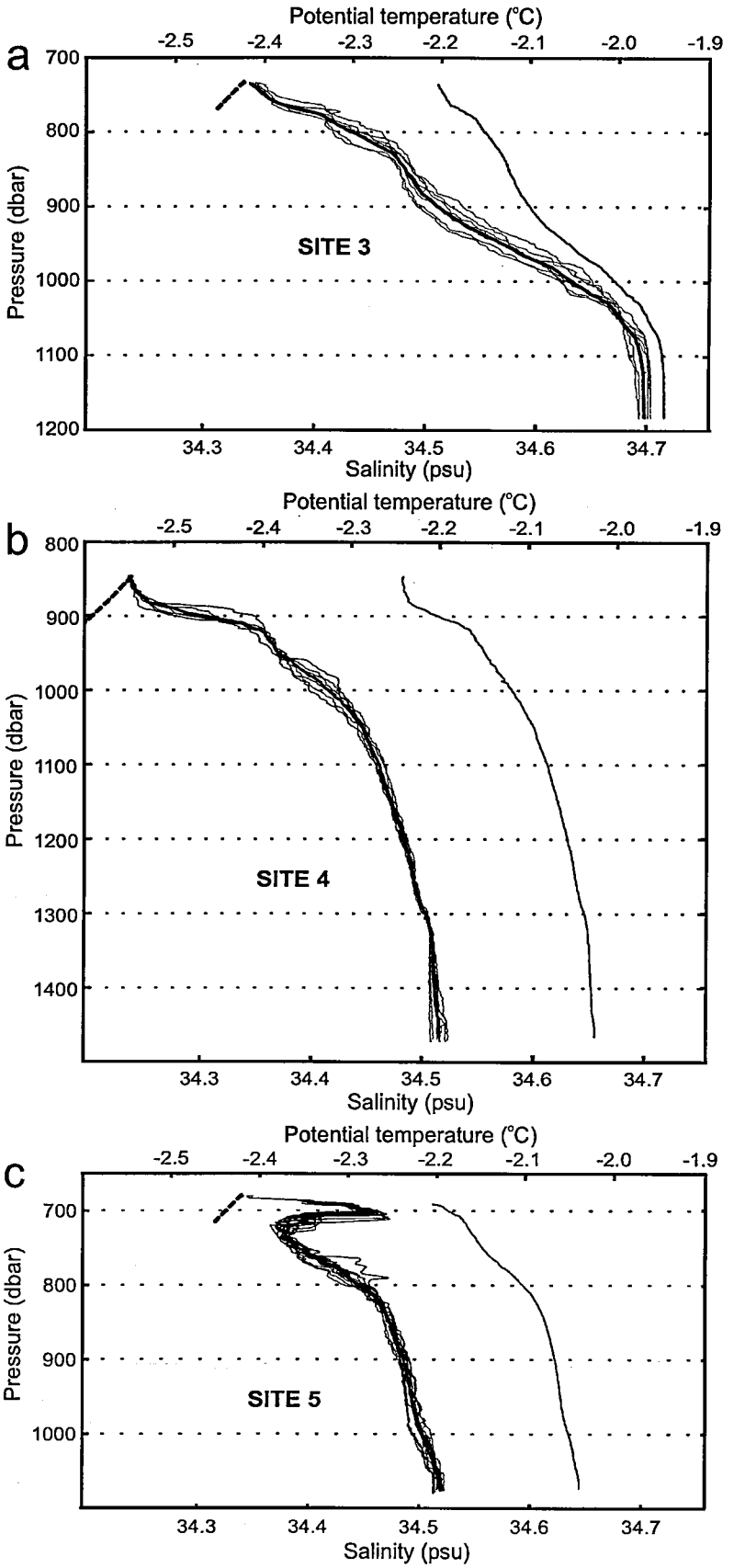

Figure 2.8 Profiles of potential temperature θ and salinity S for **(a)** Site 3, **(b)** Site 4 and **(c)** Site 5. The mean θ profiles are the thick line on the left; the mean salinity profile is the thin line on the right. The raw θ profiles (thin lines behind the mean θ profile) show the degree of variability in the water columns. The thick dashed lines show the upper part of the in situ freezing point. (Figures **(b)** and **(c)** modified from *Nicholls et al.* [2001]).

base of the ice shelf was found to be at a pressure of 730 dbar, and the deepest profile touched the seabed at 1216 dbar. One profile found the seabed at only 1196 dbar, implying a current driven lateral motion of the probe and significant seabed topography. The profile in Figure 2.8a shows a 150-m deep, well mixed layer at the bottom of the water column, overlain by a layer whose potential temperature and salinity decreases towards the ice base, reaching -2.41°C and 34.51 psu. The in situ water temperature close to the ice shelf base was between 0.040°C and 0.051°C warmer than the in situ pressure freezing point of -2.444°C, consequently melting will occur [*Nicholls and Makinson*, 1998]. The lower mixed layer had a potential temperature and salinity of -1.97°C and 34.72 psu. As the surface freezing point of this water mass is less than -1.91°C, the entire water column is defined as ISW.

Site 4 was located between Berkner Island and the Dufek coast, 12 km south of Berkner Island. A series of 6 CTD profiles was made over a period of 7 hours through the 621 m water column and 2 water samples were collected. With a maximum potential temperature of -2.20°C, the entire water column is below the surface freezing point (-1.90°C) and is therefore again ISW by definition. At the seabed the potential temperature and salinity are -2.20°C and 34.64 psu. The water cools and freshens towards the ice shelf base (Figure 2.8b), ultimately reaching -2.55°C and 34.48 psu, with the temperature not significantly different from the in situ freezing point [*Nicholls et al.*, 2001].

Lying between Berkner Island and Henry Ice Rise, Site 5 was located 17 km west of the south-west coast of Berkner Island. Here, 13 CTD profiles through the 402-m water column were obtained over 5 hours. At the seabed the potential temperature and salinity are the same as those at Site 4 (-2.20°C and 34.64 psu). Towards the ice shelf base the water cools and freshens, ultimately reaching -2.32°C and 34.51 psu (Figure 2.8c). However, over the upper 50 m, the temperature increases 0.1°C over a few metres before rapidly decreasing

again towards the ice-ocean interface (Figure 2.8c). At the ice base melting will occur as the measured water temperature was 0.07°C warmer than the pressure freezing point [*Nicholls et al.*, 2001]. At Site 5, retrieval of the CTD profiler and integral water sampler was not possible because the instrument persistently caught at the ice shelf base and the wire had to be cut, hence no water samples were recovered at this site.

2.4.2 Thermistor cable

At both sites 1 and 2 thermistor cables had been permanently deployed to measure the temperature throughout the water column and within the ice shelf over a number of years. No thermistor cables were deployed at either Site 4 or 5. However, at Site 3 a thermistor cable was deployed to measure temperature in the upper 20 m of the water column and at points within the iceshelf, mostly close to the ice shelf base (Figure 2.9a).

2.4.3 CTP mooring data

At sites 3, 4 and 5, the moorings included five units to measure both temperature and conductivity and the positions of the instruments in the water column are shown in Figure 2.9. However, the resolution of the conductivity cells was poor, making it difficult to give useful salinity data because of the very small salinity range found under the ice shelf. The temperature sensors provided useful time series of water column evolution and confirm the presence of seasonal changes.

2.4.4 Current meter mooring data

The mooring at Site 3 contained two conventional vane and rotor current meters and their positions are shown in Figure 2.9a. As a result of technical problems the upper current meter could not be read at the same time as the other instruments, thus no record is available from that current meter. An 8-month excerpt from the lower current meter is shown in Figure 2.10a. The two traces give the currents along and perpendicular to the

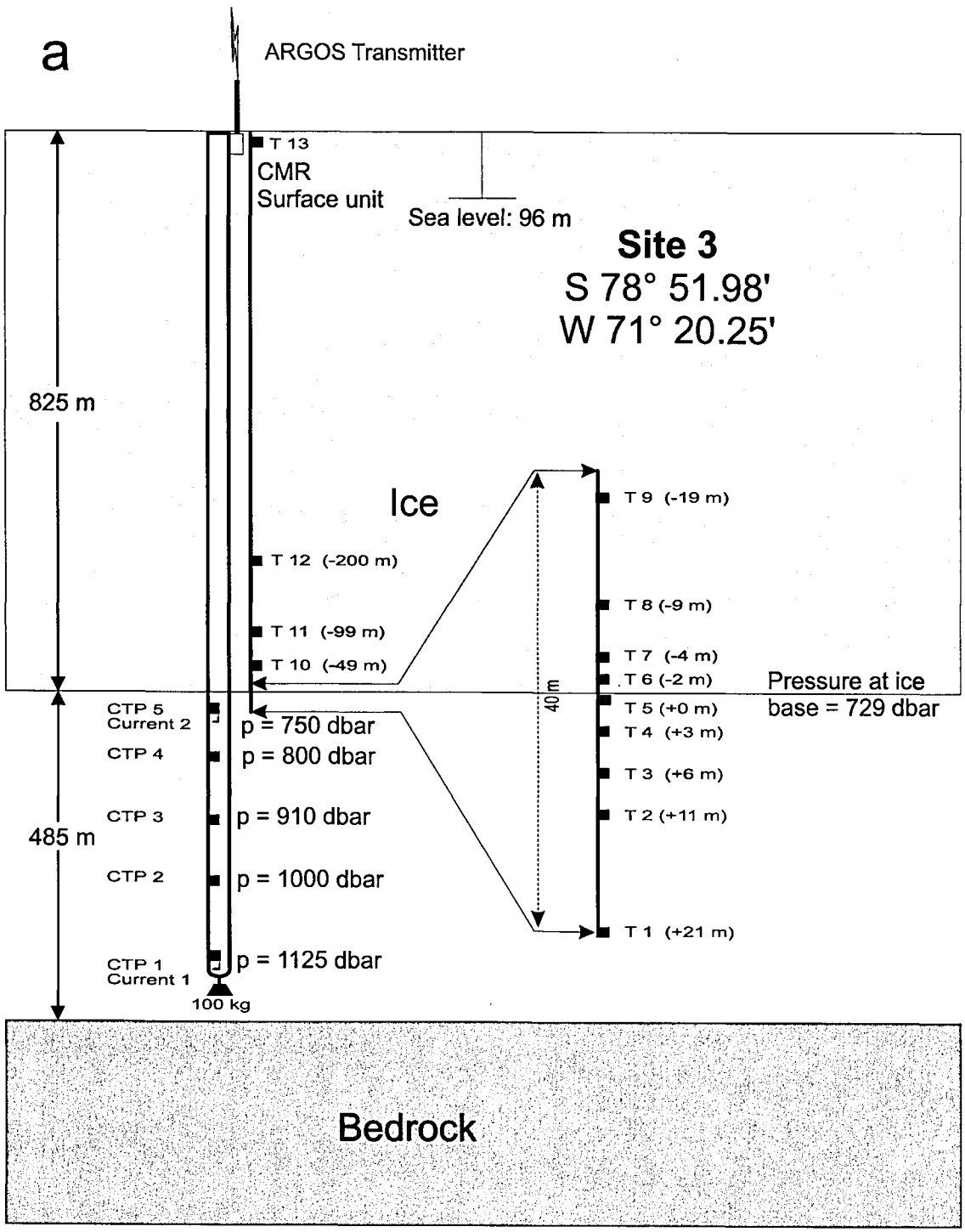

Figure 2.9 (a) Diagram showing the locations of CTP units, current meters and thermistors on the mooring at Site 3.

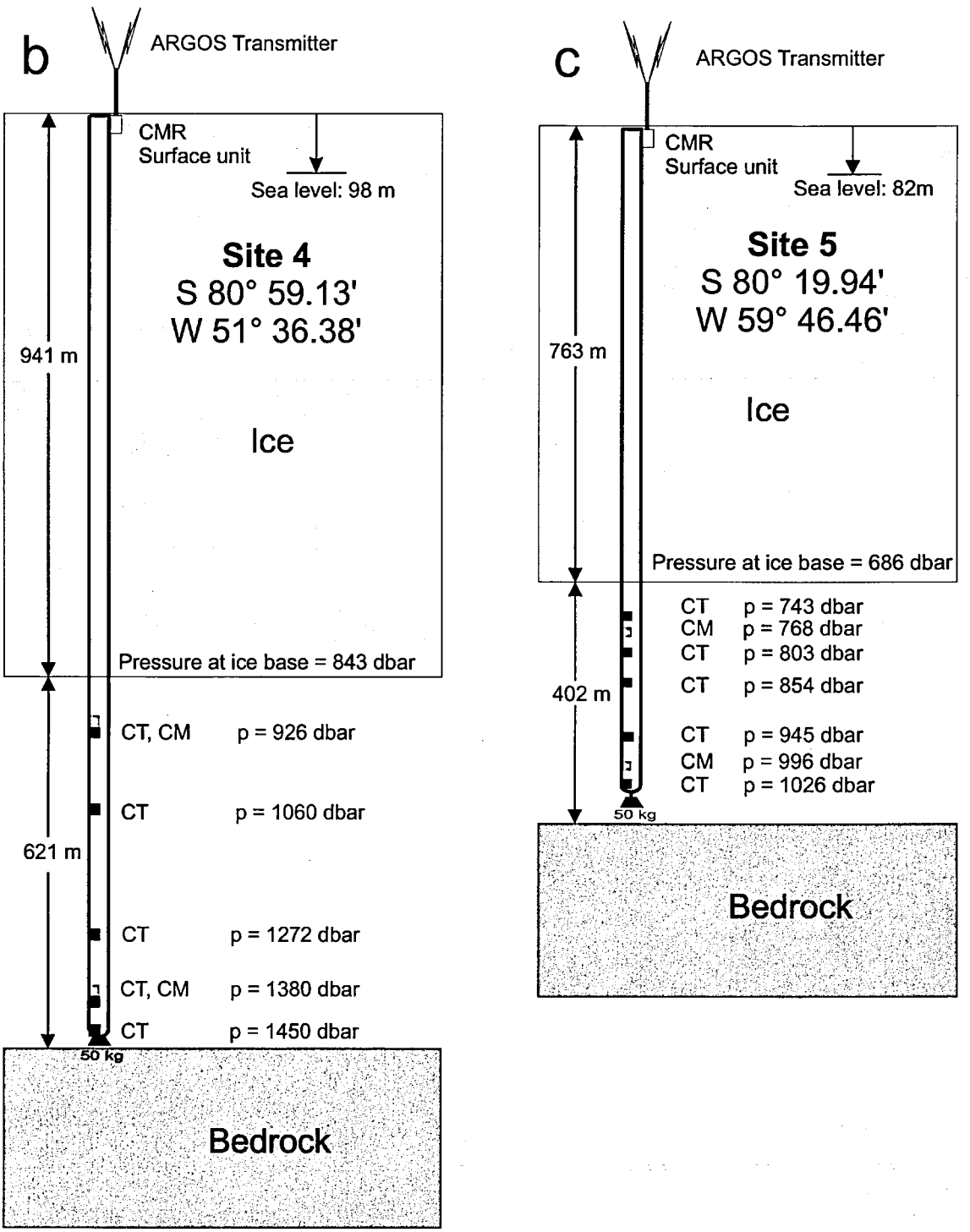

Figure 2.9 (b) and **(c)** Diagram showing the locations of CT units and current meters at Site 4 and Site 5.

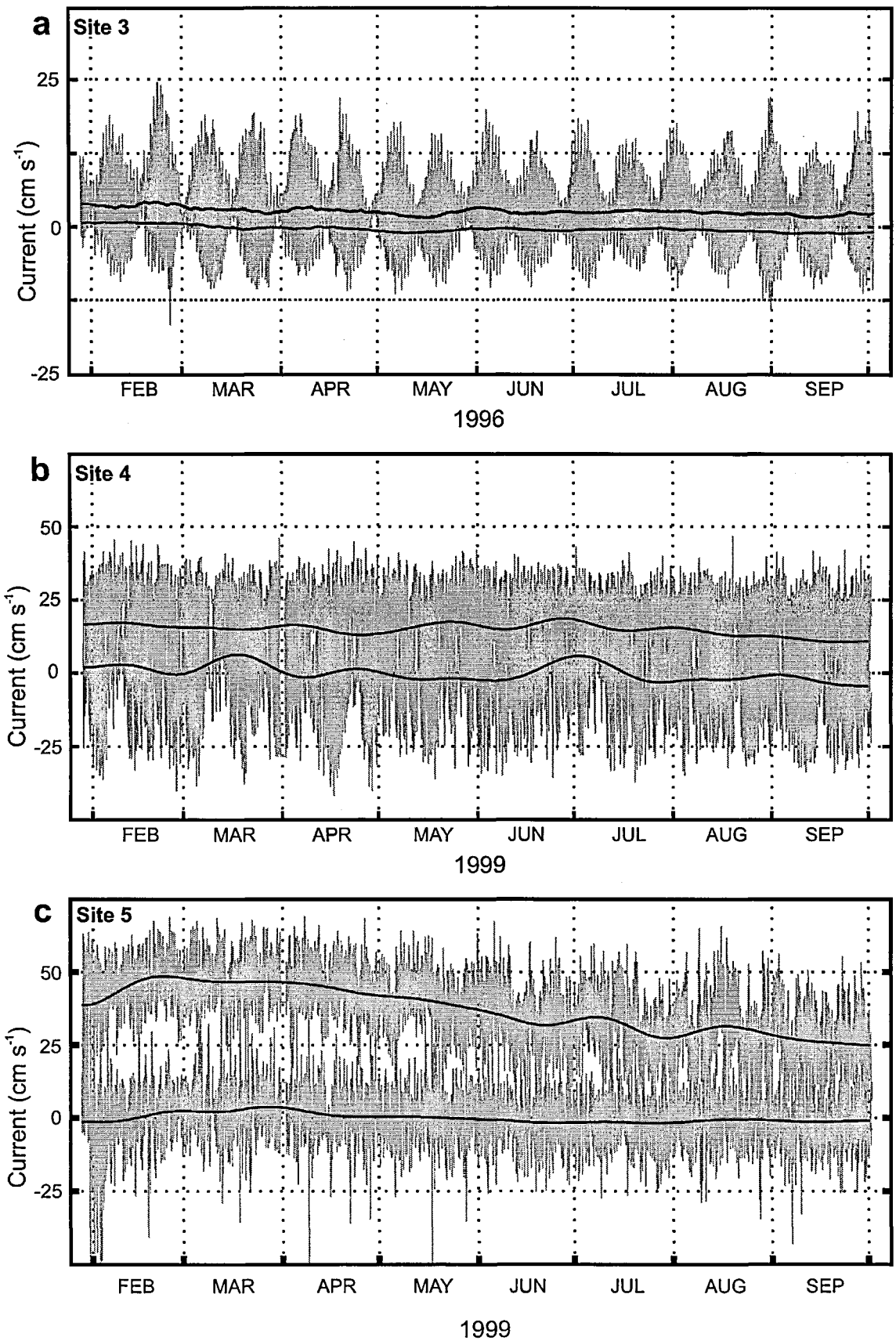

Figure 2.10 Raw and filtered data from selected instruments from the moorings at **(a)** Site 3 (lower current meter), **(b)** Site 4 (upper current meter) and **(c)** Site 5 (upper current meter). The currents have been decomposed into the component across the mean flow (average value of zero) and the component in the direction of the mean flow. Note that the velocity range and mean flow is much smaller in **(a)**. (**(b)** and **(c)** from *Nicholls et al.* [2001]).

direction of the mean flow. There is clearly a dominant semi-diurnal tidal signal, largely aligned along the coast and superimposed on a 0.04-m s^{-1} net southerly flow along the coast [*Nicholls et al.*, 1997].

The deepest current meter unit at Site 4 (Figure 2.9b) used a conventional vane and rotor system, the same as used at Site 3, but there was no communication with this instrument. The upper current meter employed a doppler current sensor as is used in the Anderaa RCM9. The mean velocity of 0.15 m s^{-1} dominates the tides and flows in an easterly direction almost parallel to the southern coast of Berkner Island [*Nicholls et al.*, 2001].

Both units at Site 5 were doppler current meters and their positions are shown in Figure 2.9c. The deepest current meter stopped working after 143 days. The key feature from both current meters is the magnitude of the mean southerly flow velocity along the western coast of Berkner Island with the upper current meter data shown in Figure 2.10c. The maximum mean flow of 0.43 m s^{-1} and 0.49 m s^{-1} for the upper and lower current meters over the record swamps the tidal signal [*Nicholls et al.*, 2001].

2.5 References

Clough, J.W., and B.L. Hansen, The Ross Ice Shelf Project, *Science, 203*, 433-434, 1979.

Cooper, S., K.W. Nicholls, E.M. Morris, and M.H. Talbot, Ice/Ocean studies on George VI Ice Shelf 1987/88, British Antarctic Survey, Cambridge, 1988.

Foldvik, A., T. Gammelsrød, N. Slotsvik, and T. Tørresen, Oceanographic conditions on the Weddell Sea Shelf during the German Antarctic Expedition 1979/80, *Polar Research, 3* (2), 209-226, 1985.

Foster, T.D., The temperature and salinity fine structure of the ocean under the Ross ice shelf, *Journal of Geophysical Research, 88* (C4), 2556-2564, 1983.

Grosfeld, K., and N. Blindow, Determination of Ice-Shelf Bottom Melting by Time-Domain Reflectometry, *Journal of Glaciology, 39* (132), 353-356, 1993.

Humphrey, N., and K. Echelmeyer, Hot-Water Drilling and Bore-Hole Closure in Cold Ice, *Journal of Glaciology, 36* (124), 287-298, 1990.

Iken, A., K. Echelmeyer, and W. Harrison, A light-weight hot water drill for large depths: experiences with drilling on Jakobshavns Glacier, Greenland, in *Proceedings of the Third International Workshop on Ice Drilling Technology*, edited by C. Rado, and D. Beaudoing, pp. 123-136, Laboratoire de Glaciologie et Geophysique de l'Envinornnment, St. Martin d'Heres, Grenoble, 1989.

Johnson, M.R., and A.M. Smith, Seabed topography under the southern and western Ronne Ice Shelf, derived from seismic surveys, *Antarctic Science, 9* (2), 201-208, 1997.

Koci, B.R., Hot water drilling in Antarctic firn and freezing rates in water filled boreholes, in *Ice Drilling Technology, CRREL Special Report 84-24*, edited by G. Holdsworth, K.C. Kuivinen, and J.H. Rand, pp. 101-103, CRREL, Hanover, NH, 1984.

Lothe, T., IFIX - Inductive Data Acquisition System - System for sub ice shelf data acquisition, in *Filchner Ronne Ice Shelf Programme Report No 13*, edited by H. Oerter, pp. 30-39, Alfred-Wegener-Institute for Polar and Marine Research, Bremerhaven, Germany, 2000.

Makinson, K., The Bas Hot-Water Drill - Development and Current Design, *Cold Regions Science and Technology, 22* (1), 121-132, 1993.

Makinson, K., Bas hot water drilling on Ronne Ice Shelf, *Memoirs of National Institute of Polar Research special issue, 49*, 192-202, 1994.

Makinson, K., Hot water drilling on Ronne Ice Shelf 1995/96, in *Filchner Ronne Ice Shelf Programme Report No 10*, edited by H. Oerter, pp. 55-57, Alfred-Wegener-Institute for Polar and Marine Research, Bremerhaven, Germany, 1996.

Nicholls, K.W., and A. Jenkins, Temperature and Salinity beneath Ronne Ice Shelf, Antarctica, *Journal of Geophysical Research, 98* (C12), 22553-22568, 1993.

Nicholls, K.W., and K. Makinson, Ocean circulation beneath the western Ronne Ice Shelf, as derived from in situ measurements of water currents and properties, in *Ocean, Ice, and Atmosphere: Interactions at the Antarctic Continental Margin*, edited by S.S. Jacobs, and R.F. Weiss, pp. 301-318, American Geophysical Union, Washington DC, 1998.

Nicholls, K.W., K. Makinson, and M.R. Johnson, New oceanographic data from beneath Ronne Ice Shelf, Antarctica, *Geophysical Research Letters, 24* (2), 167-170, 1997.

Nicholls, K.W., K. Makinson, and A.V. Robinson, Ocean Circulation beneath the Ronne Ice Shelf, *Nature, 354* (6350), 221-223, 1991.

Nicholls, K.W., S. Østerhus, K. Makinson, and M.R. Johnson, Oceanographic conditions south of Berkner Island, beneath Filchner-Ronne Ice Shelf, Antarctica, *Journal of Geophysical Research, 106* (C6), 11481-11492, 2001.

Nøst, O.A., and A. Foldvik, A Model of Ice-Shelf Ocean Interaction with Application to the Filcher-Ronne and Ross Ice Shelves, *Journal of Geophysical Research, 99* (C7), 14243-14254, 1994.

Nøst, O.A., and S. Østerhus, Impact of grounded icebergs on the hydrographic conditions near the Filchner Ice Shelf., in *Ocean, Ice, and Atmosphere: Interactions at the Antarctic Continental Margin*, edited by S.S. Jacobs, and R. Weiss, pp. 257-266, AGU, Washington DC, 1998.

Østerhus, S., and O. Orheim, Studies through Jutulgryta, Fimbulisen in the 1991/92 season, in *Filchner Ronne Ice Shelf Programme Report No 6*, edited by H. Oerter, pp. 103-109, Alfred-Wegener-Institute for Polar and Marine Research, Bremerhaven, Germany, 1992.

Paren, J.G., and S. Cooper, Thermal regime of George VI Ice Shelf, Antarctic Peninsula, *Annals of Glaciology, 11*, 206, 1988.

Richards, D.L., and H. Melling, An oceanographic bottle system for CTD calibration, *Oceans, 87*, 183-187, 1987.

Robinson, A., K. Makinson, and K. Nicholls, The oceanic environment beneath the north-west Ronne Ice Shelf, Antarctica, *Annals of Glaciology, 20*, 386-390, 1994.

Robinson, A.V., and K. Makinson, Ocean circulation beneath Ronne Ice Shelf, in *Filchner Ronne Ice Shelf Programme Report No 7*, edited by H. Oerter, pp. 47-52, Alfred-Wegener-Institute for Polar and Marine Research, Bremerhaven, Germany, 1994.

Srikanta Jois, S., Finite element approach for determining temperature variation in ice cores, in *PICO*, University of Alaska, Fairbanks, Alaska 99775, 1993.

Vaughan, D.G., J. Sievers, C.S.M. Doake, G. Grikurov, H. Hinze, V.S. Pozdeev, H. Sandhäger, H.W. Schenke, A. Solheim, and F. Thyssen, Map of subglacial and seabed topography 1:2000000 Filchner-Ronne-Schelfeis, Antarktis, Institut für Angewandte Geoäsie, Frankfurt am Main, Germany, 1994.

CHAPTER 3

Two-Dimensional Barotropic Tidal Model

3.1 Introduction

Sparse observations of tidal sea surface motions and tidal currents provide only the most basic description of tidal motions in the Weddell Sea. Numerical simulations using 2-D barotropic tidal models of the Weddell Sea tides have been performed and provide the most effective way to extend the maps of tidal elevations and phases not covered by observations [*Genco et al.*, 1994; *Robinson*, 1996; *Smithson et al.*, 1996; *Robertson et al.*, 1998]. Additionally tidal current data are available from the models. As a source of energetic currents within large areas of the sub-ice shelf cavity, tides may represent the most important process driving the water column and facilitating melting at the ice shelf base. The model data provide estimates for the tidal energy budget, vertical mixing that results from turbulence at the seabed and ice shelf base [*Robinson*, 1996; *Robertson et al.*, 1998] (Chapter 4) and the generation of tidal residual currents (Chapter 5); these are processes that could assist in the transformation of water masses beneath FRIS and over the continental shelf. The numerical model described in this chapter has been successfully used in several previous studies [e.g. *Flather*, 1994; *Tsimplis et al.*, 1995], including the Weddell Sea [*Robinson*, 1996; *Smithson et al.*, 1996], though at a much coarser resolution. In the following two chapters this tidal model will be used to assess depth-averaged tidal currents, vertical mixing and tidal residual currents close to and beneath FRIS.

3.2 Numerical tidal model

3.2.1 Governing equations

The tidal model used in this study is the 'storm surge' tidal model developed at the Proudman Oceanographic Laboratory [*Flather*, 1994]. The model is based on depth-averaged equations of continuity and motion in spherical polar coordinates that include terms for advection, Coriolis force, bottom drag, lateral viscosity and astronomical and surface forcing. The equation of continuity (conservation of volume) may be written in the form

$$\frac{\partial \zeta}{\partial t} + \frac{1}{R\cos\varphi}\left[\frac{\partial}{\partial \chi}(Du) + \frac{\partial}{\partial \varphi}(Dv\cos\varphi)\right] = 0 \tag{3.1}$$

and the equations of motion for each coordinate direction that relate the acceleration of the water to the forces acting on it are

$$\frac{\partial v}{\partial t} + \frac{u}{R\cos\varphi}\frac{\partial v}{\partial \chi} + \frac{v}{R}\frac{\partial v}{\partial \varphi} + \frac{u^2\tan\varphi}{R} + 2\omega\sin\varphi u = -\frac{g}{R}\frac{\partial}{\partial \varphi}(\zeta + \zeta_b - \bar{\zeta}) - \frac{G_b}{\rho D} + A_h^2\nabla v \quad \text{and} \tag{3.2}$$

$$\frac{\partial u}{\partial t} + \frac{u}{R\cos\varphi}\frac{\partial u}{\partial \chi} + \frac{v}{R}\frac{\partial u}{\partial \varphi} - \frac{uv\tan\varphi}{R} - 2\omega\sin\varphi v = -\frac{g}{R\cos\varphi}\frac{\partial}{\partial \chi}(\zeta + \zeta_b - \bar{\zeta}) - \frac{F_b}{\rho D} + A_h^2\nabla u, \tag{3.3}$$

where:

t	time,
χ, φ	longitude and latitude, respectively,
ζ	elevation of the sea surface relative to the earth,
ζ_s	elevation of the sea surface above its undisturbed level,
ζ_b	elevation of the seabed above its undisturbed level,
$\bar{\zeta}$	the equilibrium tide,

u, v	east and north components of the depth mean current,
F_b, G_b	east and north components of the bottom stress, τ,
D	water depth,
ρ	density of sea water (assumed constant and uniform),
R	radius of the earth,
g	gravitational acceleration,
ω	angular speed of rotating earth,
A_h	horizontal eddy viscosity.

The relationships between the various elevations and depths are shown in Figure 3.1. At the seabed, the stress, τ_b, is related to the depth mean current, U, using a quadratic friction law

$$\tau_b = C_d \rho U|U|, \tag{3.4}$$

where C_d is the coefficient of bottom friction and set to 0.0025. The stress between the base of the ice shelf and the underlying sea water is not included in the model. However, beneath the area covered by ice shelf C_d was doubled to account for the additional drag at the

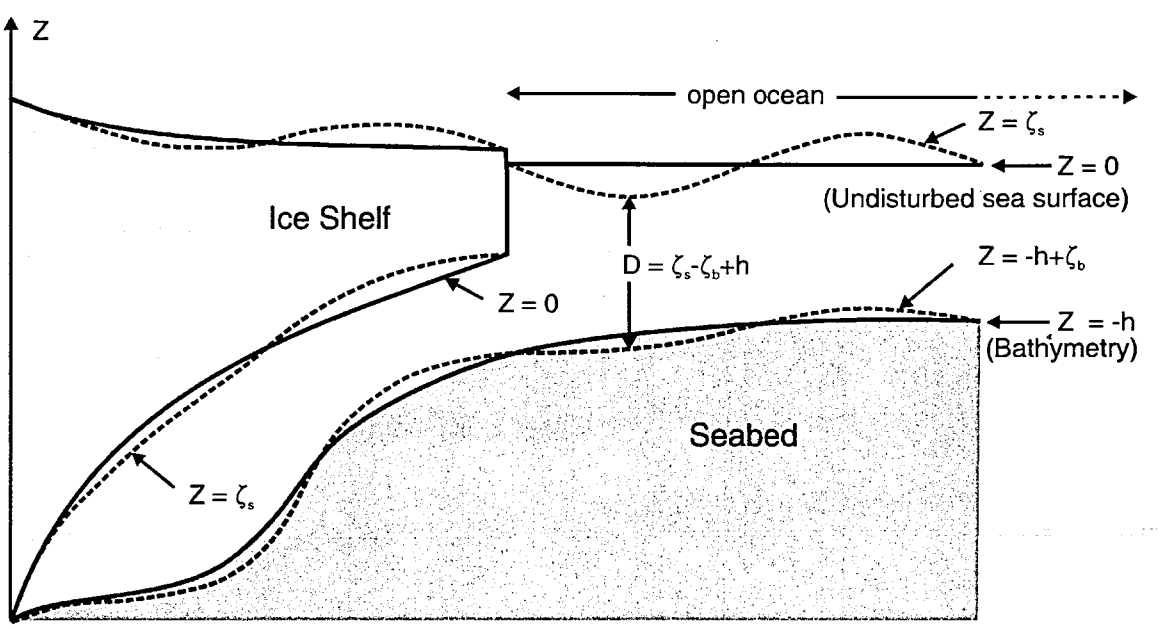

Figure 3.1 Schematic diagram showing the relationship between the various depths and elevations used in the model [after *Smithson et al.*, 1996]. Under the ice shelf, the level of the sea surface ($z = \zeta_s$) is coincident with the base of the ice shelf. The instantaneous water column depth, D, is the distance from the (distorted) seabed to either the base of the ice shelf (under the ice shelf) or the sea surface (in the open ocean).

ice-ocean interface, a technique used in other sub-ice tidal shelf studies [*MacAyeal*, 1984; *Smithson et al.*, 1996]. Apart from providing a second frictional surface and reducing the water column thickness, the ice shelf has no other influence on the tides in this model.

The horizontal eddy viscosity is taken to be 5.0 $m^2 s^{-1}$ over the whole domain though this has little influence on the model results [*Smithson et al.*, 1996]. At the coastal boundaries the current component normal to the boundary is set to zero and the initial model conditions consist of no currents and an undisturbed sea surface. For numerical stability the time step of the integration (Δt) in the model must satisfy the Courant-Friedrichs-Lewy (CFL) condition

$$\Delta t < \frac{\Delta s}{\sqrt{2gD}} \tag{3.5}$$

everywhere within the model domain. In (3.5) Δs is the distance between grid nodes. The grid used in the model has a regular spacing of 4′ latitude by 15′ longitude, corresponding to 7.4 km north-south and ranging from 9 km to 3.4 km east-west. This gives a time step Δt for the integration of 15 s, ensuring the CFL condition is satisfied throughout the domain.

The depth-averaged equations of continuity and motion are discretised onto the model grid that uses the Arakawa "C grid". The equations of motion and continuity are solved using an explicit finite difference method. The full details of the numerical scheme have been given by *Flather* [1994].

3.2.2 Model domain

The extent of the model domain is shown in Figure 3.2, and lies between latitudes 71°S and 84°S, and longitudes 15°W and 90°W. This encompasses the entire southern Weddell Sea continental shelf, including the region covered by FRIS.

3.2.2.1 Bathymetry

The bathymetry in several parts of the domain is not well known, particularly over the western Weddell Sea and under the ice shelves; bathymetric errors are therefore likely be significant. North of 75°S the bathymetry for the model is taken from the U.S. Naval Oceanographic Office Digital Bathymetric Data Base 5 (DBDB5) data set [*Van Wyckhouse*, 1973]. In that data set a shallow region known as the Belgrano Bank (73°S, 50°W), which lies near the continental shelf break, has a minimum water depth of 10 m. The General

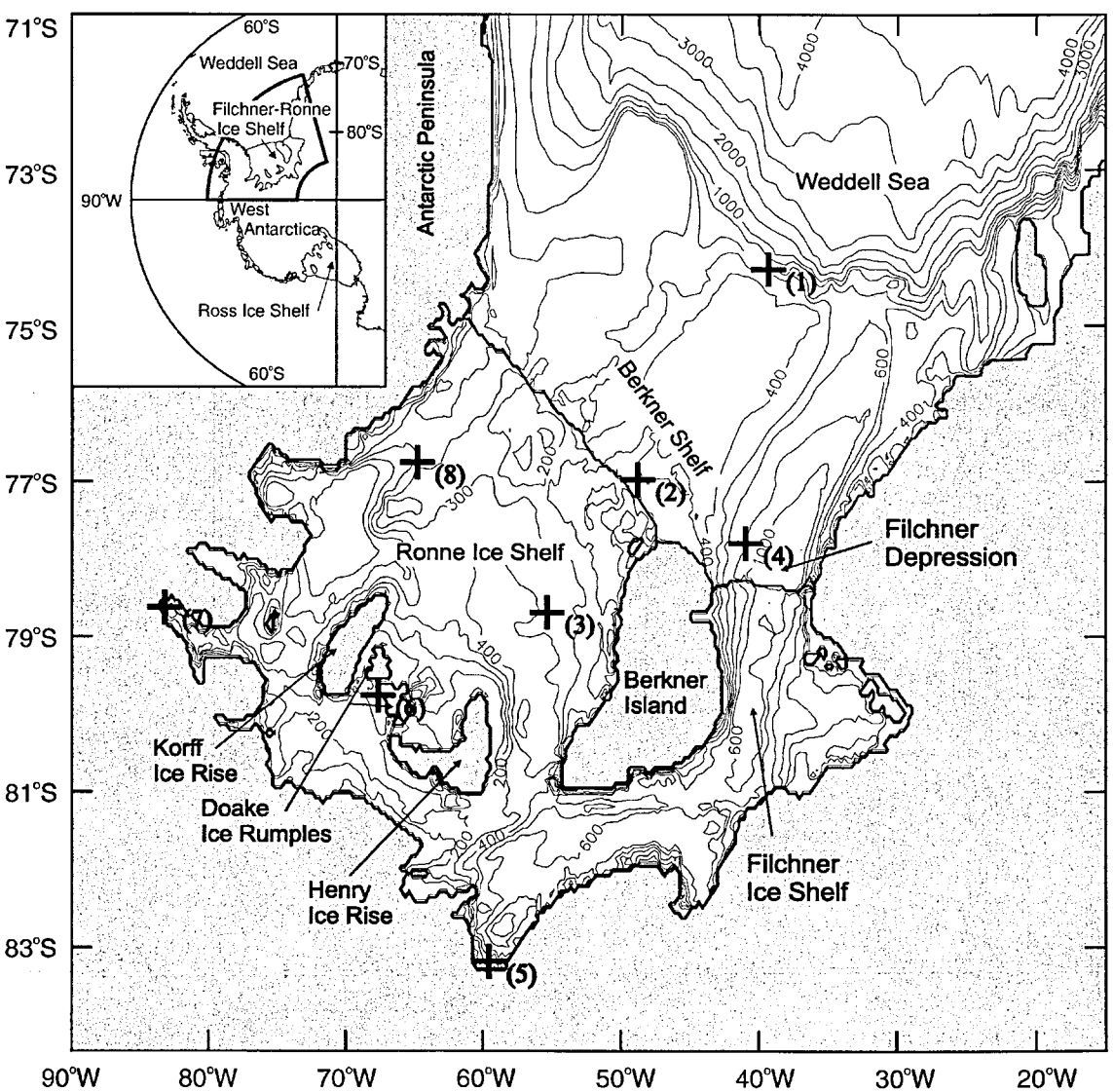

Figure 3.2 Map showing the model domain. The darkest shading indicates areas of grounded ice, and the lighter shading indicates the floating ice shelf. The contours give water column depth in metres which is water column thickness under the ice shelf and bathymetry elsewhere. The crosses indicate the location at which there are tidal elevation measurements used for comparison with the model in Figure 3.4. The inset indicates the region covered by the model domain.

Bathymetric Chart of the Oceans (GEBCO) data set of *Johnson et al.* [1983], which includes ship data from Belgrano Bank, and recent cruise data from this area (K. W. Nicholls, personal communication, 1998), suggests a minimum of no less than 400 m in this area. In the domain described here the minimum depth has been increased to 400 m, similar to the depth of the surrounding continental shelf. Geophysical airborne data from the western Weddell Basin [*LaBrecque and Ghidella*, 1997] suggest that the correct position of the southern section of Larsen continental shelf edge lies as much as 100 km to the east of the DBDB5 position and confirmed by Ice Station Weddell [*Gordon et al.*, 1993]. A correction has not been included in the present model bathymetry. South of 75°S bathymetry has been taken from the digital data set prepared by *Vaughan et al.* [1994], updated with more recent seismic data from the areas south of Berkner Island, and Korff and Henry Ice Rises [*Mayer et al.*, 1995; *Johnson and Smith*, 1997].

In areas not covered by ice shelf, bathymetry and water column thickness are the same. Over these areas the water column thickness ranges from 4000 m in the Weddell Sea basin to less than 250 m on the continental shelf, the shallowest being the Berkner Shelf, north of Berkner Island (Figure 3.2). Elsewhere the water column thickness is modified by the presence of the ice shelf.

3.2.2.2 Ice shelf thickness

Ice thickness of FRIS ranges from less than 200 m close to the ice front to almost 2000 m at the grounding lines of some ice streams. The ice thickness was determined by *Vaughan et al.* [1995], mainly from ERS-1 satellite altimeter data [*Seivers et al.*, 1994], by assuming the ice shelf was freely floating and inverting the surface heights. However, in areas of surface crevassing or large surface gradients, typically close to grounding lines, interpolation between satellite data and known thicknesses at grounding lines was used.

Also the ERS-1 satellite coverage was restricted to north of 82°S, so interpolation using known depths south of 82°S was applied.

3.2.2.3 Sub-ice shelf cavity

Beneath FRIS the model uses the water column thickness, defined as the difference between seabed depth and ice shelf draft. The depth of the ice-ocean interface (D_{io}) was derived from the ice shelf thickness (H) using [*Vaughan et al.*, 1995]:

$$D_{io} = 0.892H - 17 \tag{3.6}$$

The gradient term is the density ratio for ice and seawater, with the 17 m offset accounting for the lower density surface firn layer. Beneath FRIS the water column thickness ranges from 100 m or less near Ronne Ice Front to more than 600 m in some of the southern regions of the ice shelf.

3.2.3 Model forcing

In this application of the 'storm surge' tidal model, no wind stress or atmospheric pressure forcing are used. The model is forced by specifying only the equilibrium tide over the domain and the sea surface heights along its open boundary as a function of time and position. Direct observations of tidal conditions along the open boundary do not exist; hence, data for the boundary were obtained by interpolation of results from a regional model [*Smithson et al.*, 1996] that was itself forced by the *Schwiderski* [1980] model. The eight largest tides are listed in Table 3.1 with the amplitudes corresponding to those given by equilibrium tidal theory, namely four semi-diurnal tides and four diurnal tides. A time series of sea surface elevation for each node along the boundary was computed using the amplitude and phase of six tidal constituents (Q_1, O_1, K_1, N_2, M_2, S_2). The tidal height, $\zeta(t)$, at a particular location may be represented by the harmonic summation

$$\zeta(t) = Z_0 + \sum_{j=1}^{n} f_j A_j \cos\left(V_j + U_j + \sigma_j(t) - \phi_j\right), \tag{3.7}$$

where:

Z_0 the mean elevation,

A_j Amplitude of constituent j,

ϕ_j Phase lag behind the equilibrium constituent j on the Greenwich meridian,

f_j, U_j Nodal modulation amplitude and phase lag with respect to the equilibrium tide,

V_j The phase of the equilibrium constituent j at Greenwich at time $t = 0$.

Table 3.1 Principal harmonic components

Name of Tide / Tidal species	Symbol	Period (Hours)	Frequency (10^{-4} s^{-1})	Magnitude Ratio M_2:100
Principal lunar / semi-diurnal	M_2	12.421	1.40519	100
Principal solar / semi-diurnal	S_2	12.000	1.45444	46.6
Large lunar elliptic /semi-diurnal	N_2	12.658	1.37880	19.2
Luni-solar / semi-diuranl	K_2*	11.967	1.45842	12.7
Luni-solar / diurnal	K_1	23.934	0.72921	58.4
Principal lunar / diurnal	O_1	25.819	0.67598	41.5
Principal solar / diurnal	P_1*	24.066	0.72523	19.4
Large lunar elliptic /semi-diurnal	Q_1	26.868	0.64959	7.9

* Constituent not used in present tidal model

3.3 Analysis of tidal data

3.3.1 Tidal record length

A harmonic least squares method of analysis was applied to the model time series data for constituent amplitude and phase. The number of constituents that can be included in the analysis is determined by the Rayleigh criterion, which states that adjacent constituents of frequencies σ_1, σ_2 must be separated by at least one complete period over the length of the record (T).

$$T = 1/(\sigma_1 - \sigma_2) \tag{3.8}$$

Thus in order to separate M_2 and N_2 for example with periods of 0.080511 and 0.078999 cycles per hour respectively, a record length of 662 hours is required. If the number of constituents had been increased from 6 to 8 by including P_1 and K_2, a record length of at least 4383 hours would be needed for the analysis, and require far more computer resources, hence their exclusion.

The model was run for an arbitrary 41.5 days with the elevations and currents being recorded hourly over the final 27.6 days. The recorded time series is long enough for the harmonic analysis method to be used to separate the six constituents that drive the model [*Foreman*, 1977]. The analysis provided tidal amplitude and phase information for elevations and currents at each grid point in the domain. The tidal current time series record was split into north-south and east-west components and analysed separately.

3.3.2 Tidal ellipse parameterization

The tidal current contribution for each constituent can be represented as a vector whose tip traces out an ellipse over the period of the constituent. A tidal current ellipse is defined by four parameters. The harmonic analysis provides amplitude (A_u, A_v) and phase (ϕ_u, ϕ_v) for the east-west and north-south components, these can be transposed to give amplitudes of the major and minor semi-axis, the angle of inclination and the phase angle. Alternatively,

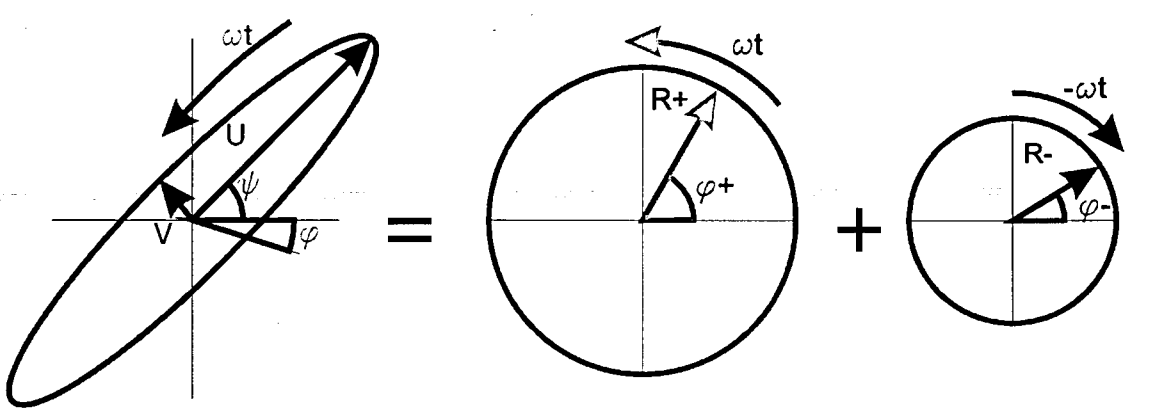

Figure 3.3 The parameters that can be used to characterise a tidal current ellipse rotating at the frequency, ω, of the tidal constituent and its two counter rotating components.

the four parameters can be the amplitude and phase of two co-rotating vectors (Figure 3.3). Using the harmonically analysed model velocity data, the amplitude and phase of the clockwise and anticlockwise rotary components are given by [*Souza and Simpson*, 1996]

$$R_+ = \left| 0.5\left(A_u^2 + A_v^2 + 2uv\sin(\phi_v - \phi_u)\right)^{1/2} \right| , \tag{3.9}$$

$$R_- = \left| 0.5\left(A_u^2 + A_v^2 - 2uv\sin(\phi_v - \phi_u)\right)^{1/2} \right| , \tag{3.10}$$

$$\phi_- = \left\{ \frac{A_v \cos\phi_v + A_u \sin\phi_u}{A_u \cos\phi_u - A_v \sin\phi_v} \right\} \text{,and} \tag{3.11}$$

$$\phi_+ = \left\{ \frac{A_v \cos\phi_v - A_u \sin\phi_u}{A_u \cos\phi_u + A_v \sin\phi_v} \right\} . \tag{3.12}$$

When viewed from above, R_- and R_+ are the purely clockwise and anticlockwise constant magnitude velocity vectors that rotate at the tidal frequency, and ϕ_- and ϕ_+ are their associated phases. These components combine to give the time-varying velocity vector that results in the tidal current ellipse [*Prandle*, 1982] and are used to determine the tidal ellipse properties:

$$U = |R_+| + |R_-| , \tag{3.13}$$

$$V = |R_+| - |R_-| , \tag{3.14}$$

$$\psi = (\phi_+ + \phi_-)/2 , \tag{3.15}$$

$$\phi = -(\phi_+ - \phi_-)/2 , \tag{3.16}$$

$$P = V/U , \tag{3.17}$$

where U and V are the semi-major and semi-minor axes and ψ and ϕ are the orientation of the semi-major axis of the ellipse and its phase angle. The ellipse polarization P is defined as the ratio of the semi-minor to the semi-major axis and ranges from a purely circular clockwise current (P = -1), through a flat or degenerate ellipse (P = 0), to a purely circular anticlockwise current (P = +1).

3.4 Model validation using elevation data

There are, unfortunately, few data available from this southern Weddell Sea region for comparison with the tidal model because of the presence of ice shelves and perennial sea ice. Tidal elevation data sets from tide gauges at open water sites, and gravimeters and tiltmeters at ice shelf sites have been used for comparison against barotropic tidal models with reasonable agreement being achieved [*Smithson et al.*, 1996; *Robertson et al.*, 1998].

To ensure that the open boundary conditions have been applied correctly to this more focused domain, the model output has been compared with observed elevation data. Both the model output and the observed constituent data are shown graphically in Figure 3.4 and show that reasonable agreement has been achieved. The tidal elevation measurement locations are shown in Figures 3.2 and 3.5. The amplitude and phase data for the various tidal constituents are essentially identical to the tabulated data presented by *Smithson et al.* [1996]. In addition, the simulated amplitude and phase characteristics for the main diurnal tide, K_1, and the main semi-diurnal tide, M_2, are shown in Figure 3.5 and are representative of other constituents in their band.

The diurnal tidal structure is relatively simple with the phase lines progressing from east to west across the southern Weddell Sea with a small increase in amplitude towards the south west as part of a resonant Kelvin wave propagating around Antarctica. The only complication lies along the continental shelf edge where the interactions of the tide with the topography leads to the formation and propagation of continental shelf waves [*Middleton et al.*, 1987], which appear as amplitude maxima along the continental shelf break. The largest tidal elevations result from the semi-diurnal tides with the M_2 tidal amplitude exceeding 1.5 m in the south west of Ronne Ice Shelf (Figure 3.5b). The semi-diurnal tides propagate as Kelvin waves around the southern Weddell Sea with amphidromic points situated near the front of Ronne Ice Shelf with the phase propagating clockwise.

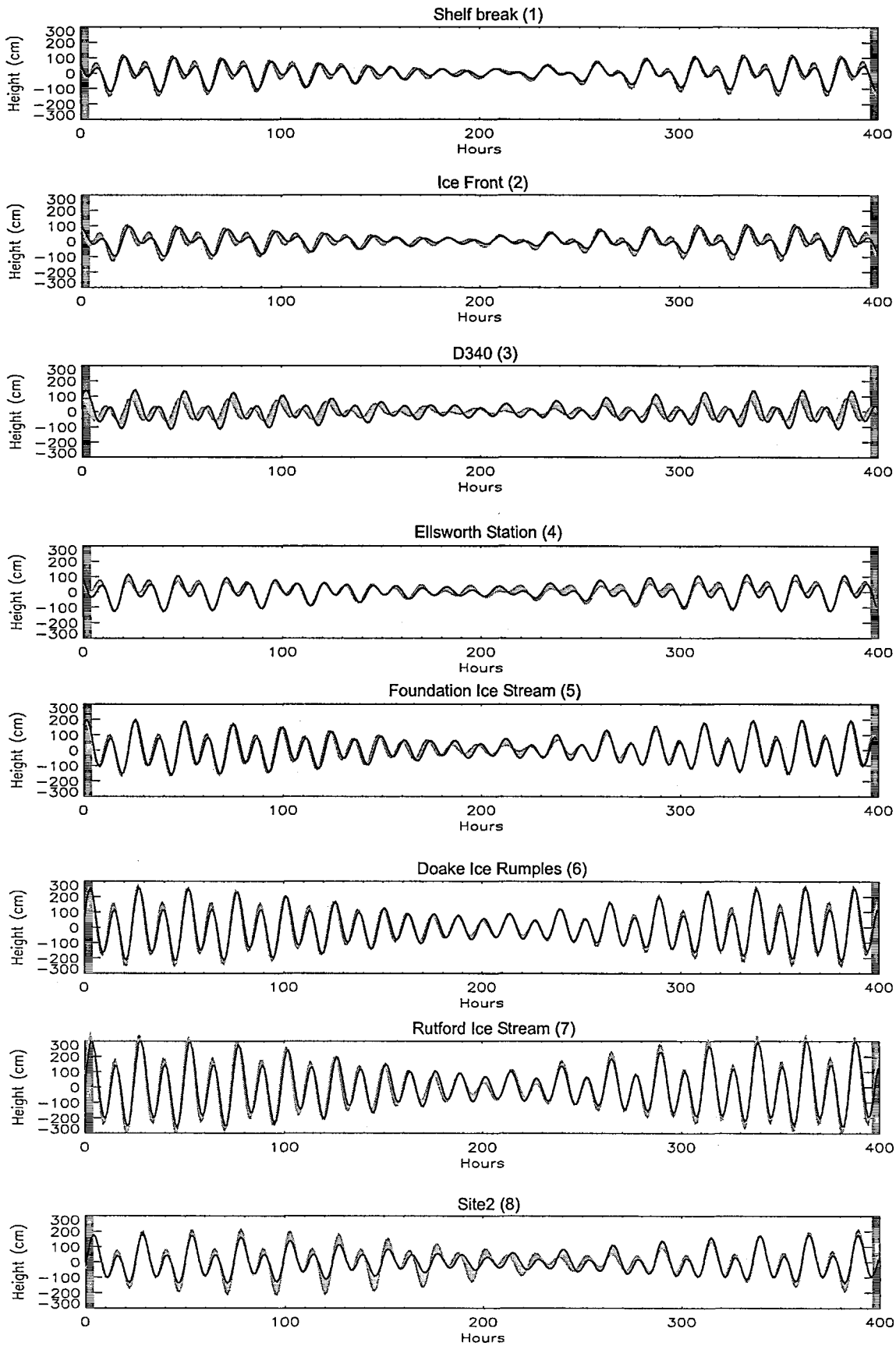

Figure 3.4 The comparison of the model results (black line)and the observed harmonic constituents (grey line) for the tidal elevation constructed from the Q_1, O_1, K_1, N_2, M_2 and S_2 constituents for a selection of sites. The comparison is made over an arbitrary 400 hour period and the site locations are marked on Figures 3.2 and 3.5.

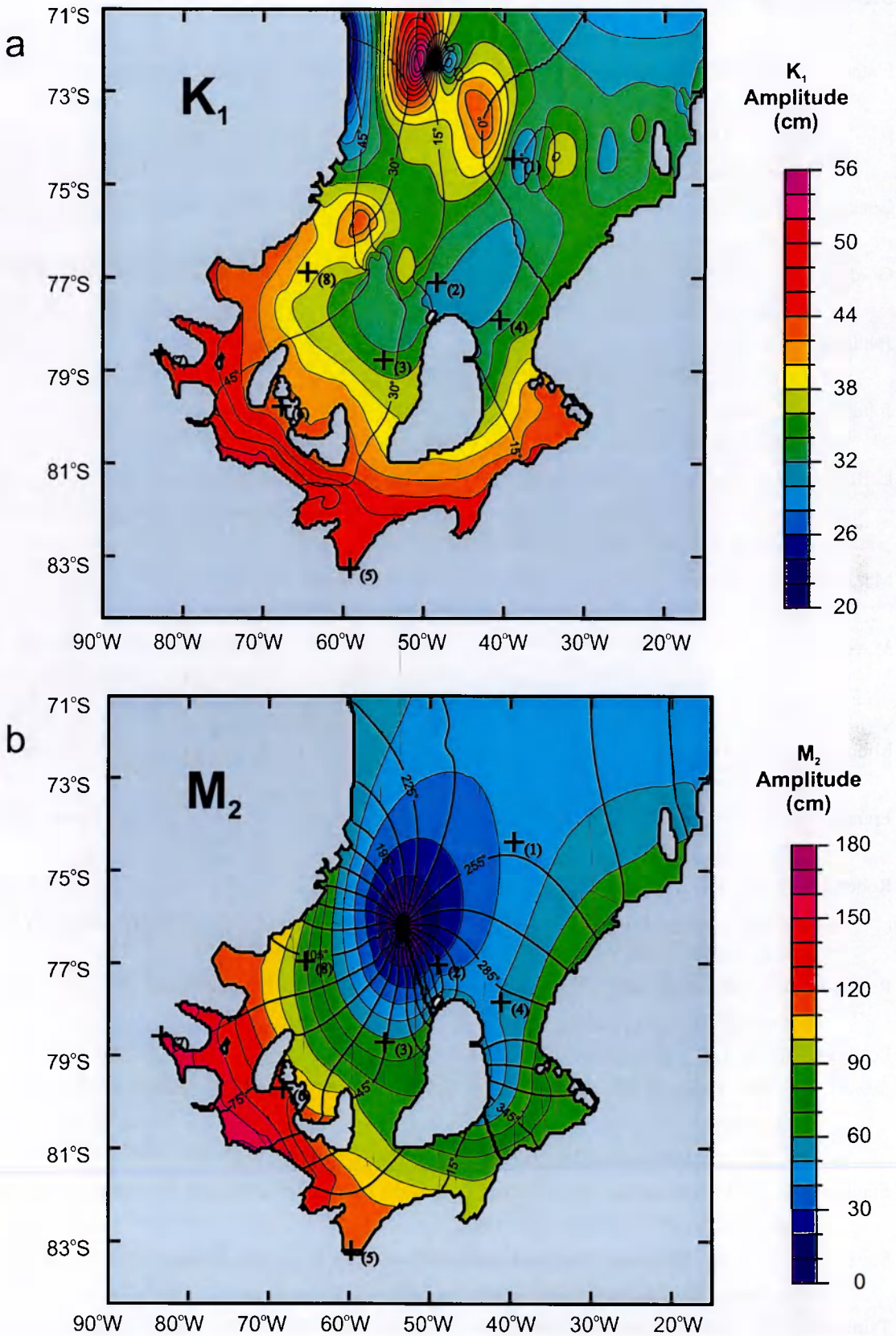

Figure 3.5 The tidal elevation amplitude and phase for **(a)** one of the principal diurnal (K_1) and **(b)** semi-diurnal (M_2) tidal constituents, which are representative of other constituents in their bands. The elevation amplitude is given by the colour scale and the phase by the contours with an interval of 15°.

3.5 References

Flather, R.A., A Storm-Surge Prediction Model for the Northern Bay of Bengal with Application to the Cyclone Disaster in April 1991, *Journal of Physical Oceanography, 24* (1), 172-190, 1994.

Foreman, M.G.G., *Manual for Tidal Currents Analysis and Prediction*, 70 pp., Institute of Ocean Sciences, Patricia Bay, Sidney, B.C., 1977.

Genco, M.L., F. Lyard, and C. Leprovost, The Oceanic Tides in the South-Atlantic Ocean, *Annales Geophysicae, 12* (9), 868-886, 1994.

Gordon, A.L., B.A. Huber, H.H. Hellmer, and A. Ffield, Deep and Bottom Water of the Weddell Seas Western Rim, *Science, 262* (5130), 95-97, 1993.

Johnson, G.L., J.R. Vanney, D.J. Drewry, and G.D. Robin, General bathymetric chart of the oceans (GEBCO), Can. Hydrogr. Serv., Ottawa, Ont., 1983.

Johnson, M.R., and A.M. Smith, Seabed topography under the southern and western Ronne Ice Shelf, derived from seismic surveys, *Antarctic Science, 9* (2), 201-208, 1997.

LaBrecque, J.L., and M.E. Ghidella, Bathymetry, depth to magnetic basement, and sediment thickness estimates from aerogeophysical data over the western Weddell Basin, *Journal of Geophysical Research, 102* (B4), 7929-7945, 1997.

MacAyeal, D.R., Numerical Simulations of the Ross Sea Tides, *Journal of Geophysical Research, 89* (C1), 607-615, 1984.

Mayer, C., A. Lambrecht, and H. Oerter, Glaciological investigations on the Foundation Ice Stream, in *Filchner Ronne Ice Shelf Programme Report No 9*, edited by H. Oerter, pp. 57-63, Alfred-Wegener-Institute for Polar and Marine Research, Bremerhaven, Germany, 1995.

Middleton, J.H., T.D. Foster, and A. Foldvik, Diurnal Shelf Waves in the Southern Weddell Sea, *Journal of Physical Oceanography, 17* (6), 784-791, 1987.

Prandle, D., The Vertical Structure of Tidal Currents, *Geophysical and Astrophysical Fluid Dynamics, 22* (1-2), 29-49, 1982.

Robertson, R., L. Padman, and G.D. Egbert, Tidal currents in the Weddell Sea, in *Ocean, Ice and Atmosphere: Interactions at the Antarctic Continental Margin, Antarct. Res. Ser.*, edited by S.S. Jacobs, and R. Weiss, pp. 341-369, AGU, 1998.

Robinson, A.V., Modelling tides of the southern Weddell Sea, M. Phil thesis, British Antarctic Survey, Cambridge, England, 1996.

Schwiderski, J.H., On charting global ocean tides, *Reviews of Geophysics, 18*, 243-268, 1980.

Seivers, J., C.S.M. Doake, J. Ihde, D.R. Mantripp, V.S. Pozdeev, B. Ritter, H.W. Schenke, F. Thyssen, and D.G. Vaughan, Validating and improving elevation data of a satellite image map of Filchner-Ronne Ice Shelf, Antarctica, *Annals of Glaciology, 20*, 347-352, 1994.

Smithson, M.J., A.V. Robinson, and R.A. Flather, Ocean tides under the Filchner-Ronne Ice Shelf, Antarctica, *Annals of Glaciology, 23*, 217-225, 1996.

Souza, A.J., and J.H. Simpson, The modification of tidal ellipses by stratification in the Rhine ROFI, *Continental Shelf Research, 16* (8), 997-1007, 1996.

Tsimplis, M.N., R. Proctor, and R.A. Flather, A two-Dimensional Tidal Model for the Mediterranean-Sea, *Journal of Geophysical Research, 100* (C8), 16223-16239, 1995.

Van Wyckhouse, R., Digital bathymetric database 5, U. S. Naval Oceanogr. Off., St. Louis, Miss., 1973.

Vaughan, D.G., J. Sievers, C.S.M. Doake, G. Grikurov, H. Hinze, V.S. Pozdeev, H. Sandhäger, H.W. Schenke, A. Solheim, and F. Thyssen, Map of subglacial and seabed topography 1:2000000 Filchner-Ronne-Schelfeis, Antarktis, Institut für Angewandte Geodäsie, Frankfurt am Main, Germany, 1994.

Vaughan, D.G., J. Sievers, C.S.M. Doake, H. Hinze, D.R. Mantripp, V.S. Pozdeev, H. Sandhäger, H.W. Schenke, A. Solheim, and F. Thyssen, Subglacial and seabed topography, ice thickness and water column thickness in the vicinity of Filchner-Ronne-Schelfeis, Antarctica, *Polarforschung, 64* (2), 75-88, 1995.

CHAPTER 4

Southern Weddell Sea Tidal Currents and Vertical Mixing

4.1 Introduction

Tidal currents are likely to be the principal source of energy for mixing between water masses in those areas of the southern Weddell Sea isolated from atmospheric forcing by the presence of ice shelves and fast ice. To determine the contribution of tidal processes to the oceanographic regime near the ice shelves the two-dimensional tidal model described in Chapter 3 is used to investigate the interaction between Filchner-Ronne Ice Shelf and the underlying ocean, in particular the contribution of tides to vertical mixing in the sub-ice shelf environment. To validate the tidal model, current meter data from moorings in the southern Weddell Sea are used, including the sub-ice shelf moorings described in Chapter 2. In this chapter the primary focus is not concerned with the precise prediction of tides for the region but to estimate the likely effects of tidal processes on the oceanography of the ice shelf environs.

Once beneath FRIS, WSW enters an unusual oceanographic environment. Within the sub–ice shelf cavity, water masses are isolated from atmospheric forcing, and tidal and thermohaline processes dominate the circulation. Once the WSW has descended to the grounding line regions, it has an in situ temperature up to 1°C higher than the pressure freezing point of seawater [*Jenkins and Bombosch*, 1995]. Occupying the lower portion of the water column, the WSW is separated from the ice shelf base by ISW that has a temperature close to the in situ freezing point. *MacAyeal* [1984a] suggests *tidal stirring* as a probable mechanism for mixing this warm, dense water up through the water column into

the overlying ISW, thereby sustaining strong melting where the WSW comes into contact with the base of the ice shelf. Thus, tides may play a crucial role in boosting the thermohaline circulation beneath the ice shelf through frictional drag at the seabed and ice shelf base giving rise to turbulence and vertical mixing through the water column.

Previous tidal models that include ice shelf cavities within their domains have already considered tidal elevations in this southern Weddell region [*Genco et al.*, 1994; *Robinson*, 1996; *Smithson et al.*, 1996; *Robertson et al.*, 1998]. Each attempted to predict the tidal constituents beneath FRIS, but none examined the effects of tidal currents on the circulation and mixing in the cavity. The only study of tidal currents beneath an ice shelf has been *MacAyeal* [1984a; 1985] who considered the cavity beneath Ross Ice Shelf.

4.2 Model results

4.2.1 Tidal current ellipses

The model current velocities are given as amplitudes and phases of the eastward and northward components of each tidal current constituent and these were used to construct current ellipses. The current ellipses for the diurnal tides Q_1, O_1, K_1 and the semi-diurnal tides N_2, M_2, S_2 are plotted every eighth grid point over the model domain in Figures 4.1a, b, c, d, e and f. Shaded and unshaded areas show regions of anticlockwise and clockwise rotation of current vectors.

In the deep Weddell Sea all current constituents are weak, with amplitudes less than 0.02 m s^{-1}. At the continental shelf break, diurnal currents are up to 5 times larger than on the continental shelf. *Middleton et al.* [1982] observed similar amplification in this region, and attributed it to the presence of diurnal barotropic shelf waves. Over the continental shelf the highest velocities (>0.5 m s^{-1} for M_2) are found in shallow areas, particularly the region south of Ronne Ice Front, close to Berkner Island. There the draft of the ice shelf

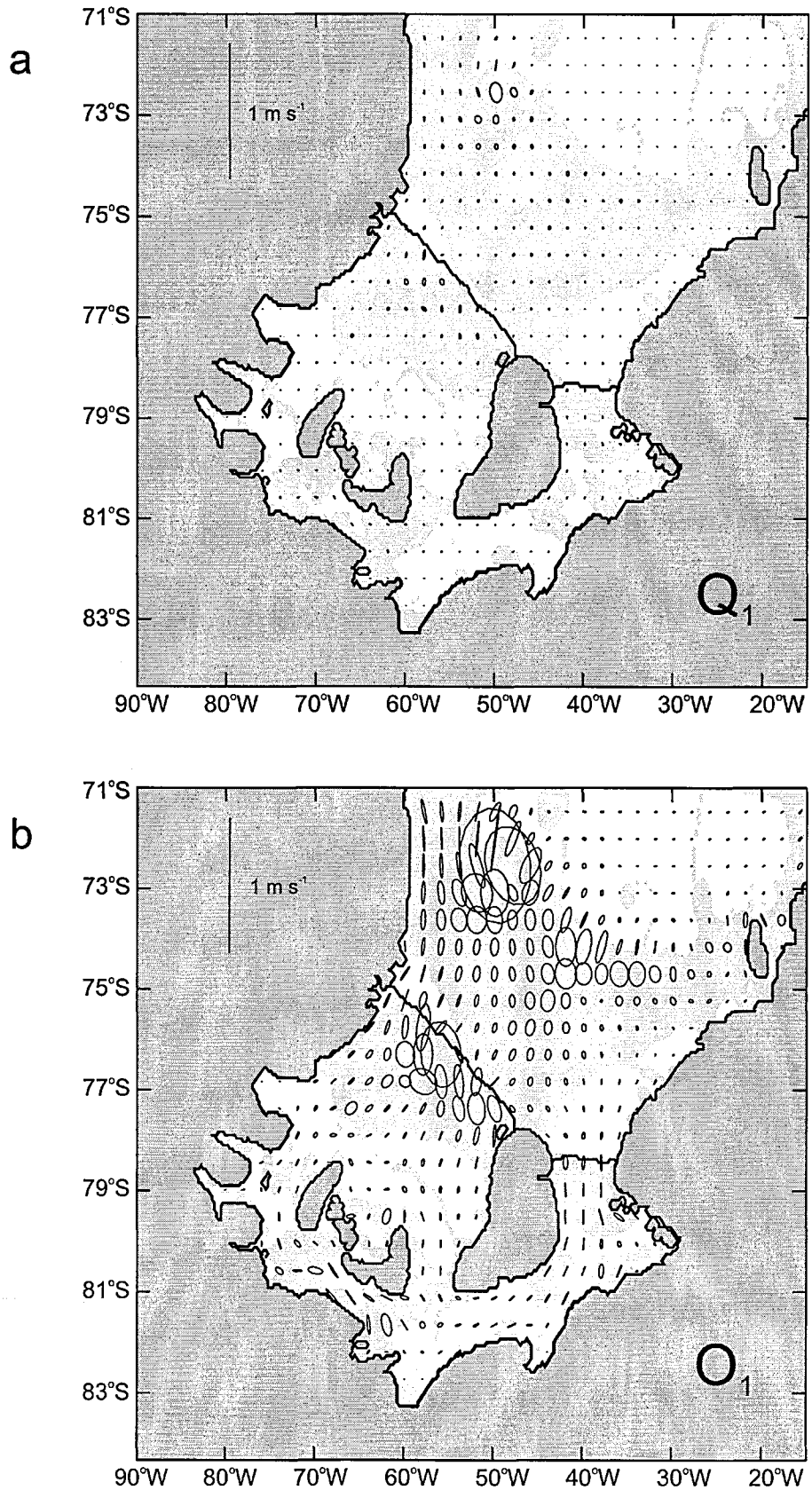

Figures 4.1a and 4.1b Modelled tidal current ellipses plotted at every eighth grid point for the **(a)** Q_1 and **(b)** O_1 tidal constituents. The lightly shaded regions indicate anticlockwise rotation of the currents vectors.

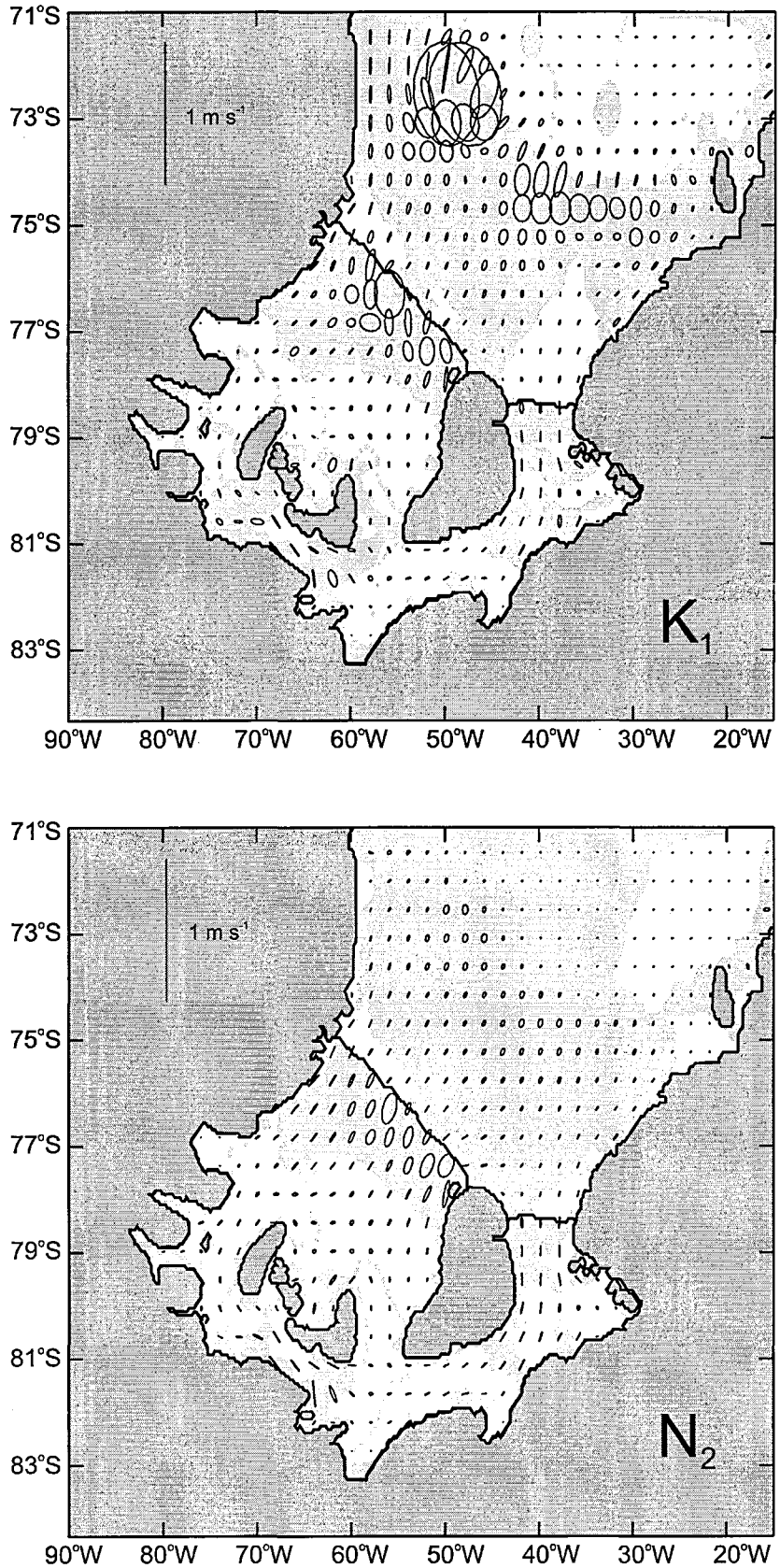

Figures 4.1c and 4.1d Modelled tidal current ellipses plotted at every eighth grid point for the **(c)** K_1 and **(d)** N_2 tidal constituents. The lightly shaded regions indicate anticlockwise rotation of the currents vectors.

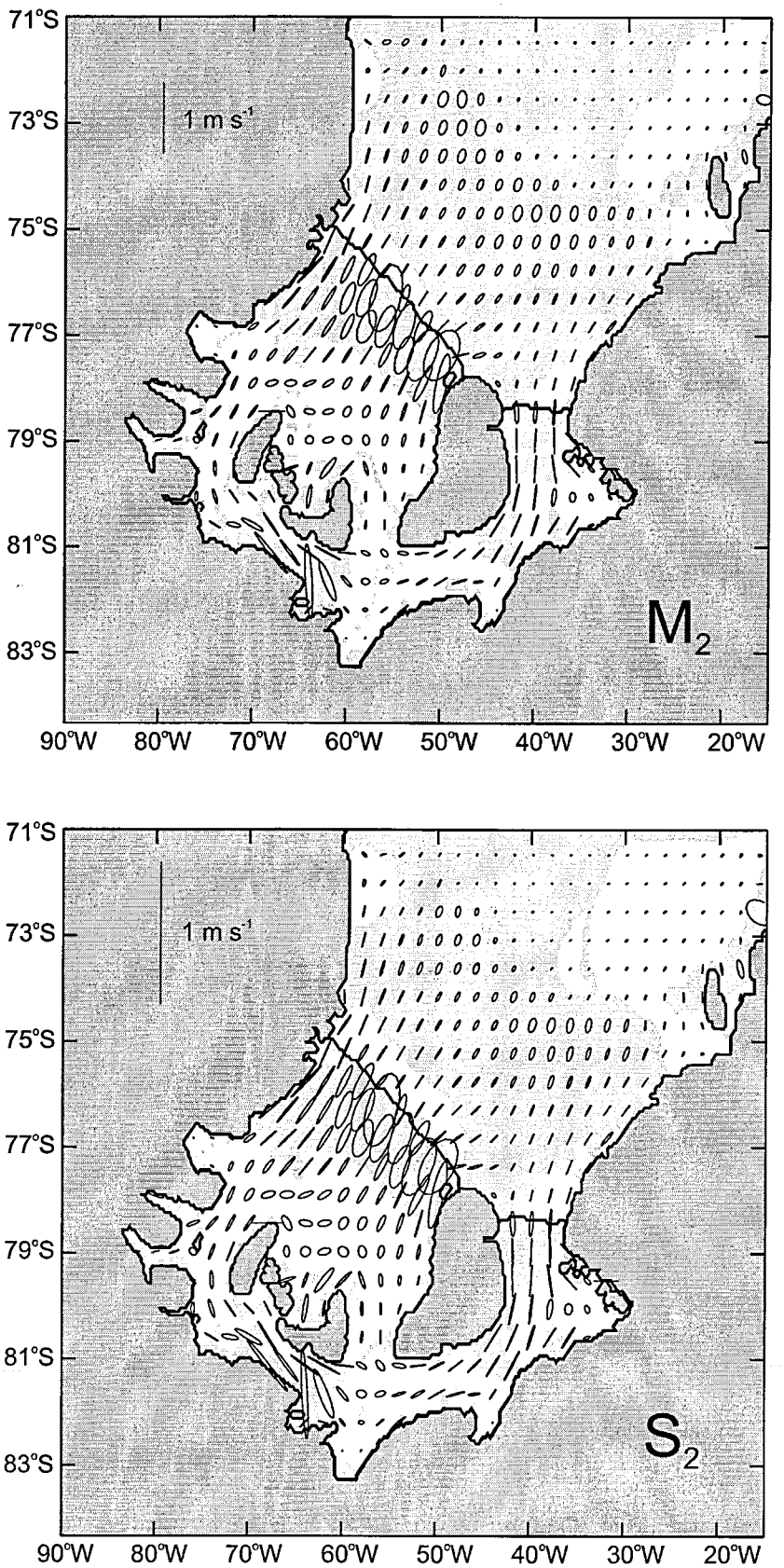

Figures 4.1e and 4.1f Modelled tidal current ellipses plotted at every eighth grid point for the **(e)** M_2 and **(f)** S_2 tidal constituents. Note that the scale bar for **(e)** is 50% smaller than for all other constituents. The lightly shaded regions indicate anticlockwise rotation of the currents vectors.

combines with shallow bathymetry to create a water column less than 100 m thick. In shallow areas the ellipses become more open, indicating a tidal current of nearly constant strength throughout the tidal cycle. Over the continental shelf close to the coast the ellipses are greatly flattened, particularly for the semi-diurnal tides, and the major axes are aligned parallel to the nearest coastline. These characteristics are consistent with a Kelvin wave propagating around the embayment. *MacAyeal* [1984b] similarly interpreted the semi-diurnal tides in the southern Ross Sea.

4.2.2 Tidal shore lead

Close to Filchner-Ronne Ice Front the oscillatory action of the tides, the tidal divergence, and offshore winds create areas of open water within the sea ice. Throughout much of the year they maintain a strip of open water, or shore lead, along the ice front [*Foldvik et al.,* 1985; *Foldvik and Gammelsrød,* 1988]. In this shore lead there is concentrated production of WSW [*Gill,* 1973], as a result of enhanced sea ice formation. Assuming the sea ice moves with the predominantly semi-diurnal tidal currents, a shore lead will be formed two times per day when the tidal current flow is away from the ice front. Conversely, when the tidal current flow is towards the ice front, the shore lead will close and any newly formed sea ice will be compacted against the ice front. Using the tidal model, the area of open water resulting from only tidal current oscillations was determined at each node along Ronne Ice Front from the product of the tidal excursion and the length of ice front. The hourly open water area that could result from tidal oscillations along Ronne Ice Front is shown in Figure 4.2 for the year 1997. The mean shore lead area is approximately 850 km^2 with peaks of almost 3000 km^2. Along Filchner Ice Front the mean shore lead area is approximately 150 km^2. Throughout the 1990's the effective ice front was significantly lengthened by a bridge of permanent sea ice that extended from the entire Filchner Ice Front to grounded ice bergs 200 km to the north. This extension is not considered in the above analysis.

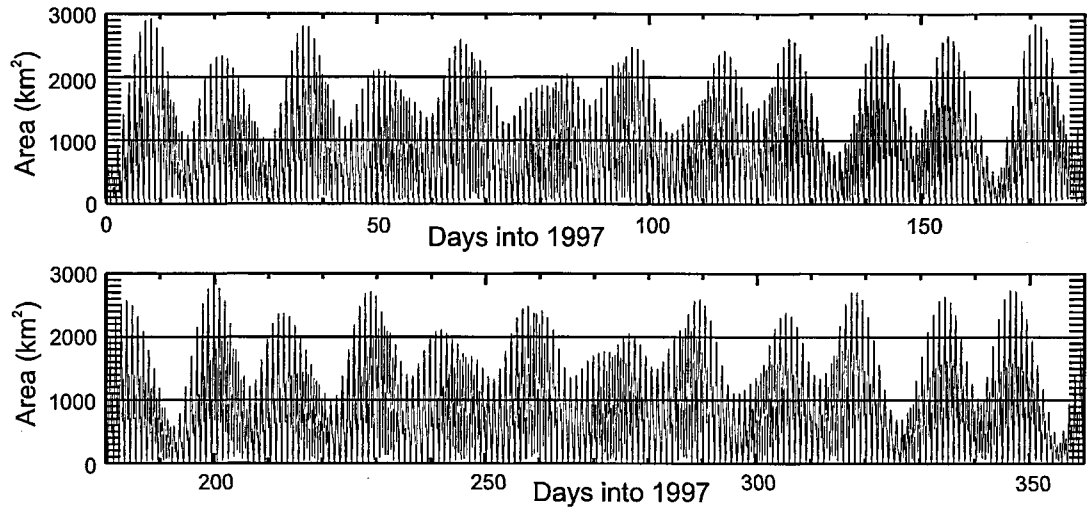

Figure 4.2 Modelled shore lead area along Ronne Ice Front resulting from purely tidal oscillations.

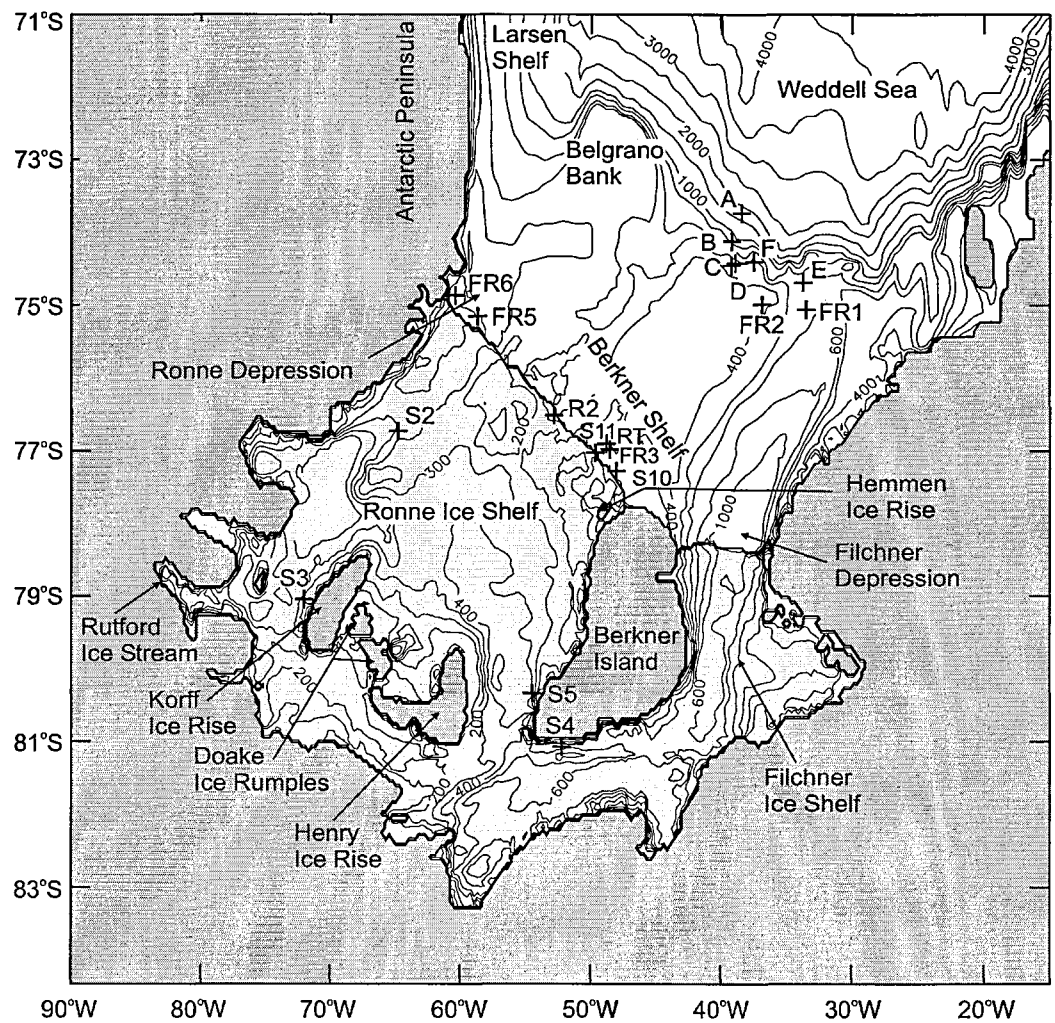

Figure 4.3. Map showing the model domain. The darkest shading indicates areas of grounded ice, and the lighter shading indicates the floating ice shelf. The contours give the water column thickness in meters. The location and name of current measurement sites used for comparison with the model are marked. The inset indicates the position of Filchner-Ronne Ice Shelf (FRIS) in the southern Weddell Sea, and the box shows the region covered by the model domain.

4.3 Field data

Ice shelves and year-round sea ice cover greatly limit the number of current meter observations from the Weddell Sea, and any current meter moorings that are deployed are under threat of damage or even removal by icebergs. A total of 19 current measurement sites that lie within the model domain are used to validate the model. The current meter sites, shown in Figure 4.3, fall into three main groups: eight continental shelf break sites lying mostly within a concentrated area along the shelf break around 74°S 39°W; seven ice front sites positioned close to or against Ronne Ice Front; and four sub–ice shelf sites, of which one is a thermistor cable site. The accuracy of the derived ellipses is chiefly dependent on the lengths of the time series, which are given in Table 4.1. The table also shows the instrument depth and the tidal species that were extracted. The observed and modelled current ellipses for the constituents extracted from the observed time series are shown in Figures 4.4 and 4.5. The modelled tidal velocities at each location have been adjusted to account for the difference between water column thickness measured at the sites and that used in the model domain.

4.3.1 Weddell Sea current meter records

At the continental shelf break, moorings were deployed and recovered by several different groups over the period 1968 to 1980 [*Elder and Seabrooke*, 1970; *Foldvik and Kvinge*, 1974; *Middleton et al.*, 1982; *Middleton et al.*, 1987]. Taking site C (Figure 4.3), which is representative of these six sites in the area, the modelled diurnal currents reproduce the observed amplification seen for K_1. Unlike the observed data set, however, the model shows amplification in O_1 also, most probably the result of incorrect bathymetry along the continental shelf break and adjacent sea [*Padman et al.*, 1998]. The absence of O_1 amplification in the observations has been attributed to the interaction of diurnal barotropic shelf waves that result from temporal variations in the mean velocity field interacting with the irregular shelf topography [*Foldvik et al.*, 1990]. The phase of the diurnal components

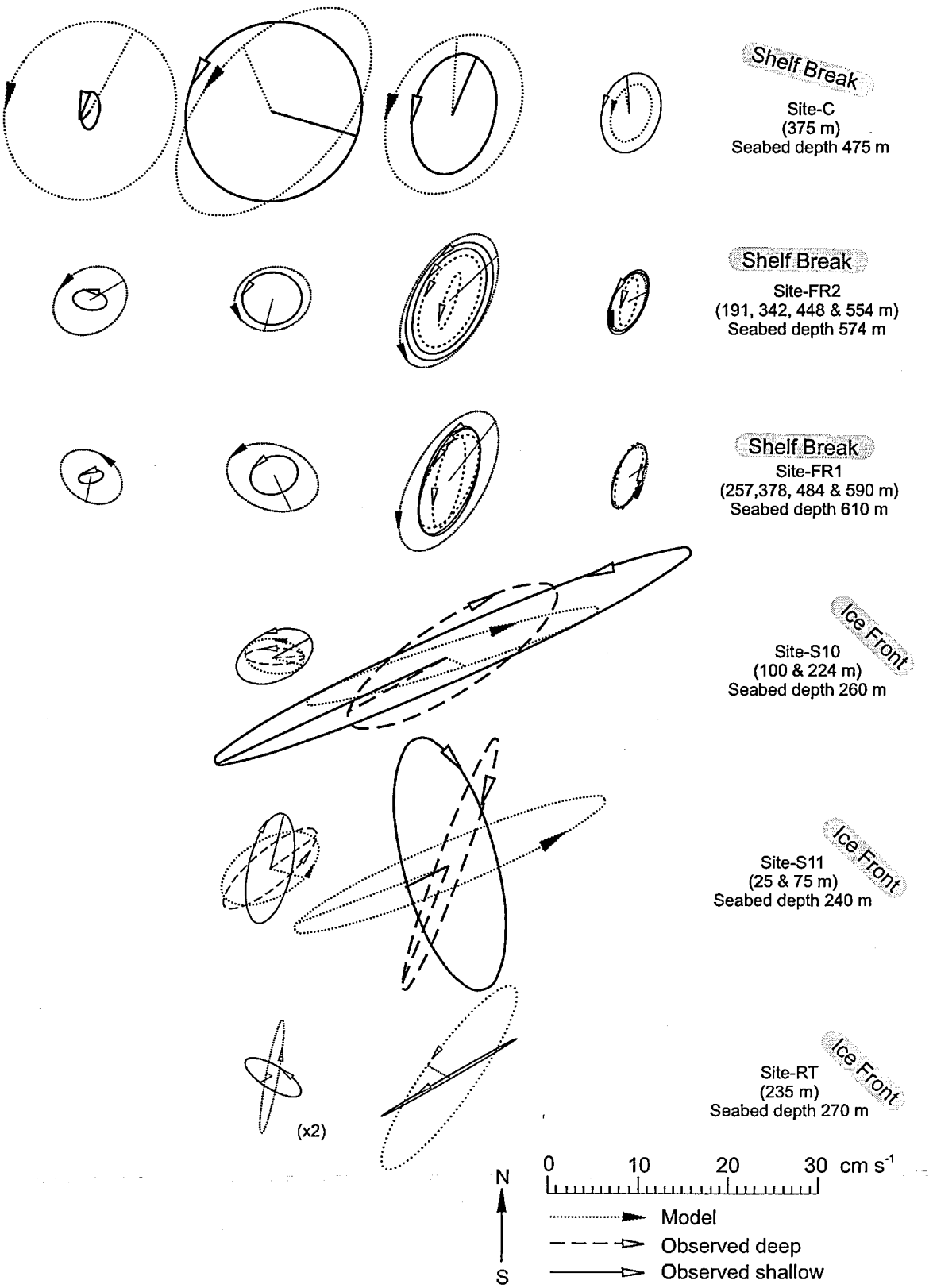

Figure 4.4 Tidal ellipses for the four largest constituents (O_1, K_1, M_2 and S_2) from the available current meter sites over the continental shelf and along Ronne Ice Front overlain with results from the model. Where the constituent is small a multiplying factor is applied and indicated. The current vector's sense of rotation is indicated by an arrow, and its phase by line from the ellipse centre. The orientation of any significant nearby topography and the depth of the instrument and seabed are indicated. The ellipses from site C are shown to represent the continental shelf break sites.

Table 4.1. Summary of Current Meter Sites Used for Comparison with the Model Results

Site	Location Type	Instrument Depth, m	Record length, days	Constituents	Reference
A	Shelf break	1815 *	419	Q_1, O_1, P_1, K_1, N_2, M_2, S_2,	*Foldvik et al.* [1990]
B	Shelf break	620 *	257	Q_1, O_1, P_1, K_1, N_2, M_2, S_2,	*Foldvik et al.* [1990]
C	Shelf break	375 *	631	Q_1, O_1, P_1, K_1, N_2, M_2, S_2,	*Foldvik et al.* [1990]
D	Shelf break	400 *	504	Q_1, O_1, P_1, K_1, N_2, M_2, S_2,	*Foldvik et al.* [1990]
E	Shelf break	375 *	257	Q_1, O_1, P_1, K_1, N_2, M_2, S_2,	*Foldvik et al.* [1990]
F	Shelf break	445 *	31	O_1, K_1, N_2, M_2, S_2	*Foldvik et al.* [1990]
FR1	Shelf break	257, 378, 484 & 590	max 837	Q_1, O_1, P_1, K_1, N_2, M_2, S_2,	*Woodgate et al.* [1998]
FR2	Shelf break	191, 342, 448 & 554	max 837	Q_1, O_1, P_1, K_1, N_2, M_2, S_2,	*Woodgate et al.* [1998]
FR3	Ice front	203	837	Q_1, O_1, P_1, K_1, N_2, M_2, S_2,	*Woodgate et al.* [1998]
FR5	Ice front	204, 305 & 551	max 830	Q_1, O_1, P_1, K_1, N_2, M_2, S_2,	*Woodgate et al.* [1998]
FR6	Ice front	261, 442 & 588	max 830	Q_1, O_1, P_1, K_1, N_2, M_2, S_2,	*Woodgate et al.* [1998]
R2	Ice front	245 & 400	435	O_1, P_1, K_1, N_2, M_2, S_2, K_2	*Foldvik et al.* [2001]
RT	Ice front	235	10	K_1, M_2	*Foldvik et al.* [2001]
S10	Ice front	100 & 224	4.5	K_1, M_2	*Foldvik et al.* [1985]
S11	Ice front	25 & 75 †	11	K_1, M_2	*Foldvik et al.* [1985]
S2	Sub–ice shelf	-‡	660	O_1, K_1, M_2, S_2	*Makinson and Nicholls* [1999]
S3	Sub–ice shelf	1125	+565	Q_1, O_1, P_1, K_1, N_2, M_2, S_2,	*Makinson and Nicholls* [1996]
S4	Sub–ice shelf	926	+356	Q_1, O_1, K_1, N_2, M_2, S_2	*Nicholls et al.* [2001]
S5	Sub–ice shelf	768 & 996	+365	Q_1, O_1, K_1, N_2, M_2, S_2	*Nicholls et al.* [2001]

* More than one current meter was present at the site; details of the instrument with greatest height above bottom are given, typically 100 m above bottom.

† The shallowest instrument was believed to be above the draft of the ice shelf.

‡ Constituents estimated from thermistor cable data.

are rather poorly reproduced by the model. For the semi-diurnal currents the model overestimates the amplitudes, though there is reasonable agreement in the phases.

More recently, moorings FR1 and FR2 were deployed from 1995 to 1997 on the northern sill of Filchner Depression to record the outflow of ISW [*Woodgate et al.*, 1998]. Both these sites are situated further from the shelf break, and there is better agreement between the model and observations. The rotation for all constituents at these sites is anticlockwise with relatively open ellipses (Figure 4.4). The model overestimates the amplitude of the currents, especially for the diurnal constituents.

4.3.2 Ice front current meter records

Using the 1986/1987 ice front position in the model, some of the seven ice front mooring locations have been moved by up to 8 km perpendicular to the ice front to take account of the 1300 m yr^{-1} advance rate [*Vaughan and Jonas*, 1996]. Hence, the relative distance from the ice front is maintained of each mooring over its deployment period. The change in water depth is minimal as the bathymetry is relatively flat around these locations. All the ice front sites except S11 were located a few kilometres offshore of the ice front. Taking the three sites with the shortest records, there is generally poor agreement in orientation and phase between the model and sites S10, S11 and RT (Figure 4.4), although the amplitudes are reproduced reasonably well. The disagreement in phase probably results from either the inability of the model to reproduce the tides accurately in close proximity to an abrupt change in the water column depth or from the limited length of the record. In addition to these short term ice front moorings, *Foldvik et al.* [1985] used a Braystoke meter close to the ice front to obtain current data at 20 m and 50 m depths. There are small differences in the direction of flow between the model and the data but the ebb and flow of the tide correspond well both in time and magnitude.

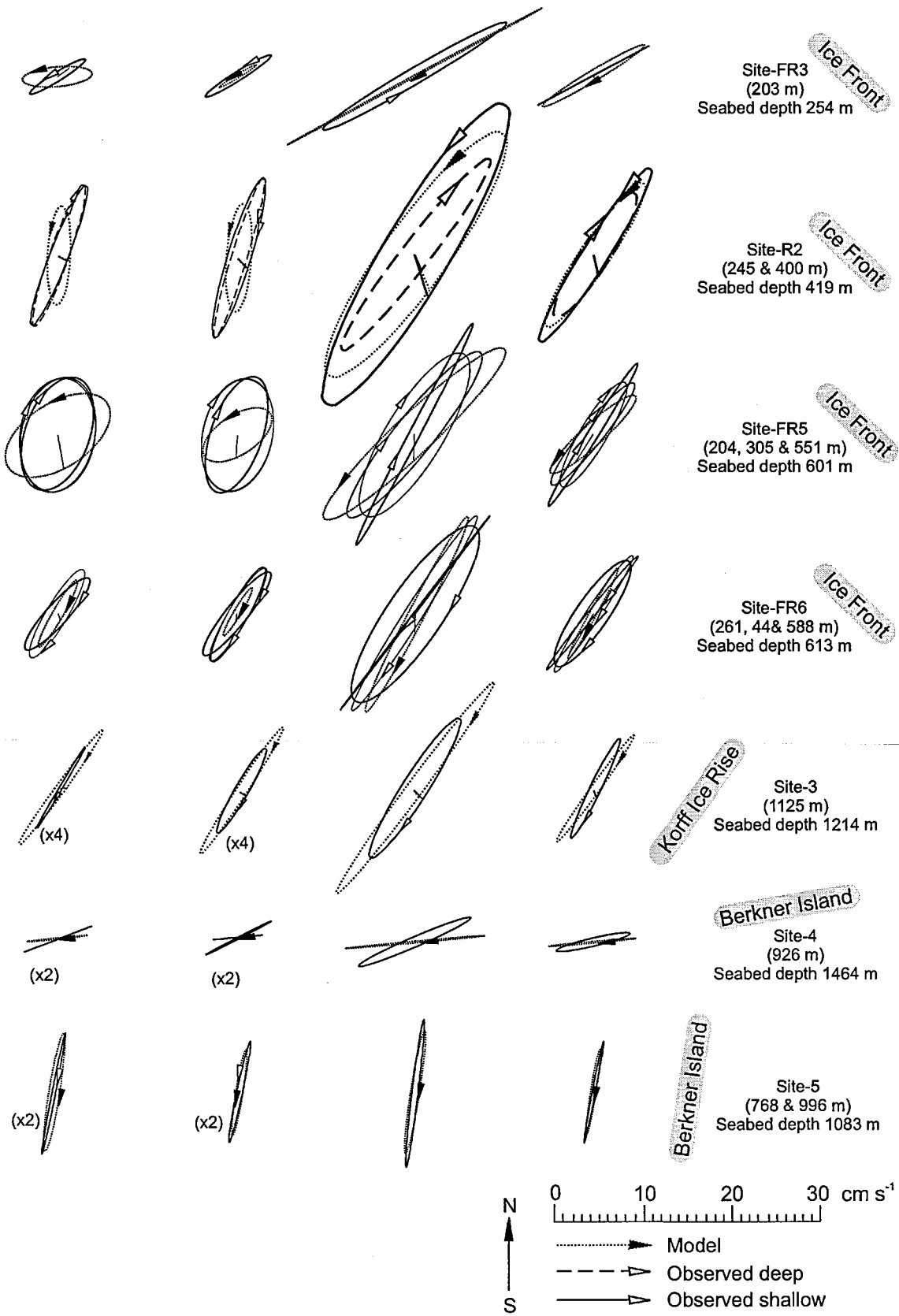

Figure 4.5 Tidal ellipses for the four largest constituents (O_1, K_1, M_2 and S_2) from the long term (>1 year) current meter sites along Ronne Ice Front and beneath FRIS overlain with results from the model. Where the constituent is small a multiplying factor is applied and indicated. The current vector's sense of rotation is indicated by an arrow, and its phase by line from the ellipse centre. The orientation of any significant nearby topography and the depth of the instrument and seabed are indicated.

The four remaining ice front sites (FR3, R2, FR5 and FR6) are the only long term ice front moorings with records exceeding one year. R2 was deployed at a distance of 4.3 km from the ice front. Two years later when the mooring was recovered this had decreased to 0.5 km [*Foldvik et al.*, 2001] illustrating the need to consider ice front advance for longer term moorings. After a further three months the mooring location would have been beneath the advancing ice shelf. At all these sites the modelled constituents are in reasonable agreement with the observations both in phase (where available) and amplitude particularly for the semi-diurnals (Figure 4.6).

4.3.3 Sub-ice shelf current meter records

Beneath the ice shelf, current meter moorings have been deployed through hot water drilled access holes. The first measure of currents came from a thermistor cable suspended beneath the ice shelf at Site 2 (S2 in Figure 4.3). Here, currents have been estimated using an assumed water column temperature profile and measuring the temperature as the cable swings through the water column. The analysis yielded the lengths of the major axes of the O_1, K_1, M_2 and S_2 ellipses and also the phase for each constituent. The method of analysis is described fully in the appendix of *Makinson and Nicholls*, [1999]. Modelled and inferred major axes amplitudes and phases generally agree to within 0.2 cm s^{-1} and 20°, the only exception being the M_2 amplitude, which was 25% (7 cm s^{-1}) lower than the value derived from the observations. Figure 4.6 show the comparison between the modelled and synthesized data.

The first direct measurement of the sub–ice shelf currents beneath FRIS was 17 km from the west coast of Korff Ice Rise at Site 3 (S3 in Figure 4.3) [*Nicholls et al.*, 1997]. A mean flow of 0.04 m s^{-1} was measured in the lower portion of the water column flowing southward along the coast of Korff Ice Rise (Figure 2.10a). The orientations of the modelled ellipses agree with the observations, and the phases differ by no more than 15°.

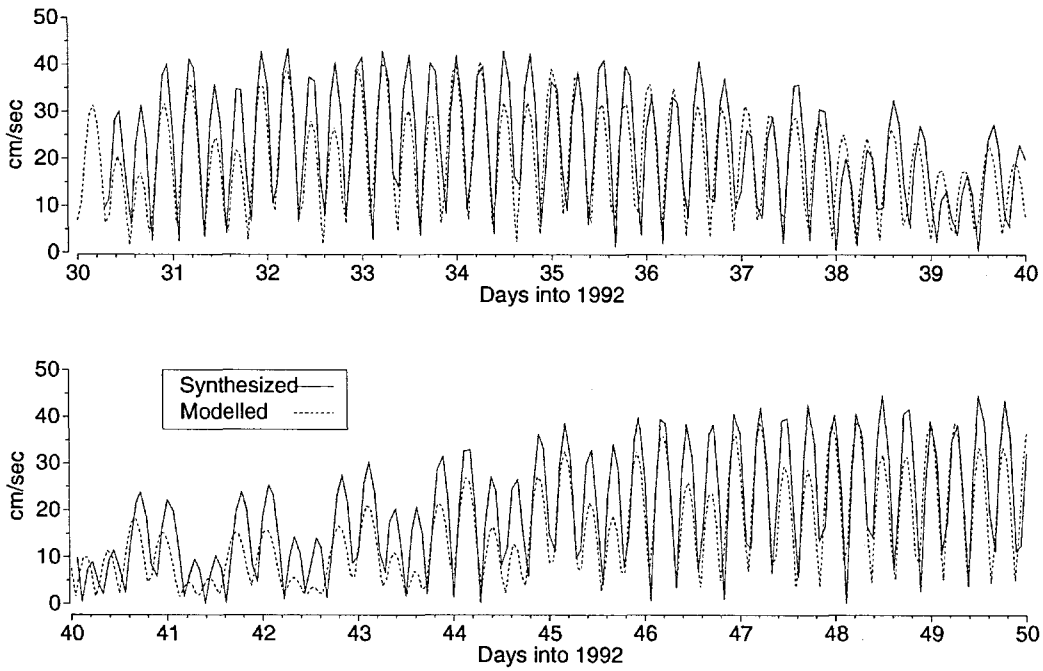

Figure 4.6 Taken from *Makinson and Nicholls* [1996]. A time series excerpt from Site 2 thermistor cable showing the comparison between the tidal model speed record and the synthesized record.

However, the major axes of the modelled currents are 30% larger than observed. During conductivity-temperature-depth (CTD) profiling at the site a bottom sensor suggested the presence of small-scale topography (~20 m) that may be responsible for these differences.

Located close to the southern coasts of Berkner Island, sites 4 and 5 are the only other direct current meter measurements from beneath FRIS. At Site 4 the mean velocity in the upper portion of the water column was found to be 0.15 m s^{-1} (Figure 2.10b). The flow was easterly parallel to the coast of Berkner Island and equivalent to the peak current during spring tides. The orientations of the modelled ellipses agree to within 15° of the observations which are aligned with the coast of Berkner Island and the phases differ by no more than 5° for both the diurnal and semi-diurnal tides. However, the major axes of the modelled semi-diurnal currents are 10% larger than observed, whereas they are 30% smaller for the diurnals. For all the constituents the ellipses are almost flat because of the

proximity of the coast 12 km to the north. At Site 5 the mean velocity was to the south and found to be 0.49 m s^{-1} at the upper instrument and 0.43 m s^{-1} at the lower instrument (Figure 2.10c) [*Nicholls et al.*, 2001]. Over the following year these high mean velocities decreased by almost 50% but still much larger than the tidal signal. The interaction of the tides at the upper current meter with the mean flow dynamics and proximity to the strongest part of the pycnocline may give rise to non-barotropic tides. Analysis of the current data gives a wide range of amplitudes and phases throughout the record. However, the lower current meter is situated in a less stratified part of the water column and analysis indicates amplitudes and phases that are more stable but which still exhibit some fluctuations. The mean results are shown in Figure 4.5, showing that the model overestimates the major axes by up to 15% but that the modelled phases are within 15° of the observed values.

4.3.4 Proxy current data

Indirect observational evidence is available to support the relative current strengths along Ronne Ice Front. *Haase* [1986] obtained a transect of surface sediment samples with a box corer and gravity corer along Ronne Ice Front within 3.5 km of the barrier. The samples showed a broad diversity of sediments, suggesting a wide range of current environments. Over Berkner Shelf the sediments consisted purely of sand. Over the shallowest areas of Berkner Shelf they contained trough bedding structures typical of a high-energy current regime, that is, velocities over 20 cm s^{-1}, 1 m above the seafloor. Observations by *Foldvik et al.* [1985], like the model results, reveal RMS water velocities of 26-30 cm s^{-1}, with peak spring velocities reaching 1 m s^{-1}. Along the central ice front is an area of intermediate water depth (400-500 m). There, silt and clay fractions were found to be high, the high clay content suggesting very low velocities of 0-2 cm s^{-1}. Over the central ice front section, mean velocities from the model are 10 cm s^{-1}, with current measurements within 20 m of the seabed at Site R2 [*Foldvik et al.*, 2001] giving essentially the same value, higher than that suggested by the sediments. However, one possibility is that a significant proportion of the

tidal velocity close to the seabed may be lost to vertical shear. On the ridge, further to the northwest, the sediments contain mainly fine sands, with current ripples indicating water velocities of at least several centimetres per second. RMS model velocities over this ridge were 18-20 cm s^{-1}. Finally, over Ronne Depression and close to the Antarctic Peninsula the gravel and mud content increases. The gravel and drop stones are of glacial origin with the muds indicating a low current regime. As with the central ice front section, modelled velocities are higher (13 cm s^{-1}) than suggested by the sediments. Two additional sample sites, 10-15 km from the ice front, exhibit an increase in silt and clay, suggesting weaker currents in the deeper waters away from the influence of the ice shelf. Modelled RMS velocities offshore from Ronne Ice Front are generally two or three times lower than the ice front currents, and in this way consistent with the sediment content.

4.3.5 Accuracy of tidal model

There are several potential sources of error in the model. As this model is purely barotropic and the generation of baroclinic tides is not considered. The forcing at the open boundary was provided by a larger area model which suffered from poorly known bathymetry. In particular, the location of the edge of the Larsen continental shelf was wrong by up to 100 km and the Schwiderski global tidal data set used to force the larger scale model is also likely to be less accurate in this region [*Le Provost et al.*, 1995]. In the present application of the model, the water column thickness over the ice shelf area is subject to errors from both the seabed depth and ice thickness, neither of which are well known at the model resolution. The location of some of the current meter sites is not ideal for testing modelled currents, such as sites at the ice front where the water column has a step change in thickness of hundreds of meters leading to significant errors in current phase, amplitude, and rotation. There will also be errors associated with the drag coefficient which is applied uniformly over the domain. Observations along the ice front clearly show different bed forms [*Haase,* 1986] which will have different drag coefficients, a problem common to all tidal models.

In addition, the drag coefficient at the ice shelf base has never been measured and a value of 0.0025 has been assumed. *Smithson et al.* [1996] and *Padman et al.* [2002] found evidence that friction coefficients of up to 0.015 beneath the ice shelf may improve the fit between modelled and observed tidal elevations, particularly near grounding lines, but at the expense of degrading the agreement of the open water sites. The potential for ice shelf flexure at the grounding lines to act as a significant sink for tidal energy was first discussed by *Doake* [1978] though *Vaughan* [1995] suggests that this mechanism does not dissipate much energy. Such an energy sink is not present in the model used in this study. Overall, however, the model has achieved a reasonable fit to the known data, successfully reproducing the general features of the tidal flow over the domain.

4.4 Tidal energy and vertical mixing

4.4.1 Mean water speed

Tidal currents are likely to provide the principal source of energy for mixing within the sub-ice shelf cavity and the most effective mixing will be associated with the strongest tidal currents. To determine the mean tidal currents the modelled constituents were combined and averaged over a spring-neap cycle to calculate the average root mean square (RMS) water speed over the domain (Figure 4.7). Average RMS speeds greater than 0.2 m s^{-1} are highlighted, and average RMS spring tide speeds are typically double the values shown in Figure 4.7. Of the three regions where the average currents are high, two correspond to areas of relatively shallow water (<200 m): the area south of Ronne Ice Front and south of Henry Ice Rise. The third region, where the water column is 400 m, is centred on Belgrano Bank. This area is subject to tidal amplification in the diurnal band (Figures 4.4) resulting in high RMS speeds.

4.4.2 Tidal energy flux

The tidal energy flux vectors were computed over the model domain using $\mathbf{u}(g\rho D\eta+\rho D½|\mathbf{u}|^2)$, where $\mathbf{u}$ is the depth-averaged tidal velocity, D is the water column thickness, η is the displacement of the sea surface from the equilibrium level, g is the gravitational acceleration, and ρ is the seawater density in this region (1028 kg m^{-3}). The first term, representing the work done against pressure forces during the tidal cycle, dominates over the kinetic energy term. Figure 4.8 is a map of the energy flux vectors and shows a proportion of the main energy flux from the Weddell Sea crossing the continental shelf via the Filchner Depression, before propagating beneath Filchner Ice Shelf. Once beneath the ice shelf most of the flux circulates clockwise south of the ice rises. A small portion branches to the north, between Henry Ice Rise and Berkner Island. Most of the energy beneath the ice shelf is associated with the semi-diurnal Kelvin wave that propagates around the embayment.

4.4.3 Tidal dissipation

Energy transfer from tidal currents to turbulent mixing is provided by the flow of tidal currents over the seabed and ice shelf base. Frictional drag at these surfaces produces vertical shear and the resultant turbulence causes vertical mixing through the water column. Assuming a quadratic drag law, the rate of dissipation of energy by surface friction ϵ is proportional to the cube of the depth-averaged velocity $\mathbf{u}$ and is given by $\epsilon=\rho C_d|\mathbf{u}|\mathbf{u}\cdot\mathbf{u}$. Variables ρ and C_d are the density of seawater and the bottom friction coefficient which are assigned the values used in the model run (1028 kg m^{-3} and 0.0025). As in the model run, to account for the presence of the ice shelf base as a second frictional surface, the bottom friction coefficient was doubled for grid points covered by ice shelves. As energy dissipation is proportional to the cube of the water speed, areas of high dissipation are spatially similar to those with high currents, that is, areas of shallow water. The distribution of tidal energy dissipation is shown in Figure 4.9.

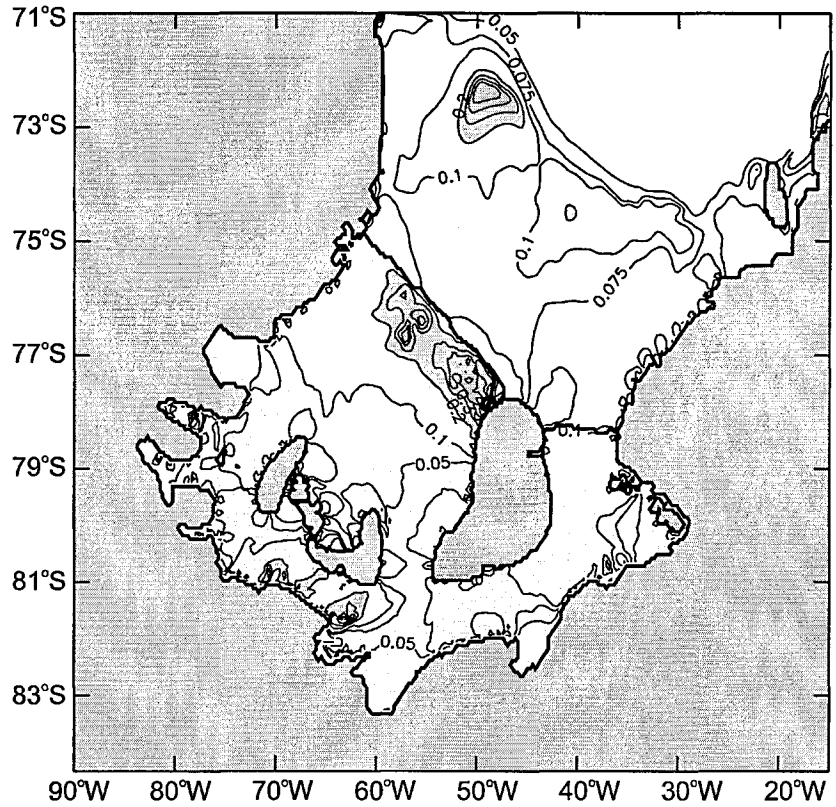

Figure 4.7 A contour plot of the average RMS water speeds over the model domain, with speeds greater than 0.2 m s^{-1} heavily shaded. The highest speeds are found in the shallow region south of Ronne Ice Front and Belgrano Bank with peak spring speeds typically three times greater than the average speeds.

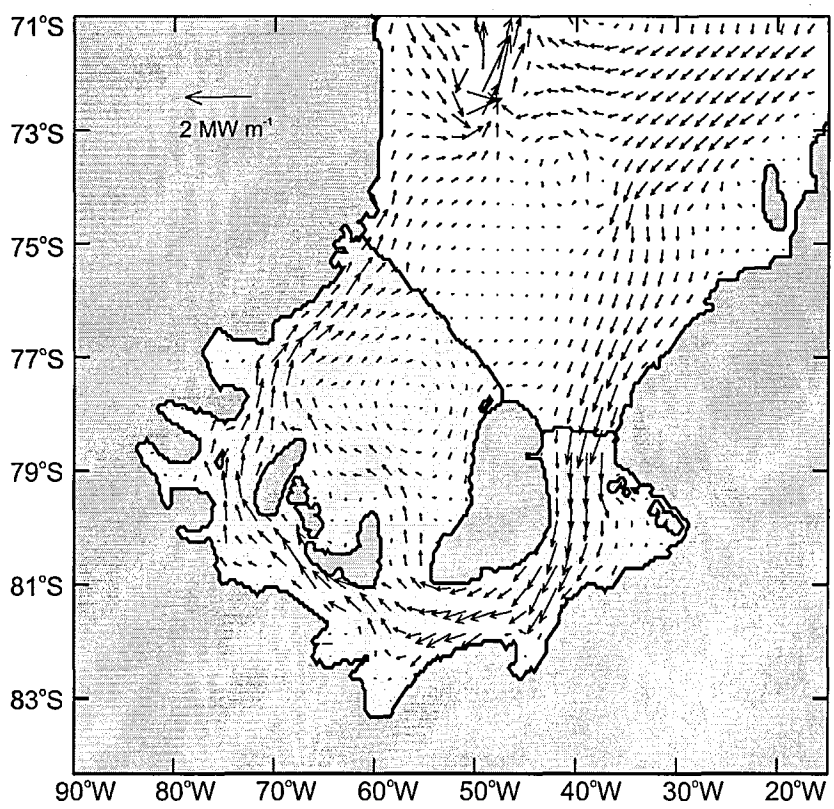

Figure 4.8 Average tidal energy flux vectors are plotted for every eighth grid point of the model domain. The majority of the energy flux enters the sub–ice shelf cavity via the Filchner Depression.

The total dissipation over FRIS is 25 GW, nearly an order of magnitude greater than the 3.5 GW dissipated beneath Ross Ice Shelf [*MacAyeal*, 1984b] and accounting for approximately 1% of the world's total tidal dissipation budget. Almost three quarters of the energy is lost in the shallow region south of Ronne Ice Front, with most of the remainder being dissipated south of Henry Ice Rise. The highest dissipations beneath the ice shelf (>1 W m^{-2}) are near to the eastern end of Ronne Ice Front. Over the adjacent continental shelf, which has a thicker water column and therefore lower water velocities, the dissipation is significantly less: a total of 8 GW, half of which is lost in a small area around 73°S, 50°W.

4.4.4 Estimated basal melt rates

It has been estimated that 1-2% of the tidal energy dissipated at frictional surfaces is available for vertical mixing of the water column [*Fearnhead*, 1975; *Schumacher et al.*, 1979]. The power required to mix the water column is the power needed to distribute fresh water melted from the ice shelf base through the water column and is therefore dependent on the melt rate m. The power required is given by $2m\rho\beta gSD$ where $\beta = 1/\rho\ (\partial\rho/\partial S) = 0.8 \times 10^{-3}\ (‰)^{-1}$, S is the salinity of WSW (34.75 ‰) in the lower half of the water column, and D is the water column thickness. The power available from tidal dissipation is $\alpha\rho C_d|\mathbf{u}|\mathbf{u}\cdot\mathbf{u}$, where α (0.015) is the fraction of total energy estimated to be available for vertical mixing. Therefore for a water column to be well mixed, the melt rate m must be less than $m_m = \alpha\rho(C_d|\mathbf{u}|\mathbf{u}\cdot\mathbf{u})/(1/2\rho\beta gSD)$ [*MacAyeal*, 1984b]. Conversely, in areas where melt rates are greater than m_m, stratification will prevail. Figure 4.10 shows the pattern of distribution of m_m, over the domain. The figure indicates the pattern of distribution rather than definitive values, based on best estimates of the parameters which can be varied, for example, the fraction and composition of WSW in the lower portion of the water column [*Nicholls and Makinson*, 1998]. Direct verification of the extent of a stratified or well mixed water column is limited by scarcity of observations. Likewise, basal melt rates are

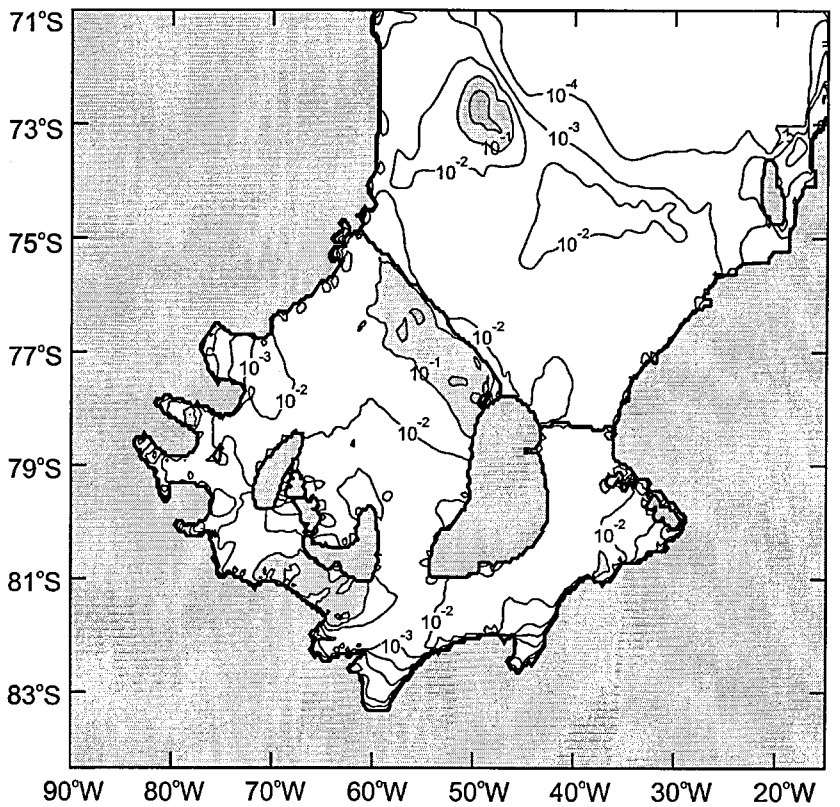

Figure 4.9 A contour plot of the average tidal dissipation (W m^{-2}) on a $\log_{10}$ scale, with shading indicating dissipation values greater than 0.1 W m^{-2}.

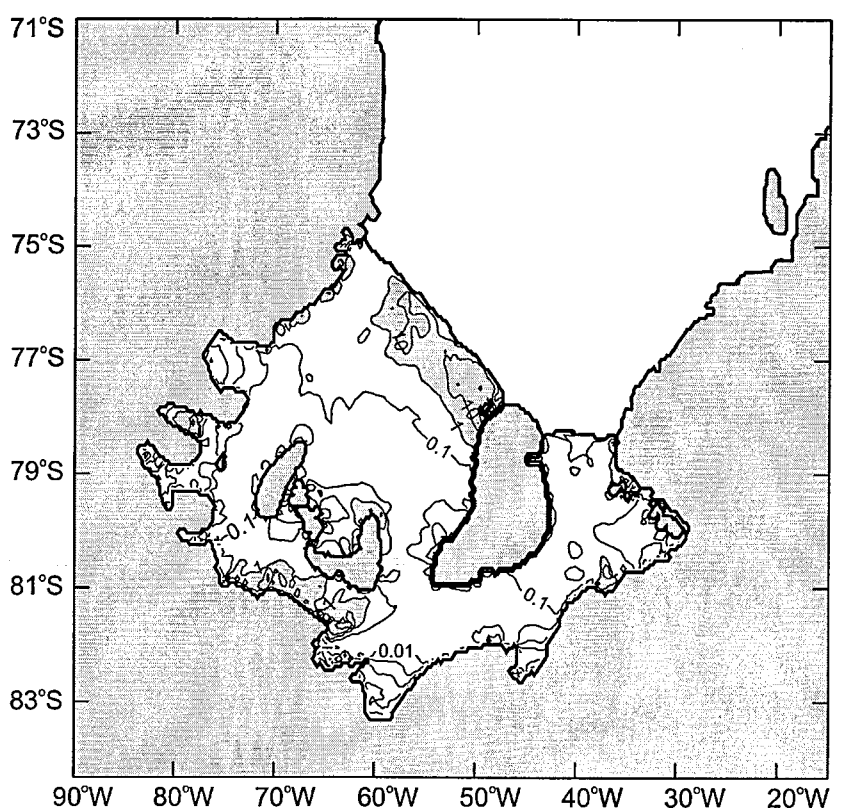

Figure4.10 The minimum basal melt rate required to maintain stratification of the water column contoured using a $\log_{10}$ scale. Areas where basal melt rate to maintain stratification is above 1 m yr^{-1} are highlighted.

poorly known and are normally determined using indirect approaches such as glaciological measurements [*Jenkins and Doake*, 1991], ice shelf temperature profiles [*Grosfeld et al.*, 1992] and oceanographic data [*Nicholls and Makinson*, 1998].

4.4.5 Observed melt rates

Near Ronne Ice Front melt rates of 1.5-6 m yr^{-1} have been determined by a number of different methods [*Kohnen*, 1982; *Jenkins and Doake*, 1991; *Grosfeld et al.*, 1992]. Here tidal oscillations force warm surface waters beneath the ice shelf, causing rapid melting [*Gammelsrød and Slotsvik*, 1981], particularly during summer months when there is an additional heat input into the offshore ocean water. Despite the high melt rates, the model results predict that the water column will be well mixed, for m_m in these areas is over 10 m yr^{-1} (Figure 4.10).

In areas of the ice shelf cavity where ice crystals form in the water column [*Bombosch and Jenkins*, 1995], such as the central Ronne Ice Shelf [*Robin et al.*, 1983; *Nicholls et al.*, 1991], the basal melt rate is negative. The rate of negative melt depends on whether the ice crystals are held in suspension, or whether they are deposited on the ice shelf base. Ice crystals suspended in the water column provide additional buoyancy, and consequently contribute to the stratification [*Jenkins and Bombosch*, 1995]. Tidal stirring, when $m_m<0$, therefore has the effect of reducing the deposition of ice at the ice shelf base and therefore enhancing stratification but also of mixing warmer water up through the water column.

Closer to the grounding lines, where the ice shelf is thickest, the pressure freezing point of seawater is depressed by up to 1°C, and relatively high basal melt rates are possible if WSW is mixed up through the water column. Indeed, melt rates of between 3.5 and 7 m yr^{-1} have been calculated within 20 km of the grounding line of Rutford Ice Stream [*Jenkins and Doake*, 1991; *Corr et al.*, 1996; *Smith*, 1996]. Here, however, the model predicts that the

water column is stratified, as $m>m_m$ (Figure 4.10). In these areas, the high vertical heat fluxes necessary to maintain such basal melt rates are probably induced by shear between the deeper, warmer water and plumes of ISW rapidly ascending the steep basal slope [*MacAyeal*, 1984b; *Jenkins*, 1991]. Such ISW plumes could be initiated very near the grounding line where the water column finally pinches out, and where tidal mixing is likely to be locally high. The pinching out of the water column is not properly represented at the resolution of the tidal model. An extended region of thin cavity south of Henry Ice Rise leads to m_m exceeding 10 m yr^{-1} (Figure 4.10), and a well mixed water column is therefore likely. In this area the basal melt rate is expected to be high compared with nearby stratified areas.

Beneath FRIS, vertical mixing competes with the stratifying influence of basal melting. Tidal fronts separate the abrupt changes in water properties caused by variations in the level of vertical mixing between well mixed and stratified regions [*Simpson*, 1981]. The balance between tidal mixing and buoyancy input from basal melting therefore determines frontal positions. A tidal front causes an inclination of isopycnals which leads to along-front geostrophic currents. The model predicts tidal fronts near the ice front where the direction of any induced flow would be along the front towards the southeast (Figure 4.10). Beneath the ice shelf, however, the small density contrasts that are possible across a mixing front (0.2 kg m^{-3}) are likely to be too weak for the development of significant frontal flows.

4.5 Summary and conclusions

A depth-averaged barotropic tidal model has been used to simulate the tidal currents of the southern Weddell Sea. In total, six tidal constituents (Q_1, O_1, K_1, N_2, M_2, S_2) were modelled. There is reasonable agreement between the results from the model and the limited number of available current meter records, given the potentially large errors in bathymetric and ice shelf thickness data used to determine the water column thickness, particularly away from

the Filchner-Ronne Ice Front region where only sparse data coverage is available. The largest deviations between measurements and model are found in the diurnal band. However, the model results demonstrate that oscillatory tidal currents are likely to play an important role in the oceanic processes beneath and in the vicinity of Filchner-Ronne Ice Shelf.

The strongest tidal currents are found on Berkner Shelf along Ronne Ice Front. Where the ice shelf significantly reduces the water column thickness, tidal currents peak at over 1 $m\,s^{-1}$ during spring tides. In this area, average tidal excursions of up to 15 km beneath the ice shelf, and up to 5 km in the open sea, help maintain a shore lead and therefore the production of WSW. Energy dissipation by bottom friction is highest in shallow water regions, particularly beneath the ice shelf where the total energy dissipation, approximately 25 GW, accounts for almost 1% of the global energy budget [*Tsimplis et al.*, 1995]. A consequence of the energy dissipation is vertical mixing through the water column. Along 350 km of Ronne Ice Front the combination of strong residual currents, large tidal excursions and vigorous mixing gives rise to a region where the model predicts strong melting. Along this section of ice front and up to 70 km inshore, melting averages 2-3 m yr^{-1} [*Kohnen*, 1982; *Jenkins and Doake*, 1991; *Grosfeld et al.*, 1992] which is consistent with the model predictions, giving a net loss of 50-75 $km^3\,yr^{-1}$, equivalent to 11-16 cm yr^{-1} over the whole FRIS. In the deeper regions of the ice shelf cavity where energy dissipation is low, vertical mixing is likely to play only a small role in modifying the water column structure.

4.6 References

Bombosch, A., and A. Jenkins, Modeling the Formation and Deposition of Frazil Ice beneath Filchner-Ronne Ice Shelf, *Journal of Geophysical Research, 100* (C4), 6983-6992, 1995.

Corr, H., M. Walden, D.G. Vaughan, C.S.M. Doake, A. Bombosch, A. Jenkins, and R.M. Frolich, Basal melt rates along the Rutford Ice Stream, in *Filchner Ronne Ice Shelf Programme Report No 10*, edited by H. Oerter, pp. 11-15, Alfred-Wegener-Institute for Polar and Marine Research, Bremerhaven, 1996.

Doake, C.S.M., Dissipation of tidal energy by Antarctic ice shelves, *Nature, 275*, 304-305, 1978.

Elder, R.B., and J.M. Seabrooke, Oceanography of the Weddell Sea, *U. S Coast Guard Oceanogr. Rep, 30*, 1970.

Fearnhead, P.G., On the formation of fronts by tidal mixing around the British Isles, *Deep-Sea Research, 22*, 311-321, 1975.

Foldvik, A., and T. Gammelsrød, Notes on Southern Ocean hydrography, sea-ice and bottom water formation, *Palaeogeography, Palaeoclimatology, Palaeoecology, 67*, 3-17, 1988.

Foldvik, A., T. Gammelsrød, E. Nygaard, and S. Østerhus, Current meter measurements near Ronne Ice Shelf, Weddell Sea: Implications for circulation and melting underneath the Filchner-Ronne ice shelves, *Journal of Geophysical Research*, 2001.

Foldvik, A., T. Gammelsrød, N. Slotsvik, and T. Tørresen, Oceanographic conditions on the Weddell Sea Shelf during the German Antarctic Expedition 1979/80, *Polar Research, 3* (2), 209-226, 1985.

Foldvik, A., and T. Kvinge, Bottom currents in the Weddell Sea, Univ. of Bergen, Bergen, Norway, 1974.

Foldvik, A., J.H. Middleton, and T.D. Foster, The Tides of the Southern Weddell Sea, *Deep-Sea Research, 37* (8), 1345-1362, 1990.

Gammelsrød, T., and N. Slotsvik, Hydrographic and current measurements in the southern Weddell Sea 1979/80, *Polarforschung, 51* (1), 101-111, 1981.

Genco, M.L., F. Lyard, and C. Le Provost, The Oceanic Tides in the South-Atlantic Ocean, *Annales Geophysicae, 12* (9), 868-886, 1994.

Gill, A.E., Circulation and bottom water production in the Weddell Sea, *Deep-Sea Research, 20*, 111-140, 1973.

Grosfeld, K., N. Blindow, and F. Thyssen, Bottom melting on the Filchner-Ronne Ice Shelf, Antarctica, using different mesuring techniques, *Polarforschung, 62*, 71-76, 1992.

Haase, G.M., Glaciomarine Sediments Along the Filchner Ronne Ice Shelf, Southern Weddell Sea - 1st Results of the 1983/84 Antarktis- Ii/4 Expedition, *Marine Geology, 72* (3-4), 241-258, 1986.

Jenkins, A., A One-Dimensional Model of Ice Shelf-Ocean Interaction, *Journal of Geophysical Research, 96* (C11), 20671-20677, 1991.

Jenkins, A., and A. Bombosch, Modeling the Effects of Frazil Ice Crystals on the Dynamics and Thermodynamics of Ice Shelf Water Plumes, *Journal of Geophysical Research, 100* (C4), 6967-6981, 1995.

Jenkins, A., and C.S.M. Doake, Ice-Ocean Interaction on Ronne Ice Shelf, Antarctica, *Journal of Geophysical Research, 96* (C1), 791-813, 1991.

Kohnen, H., Glaciological investigations in the frontal zone of the Filchner and Ronne Ice Shelves, *Annals of Glaciology, 3*, 160-165, 1982.

Le Provost, C., A.F. Bennett, and D.E. Cartwright, Ocean Tides for and from Topex/Poseidon, *Science, 267* (5198), 639-642, 1995.

MacAyeal, D.R., Numerical Simulations of the Ross Sea Tides, *Journal of Geophysical Research, 89* (C1), 607-615, 1984a.

MacAyeal, D.R., Thermohaline Circulation Below the Ross Ice Shelf - a Consequence of Tidally Induced Vertical Mixing and Basal Melting, *Journal of Geophysical Research, 89* (C1), 597-606, 1984b.

MacAyeal, D.R., Tidal rectification below the Ross Ice Shelf, Antarctica, in *Oceanology of the Antarctic Continental Shelf*, edited by S.S. Jacobs, pp. 109-132, American Geophysical Union, Washington DC, 1985.

Makinson, K., and K.W. Nicholls, Modelling the tidal currents beneath Ronne Ice Shelf, Antarctica, in *Filchner Ronne Ice Shelf Programme Report No 10*, edited by H. Oerter, pp. 58-67, Alfred-Wegener-Institue for Polar and Marine Research, Bremerhaven, Germany, 1996.

Makinson, K., and K.W. Nicholls, Modeling tidal currents beneath Filchner-Ronne Ice Shelf and on the adjacent continental shelf: their effect on mixing and transport, *Journal of Geophysical Research, 104* (C6), 13449-13465, 1999.

Middleton, J.H., T.D. Foster, and A. Foldvik, Low-Frequency Currents and Continental-Shelf Waves in the Southern Weddell Sea, *Journal of Physical Oceanography, 12* (7), 618-634, 1982.

Middleton, J.H., T.D. Foster, and A. Foldvik, Diurnal Shelf Waves in the Southern Weddell Sea, *Journal of Physical Oceanography, 17* (6), 784-791, 1987.

Nicholls, K.W., and K. Makinson, Ocean circulation beneath the western Ronne Ice Shelf, as derived from in situ measurements of water currents and properties, in *Ocean, Ice, and Atmosphere: Interactions at the Antarctic Continental Margin*, edited by S.S. Jacobs, and R.F. Weiss, pp. 301-318, American Geophysical Union, Washington DC, 1998.

Nicholls, K.W., K. Makinson, and M.R. Johnson, New oceanographic data from beneath Ronne Ice Shelf, Antarctica, *Geophysical Research Letters, 24* (2), 167-170, 1997.

Nicholls, K.W., K. Makinson, and A.V. Robinson, Ocean Circulation beneath the Ronne Ice Shelf, *Nature, 354* (6350), 221-223, 1991.

Nicholls, K.W., S. Østerhus, K. Makinson, and M.R. Johnson, Oceanographic conditions south of Berkner Island, beneath Filchner-Ronne Ice Shelf, Antarctica, *Journal of Geophysical Research, 106* (C6), 11481-11492, 2001.

Padman, L., H.A. Fricker, R. Coleman, S. Howard, and L. Erofeeva, A New Tidal Model for the Antarctic Ice Shelves and Seas, *Annals of Glaciology, In Press*, 2002.

Padman, L., R. Robertson, and K. Nicholls, Modelling tides in the southern Weddell Sea: updated model with new bathymetry from ROPEX, in *Filchner-Ronne Ice Shelf Programme Report No 12*, edited by H. Oerter, pp. 65-73, Alfred-Wegener-Institute for Polar and Marine Research, Bremerhaven, Germany, 1998.

Robertson, R., L. Padman, and G.D. Egbert, Tidal currents in the Weddell Sea, in *Ocean, Ice and Atmosphere: Interactions at the Antarctic Continental Margin, Antarct. Res. Ser.*, edited by S.S. Jacobs, and R. Weiss, pp. 341-369, AGU, 1998.

Robin, G.D., C.S.M. Doake, H. Kohnen, R.D. Crabtree, S.R. Jordan, and D. Moller, Regime of the Filchner-Ronne Ice Shelves, Antarctica, *Nature, 302* (5909), 582-586, 1983.

Robinson, A.V., Modelling tides of the southern Weddell Sea, M. Phil thesis, British Antarctic Survey, Cambridge, England, 1996.

Schumacher, J.D., T.H. Kinder, D.J. Pashinski, and R.L. Charnell, A structural font over the coninental shelf of the eastern bering Sea, *Journal of Physical Oceanography, 9*, 79-87, 1979.

Simpson, J.H., The Shelf-Sea Fronts - Implications of Their Existence and Behavior, *Philosophical Transactions of the Royal Society of London Series a-Mathematical Physical and Engineering Sciences, 302* (1472), 531-546, 1981.

Smith, A.M., Ice shelf basal melting at the grounding line, measured from seismic observations, *Journal of Geophysical Research, 101* (C10), 22749-22755, 1996.

Smithson, M.J., A.V. Robinson, and R.A. Flather, Ocean tides under the Filchner-Ronne Ice Shelf, Antarctica, *Annals of Glaciology, 23*, 217-225, 1996.

Tsimplis, M.N., R. Proctor, and R.A. Flather, A two-Dimensional Tidal Model for the Mediterranean-Sea, *Journal of Geophysical Research, 100* (C8), 16223-16239, 1995.

Vaughan, D.G., Tidal Flexure at Ice Shelf Margins, *Journal of Geophysical Research, 100* (B4), 6213-6224, 1995.

Vaughan, D.G., and M. Jonas, Measurement of velocity of Filchner-Ronne Ice Shelf, in *Filchner Ronne Ice Shelf Programme Report No 10*, edited by H. Oerter, pp. 111-116, Alfred-Wegener-Institute for Polar and Marine Research, Bremerhaven, Germany, 1996.

Woodgate, R.A., M. Schröder, and S. Østerhus, Moorings from the Filchner Trough and the Ronne Ice Shelf Front: Preliminary Results, in *Filchner Ronne Ice Shelf Programme Report No 12*, edited by H. Oerter, pp. 85-90, Alfred-Wegener-Institute for Polar and Marine Research, Bremerhaven, Germany, 1998.

CHAPTER 5

Southern Weddell Sea Residual Tidal Currents

5.1 Introduction

In addition to their contribution to vertical mixing, tidal oscillations over topographic features can drive steady barotropic circulations, or tidal residual currents, that contribute to the large-scale transport of heat, salt, and other tracers. In this chapter the mechanisms that generate residual tidal currents are described, followed by a detailed description of the model output and comparison with CTD and current meter observations, particularly along Ronne Ice Front. The impact that residual currents have on the ice shelf morphology, ice front hydrography and mass transport are also discussed.

It has been shown that extensive residual currents are produced by tidal flow over submarine banks and other steep topography [*Loder*, 1980; *Robinson*, 1981]. The mechanism that generates a residual tidal current at the ice front is given by way of an example. As a fluid parcel is advected by the tidal current into the ice shelf cavity, the shallower water column requires the flow to speed up in order to transport the same volume of water. Beneath the ice shelf, the front part of the water parcel has a higher velocity and hence a larger Coriolis force than the part in open water (Figure 5.1a). The anticlockwise torque (Southern Hemisphere) creates a net anticlockwise rotation or vorticity that is advected into the cavity by the tidal flow (Figure 5.1b). When the tidal current reverses, the process is repeated but forms a net clockwise rotation offshore of the ice front. Averaged over a tidal cycle, counter rotating currents are generated along the ice front, leaving a mean Eulerian residual current that flows parallel to the ice front with the ice shelf to its left

(Figure 5.1b). It is this Eulerian residual current and can be detected using moored current meters.

Across the southern Weddell Sea continental shelf, Filchner-Ronne Ice Front is a dominant topographic feature, inducing a step change in water column thickness of up to 75%. The strongest tidal currents along Ronne Ice Front are found on Berkner Shelf, where the ice shelf significantly reduces the water column thickness, and where tidal currents peak at over 1 m s^{-1} during spring tides. Clearly the combination of strong tidal currents and rapid changes in water column thickness is likely to result in residual tidal currents. Numerical modelling of the tides beneath Ross Ice Shelf by *MacAyeal* [1985] concluded that tidal residual currents were present along the ice front and could play a major role in driving currents across the ice front, helping to ventilate the sub-ice shelf cavity.

In addition to the Eulerian residual currents a water parcel may experience Stokes Drift resulting from the spatial variations in the characteristics of the oscillatory tidal current (Figure 5.1c). This means that the paths actually followed by a water parcel, which are needed when investigating net fluxes, cannot be determined from Eulerian residuals alone. Stokes Drift is typically one third the size and in the opposite direction to the Eulerian residual flow [*Loder*, 1980]. It is greatest where the rotation of the tidal ellipse reverses across the ice front with a fluid parcel being advected more strongly over the shallower region and acquiring a net displacement. The net water parcel motion because of tidal activity is the sum of the Eulerian residual current and Stokes Drift, resulting in the Lagrangian residual current.

Besides the transport of mass and properties by residual currents, other mechanisms are present that result in a property flux rather than a mass flux across the ice front. Considering the tides in purely oscillatory terms over a long period, no net mass flow

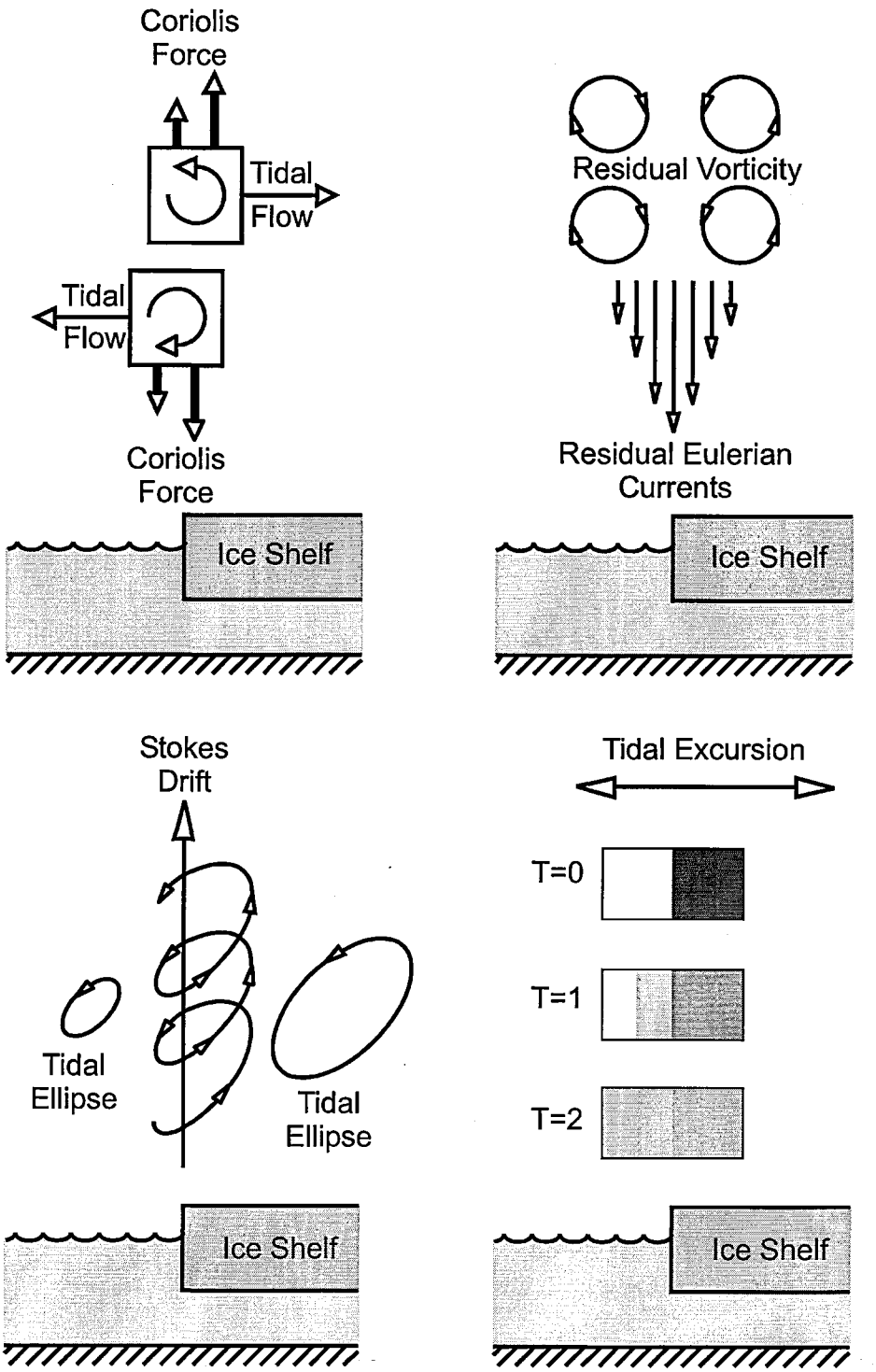

Figure 5.1 A series of schematics showing ice front processes associated with tidal oscillatory currents. **(a)** Two phases of tidal flow across an ice front with thick arrows indicating the Coriolis forces acting on the sides of a fluid parcel giving a net vorticity. **(b)** Shows the net vorticity and the resulting mean flow pattern along the ice front with the residual current flowing parallel to the ice front. **(c)** Tidal current ellipses either side of the ice front vary in size resulting in mean flow (Stokes Drift) along the ice front in the opposite direction to the Eulerian residual current. **(d)** Intense mixing close to and across the ice front may lead to the diffusion of properties across the ice front without a net mass transport.

between the open sea and sub-ice shelf cavity occurs. However, because of the effects of mixing, the flow field is not completely reversible and some water mass properties are left behind when the flow reverses (Figure 5.1d). This results in an exchange of properties such as salt, heat and other tracers, producing a transport of water mass properties between the open sea and sub-ice shelf cavity [*Wunsch*, 1996].

In three-dimensional circulation models that include ice shelves the circulation system is driven by buoyancy fluxes because of melting and freezing of ice and horizontal pressure gradients at the boundary between the cavity and the open ocean [e.g. *Grosfeld et al.*, 1997]. In the *Grosfeld et al.* [1997] sub-ice shelf model, the ice front represents a natural barrier to flow across the ice front except at the sidewalls of deep depressions such as in Ronne or Filchner Depressions. However, another three-dimensional model based on the Miami Iso-Pycnic Coordinate Model (MICOM) and modified for under ice shelf circulation, shows a seasonal inflow in Ronne Depression that begins in the first half of the winter and ends in the early summer unhindered by the presence of the ice front [*Jenkins and Holland*, In press]. Given the potential restrictions imposed by the ice front in some three-dimensional models, residual tidal currents may be significant in the exchange of water masses across the ice front and in influencing the local hydrography.

5.2 Eulerian residual currents

Robinson [1981] showed that the strength of the residual current depends on the horizontal and vertical length scales of topography, and the magnitude of the tidal current constituents. He also noted that these residual currents will be underestimated by a tidal model if the grid spacing underrepresents the topographic gradients. Even if the topographic features are well resolved, the residual currents will be underestimated in areas where the tidal excursion is small compared with the grid size. To improve the estimation of residual currents in the barotropic tidal model the node density was increased from 15 to 35 nodes per degree of

latitude and from 4 to 8 nodes per degree of longitude. For the area of the ice front this yields a grid spacing of less than 3.5 km. To comply with the CFL condition, the time step was reduced from 15 to 8 s. All other parameters remained the same. As before, harmonic analysis was used to find the phase and amplitude of the principal tidal.

5.2.1 Model results

Tidally driven residuals result from the interplay of earth rotation and depth variations. These effects are governed by the depth averaged vorticity balance derived by taking the curl of the two-dimensional depth-averaged momentum equation. One of the resulting terms expresses the change in relative vorticity necessary to maintain the conservation of potential vorticity in the absence of friction [*Robinson*, 1981].

$$\frac{d\omega}{dt} = \frac{(\omega + f)}{(h+\zeta)} \frac{d}{dt}(h+\zeta) \tag{5.1}$$

Here, ω is the frequency of the tidal current, f is the local Coriolis parameter, h is the water depth and ζ is the tidal elevation above mean sea level. An estimate of $\Delta\omega$ can be made as the fluid element takes time t to pass through the localized region of vorticity generation (in this case the ice front).

$$\Delta\omega = \frac{d\omega}{dt}\Delta t \tag{5.2}$$

For equation 5.1 the resulting term is

$$\Delta\omega = \left(\frac{\omega + f}{h+\zeta}\right)\Delta(h+\zeta) \quad , \tag{5.3}$$

so that $\Delta\omega$ is independent of the speed of the water and depends directly on the depth variation. By neglecting ζ compared with h, and ω is considered to be much less than f, the maximum velocity in the ice front jet V_a, can be estimated by integrating the vorticity with the distance from the edge of the vorticity region to the centre. Therefore,

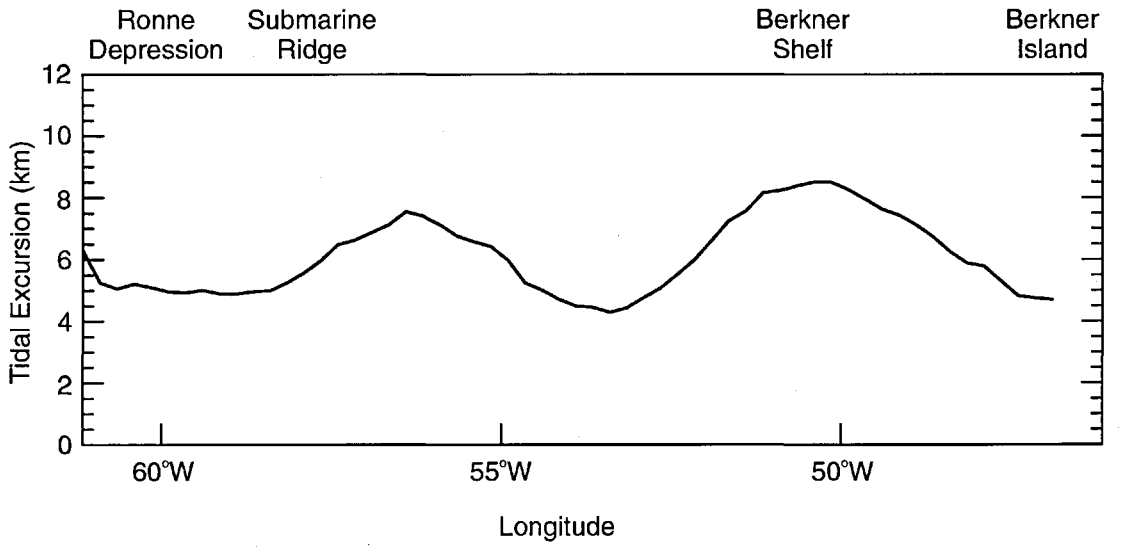

Figure 5.2 Maximum tidal excursion just offshore of Ronne Ice Front. The average excursion is typically half the maximum whereas beneath the ice shelf the reduction in water column thickness leads to excursions two to three times greater.

Robinson [1981] found that an adequate approximation for the maximum residual flow at a sharp topographic step such as occurs at the ice front is given by

$$V_a = 0.15 f(\Delta h/h)E, \tag{5.4}$$

where $\Delta h/h$ is the depth change ratio of the topographic feature, provided its spatial extent is less than the tidal excursion E, perpendicular to the feature. The barotropic tidal model was used to determine the maximum tidal excursions offshore of Ronne Ice Front (Figure 5.2) with sub-ice shelf excursions being up to three times larger. As an example using (5.4), water column thickness changes of 300 to 100 m in the ice front region of Berkner Shelf, coupled with 8 km average tidal excursions perpendicular across the ice front, will induce a maximum residual Eulerian velocity of 11 cm s^{-1} parallel to the ice front with a mean of around 6 cm s^{-1}. The agreement between this value and the tidal model prediction (7-8 cm s^{-1}) gives confidence that the model resolution in this area is adequate to represent the tidal residuals fully. The Eulerian residual current vectors were determined by harmonically analysing the current time series and subtracting the tidal constituents to leave the mean Eulerian flow. The Eulerian residual current vectors over the model domain are shown in Figure 5.3.

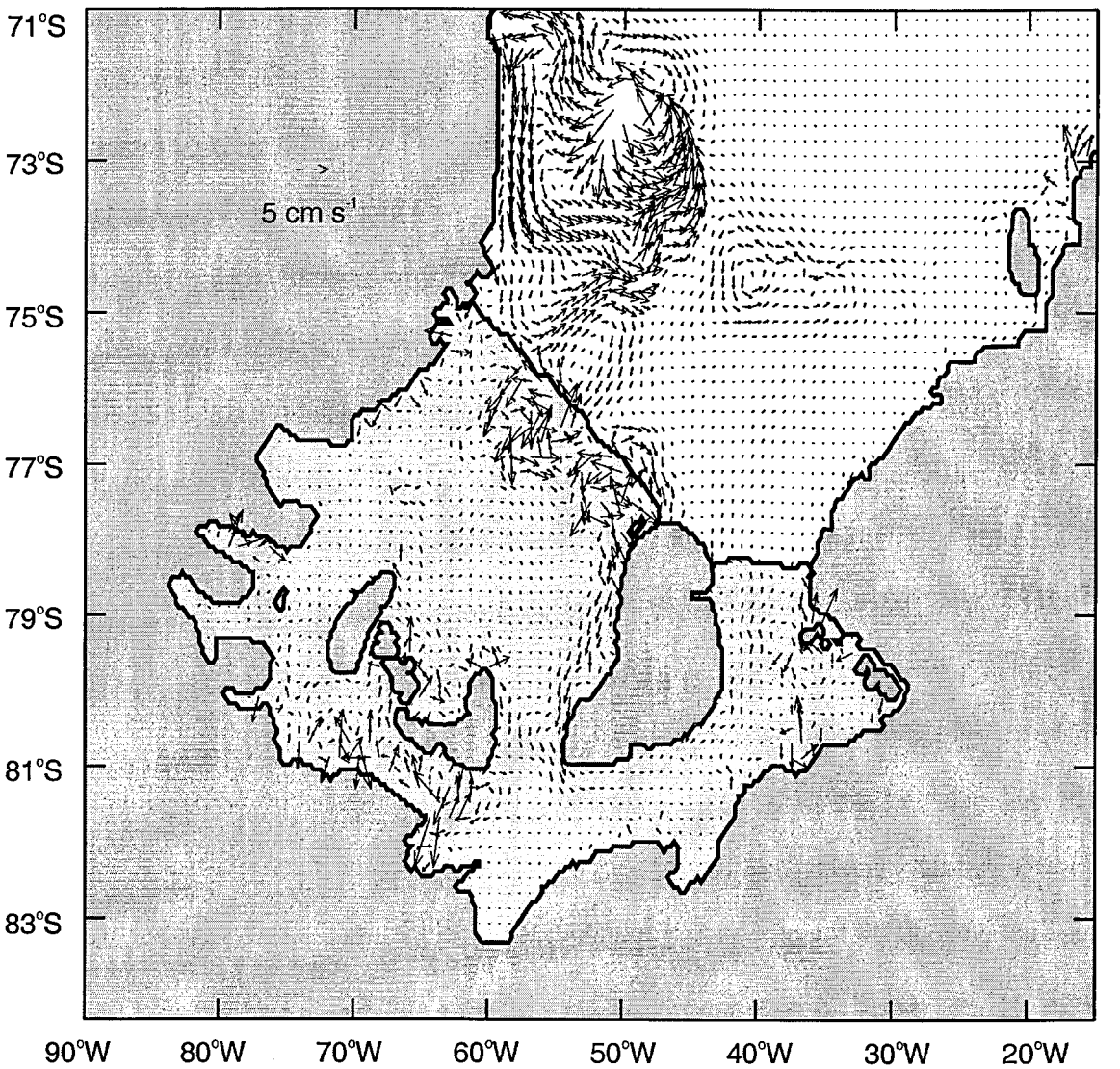

Figure 5.3 Eulerian residual current vectors are plotted for every seventh grid point of the model domain. The darkest shading represents grounded ice and the lighter shading the floating ice shelf.

5.2.2 Field data

Tidal residuals are one of several mechanisms that can force a mean current. Although it is not possible to separate tidal residuals from other forcings, it is useful to see where they dominate the mean flow by looking at actual measured mean currents. The highest tidal residual currents are associated with the ice front of Ronne Ice Shelf that has several current meter deployments along its length at S10, S11, R2, FR3, FR5 and FR6 (Figure 4.3). S11 was at the ice front itself, and the record showed a mean surface current of 8 cm s^{-1} directed northwest along the ice front. Below the ice shelf draft, however, at a depth of 75 m, the

measured mean current was 4 cm s^{-1} to the west [*Foldvik et al.*, 1985]. S10 was located 10 km offshore, close to the centre of an offshore gyre in the modelled residuals. The current meter record showed a mean current of approximately 2 cm s^{-1}, directed to the northwest at 100 m depth and to the northeast at 224 m depth [*Foldvik et al.*, 1985]. For this location the model predicted a residual of 1.5 cm s^{-1} to the northwest. In both cases the model is in closest agreement with the near surface measurements. Two other moorings that lie close together on Berkner Shelf are RT, a short term mooring and FR3 spanning two years. Over a ten-day period a mean current of 5.3 cm s^{-1} directed slightly south of west towards the ice shelf [*Foldvik et al.*, 2001] was observed 35 m above the seabed at RT. At FR3 the mean flow was 2 cm s^{-1} to the northwest at a height of 25 m from the seabed, much less than at RT. However, the record had strong seasonal variations with flow reversals during winter and spring with peak flows of approximately 7 cm s^{-1} parallel to the ice front [*Woodgate et al.*, 1998]. The peak residual flows are similar to the observed residuals at RT and S11 and consistent with the model results but clearly the flow reversals oppose the residual current forcing at the ice front and must result from other large scale circulation processes.

Further west along Ronne Ice Front, R2 had two current meters deeper than the draft of the nearby ice shelf at depths of 245 m and 400 m in a 419-m water column. The residual currents were approximately 8 cm s^{-1} parallel to the ice front and 9 cm s^{-1} west towards the ice front with no obvious seasonal signal in the current measurements [*Foldvik et al.*, 2001]. At this location, which is situated between two residual ice front gyres, the modelled residuals are close to zero. Applying (5.4) gives a maximum residual current of only 4.5 cm s^{-1}, considerably less than the observed mean currents.

Two long term moorings were located at either side of Ronne Depression, FR5 was on the eastern side and FR6 was close to the Antarctic Peninsula on the western side of the

depression. The upper two instruments at FR5 had a mean flow of 1.6-2.7 cm s^{-1} northwest parallel to ice front while the lowest instrument had a weak current (~ 1 cm s^{-1}) in the opposite direction. The upper instrument was shallower than the ice shelf base but the flow direction would also be consistent with offshore winds [*Woodgate et al.*, 1998]. At FR6 the mean flow was highest farther away from the seabed and ranged from 4.5 to 6.0 cm s^{-1} slightly south of west towards and under ice shelf [*Woodgate et al.*, 1998]. The model residuals at these two locations are weak (< 1 cm s^{-1}) and to the southeast. Using (5.4), the maximum residual currents would be approximately 3 cm s^{-1} northwest along the ice front. At both locations and within Ronne Depression other mechanisms clearly dominate the ocean circulation.

In deeper water areas with less tidal activity and large topographic gradients, such as Filchner Ice Front, the residuals will be underestimated because of insufficient model resolution. At Filchner Ice Front the average tidal excursion is approximately 1.1 km and the water column thickness changes from 1100 to 600 m. This gives an expected residual current, V_a, of 1.0 cm s^{-1}, compared with the model prediction of 0.25 cm s^{-1}. At the continental shelf break a similar effect is seen where steep gradients and small tidal excursions lead to an underestimation of residual currents by up to 50%. The Filchner Ice Front and the steep continental slope represent an extreme; in most areas the significant residual currents are adequately resolved.

Within the ice shelf cavity, the flow around Berkner Island (Figure 5.3), is the largest residual current entirely beneath the ice shelf with velocities of up to 3 cm s^{-1} along the western coast that decrease to less than 1 cm s^{-1} in the south. Moorings deployed beneath the ice shelf at sites 5 and 4 were close to the southern tip of Berkner Island and may have observed this weak residual flow, but the observed mean flow at Site 5 was 49 cm s^{-1} to the south and at Site 4, 15 cm s^{-1} to the east [*Nicholls et al.*, 2001]. Such high currents are

attributed to a strong recirculating flow driven by melting and freezing processes within the sub-ice shelf cavity.

5.3 Lagrangian residual currents

The Lagrangian motion of water parcels, or tracers, was determined from the hourly Eulerian velocity data from the model by trilinear interpolation onto 2-minute intervals. A tricubic spline interpolation gave no significant improvement in the results. Examples of the Lagrangian motion of three tracers over a 35-day period are shown in Figure 5.4a, illustrating the combination of oscillatory and residual currents. Using a 49-hour low-pass filter, the tracer trajectories were smoothed and are indicated by the heavy lines. In Figure 5.4b the 44 smoothed tracer trajectories show a particular point near the ice front, indicated by a cross, north of which they continue along the ice front, and south of which the tracers are drawn under the ice shelf. This example illustrates the capacity of the residual tidal currents to transport water into and out of the ice shelf cavity. Unlike the purely oscillatory tidal motion, this mechanism is capable of ventilating the cavity well beyond one tidal excursion. Figure 5.5 shows the Lagrangian trajectories for the southern Weddell Sea over a five-week period, with the pattern of currents almost identical to the Eulerian residual currents.

In order to determine mean Lagrangian velocities, tracer trajectories must be averaged over a sufficiently long time period. For each grid node a tracer was introduced every hour for 709 hours, the period of almost exactly two spring neap cycles. The Lagrangian trajectory of each tracer was determined using the interpolation method described above and recorded over a 100-hour period. Each trajectory was low-pass filtered with a 49-hour cutoff to remove the oscillatory part of the tide. The displacement of the tracer was calculated over the central 50-hour period. Finally, the mean of all 709 tracer displacements yielded a representation of the mean Lagrangian velocity at the position where the tracers were

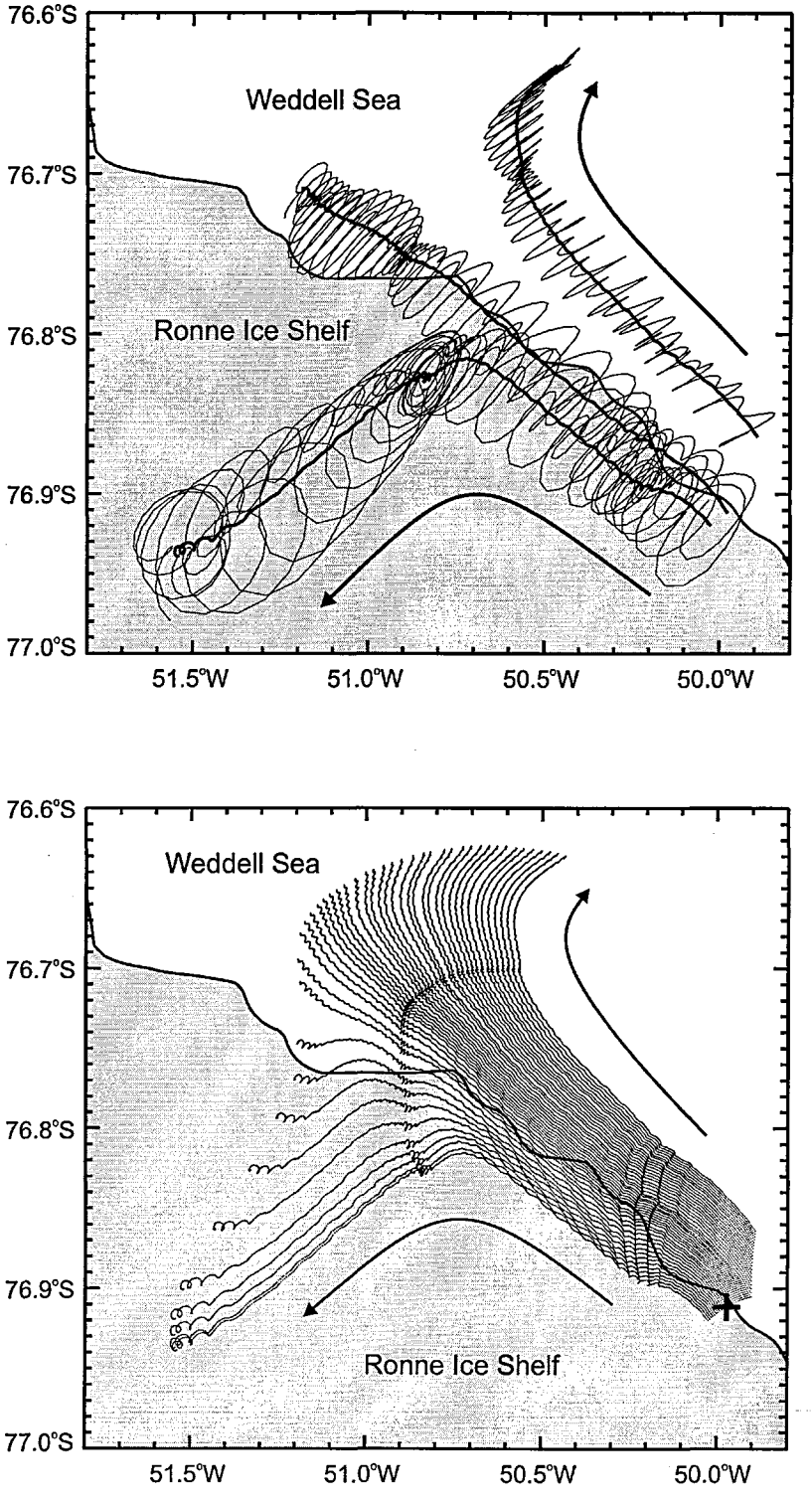

Figure 5.4 Examples of Lagrangian tracer trajectories over a 35 day period in the area of the ice front shown by the box in Figure 5.7. The arrows indicate the direction of flow. **(a)** Three Lagrangian tracer trajectories with smoothed trajectories indicated by the heavy lines. **(b)** Smoothed trajectories of 44 tracers with an initial spacing of approximately 200 m. The plus indicates where tracers either remain in open water or enter the sub-ice shelf as the flow bifurcates.

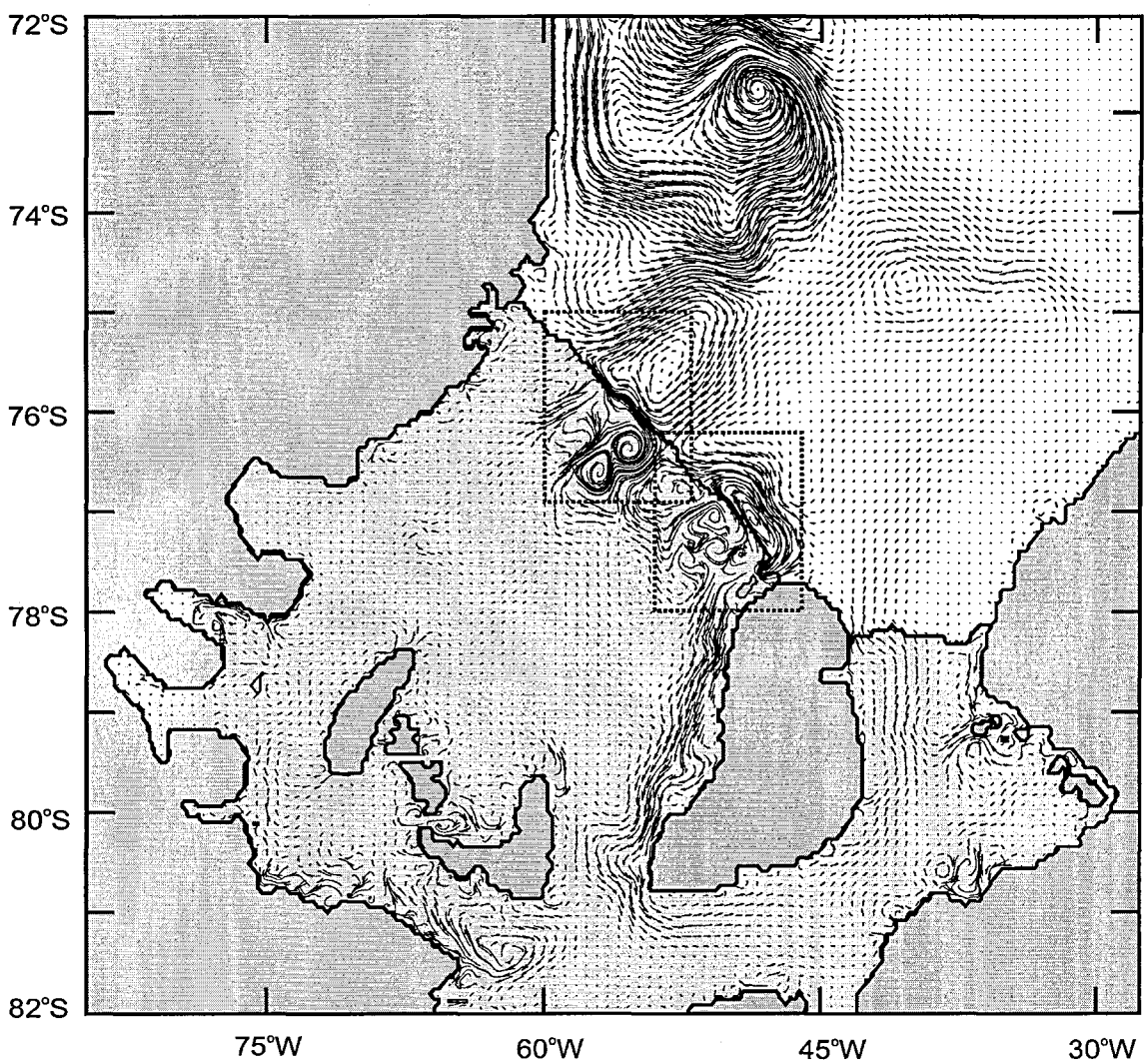

Figure 5.5 The Lagrangian residual tidal currents (tracer paths) obtained by removing the oscillatory components from the time series of water current. These mean currents are strongest over the western continental shelf, along Ronne Ice Front and the western coast of Berkner Island, and south of Henry and Korff Ice Rises. The boxes indicate the regions shown in Figures 5.7 and 5.8.

originally introduced. Volume fluxes could then be determined by integrating the product of the mean Lagrangian velocities and water column thickness across sections. To test the consistency of the mean Lagrangian circulation, the net volume flux over sections bounded by coastlines was calculated. Several sections, including the front of FRIS, gave net flows close to zero (< 1000 $m^3 s^{-1}$), as required by mass conservation. Figure 5.6 shows a cross section of water depth, water speed, and water flux perpendicular to the western section of Ronne Ice Front at 55°W. The finite model resolution makes the step in water column thickness appear as a steep slope, with the peak flux centred on the ice front. Over the model domain strong residual Lagrangian currents are present in three main areas (Figure 5.5): the ice front region of Ronne Ice Shelf, the western continental shelf, and the western coast of Berkner Island.

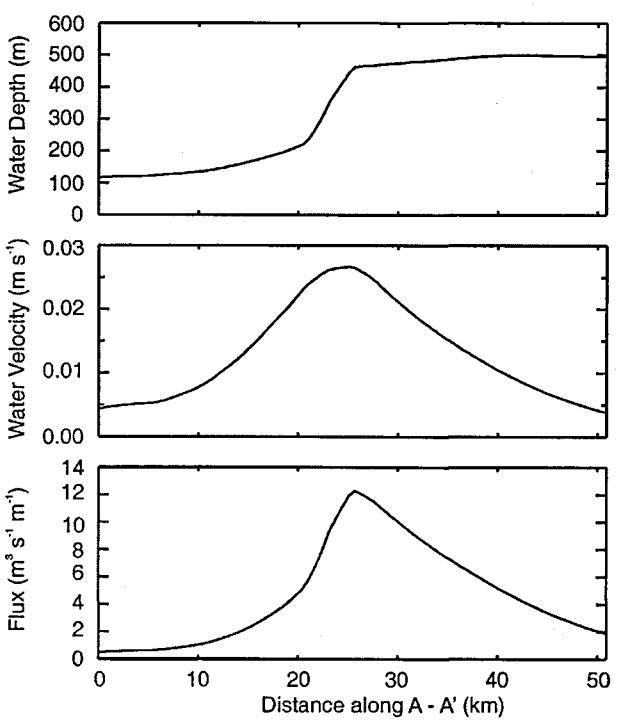

Figure 5.6 A section perpendicular to Ronne Ice Front at 55°W (A-A' in Figure 5.8) showing **(a)** the step change in the water column thickness at the ice front as represented by the model, **(b)** the mean residual water velocity parallel to the ice front with the peak velocity centered on the ice front, and **(c)** the mean volume flux across A-A', which totals 250,000 $m^3 s^{-1}$.

5.3.1 Eastern Ronne Ice Front

The greatest depth changes and highest tidal velocities are found along the ice front northwest of Berkner Island (Figure 5.7) and cause the highest residual velocities of 5.6 cm s^{-1}. This flow (A, in Figure 5.7) is northwest, parallel to the ice front, with volume transports of up to 135,000 m^3 s^{-1} at 50°W. North of the ice front there is an elongated clockwise gyre (G1) parallel to and centred 10-15 km from the ice front. The gyre extends up to 50 km northeast from its centre and has a circulation time of about 1 year. The return Lagrangian volume flux (B) associated with this Berkner Shelf gyre is 175,000 m^3 s^{-1} at up

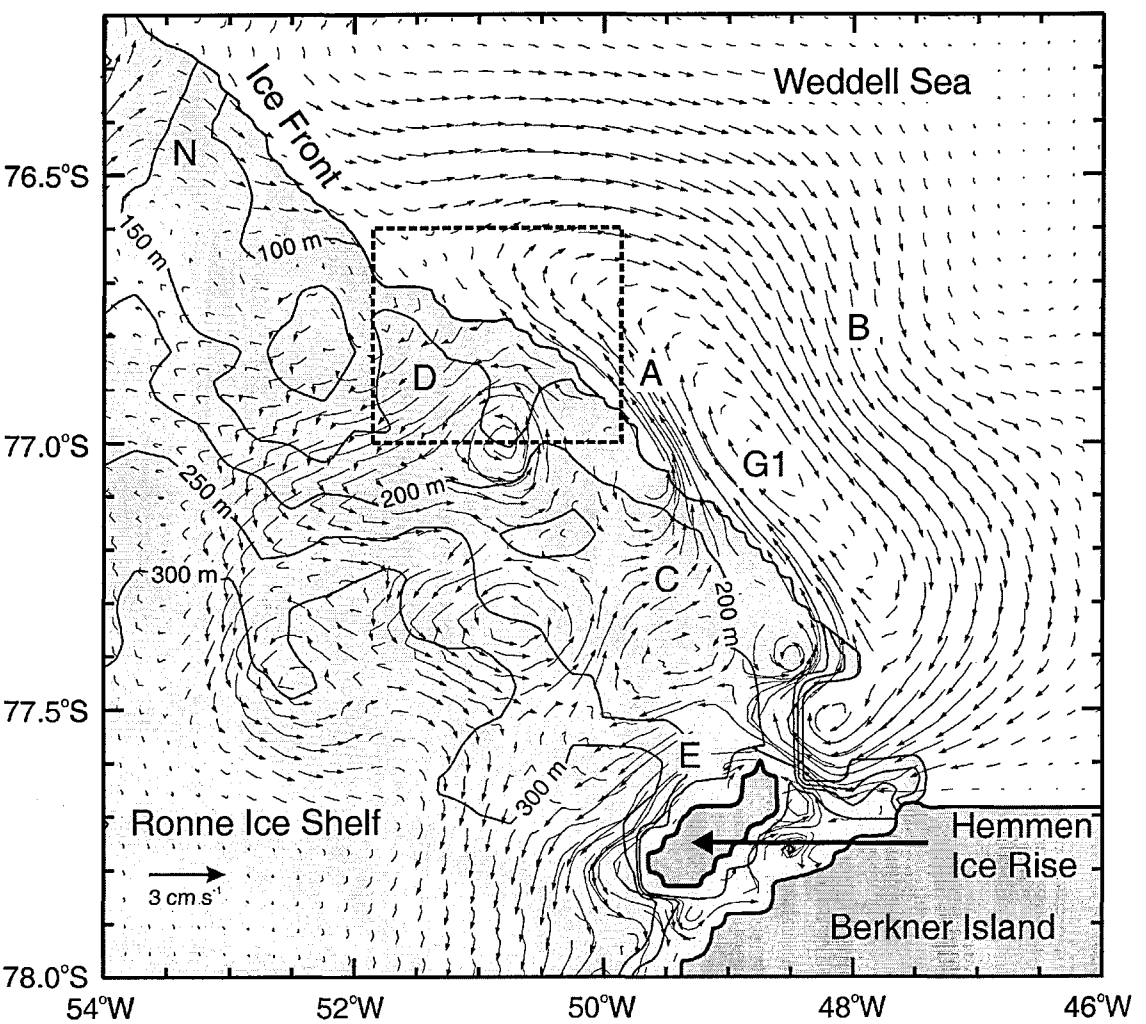

Figure 5.7 Smoothed Lagrangian residual trajectories over a 7 day period in the region of Berkner Shelf. Grounded ice is represented by the darkest shading, and floating ice shelf is represented by the lighter shading. The contours are of ice shelf draft at intervals of 50 m. The box marks the region shown in Figure 5.5.

to 2 cm s^{-1}. Beneath the ice shelf, complicated topography results in several eddies that transport water into and out of the sub–ice shelf cavity. The only outflow (C) in this region lies between 49° and 49.5°W (20,000 m^3 s^{-1}). At two locations, water flows from the shore lead into the cavity. Between 50.8°W and 51.8°W the flow along the ice front diverges, with one branch forming a diffuse inflow (D) of 80,000 m^3 s^{-1}. Farther to the east the second inflow (E) of 55,000 m^3 s^{-1} is concentrated along the western coast of Hemmen Ice Rise before it is joined from the west by a 35,000-m^3 s^{-1} flow. This combined flow then continues southwards along the Berkner Island coast.

5.3.2 Western Ronne Ice Font

The largest along-ice front flux (F in Figure 5.8) is situated between the centre of Ronne Ice Front and the submarine ridge to the east of Ronne Depression. There, between 150,000 and 300,000 m^3 s^{-1} flows parallel to a 100-km length of the ice front. The overall structure consists of anticlockwise and clockwise gyres either side of the barrier. Centred 40-50 km from the ice front, the offshore gyre (G2 in Figure 5.8) is relatively diffuse, extending more than 100 km to the northeast from its centre. Typically, velocities of 0.5 to 1 cm s^{-1} give a circulation time of 2.5 years. The total flow northeast towards the continental slope from the ice front (G) is 330,000 m^3 s^{-1}. The corresponding inflow (H) is 280,000 m^3 s^{-1} at 0.6 cm s^{-1}. Beneath the ice shelf two large circulations, each 40-50 km in diameter, merge to form a larger anticlockwise circulation. To their west residual currents are associated with the submarine ridge (Figure 4.3). Two inflows (K and M) are located at 55.4°W (50,000 m^3 s^{-1}) and at 57.3°W (70,000 m^3 s^{-1}), with two outflows (J and L) located at 54.3°W (175,000 m^3 s^{-1}) and at 56.8°W (20,000 m^3 s^{-1}). There is a point of convergence of residuals at the ice front, centred on 53.5°W. West of this point, water masses flow parallel to the ice front towards Ronne Depression. To the east, between 52°W and 53°W, there is a broad outflow (N, 20,000 m^3 s^{-1}) which becomes incorporated into the Berkner Shelf offshore gyre (G1, Figure 5.7).

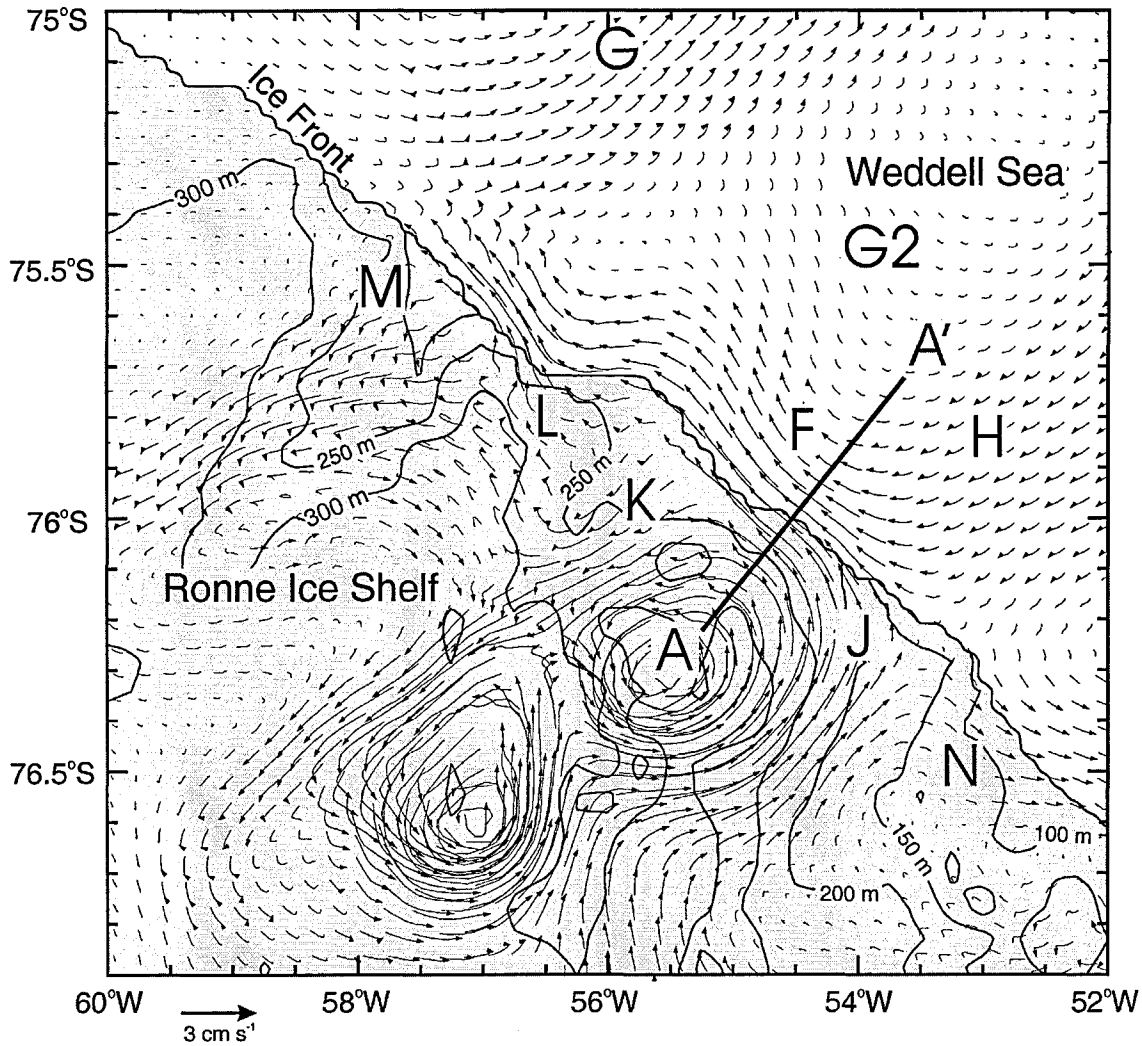

Figure 5.8 Smoothed Lagrangian residual trajectories over a 7 day period in the region of the western Ronne Ice Front. The ice shelf is represented by the shaded region and the contours give the ice shelf draft.

5.3.3 Continental Shelf

Over the continental shelf, close to the peninsula, a substantial southerly flow (1.4 cm s^{-1} and 500,000 m^3 s^{-1}) extends from 71°S (the model boundary) to 74°S (Figure 5.5) where the majority turns to the east and joins the northern tip of the gyre from the western Ronne (G2, Figure 5.8). In a similar model that extends to the northern tip of the Antarctic Peninsula, the flow appears to originate as far north as 69°S [*Robinson*, 1996]. The region around Belgrano Bank is part of the continental slope where there is significant diurnal amplification, and steep topographic gradients, resulting in strong residual currents. A large anticlockwise circulation dominates the residual current pattern over the western

continental shelf north of FRIS (Figure 5.5). Reducing the gradient of the continental slope in this region by 50% has the effect of reducing both the diurnal amplification and residual currents by a similar proportion, though the overall flow pattern remains similar. The only other location where residual currents flow south on to the continental shelf is at 74°S 43°W. There the velocities are lower, 0.3-0.4 cm s^{-1}. Over the open ocean no account is taken of any thermohaline or wind-driven circulation which are poorly known though *Gill* [1973] estimates velocities of the order of a few centimetres per second. Residual currents will clearly be modulated by currents driven by these other processes.

During 1986 three huge icebergs broke away from Filchner Ice Shelf [*Ferrigno and Gould*, 1987], two of which became grounded on Berkner Shelf between 40-45°W and 76-77°S. The model was used to determine their effect on the residual currents, assuming that the icebergs were grounded over their entire area. Without the grounded icebergs, the residual currents in this area are not significant. With them, weak residual currents form an anticlockwise flow around the bergs. Ungrounded parts of the bergs would effectively form ice front-type features and have strong associated residual flows.

5.3.4 Ice shelf cavity

The flow around Berkner Island (Figure 5.5) is the largest residual flow entirely beneath the ice shelf. At 78°S the peak velocity is 3 cm s^{-1} with a flux of 90,000 m^3 s^{-1}. As the water column thickness increases, velocities decrease but the volume flux increases to over 100,000 m^3 s^{-1}. The increased flux results from the addition of weak easterly residual flows set up along the water column contours in the central Ronne Ice Shelf. At the southern tip of Berkner Island peak velocities are only 0.5 cm s^{-1} in the 500-m water column. Beyond this point the flow turns to the east and north following the coast at velocities of between 0.2-0.4 cm s^{-1}, until eventually crossing the Filchner Ice Front with a flux of 125,000 m^3 s^{-1} and continuing northward. The time taken for a water parcel to travel to the southern tip of

Berkner Island is approximately 2 years, with another 8 years needed for it to arrive at the Filchner Ice Front.

Korff Ice Rise, Doake Ice Rumples, and Henry Ice Rise make up the areas of grounded ice that occupy the southern central region of Ronne Ice Shelf. Between these areas of grounded ice there are three channels 5-20 km wide with a water column of approximately 50 m, connecting the central and southern Ronne Ice Shelf cavity. These channels have high residual currents of up to 6 cm s^{-1} with associated flows of between 3000 and 6000 m^3 s^{-1} yielding a total flux of 10,000-15,000 m^3 s^{-1} from the southern trough to the central Ronne Ice Shelf. Either side of the channels and around the ice rises the residual currents mainly constitute a series of headland eddies. To the south of the ice rises there is a weak westerly flow (0.5-3 cm s^{-1} and 30,000-60,000 m^3 s^{-1}) found principally along the southern coast of the trough and comprising several eddies. There are also many vigorous gyres that are restricted to small coastal features and which do not contribute to the larger scale transport.

Over the southern Weddell Sea continental shelf and FRIS, only sparse bathymetric data are available because of the inaccessibility of the region. In the western Weddell Sea heavy sea ice conditions persist throughout the year, greatly limiting ship-borne observations. Beneath FRIS itself the geometry of the sub–ice shelf cavity can be determined only by a combination of seismic surveys and ice thickness data. The most tidally active regions beneath the ice shelf also have the shallowest water column, particularly in the region of the eastern Ronne Ice Front. Seismic data coverage is most dense over this area [*Vaughan et al.*, 1995], typically every 5-10 km, providing increased confidence in the model results. Elsewhere, uncertainties in the water column thickness greatly reduce confidence in the detailed model predictions. Nevertheless, the types of structure in the modelled residual current field, and strength of the flows, are expected to be representative of the actual residual tidal currents.

5.4 Impact on hydrography and ice shelf morphology

Filchner-Ronne Ice Front encompasses a wide range of current environments with different oceanographic processes, such as thermohaline circulation, residual currents and mixing, dominating different sections of the ice front hydrography. I now consider how mixing and the residual currents predicted by the barotropic model would be expected to affect the distribution of tracers (temperature and salinity) observed at Filchner-Ronne Ice Front, and the topography of the ice shelf itself in the vicinity of the ice front. CTD data have been collected along the ice front during several cruises over the last 30 years: USCGC *Glacier* in 1968 [*Elder and Seabrooke*, 1970] and in 1973 [*Carmack and Foster*, 1975]; R/V *Polarsirkel* in 1980 [*Foldvik et al.*, 1985]; *Polarstern* in 1984 [*Rohardt*, 1984]; and R/V *Lance* in 1993 [*Gammelsrød et al.*, 1994]. All the hydrographic surveys were conducted during the austral summer months with the last three spanning the majority of the Filchner-Ronne Ice Front.

5.4.1 Tidal oscillations and mixing

CTD measurements in tidally active regions are often affected by the tidal state during the measurement. One cause of this is the presence of horizontal gradients in the measured properties over the extent of the tidal excursion. Such gradients are likely near the ice front: the sudden change in water column thickness gives strong gradients in tidal energy available for vertical mixing, introducing the possibility of tidal fronts. The difference in the temperature of the water being mixed down from the upper boundary on either side of the ice front, especially during the austral summer, will compound the effect. The motion of mixing fronts back and forth across the ice front means that the results of CTD measurements made in the shore lead will be strongly influenced by the state of the tide. As an example, during spring tides on Berkner Shelf, measurements made at the ice front towards the end of a period of inflow would be sampling water that was previously 5 km offshore. Conversely, at the end of an outflow, the water being sampled will have originated

up to 15 km beneath the ice shelf. Yo-yo CTD stations close to the ice front occupied on Berkner Shelf at 50° 07'W [*Foldvik et al.*, 1985] and 50° 40'W [*Rohardt*, 1984] show that during periods of outflow there is a cooling throughout the water column, typically by a few tenths of a degree, but in extreme cases by up to 1°C in near surface waters. An additional effect influencing ice front CTD measurements results from the combination of strong mixing beneath the ice shelf and the purely periodic advection of water back and forth across the ice front. As the flow field is not completely reversible because of mixing, this is likely to result in an efficient horizontal transfer of tracers into and out of the cavity, but with no net water flow [*Wunsch*, 1996].

5.4.2 Residual currents

In the remainder of this section the effects of water mass transfer by the residual tidal currents are considered. Away from the ice front the tidal residuals are much weaker, and in the absence of knowledge of the wind or buoyancy-forced flow over the continental shelf it is not clear whether they are significant. Therefore the focus is on the ice front region, where most of the CTD stations have been located. The salinity and potential temperature sections compiled by *Foldvik et al.* [1985] are shown in Figures 5.9a and 5.9b and will be used for reference, together with smoothed Lagrangian trajectories over a 6 week period along the whole Filchner-Ronne Ice Front region (Figure 5.9c).

5.4.3 Ice shelf cavity outflows

Between 48°W and 51°W, the modelled residual flow at the ice front is almost parallel to the barrier (Figure 5.7), though there is a net outflow from beneath the ice shelf. Outflowing water would normally be expected to show signs of glacial melt in the potential temperature-salinity (θ-S) signature, and it is surprising that only one of the yo-yo sites located at the ice front revealed ISW in the water column during the outflow part of the tidal cycle [*Foldvik et al.*, 1985]. The S and θ sections presented in Figure 5.9 show no

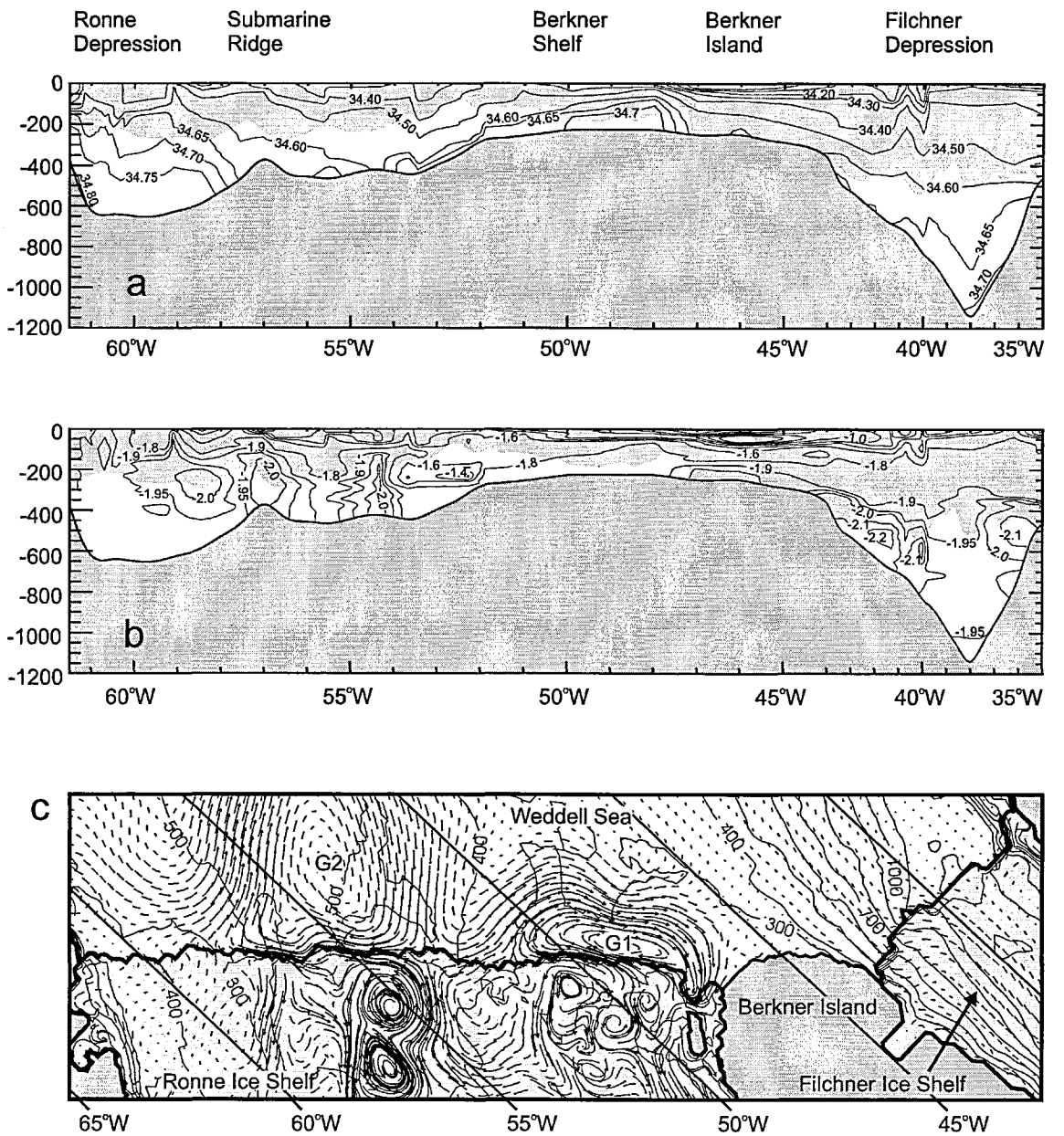

Figure 5.9 Sections of **(a)** salinity and **(b)** potential temperature along the ice front from Ronne Depression to the Filchner Depression [after *Foldvik et al.*, 1985]. The bathymetry is represented by the darkest shading, and the ice shelf draft is indicated by the lighter shading. **(c)** Lagrangian trajectories over a 6 week period in the region of Filchner-Ronne Ice Front. The contours are of water column thickness at intervals of 100 m.

evidence of a steady ISW presence in this region, and it is unclear whether there are indeed no tidally driven outflows, or whether they simply do not contain ISW. The offshore gyre (G1) in this region would be expected to increase the residence time of water on the Berkner Shelf, thereby increasing the water's salinity through sea ice formation.

West of 54°W, *Foldvik et al.* [1985] and *Rohardt* [1984] observed three ISW plumes emerging from beneath the ice shelf at 54.2°W and 56.8°W on the submarine ridge and at 58.5-59.7°W in Ronne Depression. *Gammelsrød et al.* [1994] observed ISW in the same locations but did not differentiate between the two western plumes, possibly because of the lower density of CTD stations in that area. At 53.25°W, modelled residual currents converge on the ice front, before diverging along the ice front to the east and west (Figure 5.8). West of this point any ISW emerging from beneath the ice shelf will remain close to the ice front, trapped by the flow parallel to the barrier. The modelled Lagrangian residuals predict a strong outflow between 53.9°W and 54.5°W (J) and weaker outflow associated with the submarine ridge between 56.7°W and 57°W (L). These predicted outflow locations agree with the positions of the ISW plumes observed by *Rohardt* [1984], *Foldvik et al.* [1985], and *Gammelsrød et al.* [1994]. Using the model to predict the tidal state when CTD measurements were made along the western Ronne Ice Front, the observed hydrographic features do not appear to be the result of periodic tidal excursions. Residual current outflows might therefore explain the two eastern ISW plumes observed by *Foldvik et al.* [1985] (Figure 5.9). The westernmost ISW plume (58°W) appears unlikely to be primarily the result of residual tidal currents: the residual outflow at this location is weak, at about 0.3 cm s^{-1}. The section in Figure 5.9 shows that unlike the two eastern plumes which have their temperature minima at, or close to, the seabed, the western outflow is centred around 250 m with WSW below it. This structure suggests an outflow underlain by an inflow, which is not consistent with a tidally forced barotropic current, suggesting that the western plume is driven primarily by thermohaline processes.

5.4.4 Ice shelf cavity inflows

In areas where inflows are anticipated, CTD sections at the ice front will give few indications. The maximum in the water temperature between the two eastern ISW plumes around 55.2°W (Figure 5.9b) [*Rohardt*, 1984; *Foldvik et al.*, 1985] is consistent with warmer offshore waters being drawn beneath the ice shelf. Figure 5.9 shows the residual currents in the ice front region overlaid with contours of ice shelf draft, indicating a good correlation between thinner ice shelf and the route of the inflows K and M. Farther to the east on Berkner Shelf, the model predicts inflows between 50.8°W and 51.8°W (D in Figure 5.7) and along the western side of Hemmen Ice Rise (E in Figure 5.7). The western inflow (D) appears to be associated with a thinning of the ice shelf. I believe that the thinning in the ice shelf is a result of preferential melting associated with relatively warm, tidally driven inflows. As residual currents are topographically steered, ice shelf thinning will, to some extent, influence the route of the residual flows, but the primary control on the water column thickness in these areas is the bathymetry.

5.4.5 Modified Weddell Deep Water intrusion

Foldvik et al. [1985] and *Gammelsrød et al.* [1994] interpreted the temperature maximum on the western slope of Berkner Shelf as an intrusion of MWDW formed by mixing WW and WDW. *Foster and Carmack* [1976] observed the intrusion of MWDW on the continental shelf at 40°W, up to 100 km from the shelf break. *Gammelsrød et al.* [1994] suggested that from the continental shelf break, a distance of about 450 km from the ice front, a geostrophically balanced flow of MWDW followed the 400 m isobath to the ice front, before appearing to flow beneath the ice shelf. Associated with the 400 m isobath the model gives a very weak southwesterly residual current (0.2-0.4 cm s^{-1}) (Figure 5.9c) that might contribute to the transport of MWDW across the continental shelf. The sloping isopycnals associated with the MWDW between 52°W and 53.7°W, which can be seen as sloping isohalines in Figure 5.9a, suggest a southward flow beneath the ice shelf. Predicted

residual currents in the area, however, range from zero up to 0.8 cm s^{-1} parallel to and slightly away from the ice front. In the vicinity of the intrusion, the ice shelf thins significantly, probably as the result of melting by the MWDW, combined with the effects of the western inflow (D in Figure 5.7) on Berkner Shelf.

Offshore from the ice front region, the width of the MWDW intrusion has not been measured. The residual currents at the ice front on Berkner Shelf will force water northwest along the barrier, restricting the easterly extent of the MWDW intrusion at the ice front to approximately 51.5°W. From the model results (Figure 5.9c) MWDW joins the two dominant offshore gyres (G1 and G2). In CTD sections perpendicular to the ice front at 49°W and 51°W, *Foldvik et al.* [1985] observed MWDW warmer than -1.4°C at 20-60 km from the ice front, suggesting that the MWDW is directed away from the ice front, consistent with the modelled residual gyre G1. Evidence for MWDW entrainment into the western gyre (G2) can be found in data from a station at 54°W as a small warm core (-1.51°C) 10 km from the ice front [*Foldvik et al.*, 1985].

5.4.6 Contribution of residual currents to mass transport

Along the entire Ronne Ice Front, the contribution of residual currents to water mass transport appears to be comparable to thermohaline driven flows. Observations by *Nicholls et al.* [1997] indicate a 200,000 m^3 s^{-1} thermohaline inflow of WSW that enters the deep sub–ice shelf cavity via the Ronne Depression. After transformation to ISW, this water mass is presumed to emerge from beneath the ice shelf as the plume in the Ronne Depression. Away from the Ronne Depression, in the tidally active regions of Ronne Ice Front, modelled residual currents exchange approximately 250,000 m^3 s^{-1} across the ice front, between the sub–ice shelf cavity and open sea. In this region, observations at mooring R2 (Figure 4.3) show a transport of WSW into the ice shelf cavity of 0.3-0.6 x 10^6 m^3 s^{-1}

[*Foldvik et al.*, 2001], implying that tidal residuals may contribute significantly to the total regional inflow.

Along Filchner Ice Front the model predicts a weak northward current (0.2-0.4 cm s^{-1}, 125,000 m^3 s^{-1}) at the western side of the depression. Observations by *Foldvik et al.* [1985] show corresponding ISW cores emerging at a similar locations. However, modelling of thermohaline circulations in this region by *Grosfeld et al.* [1996] and geostrophic calculations by *Carmack and Foster* [1975] gave fluxes of approximatly 400,000 m^3 s^{-1} entering and leaving the ice shelf cavity. Also, *Foldvik et al.* [1985] derived an ISW flow of about 10^6 m^3 s^{-1} at the shelf break associated with Filchner Depression. As in the case of the Ronne Depression, the model suggests that the hydrography across Filchner Depression is dominated by thermohaline processes with tidal residuals playing a minor or insignificant role.

5.5 Summary and conclusions

The application of this depth-averaged model has yielded a description of the tidally generated residual currents which has been supported by only some of the available ice front observations. However, these residuals appear to play an important role in the transfer of water between the sub–ice shelf cavity and the adjacent continental shelf. Along the eastern section of Ronne Ice Front the water column thickness reduces from 250 m to less than 100 m. Modelled Lagrangian residual currents reach mean velocities of 5 cm s^{-1} in this area. Farther to the west these currents transport up to 250,000 m^3 s^{-1} along the ice front. In addition to the along ice front flows there are a number of specific locations where Lagrangian residual currents transport water masses into and out of the sub–ice cavity of FRIS. The rate of exchange totalling approximately 350,000 m^3 s^{-1} is less than estimates attributed to thermohaline circulation but are of the same order. Ship-borne hydrographic observations along the ice front support many of the model predictions. Lagrangian residual

flows from the cavity coincide with observations of ISW plumes, and ice shelf thinning coincides with flows entering the cavity, consistent with warmer offshore water being imported and causing preferential melting.

Away from the ice front, where residual currents are weaker, it is unclear to what extent they influence the hydrography. Over the open ocean the effect of tidal residuals will combine with the wind and thermohaline forcing; it is not clear which effect will dominate. In the deep water areas beneath FRIS, particularly the Filchner and Ronne Depressions, residual currents are weak, and it is assumed that thermohaline flows dominate. The largest residual flow that penetrates deep beneath the ice shelf transports approximately 100,000 $m^3 s^{-1}$ of water anticlockwise around Berkner Island. The flow originates on the Berkner Shelf, west of Berkner Island, and finally emerges from beneath the western end of Filchner Ice Front.

Probably the most important result from this study of tidal currents and their residuals has been to show that tidal processes strongly influence the oceanographic conditions in the vicinity of Ronne Ice Front and can explain many of the observations made in the shore lead. The combination of vigorous mixing, large tidal excursions, and strong Lagrangian residual currents has a dominant effect on the hydrography beneath about 60% of Ronne Ice Front.

5.6 References

Carmack, E.C., and T.D. Foster, Circulation and distribution of oceanographic properties near Filchner Ice Shelf, *Deep Sea Res*, 77-90, 1975.

Elder, R.B., and J.M. Seabrooke, Oceanography of the Weddell Sea, *U. S Coast Guard Oceanogr. Rep, 30*, 1970.

Ferrigno, J.G., and W.G. Gould, Substantial changes in the coastline of Antarctica revealed by satellite imagery, *Polar Record, 23*, 577-583, 1987.

Foldvik, A., T. Gammelsrød, E. Nygaard, and S. Østerhus, Current meter measurements near Ronne Ice Shelf, Weddell Sea: Implications for circulation and melting underneath the Filchner-Ronne ice shelves, *Journal of Geophysical Research, 106* (C3), 4463-4477, 2001.

Foldvik, A., T. Gammelsrød, N. Slotsvik, and T. Tørresen, Oceanographic conditions on the Weddell Sea Shelf during the German Antarctic Expedition 1979/80, *Polar Research, 3* (2), 209-226, 1985.

Foster, T.D., and E.C. Carmack, Frontal zone mixing and Antarctic Bottom Water formation in the southern Weddell Sea, *Deep-Sea Research, 23*, 301-317, 1976.

Gammelsrød, T., A. Foldvik, O.A. Nøst, Ø. Skagseth, L.G. Anderson, E. Fogelqvist, K. Olsson, T. Tanhua, E.P. Jones, and S. Østerhus, Distribution of water masses on the continental shelf in the Southern Weddell Sea, in *The polar oceans and their role in shaping the global environment*, edited by O.M. Johannesen, R.D. Muench, and J.E. Overland, pp. 159-176, AGU, Washington DC, 1994.

Gill, A.E., Circulation and bottom water production in the Weddell Sea, *Deep-Sea Research, 20*, 111-140, 1973.

Grosfeld, K., R. Gerdes, and J. Determann, Thermohaline circulation beneath and in front of Filchner Schelfeis, in *Filchner Ronne Ice Shelf Programme Report No 10*, edited by H. Oerter, pp. 32-37, Alfred-Wegener-Institute for Polar and Marine Research, Bremerhaven, Germany, 1996.

Grosfeld, K., R. Gerdes, and J. Determann, Thermohaline circulation and interaction between ice shelf cavities and the adjacent open ocean, *Journal of Geophysical Research, 102* (C7), 15595-15610, 1997.

Jenkins, A., and D.M. Holland, A model study of ocean circulation beneath Filchner-Ronne Ice Shelf, Antarctica: implications for bottom water formation., *Geophysical Research Letters*, In press.

Loder, J.W., Topographic rectification of tidal currents on the sides of Georges Bank, *Journal of Physical Oceanography, 10*, 1399-1416, 1980.

MacAyeal, D.R., Tidal rectification below the Ross Ice Shelf, Antarctica, in *Oceanology of the Antarctic Continental Shelf*, edited by S.S. Jacobs, pp. 109-132, American Geophysical Union, Washington DC, 1985.

Nicholls, K.W., K. Makinson, and M.R. Johnson, New oceanographic data from beneath Ronne Ice Shelf, Antarctica, *Geophysical Research Letters, 24* (2), 167-170, 1997.

Nicholls, K.W., S. Østerhus, K. Makinson, and M.R. Johnson, Oceanographic conditions south of Berkner Island, beneath Filchner-Ronne Ice Shelf, Antarctica, *Journal of Geophysical Research, 106* (C6), 11481-11492, 2001.

Robinson, A.V., Modelling tides of the southern Weddell Sea, M. Phil thesis, British Antarctic Survey, Cambridge, England, 1996.

Robinson, I.S., Tidal Vorticity and Residual Circulation, *Deep-Sea Research Part a-Oceanographic Research Papers, 28* (3), 195-212, 1981.

Rohardt, G., Hydrographische untersichungen am rand des Filchner Shelfeises, *Ber. Zur Polarforschung, 19*, 137-143, 1984.

Vaughan, D.G., J. Sievers, C.S.M. Doake, H. Hinze, D.R. Mantripp, V.S. Pozdeev, H. Sandh,,ger, H.W. Schenke, A. Solheim, and F. Thyssen, Subglacial and seabed topography, ice thickness and water column thickness in the vicinity of Filchner-Ronne-Schelfeis, Antarctica, *Polarforschung, 64* (2), 75-88, 1995.

Woodgate, R.A., M. Schröder, and S. Østerhus, Moorings from the Filchner Trough and the Ronne Ice Shelf Front: Preliminary Results, in *Filchner Ronne Ice Shelf Programme Report No 12*, edited by H. Oerter, pp. 85-90, Alfred-Wegener-Institute for Polar and Marine Research, Bremerhaven, Germany, 1998.

Wunsch, C., *The Ocean Circulation inverse Problem*, Cambridge University Press, New York, 1996.

CHAPTER 6

One-Dimensional Vertical Mixing Model

6.1 Introduction

The tidal model described in Chapter 3 has been used to estimate the tidal energy dissipated beneath FRIS in Chapter 4. This has been used to determine its contribution to basal melt rates and infer if the water column was well mixed or stratified. The highest melt rates were associated with the highest currents, and areas with a potentially well mixed water column were identified. However, the tidal model cannot resolve the vertical structure of the sub-ice shelf water column or its evolution. The vertical fluxes and the interaction with the ice shelf base will be controlled by a combination of upwelling (larger scale advective processes) and vertical mixing (local diffusive processes). Large scale advection is the focus of sub-ice shelf circulation models. However, local diffusive processes require a model that provides a clearer description of the sub-ice shelf water column to examine the vertical distribution of turbulence in the water column from tidal processes and mean flows. This chapter describes the choice of mixing scheme and details the boundary conditions at the seabed and ice shelf base. A number of comparative test cases are then used to check the performance of the model.

Turbulence is an eddying motion with a wide spectrum of eddy sizes and fluctuation frequencies. Large eddies interact with the mean flow and extract energy from it. These eddies interact with other eddies and feed smaller scale energy eddies, transferring energy from the larger to smaller scales. This process is known as the energy cascade of turbulence. At the end of this energy cascade, the smallest eddies are on the scale of viscous

forces, and at this scale dissipation takes place. Mixing through a water column results from vertical motions and overturning because of the presence of turbulence. In a homogeneous water column, the supply of energy required to mix the entire water column is only that needed to overcome friction. However, in a stratified water column work must be done to raise dense water and lower light water and thus stratification acts as a moderator of turbulence.

A solid surface exerts frictional stress on the flow, bringing the velocity to zero at the boundary and generating a turbulent boundary layer. This layer extends from near the boundary surface into the water column to a depth at which the influence of the boundary eddies are negligible (Figure 6.1). In the ocean beneath an ice shelf, turbulence is generated by mean and tidal flows and by negative surface buoyancy fluxes, such as during salt release during ice formation. Turbulence is reduced by dissipation within the mixed layer and inhibited by stabilising buoyancy fluxes, such as during basal melting. The vertical structure and the vertical fluxes are largely controlled by the vertical mixing and therefore vertical distribution of turbulence in the water column.

Currently, no universally accepted turbulent mixing model exists, and several approaches can be used. The earliest models were bulk or integrated models, where the mixed layer is a well defined homogenous layer that is considered as a single entity. As a result, the equations are integrated across the mixed layer on the assumption that mean quantities are almost uniform throughout. The advance (entrainment) and retreat (detrainment) of the mixed layer depends on the parameterization of the fluxes at its base. *Kraus and Turner* [1967] used this method to model the seasonal thermocline in the north Pacific Ocean. Other studies have also used this type of model, with modifications, to study the upper ocean response to heating, cooling and wind mixing at diurnal to seasonal time scales [*Niiler*, 1975; *Garwood*, 1977; *Price et al.*, 1986]. These models are relatively simple and

provide an insight into the mixed layer evolution. However, such models do not resolve the vertical structure and cannot therefore be used to investigate the details of mixing and vertical fluxes in the water column.

The second type of models are diffusion models that attempt directly to parameterise the turbulent mixing and diffusion in the mixed layer. These can be differentiated into two common approaches: empirical and statistical closure models. For the empirical approach, the parameterization can be taken from theoretical and observational data of the mixed layer and so contain empirical or semiempirical formulations for turbulent diffusion [*Large et al.*, 1994]. Closure models are based on the Reynolds decomposition of momentum and scalar fields into mean and fluctuating fields and turbulence quantities are closed at the second [*Mellor and Yamada*, 1982] or third moment [*Andre and Lacarrere*, 1985].

In oceanography, the current most widely spread empirical turbulence closure is the K-Profile Paramaterisation (KPP) model introduced by *Large et al.* [1994]. Here profiles for eddy viscosity and eddy diffusivity are constructed from Monin-Obukhov similarity theory. The Monin-Obukhov length scale represents the depth of the fluid to which stratification confines eddies. This is based on the strength of the friction velocity and down-gradient fluxes without consideration of statistical moments [*Burchard and Bolding*, 2001]. The K-profile approach also needs an equation for the mixed layer depth. This equation accounts for the deepening and shallowing of the mixed layer as a result of convection and stabilizing surface buoyancy fluxes.

Both Mellor-Yamada (MY) models and the k-ϵ model are popular turbulence closure models (k-ϵ represents turbulent kinetic energy and its dissipation). They are two-equation turbulence closure models that include prognostic equations for turbulent kinetic energy (TKE) and a length scale used to calculate eddy viscosities and vertical diffusivities. Each

of the models reacts in a similar way to stability functions and internal wave models [*Burchard et al.*, 1998]. The application of both types of models to observations clearly demonstrate their similarity [*Burchard and Petersen*, 1999]. The models are based on the same equation for conservation of TKE but differ in some features of the length scale equation. The MY scheme includes an integral measure in the sink term to reproduce the log law boundary whereas k-ϵ reflects this law automatically.

The MY models were proposed as a hierarchy of turbulent closure models for geophysical boundary layer flows [*Mellor and Yamada*, 1982] and their level-2.5 version has been used extensively in geophysical applications [e.g. *Lynch et al.*, 1996] and numerous modifications have been suggested [*Galperin et al.*, 1988; *Kantha and Clayson*, 1994; *Burchard and Baumert*, 1995; *D'Alessio et al.*, 1998; *Canuto et al.*, 2001]. The model constants are empirical and optimised to different turbulent flows in the laboratory. These constants are assumed to apply to other situations including geophysical flows despite neglecting the effects of rotation. However, *Kantha et al.* [1989] were able to confirm that rotation does not have a profound effect on small scale turbulence characteristics in geophysical flows and the effects are generally small. These models are known to have too little entrainment during convection and the related problem of too little mixing across stabilizing density gradients [*Large et al.*, 1994]. Here, large scale structures with regions of down welling and up welling stir the mixed layer, clearly a situation not well represented by local models based on a diffusion concept and a reason cited for the development of the KPP model.

Comparisons between two bulk mixed-layer models and the models of MY by *Martin* [1985] for the ocean mixed layer found that the MY model significantly underpredicted the mixed layer depth. Furthermore, by comparing the MY2.5 model with a bulk model and a non-local model, *Large and Crawford* [1995] found that the nonlocal model could better

predict mixing at the base of the mixed layer and deep into the thermocline. In order to address some deficiencies of the MY2.5 model, parameterizations have been added for mixing in the thermocline to simulate the effects of shear instability and internal wave breaking [*Mellor and Kantha*, 1989; *Kantha and Clayson*, 1994]. Dissipation measurements in the Irish Sea were used by *Simpson et al.* [1996] for inter comparison of different versions of the MY models. They found that the measured dissipation rate in the stratified region could only be reproduced by including an internal wave parameterization.

In the sub-ice shelf environment local horizontal homogeneity is assumed, making the model one-dimensional. The effects of vertical advection are ignored and other processes such as frazil ice formation and its accumulation at the ice shelf base are not considered. Also, there is no need to account for open ocean parameters such as breaking surface waves, Langmuir circulation and absorption of radiation. In their place is an upper mixed layer that results from the direct contact with the ice shelf base. Here, melting at the ice-ocean interface must be considered together with the mixing of melt water into the interior of the water column. In situations where convection does not dominate, the MY2.5 scheme has been fairly successful in simulating observations at a stratified and non-stratified site in the Irish Sea [*Simpson et al.*, 1996]. Other model simulations using the MY2.5 scheme have been able to reproduce water column dynamics [*Luyten et al.*, 1996; *Burchard et al.*, 1998] indicating that the MY2.5 scheme is suited to this sub-ice shelf application.

6.2 Mean flow equations

6.2.1 Transport of mass

The one-dimensional model uses an implicit finite difference scheme to integrate the horizontal velocity components (u, v) of the momentum equations

$$\frac{\partial u}{\partial t} = -\frac{1}{\rho}\frac{\partial p}{\partial x} + fv + \frac{\partial}{\partial z}\left(K_M \frac{\partial u}{\partial z}\right) \text{ and} \tag{6.1}$$

$$\frac{\partial v}{\partial t} = -\frac{1}{\rho}\frac{\partial p}{\partial y} - fu + \frac{\partial}{\partial z}\left(K_M \frac{\partial v}{\partial z}\right), \tag{6.2}$$

with x and y positive in the east and north directions and z increasing positively upwards, with $z = 0$ at the ice-ocean boundary and $z = -h$ at the seabed. Here, K_M is the vertical eddy viscosity ($m^2\ s^{-1}$), f is the Coriolis parameter and p is pressure.

6.2.2 Surface forcing

Three different contributions to the forcing of the model are made via the pressure gradient term in (6.1 and 6.2). These are given by

$$\frac{1}{\rho}\frac{\partial p}{\partial x} = -S_x g \sin(\omega t - \phi_x) + g\left(\frac{\partial \eta}{\partial x}\right)_{nontidal} + g(h-z)\frac{\partial \rho}{\partial x} \text{ and} \tag{6.3}$$

$$\frac{1}{\rho}\frac{\partial p}{\partial y} = -S_y g \sin(\omega t - \phi_y) + g\left(\frac{\partial \eta}{\partial y}\right)_{nontidal} + g(h-z)\frac{\partial \rho}{\partial y} \ . \tag{6.4}$$

The first term is an oscillating sea surface gradient that provides tidal forcing, where g the gravitational acceleration and ω is the tidal frequency; S_x, S_y and ϕ_x, ϕ_y are the prescribed tidal surface slope amplitudes and phases. A phase difference of $\pi/2$ is maintained between ϕ_x and ϕ_y, while the amplitudes of the tidal slopes are determined from

$$S_x = \frac{U(\omega + Pf)}{g} \quad \text{and} \tag{6.5}$$

$$S_y = \frac{U(f + P\omega)}{g} \ , \tag{6.6}$$

where U determines the maximum speed of the tidal current (semi-major axis) and P, which ranges between ±1.0, controls the polarization of the tidal current ellipse. More details on the derivation of (6.5) and (6.6) are given in the appendix. The second term in (6.3) and

(6.4) represents a mean surface slope required to drive mean flows, and the effect of horizontal density gradients is represented in the final term.

6.2.3 Boundary conditions

The boundary layers are generally considered to be made up of three regions: the viscous sub-layer or bed layer, the logarithmic layer and outer layer or Ekman layer (Figure 6.1). The subviscous layer is the region in which the turbulent and viscous stresses are of the same order of magnitude and is about a centimetre thick. Above this is the logarithmic layer

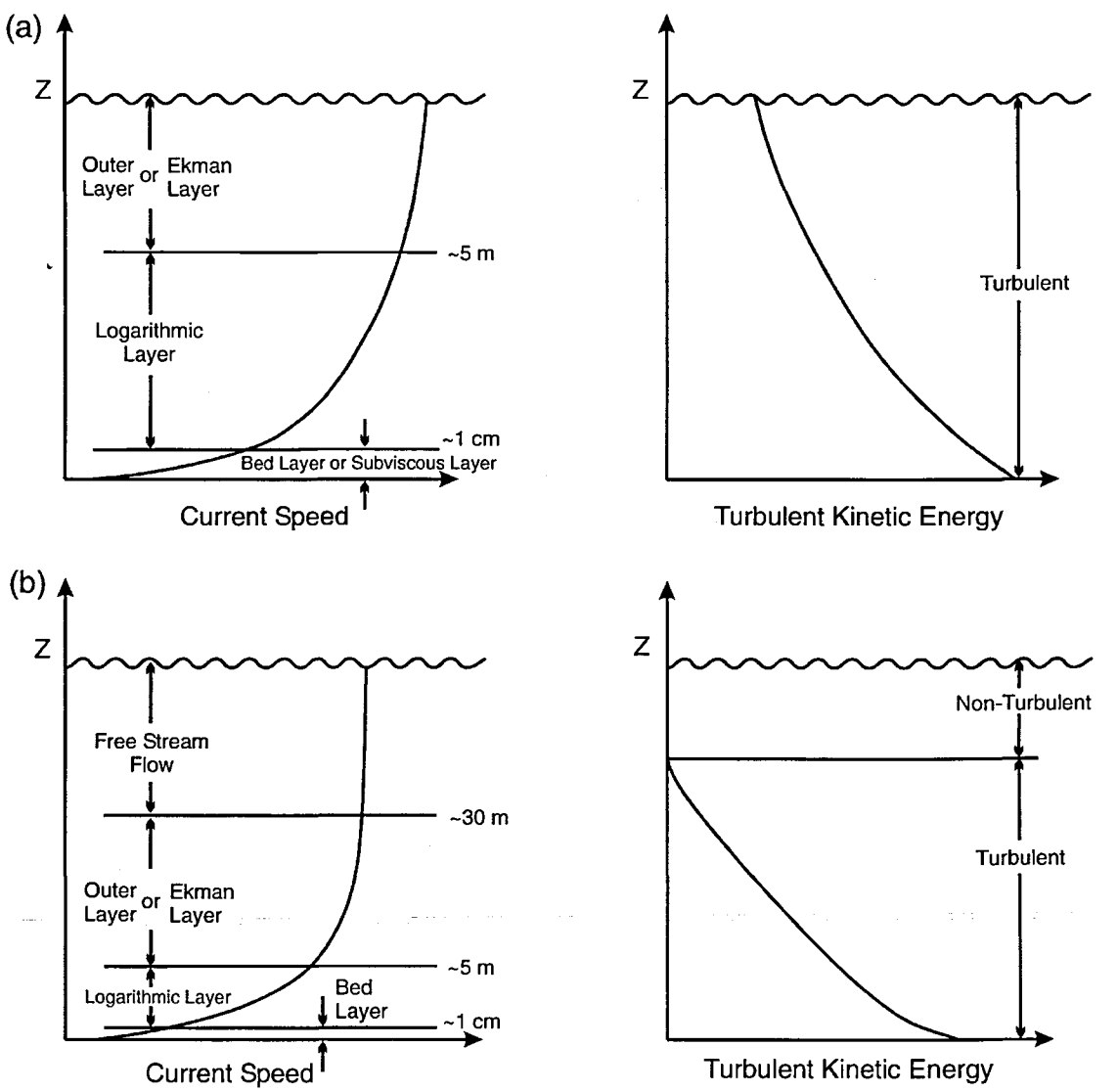

Figure 6.1 Taken from *Soulsby* [1983]. Schematic of the subdivision of the sea bed boundary layer. **(a)** shows the boundary layer occupying the entire water column and **(b)** shows a water column deeper than the boundary layer. The shear stress profile is similar to that for energy, but tends to zero towards the surface of **(b)**. The various layers are not to scale.

that extends a few metres away from the boundary. Here, neither the bed nor free stream flow affect the local dynamics, turbulent mixing dominates and the velocity and turbulence profiles take simple and universal forms; thus a mixing length strategy is used to describe the eddy viscosity. Beyond this is the outer layer or Ekman layer. Here the influence of the earth's rotation causes the current to turn progressively anticlockwise (in the Southern Hemisphere) with distance from the bed. This layer extends some tens of metres away from the boundary. The edge of the boundary layer merges with the free stream or geostrophic flow in which there is no influence from boundary friction.

In the logarithmic layer the drag coefficient (C_d) is most commonly determined at Z_b = 1 m, the distance away from the boundary

$$C_d = \frac{u_*^2}{V_b^2} = \left[\frac{1}{\kappa}\ln\frac{Z_b}{Z_0}\right]^{-2}, \tag{6.7}$$

where u_* is the friction velocity, V_b is the velocity adjacent to the boundary, Z_0 is the roughness height and κ=0.4 is von Kármán's constant. In this model the middle of the layer adjacent to the boundary is at Z_b = 0.5 m and the boundary condition for the momentum equation is

$$K_M \frac{\partial(u,v)}{\partial z} = u_*^2 = C_d(u,v)\sqrt{u^2+v^2}\,. \tag{6.8}$$

6.2.3.1 Seabed

Appropriate values of Z_0 or C_d can be given provided the nature of the underlying seabed is known. *Soulsby* [1983] shows typical values of the roughness length and drag coefficient for different seabed types. A drag coefficient of 0.0025 lies close to the many observations for mud, silt and sand, and is a figure that is widely used. However, for a gravel or rippled sand environment increased roughness length results from form drag. In these situations Z_0 increases to 0.3-1.0 cm giving a corresponding C_d of 0.0047-0.0075, illustrating the potential problems of using a constant drag coefficient. At the seabed a quadratic drag law

is applied. This relates the shear stress to the boundary velocity via the dimensionless quadratic drag coefficient. In this model the middle of the layer adjacent to the boundary is at 0.5 m corresponding to $C_d = 0.00303$, equivalent to $C_d = 0.0025$ at 1 m.

6.2.3.2 Ice shelf base

Measurements of ice-water drag coefficients have been limited to sea ice (single year and multi year) and landfast ice [*Shirasawa and Ingram*, 1991]. Measurements are usually made in the middle of large floes to avoid the effects of pressure keels, with observed values of C_d ranging from 0.0013 to 0.034 but with the majority being less than 0.008. One can speculate that the underside of sea ice is likely to be rather different to the base of an ice shelf. No observations to determine Z_0 or C_d have been made beneath an ice shelf in either freezing or melting areas. The ice could be very smooth or rippled (like sand) or fluted in melting areas, with freezing areas most closely resembling sea ice. However, tidal modelling by *Smithson et al.* [1996] and *Padman et al.* [2002] found evidence that friction coefficients of up to 0.015 beneath the ice shelf may improve the fit between modelled and observed tidal elevations, particularly near grounding lines, but at the expense of degrading the agreement of the open water sites. Since no clear drag coefficient is available for the ice shelf base the same value as used at the seabed is applied, again using a quadratic drag law.

6.3 Turbulence model

6.3.1 Stability functions

In this model, the effects of turbulence in transferring momentum and mixing heat and salt are determined by the widely used, level 2.5 turbulence closure scheme of *Mellor and Yamada* [1982] incorporating the modifications of *Galperin et al.* [1988]. This provides vertical diffusivities that depend on the interaction of flow and stratification, and are provided by the relation

$$K_M, K_H, K_q = q\, l\, (S_M, S_H, S_q), \tag{6.9}$$

where $q^2/2$ is the TKE, l is turbulence mixing length scale and S_M , S_H and S_q are stability functions related to the Richardson number, used by *Mellor and Yamada* [1982] and defined as

$$S_M = \frac{(g_2 - g_3 G_h)}{(1 - g_4 G_h)(1 - g_5 G_h)} \quad , \quad S_H = \frac{g_6}{(1 - g_4 G_h)} \quad , \quad S_q = 0.2 \qquad (6.10, 6.11, 6.12)$$

where

$$G_h = \frac{l^2}{q^2} \frac{g}{\rho_0} \frac{\partial \rho}{\partial z} \quad , \qquad (6.13)$$

and the values of g2 .... g6 are given below in Table 6.1.

Also from *Galperin et al.* [1988] an upper bound on the mixing length under stable stratification is enforced.

$$l \leq \frac{0.53q}{\sqrt{-\frac{g}{\rho_0}\frac{\partial \rho}{\partial z}}} \qquad (6.14)$$

Together with (6.13) this gives an effective lower limit $G_h \geq -0.28$. Under unstable stratification, (6.13) implies an upper limit $G_h \leq 0.0288$ to prevent the computation of negative diffusivity.

I	II	III
$A_1 = 0.92$	$g_0 = 1.0 - 6A_1/B_1$	$g_0 = 0.66747$
$A_2 = 0.74$	$g_1 = 6A_1 + B_2$	$g_1 = 15.620$
$B_1 = 16.6$	$g_2 = A_1(g_0 - 3C_1)$	$g_2 = 0.39327$
$B_2 = 10.1$	$g_3 = 3A_1A_2[(B_2 - 3A_2)g_0 - 3C_1g_1]$	$g_3 = 3.0858$
$C_1 = 0.08$	$g_4 = 3A_2g_1$	$g_4 = 34.676$
	$g_5 = 9A_1A_2$	$g_5 = 6.1272$
	$g_6 = A_2g_0$	$g_6 = 0.49393$

Table 6.1. Summary of experimental constants associated with vertical closure. Column I contains the Mellor and Yamada [1982] constants. Column II contains the formulae from Galperin et al. [1988] used in equations (6.10) (6.11) (6.12) with their numeric values in Column III.

6.3.2 Mellor and Yamada level 2.5 turbulent closure equations

The local evolution of both q and l are given by

$$\frac{\partial q^2}{\partial t} = \frac{\partial}{\partial z}\left(K_q \frac{\partial q^2}{\partial z}\right) + K_M\left[\left(\frac{\partial u}{\partial z}\right)^2 + \left(\frac{\partial v}{\partial z}\right)^2\right] + \frac{2g}{\rho_0} K_H \frac{\partial \rho}{\partial z} - \frac{2q^3}{B_1 l} \tag{6.15}$$

$$\frac{\partial q^2 l}{\partial t} = \frac{\partial}{\partial z}\left(K_q \frac{\partial q^2 l}{\partial z}\right) + lE_1 K_M\left[\left(\frac{\partial u}{\partial z}\right)^2 + \left(\frac{\partial v}{\partial z}\right)^2\right] + \frac{lE_1 g}{\rho_0} K_H \frac{\partial \rho}{\partial z} - lw\frac{q^3}{B_1 l} \tag{6.16}$$

The terms on the right-hand side are, respectively, the vertical turbulent diffusion, the shear production, the buoyancy production and dissipation of turbulent kinetic energy. It is worth noting that the buoyancy production is a source of TKE for unstable stratification and a sink of TKE for stable stratification. B_1 and E_1 are empirical constants, ρ_0 is the seawater reference density and K_q is the vertical turbulent diffusivity for q^2 and $q^2 l$. The wall proximity parameter (w) is a function of the macro length scale (l) and a prescribed barotropic length scale (l_z) and is given by

$$w = 1 + E_2\left(l/l_z\right)^2, \tag{6.17}$$

where E_2 is an empirical constant. In well mixed turbulent flows the growth of eddies is constrained by the presence of both the seabed and surface. *Mellor and Yamada* [1982] introduced a z-dependent mixing length, l_z, in order to ensure the logarithmic velocity profile in steady state boundary layers. Near the seabed or ice shelf base, the asymptotic behaviour of l is constrained such that its value is given by the product of the von Kármán constant and the distance from the boundary. Therefore, $l = \kappa Z_b$ is used near the boundaries and encompassed within the classic parabolic profile of l_z [*Mellor and Yamada*, 1982]

$$l_z = \kappa \frac{d_b d_s}{d_b + d_s}, \tag{6.18}$$

where d_s is the distance from the surface and d_b the distance from the bottom. Another function (triangular) that fulfills the requirements has also been used successfully by *Burchard et al.* [1998]

$$\bar{l_z} = \kappa \min(d_b, d_s). \tag{6.19}$$

6.4 Water column properties

6.4.1 Vertical diffusion

Both heat and salt are conserved in the model and their vertical diffusion within the water column are governed in the model by

$$\frac{\partial(T,S)}{\partial t} = \frac{\partial}{\partial z}\left(K_H \frac{\partial(T,S)}{\partial z}\right) \tag{6.20}$$

where K_H is the vertical eddy diffusivity, T is the water temperature and S, the water salinity. At the seabed there is no flux of heat or salt. At the ice-ocean interface, phase changes during melting or freezing give rise to heat and freshwater fluxes, which will be considered later in this section.

6.4.2 Equation of state for seawater

The equation of state is given by the UNESCO formula for sea water [*Gill*, 1982] and has the form

$$\rho = \rho(T,S), \tag{6.21}$$

where the seawater density (ρ) is related to temperature and salinity and is evaluated at constant pressure within the mixing model.

6.4.3 Temperature and salinity transfer coefficients

At the ice-ocean interface melting is a function of temperature, salinity and speed of the water adjacent to the interface. As they approach the interface, eddies are suppressed and

the eddy diffusivity decreases to a point where molecular diffusion becomes the principal transfer mechanism for heat and salt. The parameterization of transfer coefficients for heat (γ_t) and salt (γ_s) follows *Kader and Yaglom* [1972]

$$\gamma_t = \frac{u_*}{2.12\ln(u_* D/\nu) + 12.5\,\mathrm{Pr}^{2/3} - 9} \quad \text{and} \tag{6.22}$$

$$\gamma_s = \frac{u_*}{2.12\ln(u_* D/\nu) + 12.5Sc^{2/3} - 9} \quad , \tag{6.23}$$

where Pr and Sc are the molecular Prandtl and Schmidt numbers for seawater, ν is the kinematic viscosity, u_* is the friction velocity and D is the thickness of the model layer adjacent to the ice shelf.

6.4.4 Basal melting and freezing point of seawater

Using (6.22) and (6.23), *Nicholls and Makinson* [1998] derived an expression relating the temperature and salinity at the ice-ocean interface, and the flow of the layer adjacent to the interface to determine basal melt rate under FRIS. Further modifications were made by *Nicholls et al.*[2001] by incorporating a factor for the ice temperature gradient at the ice shelf base [*Holland and Jenkins*, 1999]. Thus, the basal melt rate, m (negative for melting) is given by

$$m = \frac{\gamma_t (T_b - T_f)}{aS_b \dfrac{\gamma_t}{\gamma_s} - \dfrac{L}{c_w} - (T_i - T_f)\dfrac{c_i}{c_w}} \quad , \tag{6.24}$$

where T_b and S_b are the temperature and salinity of the seawater in the model layer adjacent to the ice-ocean interface; c_w and c_i are the specific heat capacities of seawater and ice; L and T_i are the latent heat of ice fusion and ice shelf surface temperature. T_f is the pressure freezing point for seawater of salinity S_f at the ice-ocean interface and is determined from the linear form of pressure freezing point relationship [*Millero*, 1978]

$$T_f = aS_f + b + cp_{io} \quad , \tag{6.25}$$

where a, b and c are physical constants (-0.0573°C psu^{-1}, 0.0832°C and 7.61×10^{-4} °C dbar^{-1} respectively), and p_{io} is the pressure at the ice-ocean interface in dbar. From (6.24) the basal melt rate is mainly dependent on the water current in the layer adjacent to the ice shelf base and the temperature difference between the water in that layer and its freezing point.

6.4.5 Mixing water masses

During the production of melt water, heat is required to warm the ice to the in-situ melting point and melt the ice before mixing. Assuming the salinity of the ice is zero, the bulk change in temperature (ΔT) for the 1 m thick layer adjacent to the ice shelf base over the time step (Δt) is prescribed by

$$\Delta T = \frac{\Delta M}{M_b + \Delta M}\left(- \frac{c_i}{c_w}\left(T_f - T_i\right) - \frac{L}{c_w} - \left(T_b - T_f\right)\right) \quad , \tag{6.26}$$

where ΔM is the melt water mass determined from (6.24) and M_b is the layer water mass. Within the large brackets of (6.26), three terms contribute to the temperature change through warming the ice, melting the ice and warming the resulting melt water. Likewise the bulk change in salinity (ΔS) that results from dilution by meltwater is prescribed by

$$\Delta S = -\frac{\Delta M}{M_b + \Delta M} S_b \quad . \tag{6.27}$$

6.5 Internal wave activity

A weakness of all local turbulence models is that they do not account for the often highly active stably stratified but strongly sheared thermocline/halocline region immediately below the mixed layer. Schemes have been added to overcome these shortcomings for the MY2.5 scheme. These simple schemes do not seek to model the processes occurring, but parameterize the mean effect of these processes on mixing.

6.5.1 Mellor parameter

The introduction of an additional term in the turbulence equations was suggested by *Mellor and Kantha* [1989] to account for the additional shear induced by internal waves in the presence of stable stratification (Brunt-Väisälä frequency, $N^2 > 0$). As internal wave energy is known to depend on N^2, the internal wave shear term αN^2 is added to the shear terms in both turbulent transport equations. For stable stratification the modified shear production term is used in (6.15) and (6.16)

$$K_M\left[\left(\frac{\partial u}{\partial z}\right)^2+\left(\frac{\partial v}{\partial z}\right)^2+\alpha N^2\right], \tag{6.28}$$

where a value of $\alpha = 0.7$ was suggested after estimating the differences between observed and modelled shear profiles.

6.5.2 Kantha and Clayson parameter

This parameterization incorporates diffusivities below the mixed layer. *Large et al.* [1994] suggested two different contributions to diffusivities: shear instability (SI) and internal waves (IW). The shear instability-induced viscosity and diffusivities are modelled as a strongly decreasing function of the gradient Richardson number Ri_g

$$Ri_g = \frac{N^2}{\left(\frac{\partial u}{\partial z}\right)^2+\left(\frac{\partial v}{\partial z}\right)^2} \tag{6.29}$$

with the shear instability-induced viscosities and diffusivities being determined by a strongly decreasing function of the gradient Richardson number,

$$K_M^{SI} = K_H^{SI} = \begin{cases} 0, & for \quad Ri_g > 0.7, \\ 5\times 10^{-3}\left[1-\left(\frac{Ri_g}{0.7}\right)^2\right]^3, & for \quad 0 < Ri_g < 0.7, \\ 5\times 10^{-3}, & for \quad Ri_g < 0. \end{cases} \tag{6.30}$$

In contrast however, it is assumed that the internal wave induced viscosities and diffusivites are constant, $K_M^{IW} = 10^{-4}$; $K_H^{IW} = 5\times 10^{-5}$ m^2 s^{-1}. Therefore, when TKE is small and

conditions will support internal waves, the sum of the shear induced and internal wave induced diffusivities replaces the diffusivities given by the model. This model was applied by *Kantha and Clayson* [1994] to different situations and was found to promote increased mixing in stably stratified situations. In the sub-ice shelf mixing model described in this chapter, the more comprehensive parameterization of *Kantha and Clayson* [1994] is used to represent the mixing associated with internal wave activity rather than the less sophisticated version of *Mellor and Kantha* [1989].

6.6 Model structure

In the model described here the water column is divided into a number of discrete intervals or layers. The vertical layer thickness is smoothly graded to give the highest resolution at the boundaries. The thickness of the two layers adjacent to each of the boundaries is set to 1.0 m. The node depth at the centre of each layer of the remaining water column (z_{rem}) is determined from [*Lynch et al.*, 1996]

$$Z_{node} = -z_{rem} + \varepsilon(z_{rem}) - \beta \sin(2\pi\varepsilon) \ , \qquad (6.31)$$

where ε increases linearly with node number, from 0 at the bottom to 1 at the top surface. For a total water column thickness of 200 m with 61 nodes, the constant β is set to give the desired layer resolution of 1.0 m near the boundaries and approximately 6 m in the mid-water column (Figure 6.2).

The values for u, v, T and S are located at the centres of the layers and K_M, K_H and K_q are positioned at the interfaces of the layers (Figure 6.2). The turbulent quantities q^2, q^2l and dissipation are all positive by definition thus the time step must be sufficiently small (typically <180 s) to avoid the occurrence of negative values. The diffusion terms are treated implicitly leading to a tridiagonal linear system of equations. Initially the model requires parameters to be set and the model initialised before the simple time loop starts and

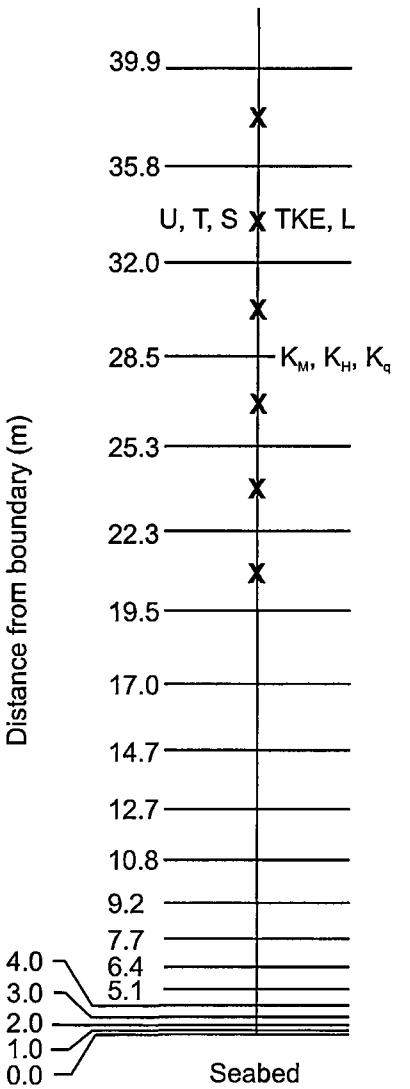

Figure 6.2 The position of the layer boundaries from the seabed (or ice shelf base) in the vertical mixing model with nodes at the centre of each layer. The grid is symmetrical about the mid-water column with 61 layers over 200 m. The layer properties are calculated at the nodes at the centre of each layer (depth determined from 6.31) and the diffusivities are calculated at the boundaries.

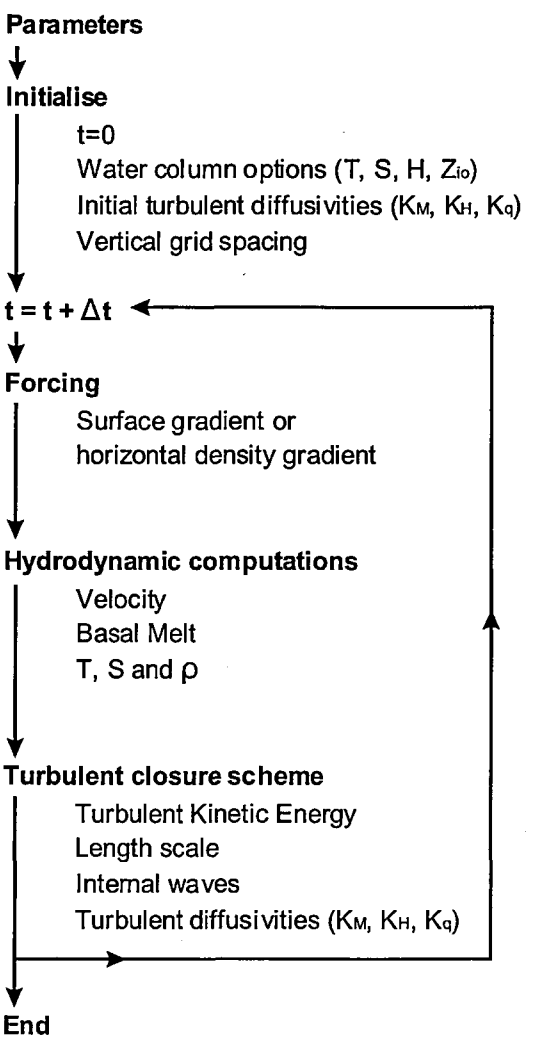

Figure 6.3 A flow diagram of the vertical mixing model, showing the component programs and data sets.

continues until a specified time is reached. Within the time loop (Figure 6.3) the forcing is used to drive mean and/or tidal currents. The current profile is determined from the momentum equations which account for the upper and lower boundary conditions. Next, the basal melt is calculated and the tracer equations for temperature and salinity update the water column structure. The turbulence equations are then used to determined the eddy viscosity and diffusivities which can be modified by internal waves and shear instabilities. The final viscosities and diffusivities are then used for the next time loop.

6.7 Model test cases

Following the comparative tests of *Burchard et al.* [1998], the performance of the model described here was checked using two steady state barotropic open channel flow situations that include comparisons with data. The tests involve a surface stress forced flow and a pressure gradient-driven flow. Also, the Kato-Phillips experiment was used to check the development of the surface mixed layer. In addition to the tests of *Burchard et al.* [1998], the water column beneath an ice shelf must evolve along the Gade mixing line in θ-S space [*Gade*, 1979] as melt from fresh water ice is mixed into the water column.

6.7.1 Surface stress

If surface stress is the only forcing for a steady state open channel, the resulting flow induces a constant stress throughout the water column. It has been shown by *Burchard et al.* [1998] that the TKE distribution is constant over the whole water column when the stability functions of *Galperin et al.* [1988] are used. In contrast, the observations show a parabolic profile (Figure 6.4a), this discrepancy is a consequence of the neglect of shear influence on the stability functions [*Burchard et al.*, 1998]. The model underestimates the eddy viscosity when using the parabolic profile of l_z but closely matches the data when using the triangular profile. However *Burchard et al.* [1998] noted that the flow in the

experiment was probably not fully developed in the centre hence the flattening of the profile in the mid water column (Figure 6.4a).

6.7.2 Pressure gradient

In this model the only forcing is a surface slope, which leads to a shear stress that linearly decreases from the seabed to the surface. The use of a parabolic l_z over-estimates the dissipation, and under-estimates K_M significantly more than the triangular l_z profile (Figure 6.4b). As in the surface stress case, the use of triangular profile for l_z provides the better fit to the dissipation and eddy viscosity profiles. As a result of these tests, the triangular profile for l_z will be used in the vertical mixing model.

6.7.3 Surface mixed layer growth

In this experiment, a mixed layer induced by a constant surface stress penetrates into a stably stratified water column. The density increases linearly down from the surface and the water depth is assumed to be infinite. A solution for the evolution of the mixed layer depth D_m, which is defined as water column with TKE > 10^{-5} m^2 s^{-2}, is given by *Price* [1979]

$$D_m(t) = 1.05 u_*^s N_0^{-1/2} t^{1/2} \quad , \tag{6.32}$$

where u_*^s is the surface friction velocity and N_0 the constant initial Brunt-Väisälä frequency. Following other authors u_*^s = 10^{-2} m s^{-1} and N_0 = 10^{-2} s^{-1}. The model closely follows the empirical solution (Figure 6.5) though it does under-estimate the mixed layer depth, a characteristic reported by several authors for the MY2.5 scheme [*Martin*, 1985; *Kantha and Clayson*, 1994].

6.6.4 Gade line mixing

The melting and mixing of fresh water ice into sea water with initial potential temperature and salinity of θ_0 and S_0, cause the water column to evolve along a straight line in θ-S space. The gradient of the straight line is given by [*Gade*, 1979]

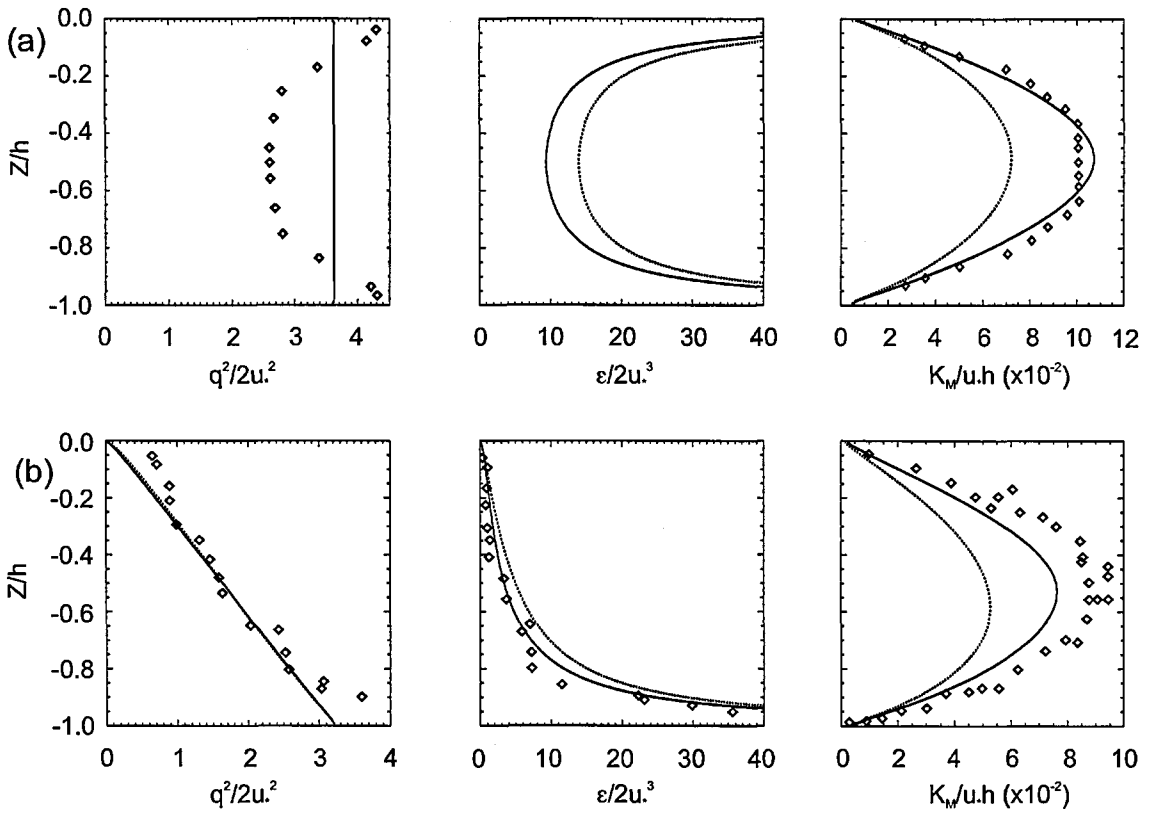

Figure 6.4 Simulations of barotropic open channel flow with comparisons against data following the comparisons made by *Burchard et al.* [1998]. **(a)** Stress-driven flow with data points from *Telbany And Reynolds*, [1982]. **(b)** Pressure gradient-driven flow with data points from *Nakagawa et al.*, [1975], *Jobson and Sayre*, [1970] and *Ueda et al.*, [1977]. The solid line results from using the model with a triangle-shaped L_z (6.19) and the dashed line using a parabola-shaped L_z (6.18).

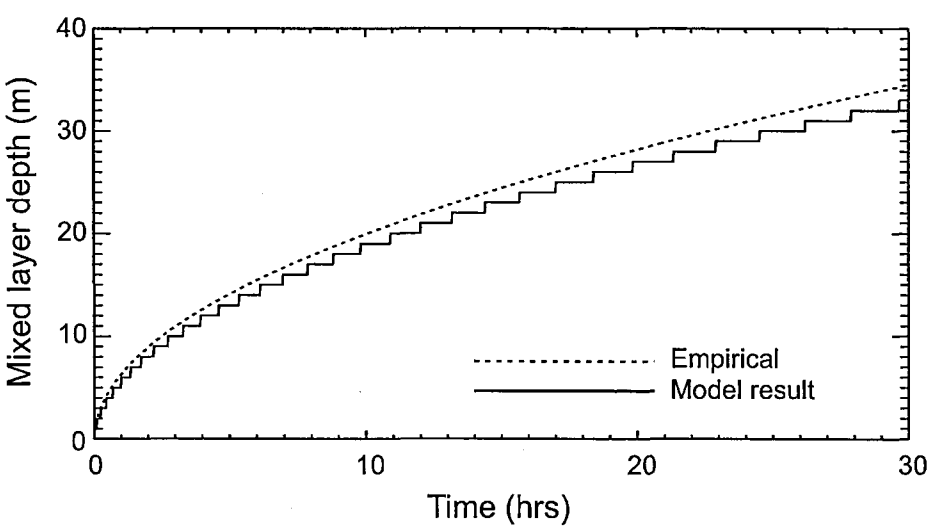

Figure 6.5 The development of the mixed-layer depth (defined as the deepest point in the water column with TKE > 10^{-5} m^2 s^{-2}) for the simulation of the Kato-Phillips experiment [*Kato and Phillips*, 1969]. Here the vertical resolution of the model was set to 1 m.

$$\frac{d\theta}{dS} = \frac{L}{S_0 c_w} + \frac{(\theta_f - T_i)c_i}{S_0 c_w} + \frac{(\theta_0 - \theta_f)}{S_0}, \tag{6.33}$$

where θ_f is the potential temperature at which ice melts at the ice-shelf base. For conditions appropriate to the cavity beneath FRIS, the latent heat of the ice in the first term dominates giving a gradient of 2.4 °C psu^{-1}. Where the ice is colder eg. -30°C then the gradient is increased to 2.8°C psu^{-1} through the contribution of the second term. The third term considers the cooling of the seawater to freezing point, though the effect is not significant. To test the ice-ocean melting and mixing component of the model, and the conservation of temperature and salinity, the evolution of the water column characteristics has been compared with the Gade mixing line and found to match the calculated gradients.

6.7.5 Distribution of turbulent kinetic energy

To examine the time variability of TKE beneath an ice shelf and its variation within the water column, a series of plots of TKE over a tidal cycle are shown in Figure 6.6a. In the lower half of this 200-m homogeneous water column the mean TKE decreases with distance away from the boundary. The phase shift in the TKE maximum higher in the water column compared with the boundary, is associated with the phase shift in the local shear production that results from differences between the near boundary currents and those farther away. Also, TKE generated at the boundary diffuses into the water column away from the boundary. This contributes to the phase shift, although the contribution is small compared with the local shear production. However, by plotting the mean shear production and the mean dissipation over a tidal cycle, the diffusion of TKE away from the boundary is shown by the shift in the mean dissipation towards the middle of the water column (Figure 6.6b), i.e. if no diffusion occurred these two lines would coincide. By contouring a time series of TKE, the phase shift away from the boundaries becomes more apparent (Figure 6.6c and 6.6d). Initially the water column is homogeneous and the TKE is symmetrical about the middle of the water column. Melting is initiated and stratification

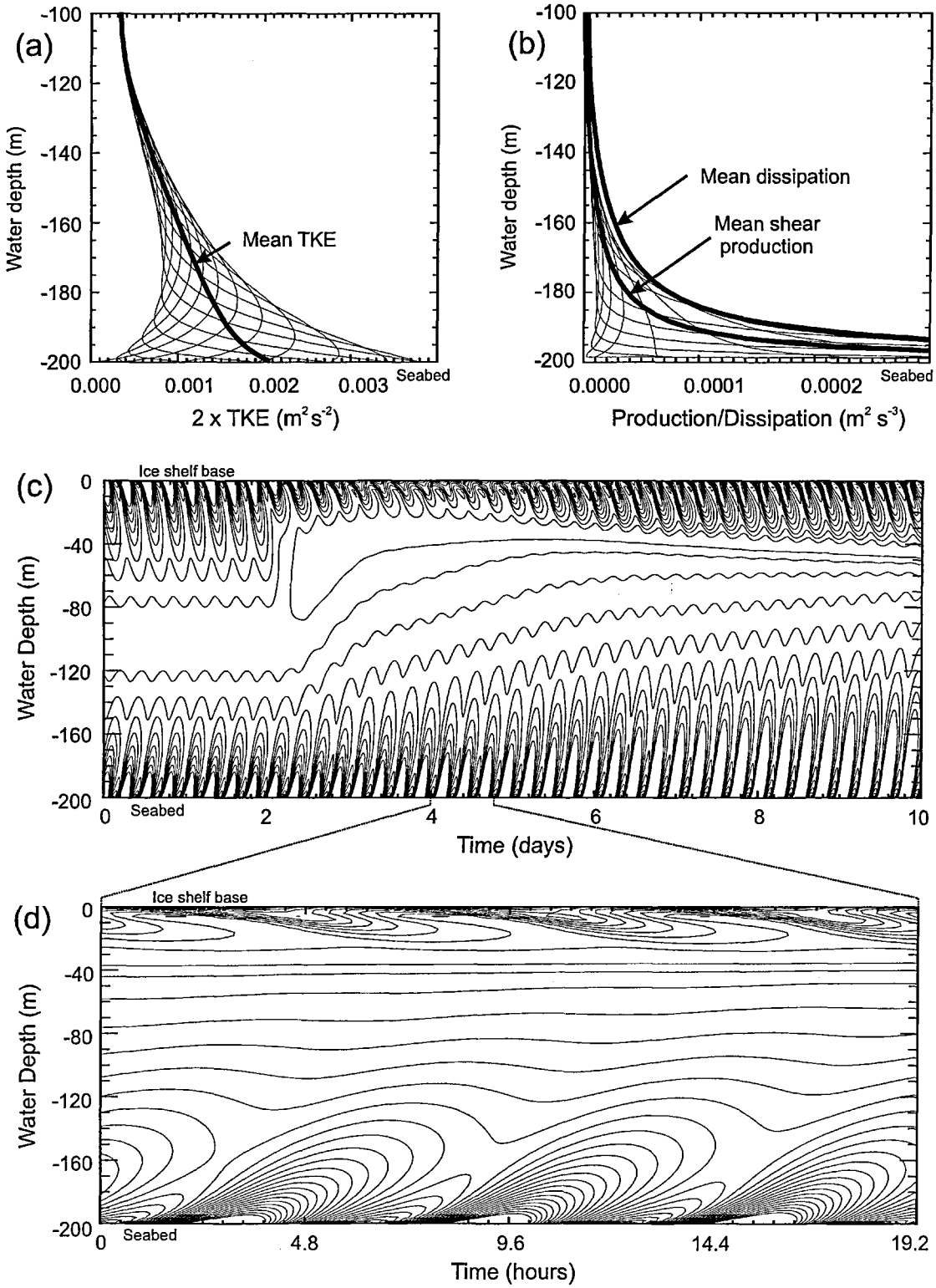

Figure 6.6 (a) Plots of TKE over the lower half of a homogeneous 200-m water column beneath an ice shelf. The plots are over an M_2 tidal cycle and the mean TKE is shown by the thick line. **(b)** Same as **(a)** but plots are for shear production of TKE over the tidal cycle with the mean shear and mean dissipation also shown. **(c)** Contour plot of TKE, initially for a homogeneous water column (2 days) followed by basal melting and subsequent stratification of the water column and deepening of an upper mixed layer (contour interval 4 x 10^{-5} m^2 s^{-2} and maximum of 0.00036 m^2 s^{-2}) and **(d)** is an excerpt of **(c)** with a contour interval of 2.5 x 10^{-5} m^2 s^{-2} and a maximum of 0.006 m^2 s^{-2}.

develops, suppressing the production of TKE in the upper half of the water column. The upper mixed layer develops and deepens over the remainder of the plot. Two TKE maxima occur close to the time of maximum current near the boundary because of the ebb and flow of the tidal current.

The one-dimensional vertical mixing model described in this chapter will be applied to the high latitude sub-ice shelf water column. It will be used, in the following chapter, to examine vertical profiles of tidal currents, water column structure, vertical mixing and basal melting beneath Filchner-Ronne Ice Shelf.

6.8 References

Andre, J.C., and P. Lacarrere, Mean and turbulent structures of the oceanic surface layer as determined from one-dimensional third order simulations, *Journal of Physical Oceanography, 15*, 121-132, 1985.

Burchard, H., and H. Baumert, On the Performance of a Mixed-Layer Model-Based on the Kappa- Epsilon Turbulence Closure, *Journal of Geophysical Research, 100* (C5), 8523-8540, 1995.

Burchard, H., and K. Bolding, Comparative analysis of four second-moment turbulence closure models for the oceanic mixed layer., *Journal of Physical Oceanography, 31*(8), 1943-1968, 2001.

Burchard, H., and O. Petersen, Models of turbulence in the marine environment - a comparative study of two-equation turbulence models, *Journal of Marine Systems, 21* (1-4), 29-53, 1999.

Burchard, H., O. Petersen, and T.P. Rippeth, Comparing the performance of the Mellor-Yamada and the k-epsilon two-equation turbulence models, *Journal of Geophysical Research, 103* (C5), 10543-10554, 1998.

Canuto, V.M., A. Howard, Y. Cheng, and M.S. Dubovikov, Ocean turbulence. Part I: One-point closure model - Momentum and heat vertical diffusivities, *Journal of Physical Oceanography, 31* (6), 1413-1426, 2001.

D'Alessio, S.J.D., K. Abdella, and N.A. McFarlane, A new second-order turbulence closure scheme for modeling the oceanic mixed layer, *Journal of Physical Oceanography, 28* (8), 1624-1641, 1998.

Gade, H.G., Melting of Ice in Sea Water: A Primitive Model with Application to the Antarctic Ice Shelf and Icebergs, *Journal of Physical Oceanography, 9* (1), 189-198, 1979.

Galperin, B., L.H. Kantha, S. Hassid, and A. Rosati, A Quasi-Equilibrium Turbulent Energy-Model for Geophysical Flows, *Journal of the Atmospheric Sciences, 45* (1), 55-62, 1988.

Garwood, R.W., An oceanic mixed layer model capable of simulating cyclic states, *Journal of Physical Oceanography, 7*, 455-468, 1977.

Gill, A.E., *Atmosphere-Ocean Dynamics*, 662 pp., Academic Press, Orlando, Florida, 1982.

Holland, D.M., and A. Jenkins, Modeling thermodynamic ice-ocean interactions at the base of an ice shelf, *Journal of Physical Oceanography, 29* (8), 1787-1800, 1999.

Jobson, H.E., and W.W. Sayre, Vertical mass transfer in open channel flow, *96* (HY3), 703-724, 1970.

Kader, B.A., and A.M. Yaglom, Heat and mass transfer laws for fully turbulent wall flows, *International Journal of Heat and Mass Transfer, 15*, 2329-2351, 1972.

Kantha, L.H., and C.A. Clayson, An Improved Mixed-Layer Model for Geophysical Applications, *Journal of Geophysical Research, 99* (C12), 25235-25266, 1994.

Kantha, L.H., A. Rosati, and B. Galperin, Effect of Rotation on Vertical Mixing and Associated Turbulence in Stratified Fluids, *Journal of Geophysical Research, 94* (C4), 4843-4854, 1989.

Kraus, E.B., and J.S. Turner, A one-dimensional model of the seasonal thermocline II. The general theory and its consequences, *Tellus, 19*, 98-105, 1967.

Kato, H., and O.M. Phillips, On the penetration of a turbulent layer into a stratified fluid, *Journal of Fluid Mechanics, 37*, 643-655,1969.

Large, W.G., and G. Crawford, Observations and simulations of upper ocean response to wind events during the Ocean Storms Experiment, *Journal of Physical Oceanography, 25*, 2831-2852, 1995.

Large, W.G., J.C. McWilliams, and S.C. Doney, Oceanic Vertical Mixing - a Review and a Model with a Nonlocal Boundary-Layer Parameterization, *Reviews of Geophysics, 32* (4), 363-403, 1994.

Luyten, P.J., E. Deleersnijder, J. Ozer, and K.G. Ruddick, Presentation of a family of turbulence closure models for stratified shallow water flows and preliminary application to the Rhine outflow region, *Continental Shelf Research, 16* (1), 101-130, 1996.

Lynch, D.R., J.T.C. Ip, C.E. Naimie, and F.E. Werner, Comprehensive coastal circulation model with application to the Gulf of Maine, *Continental Shelf Research, 16* (7), 875-906, 1996.

Martin, P.J., Simulation of the Mixed Layer at OWS November and Papa with Several Models, *Journal of Geophysical Research, 90* (NC1), 903-916, 1985.

Mellor, G.L., and L. Kantha, An Ice-Ocean Coupled Model, *Journal of Geophysical Research, 94* (C8), 10937-10954, 1989.

Mellor, G.L., and T. Yamada, Development of a Turbulence Closure-Model for Geophysical Fluid Problems, *Reviews of Geophysics, 20* (4), 851-875, 1982.

Millero, F.J., Freezing point of sea water, Eighth Report of the Joint Panel of Oceanographic Tables and Standards, Appendix 6, *UNESCO Technical Papers in Marine Science, 28*, 29-31, 1978.

Nakagawa, H., I. Nezu, and H. Ueda, Turbulence in open channel flow over smooth and rough beds, *241*, 155-168, 1975.

Nicholls, K.W., and K. Makinson, Ocean circulation beneath the western Ronne Ice Shelf, as derived from in situ measurements of water currents and properties, in *Ocean, Ice, and Atmosphere: Interactions at the Antarctic Continental Margin*, edited by S.S. Jacobs, and R.F. Weiss, pp. 301-318, American Geophysical Union, Washington DC, 1998.

Nicholls, K.W., S. Østerhus, K. Makinson, and M.R. Johnson, Oceanographic conditions south of Berkner Island, beneath Filchner-Ronne Ice Shelf, Antarctica, *Journal of Geophysical Research, 106* (C6), 11481-11492, 2001.

Niiler, P.P., Deepening of the wind-mixed layer, *Journal of Marine Research, 33*, 405-422, 1975.

Padman, L., H.A. Fricker, R. Coleman, S. Howard, and L. Erofeeva, A New Tidal Model for the Antarctic Ice Shelves and Seas, *Annals of Glaciology, In Press*, 2002.

Price, J.F., On the scaling of stress-driven entrainment experiments, *Journal of Fluid Mechanics, 90*, 509-529, 1979.

Price, J.F., R.A. Weller, and R. Pinkel, Diurnal Cycling - Observations and Models of the Upper Ocean Response to Diurnal Heating, Cooling, and Wind Mixing, *Journal of Geophysical Research, 91* (C7), 8411-8427, 1986.

Shirasawa, K., and R.G. Ingram, Characteristics of the turbulent oceanic boundary layer under sea ice. Part 1: A review of the ice-ocean boundary layer, *J. Marine Systems, 2*, 153-160, 1991.

Simpson, J.H., W.R. Crawford, T.P. Rippeth, A.R. Campbell, and J.V.S. Cheok, The vertical structure of turbulent dissipation in shelf seas, *Journal of Physical Oceanography, 26* (8), 1579-1590, 1996.

Smithson, M.J., A.V. Robinson, and R.A. Flather, Ocean tides under the Filchner-Ronne Ice Shelf, Antarctica, *Annals of Glaciology, 23*, 217-225, 1996.

Soulsby, R.L., The bottom boundary layer of the shelf sea, in *Physical oceanography of Coastal and Shelf Seas*, edited by B. Johns, pp. 189-226, New York, 1983.

Telbany, M.M.M.E., and A.J. Reynolds, The structure of turbulent plane Couette flow, *104*, 367-372, 1982.

Ueda, H., R. Moller, S. Komori, and T. Mizushina, Eddy diffusivity near the free surface of open channel flow, *20*, 1127-1136, 1977.

CHAPTER 7

Application of Vertical Mixing Model to the Cavity Beneath Filchner-Ronne Ice Shelf

7.1 Introduction

In this chapter the vertical mixing model described in Chapter 6 is applied to the cavity beneath FRIS. First, it is applied to locations with sub-ice shelf observations that give some measure of basal melt rates. The model is then used to calculate the contribution of tidal activity to the vertical heat flux and basal melt rate and evaluate the impact of the semi-diurnal critical latitude and stratification on current profiles, both beneath the ice shelf and just offshore of Ronne Ice Front. Also, the effects of tidal ellipse polarization on vertical mixing and basal melting are considered over a wide range of tidal current amplitudes. These results are used to assess the likely vertical mixing conditions beneath various regions of FRIS where no observations exist. Finally, the impact of tidal activity on the shallow Ronne Ice Front region is considered, with an examination of the extent to which water masses are modified as they pass through this region.

Direct oceanographic measurements from beneath FRIS confirm that WSW, a product of sea ice formation north of the ice shelf, flows into the sub-ice shelf cavity [*Nicholls and Makinson*, 1998; *Nicholls et al.*, 2001]. This relatively warm, dense water occupies the lower portion of the water column in an environment isolated from atmospheric forcing, in which tidal and thermohaline processes are thought to dominate the circulation. *MacAyeal* [1984b] suggested *tidal stirring* as a probable mechanism for mixing WSW up

through the sub-ice shelf water column to be transformed, through melting at the underside of the ice shelf, into ISW.

In the cavity beneath an ice shelf frictional stress at both the seabed and the ice shelf base influences the vertical structure of tidal currents, induces vertical mixing and enables the development of two well-defined mixed boundary layers. Where fixed ice cover is present and tidal currents in deep water are weak, the frictional boundary layers occupy a small fraction of the water column. However, in shallow water with strong tidal currents, they can occupy the entire water column, dominating the tidal current structure and associated vertical mixing [*Prinsenberg and Bennett*, 1989]. Tidal simulations for the southern Weddell Sea show that the mean barotropic tidal currents beneath FRIS attain speeds of up to 0.2 - 0.5 m s^{-1}, with peak velocities reaching 1 m s^{-1} (Chapter 4) [*Robertson et al.*, 1998]. Close to Ronne Ice Front, and along grounding lines of FRIS where the ice first comes afloat, these tidal currents are thought to result in significant levels of vertical mixing, and high basal melt rates.

7.1.1 Ellipse polarization

To determine the influence of vertical tidal mixing on melting beneath Ross Ice Shelf, *Scheduikat and Olbers* [1990] developed two one-dimensional mixed layer models, thermodynamically coupled to an ice shelf, one with two layers and one with three layers. Both were Kraus and Turner type models [*Kraus and Turner*, 1967], which were forced by a barotropic tidal current. In the two layer model, the horizontally homogeneous upper mixed layer interacted with the ice shelf while the lower layer remained passive and represented an infinite heat and salt reservoir. In the three layer model, the bottom layer was treated as a mixed layer and included the advection of heat and salt, while a third layer was introduced between the two mixed layers. With the two-layer model it was found that basal melting or freezing was strongly dependent on the ratio of the major and minor axes of the

tidal current ellipse. Flat or degenerate ellipses yielded cyclic currents with the top layer entraining and then detraining water from the layer below. When the current was at its maximum during the tidal cycle, entrainment and melting would occur. With open, circular ellipses there was little or no entrainment from the layer below and heat lost from the upper layer to the ice shelf gave a small amount of freezing, irrespective of the tidal current amplitude. The three-layer model gave similar results, but with reduced melt rates resulting from a better representation of the thermocline. *Scheduikat and Olbers* [1990], however, did not include the effects of the earth's rotation.

Using a one-dimensional turbulence closure model that included the earth's rotation, *Simpson and Sharples* [1994] considered the effects of tidal current ellipse polarization on tidal front behaviour. Polarization (P) is used to define the shape and sense of rotation of a tidal current ellipse

$$P = \pm V/U \,, \tag{7.1}$$

where U and V are the semi-major and semi-minor axes of the tidal current ellipse, respectively. The polarization ranges from a purely circular clockwise current (P = -1), through a flat or degenerate ellipse (P = 0), to a purely circular anticlockwise current (P = +1). With the inclusion of rotation, *Simpson and Sharples* [1994] found that predominantly clockwise tidal currents (in the Northern Hemisphere) produced substantial differences in the predicted positions of fronts over previous non-rotational models, with fronts extending into deeper waters where the polarization was increasingly negative.

The rotational effect on vertical mixing is accounted for by decomposing the elliptical tidal current into purely anticlockwise (R_+) and clockwise (R_-) components and considering their respective frictional boundary layers. The two constant magnitude rotary velocity components rotate at the tidal frequency, and each has a characteristic frictional boundary layer thickness, δ_+ and δ_-, given by *Prandle* [1982]:

$$\delta_+ \approx \left(\frac{2K_M}{|\omega + f|}\right)^{1/2} \quad \text{and} \quad \delta_- \approx \left(\frac{2K_M}{|\omega - f|}\right)^{1/2}, \qquad (7.2 \text{ and } 7.3)$$

where K_M is the eddy viscosity, f is the Coriolis parameter and ω the frequency of the tidal oscillation. Assuming a constant eddy viscosity for semi-diurnal tides at northern mid-latitudes the thickness of the clockwise frictional boundary layer will be about three times greater than for the anticlockwise frictional boundary layer. An effective combined boundary layer thickness (δ) is suggested by *Soulsby* [1983]

$$\delta = \frac{(R_+\delta_+ + R_-\delta_-)}{(R_+ + R_-)}. \qquad (7.4)$$

Consequently, tidal currents with more negative polarizations in the Northern Hemisphere have thicker boundary layers allowing mixing to penetrate farther into the water column interior and tidal fronts to advance into deeper water.

The spatial variability of the tidal currents beneath FRIS was determined in Chapter 4 using a two-dimensional depth-averaged barotropic tidal model of the southern Weddell Sea. The modelled amplitudes of R_+ and R_- for M_2 and S_2 in the southern Weddell Sea are shown in Figures 7.1 and 7.2. The corresponding M_2 and S_2 tidal ellipse polarizations over this region are shown in Figure 7.3. Other semi-diurnal tidal constituents exhibit an almost identical pattern of polarization with regions of strongly positive and negative polarization present beneath FRIS, suggesting a wide range of boundary layer depths.

7.1.2 Critical latitude

7.1.2.1 Northern Hemisphere

At high northern latitudes the boundary layer of R_- is much thicker than that of the R_+ component for semi-diurnal tides as $|\omega - f|$ tends to zero as the critical latitude (φ_{crit}) is

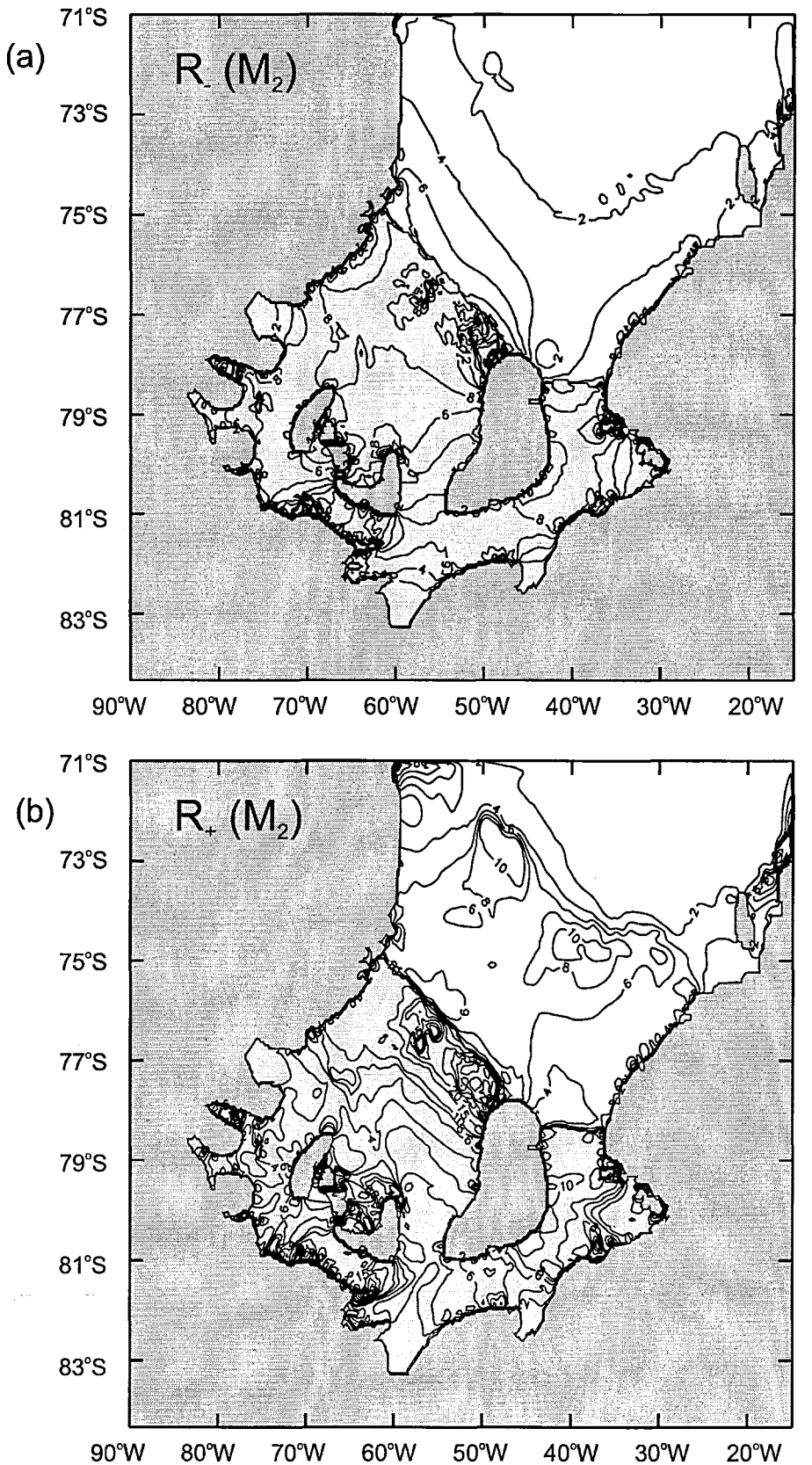

Figure 7.1 Contour plots of the amplitude of the M_2 rotary components. **(a)** The clockwise component R_- with a contour interval of 2 cm s^{-1} and **(b)** the anticlockwise component R_+ with a contour interval of 2 cm s^{-1} and 5 cm s^{-1} above 10 cm s^{-1}.

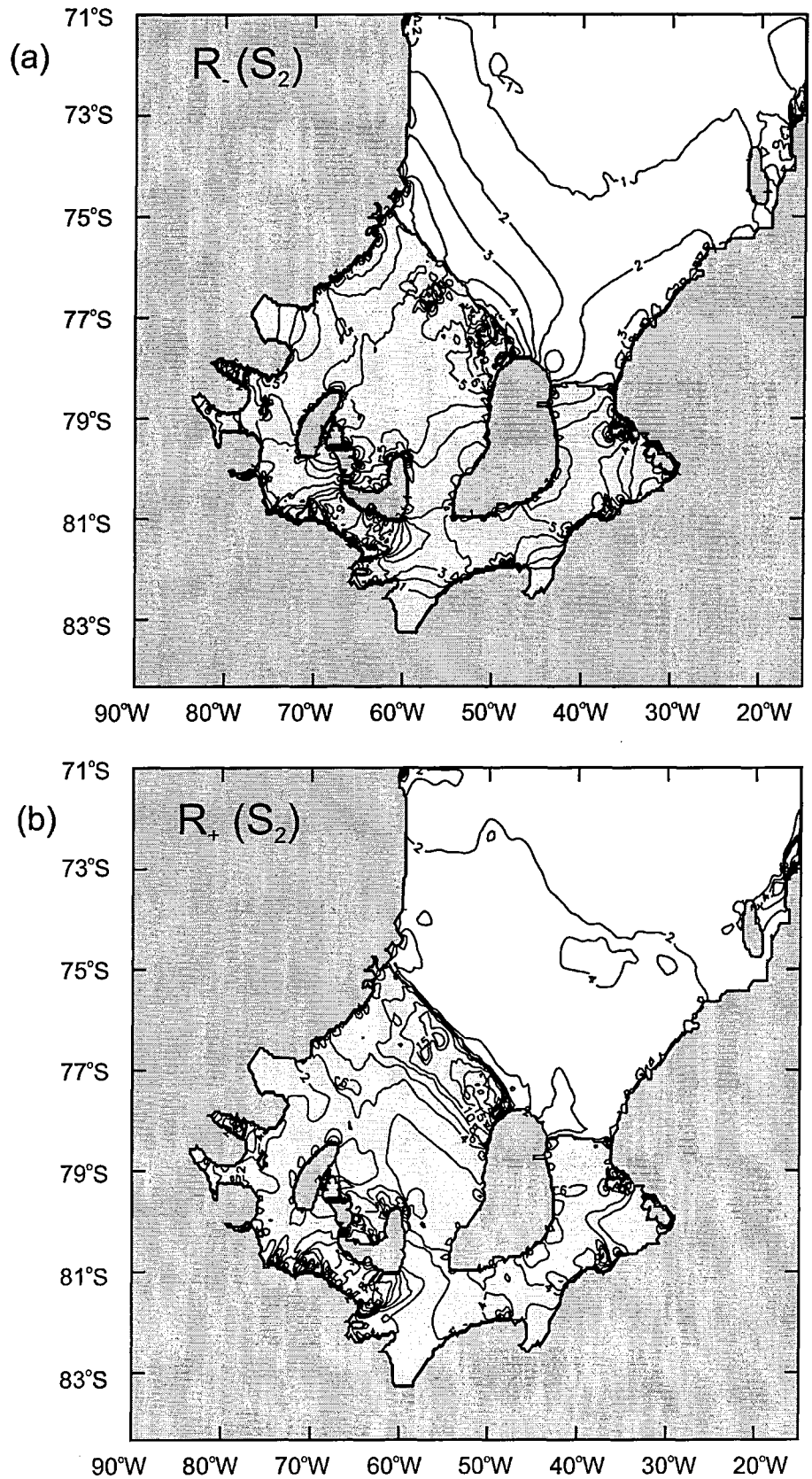

Figure 7.2 Contour plots of the amplitude of the S_2 rotary components. **(a)** The clockwise component R_- with a contour interval of 1 cm s^{-1} and **(b)** the anticlockwise component R_+ with a contour interval of 2 cm s^{-1} and 5 cm s^{-1} above 10 cm s^{-1}.

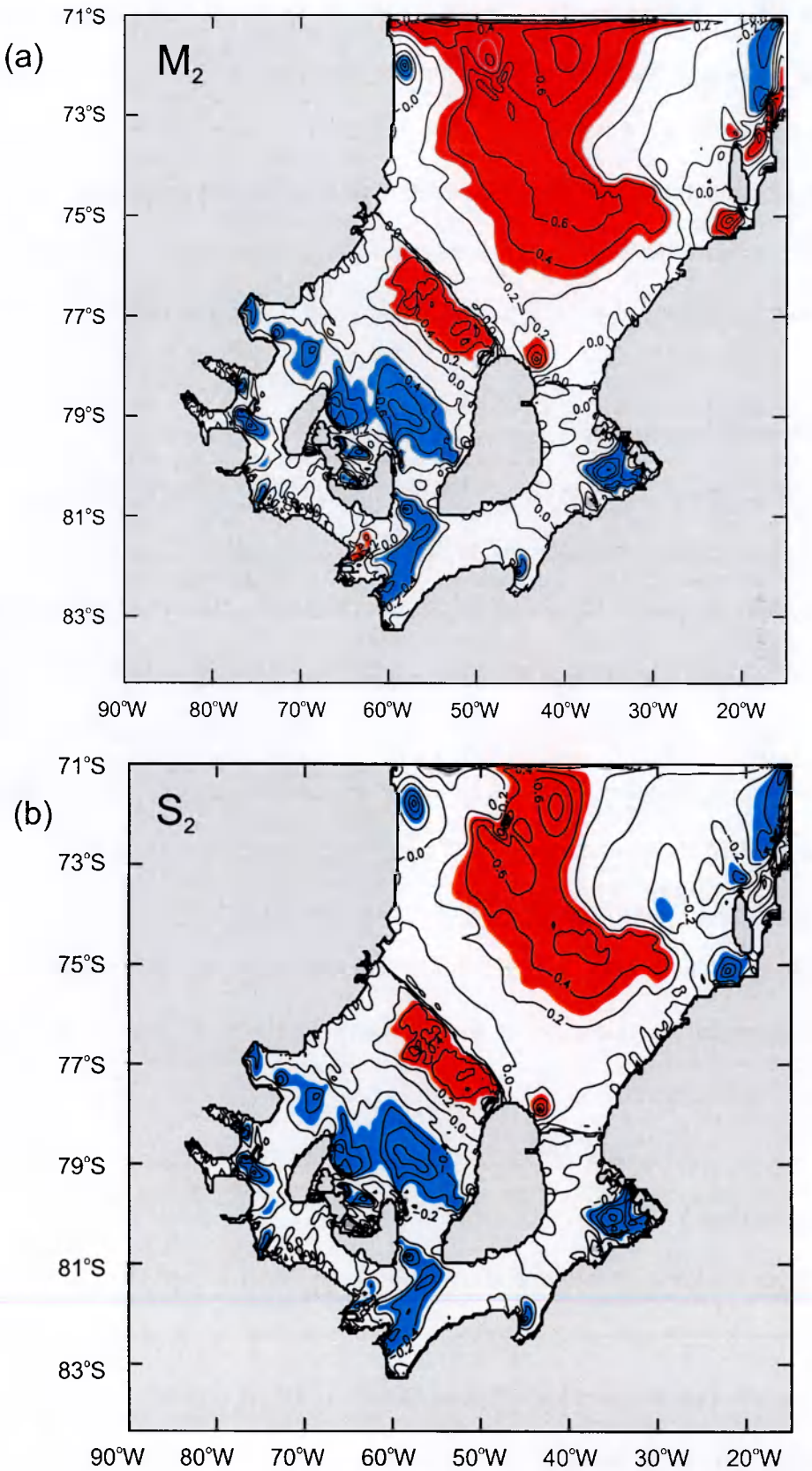

Figure 7.3 **(a)** The M_2 and **(b)** the S_2 tidal current ellipse polarisation of the depth-averaged velocity for the southern Weddell Sea. The contours have a 0.2 spacing. The blue shading shows regions of strong clockwise rotation ($P < -0.3$), the red shading shows regions of strong anticlockwise rotation ($P > 0.3$).

approached. At this latitude the tidal frequency equals the Coriolis or inertial frequency, $\omega = |f| = 2\,\Omega \sin \varphi_{crit}$, where the earth's angular velocity $\Omega = 7.2921151 \times 10^{-5}$ rad s^{-1}. *Furevik and Foldvik* [1996] showed that the benthic boundary layer thickens as the M_2 critical latitude is approached (Figure 7.4a). A thicker boundary layer produces less intense shear near boundaries but extends the shear over a larger thickness of the water column (Figure 7.4b), and enhanced vertical mixing is therefore likely near the critical latitude.

7.1.2.2 Southern Hemisphere

At high southern latitudes, the boundary layer for the R_+ component is much larger than for the R_- component for semi-diurnal tides. In the southern Weddell Sea, the northwest corner of FRIS lies near the critical latitude of the M_2 tidal constituent at 74° 28' 18"S, while the southernmost areas of the ice shelf are closest to the S_2 critical latitude at 85°45'54"S. In the shallow regions close to Ronne Ice Front, south of Henry Ice Rise and along grounding lines, the combined effects of strong tidal currents and the proximity of the critical latitude will further thicken the boundary layers. This produces extensive areas over which the boundary layers may occupy the entire water column, and here, the free stream region of the tidal current will be absent. At high latitudes the diurnal tides do not exhibit these large differences between the thickness of the boundary layers of R_+ and R_- as, for these frequencies; $|f|$ is almost twice as large as ω.

7.1.3 Stratification

Boundary layer thickness is further complicated by the stratifying effect of any buoyancy input. The only source of buoyancy beneath FRIS is the net production of an estimated 1500-3000 m^3 s^{-1} of melt water [*Nicholls and Makinson*, 1998], which is critical for driving the circulation over large areas of the region and has important implications for water column structure. Buoyancy effects caused by freezing or melting under sea ice have been found to play an important role in modifying turbulent processes [*Shirasawa and Ingram*,

1991]. During melting the water column becomes stratified while the tidal forcing remains unchanged. The effect of stratification is to suppress turbulence, inhibiting the transfer of momentum and reducing the eddy viscosity, hence reducing the boundary layer thickness from the homogenous case [*Souza and Simpson*, 1996]. Further modification of the vertical tidal current structure occurs in the vicinity of the pycnocline, which becomes decoupled from the mixed layers at the seabed and ice base [*Prinsenberg and Bennett*, 1989]. Figure 7.5 (from *Prinsenberg and Bennett* [1989]) shows M_2 current profiles beneath sea ice close to the Northern Hemisphere critical latitude. R_- has large boundary layers, with the maximum amplitude coinciding with the pycnocline, while R_+ is almost constant with depth outside the immediate vicinity of the boundaries. Furthermore, near the critical latitude, the influence of eddy viscosity on the vertical tidal current profiles is significant [*Nøst*, 1994]: a small change results in a large variation in the anticlockwise component in the Southern Hemisphere, while the clockwise component remains unaffected.

Effects of tides are usually ignored within sub-ice shelf circulation models. For FRIS, this means that the estimated 25 GW of tidal energy dissipation associated with surface friction are also ignored (Chapter 4) [*Robertson et al.*, 1998]. Vertical mixing resulting from tidal currents has been parameterized only as a function of average water column speeds derived from two-dimensional barotropic tidal models [*MacAyeal*, 1984a] (Chapter 4). This parameterization is poor for high latitude regions dominated by semi-diurnal tides with a wide range of tidal current ellipse polarizations.

7.2 Model results for sub-ice shelf mooring sites

7.2.1 Model configuration

In this section, the one-dimensional mixing model simulations used a water column with 61 levels according to (6.31). The initial water column temperature and salinity are taken from the mean CTD observations at each site, along with the ice shelf draft and water

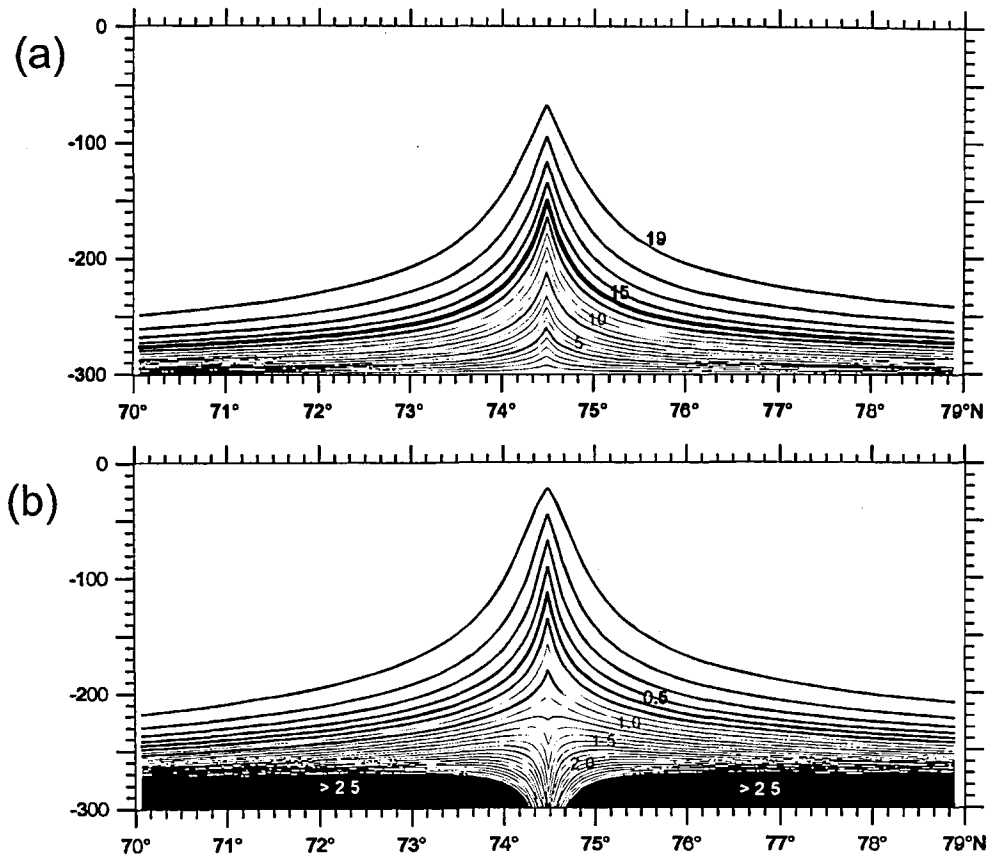

Figure 7.4 Taken from *Furevik and Foldvik* [1996]. Contours for the clockwise component of M_2 tide against depth from 70°N to 79°N in the northern hemisphere and analogous to the anticlockwise component in the southern hemisphere. **(a)** Amplitude of R_- (free stream amplitude of 20 cm s^{-1}) and **(b)** vertical shear (x 10^{-3} s^{-1}).

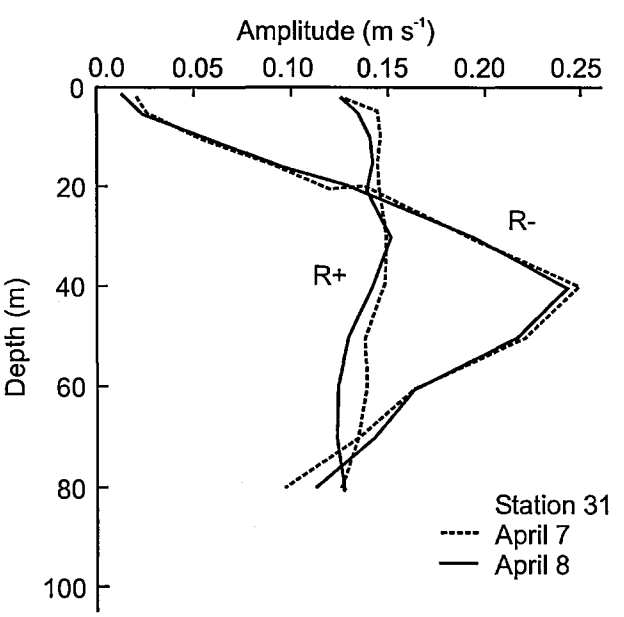

Figure 7.5 Taken from *Prinsenberg and Bennett* [1989]. Two daily mean depth profiles of M_2 rotary components' amplitudes for Station 31 in Resolute Passage, arctic Canada. Station 31 was located on sea ice within a few kilometres of the M_2 critical latitude and shows both the bottom and under-ice boundary layers. The amplitude of R_- reaches a maximum near the bottom of the pycnocline while the R_+ component is nearly constant with depth. The total water column depth was almost 100 m.

column thickness. A snow surface temperature of -27°C for FRIS is assumed [*Morris and Vaughan*, 1994]. The mixing model forcing is used to simulate the observed tidal currents and/or the mean flow. The forcing is ramped up over approximately 16 M_2 tidal cycles and the model allowed to stabilise before mixing and melting are enabled.

7.2.2 Site 3

To determine the basal melt rate at Site 3 (S3 in Figure 4.3), measurements of water temperature, salinity and flow speed are needed adjacent to the ice shelf base. From CTD observations at Site 3 (Figure 7.6), the in situ temperature close to the ice shelf base was found to vary between 0.04 and 0.05°C above the freezing point. However, current data was only available from an instrument located 396 m below the ice shelf base in the 150-m lower mixed layer. This current meter showed a weak southerly flow (0.027-0.047 m s^{-1}) associated with the inflow of WSW into the ice shelf cavity. Assuming that the mean tidal velocity (0.072 m s^{-1}) given by the lower current meter dominates the mean flow close to

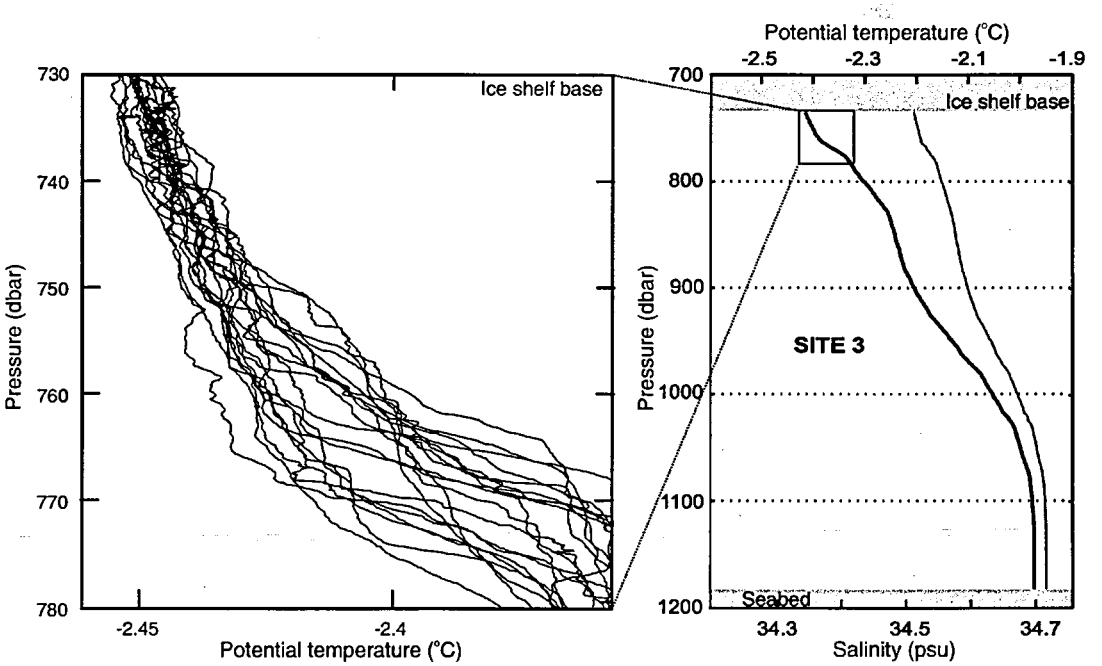

Figure 7.6 A detailed plot of the observed potential temperature in the upper 50 m of the water column at Site 3 and a plot of the mean potential temperature and salinity for the whole water column. The upper 20 m constitutes the mixed layer adjacent to the ice shelf base. The temperature variability during the observations and the temperature increase over the mixed layer are both approximately 0.01 °C.

the ice shelf base, a melt rate of 0.37 m a^{-1} is calculated using (6.24) [*Nicholls and Makinson*, 1998].

An alternative method of determining the basal melt rate is to use the temperature data from a thermistor located at the ice shelf base and the current meter data. As a result of water pressure changing the absolute calibrations of thermistors (typically ± 0.01°C), it was assumed that over the two-year record the temperature always remained at or above the in situ freezing point once the thermistors had stabilised, with the salinity remaining at 34.5 psu. Hence, a time series of basal melting (Figure 7.7a) was generated using (6.24) with the highest melt rates occurring during spring tides and seasonal minima coinciding with the peak inflow of modified WSW. Over the two-year period the integrated melt rate, based on the above assumptions, averages about 0.30 m a^{-1} (Figure 7.7b) similar to the melt rate calculated by *Nicholls and Makinson* [1998] for the period of the CTD profiling.

Using the vertical mixing model forced with 15 tidal constituents the equilibrium melt rate was below 0.01 m a^{-1}. With the inclusion of the internal wave and shear instability parameterization this increases to 0.02-0.03 m a^{-1}, but this is still an order of magnitude lower than the observed melt rates. However, warm core eddies associated with the inflow of WSW have been identified at Site 3 [*Siddall et al.*, inprep.]. These eddies extend up to the ice shelf base and pass through the site at intervals of between 5 and 11 days. They have radii of order 3 km and raise the temperatures near the ice shelf base by approximately 0.06°C [*Siddall et al.*, inprep.]. To assess the impact of warm core eddies on melting at Site 3, a synthesised basal melt time series was generated from (6.24) using a current record compiled from all the significant tidal constituents (~30) and the uppermost thermistor data. By subtracting the synthesised melt from the melt shown in Figure 7.7, the basal melting events associated with warm core eddies are resolved. The most significant melting occurs during spring tides when melt rates can reach 1.5-2.7 m a^{-1} (Figure 7.7a). By integrating

these events, the contribution of warm core eddies to the basal melt rate at Site 3 was found to be about 0.01 m a^{-1}. Clearly, the melt rate of 0.3-0.4 m a^{-1} at Site 3 cannot be attributed to the local vertical heat flux resulting from tidal currents, internal waves or warm core eddies. Advection as part of the larger scale circulation must be the primary reason for the higher melt rates.

By considering the thermistor cable and current meter data, the influence of tidal currents on the mixed layer can be seen over the spring-neap cycle. Because of temperature effects on the cable and data logger, errors arose in the thermistor calibrations of between 0.005 and 0.05°C. It was assumed that during the seasonal minima in melting, the mixed layer included all the thermistors and was at the freezing point at the ice shelf base. Taking the temperature difference between the thermistor at the ice shelf base and the other thermistors at 3, 6, 11, and 21 m below the base gives an indication of the mixed layer depth and stratification. To remove diurnal and semi-diurnal signals, a 48-hour low pass filter was applied to both the current speed and thermistor data. Figure 7.8 shows that when the mean tidal current speed is high (springs), the temperature difference across the upper 21 m of the water column is generally between 0.01 and 0.04°C. Conversely, when the speed is low (neaps) the temperature difference increases to between 0.05 and 0.07°C. During spring tides there is more vertical mixing, the mixed layer deepens, the temperature increases at the upper thermistor and decreases slightly at the deepest thermistor. During neap tides with reduced vertical mixing, the temperature changes are reversed and the stratification increases. Applying the vertical mixing model and imposing a melt rate of 0.35 m a^{-1}, the model correlates well with the thermistor data for the upper mixed layer thickness over the spring-neap cycle. However, the modelled temperature variability at the ice shelf base is an order of magnitude smaller and is most likely a consequence of non-local effects, that is, larger scale circulation.

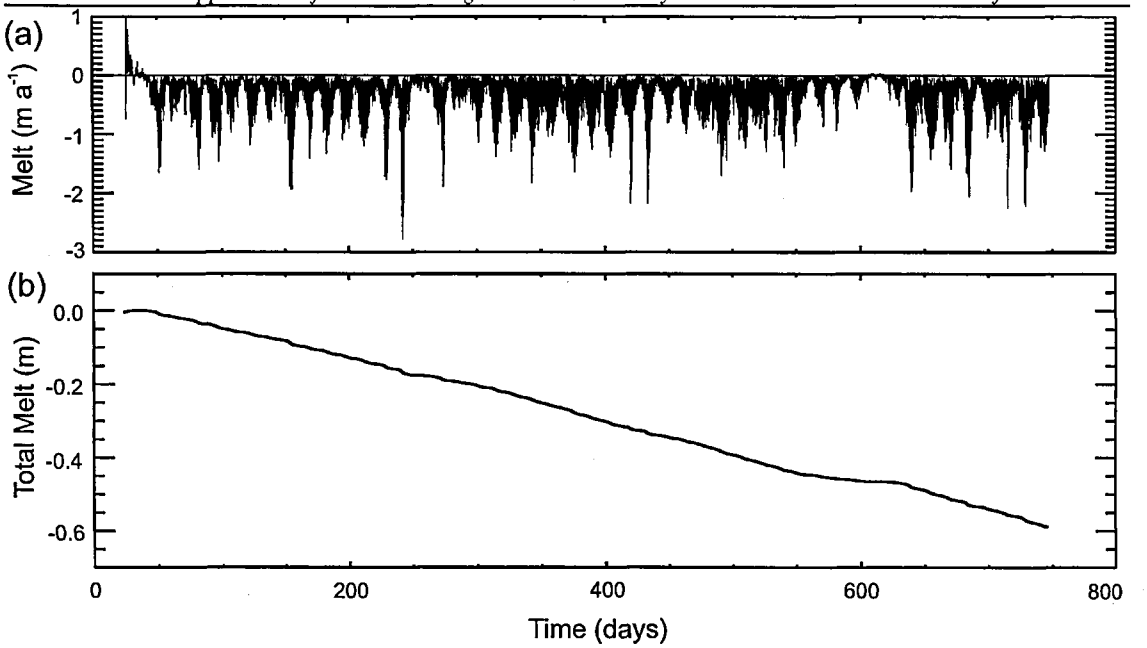

Figure 7.7 (a) Hourly melt rate at Site 3 over a two-year period beginning January 1996. Higher melt rates occurring during spring tides, with peak melt events associated with warm core eddies passing through the site during spring tides. **(b)** Cumulative total melt over the two year record with an annual melt rate of just over 0.3 m a^{-1}.

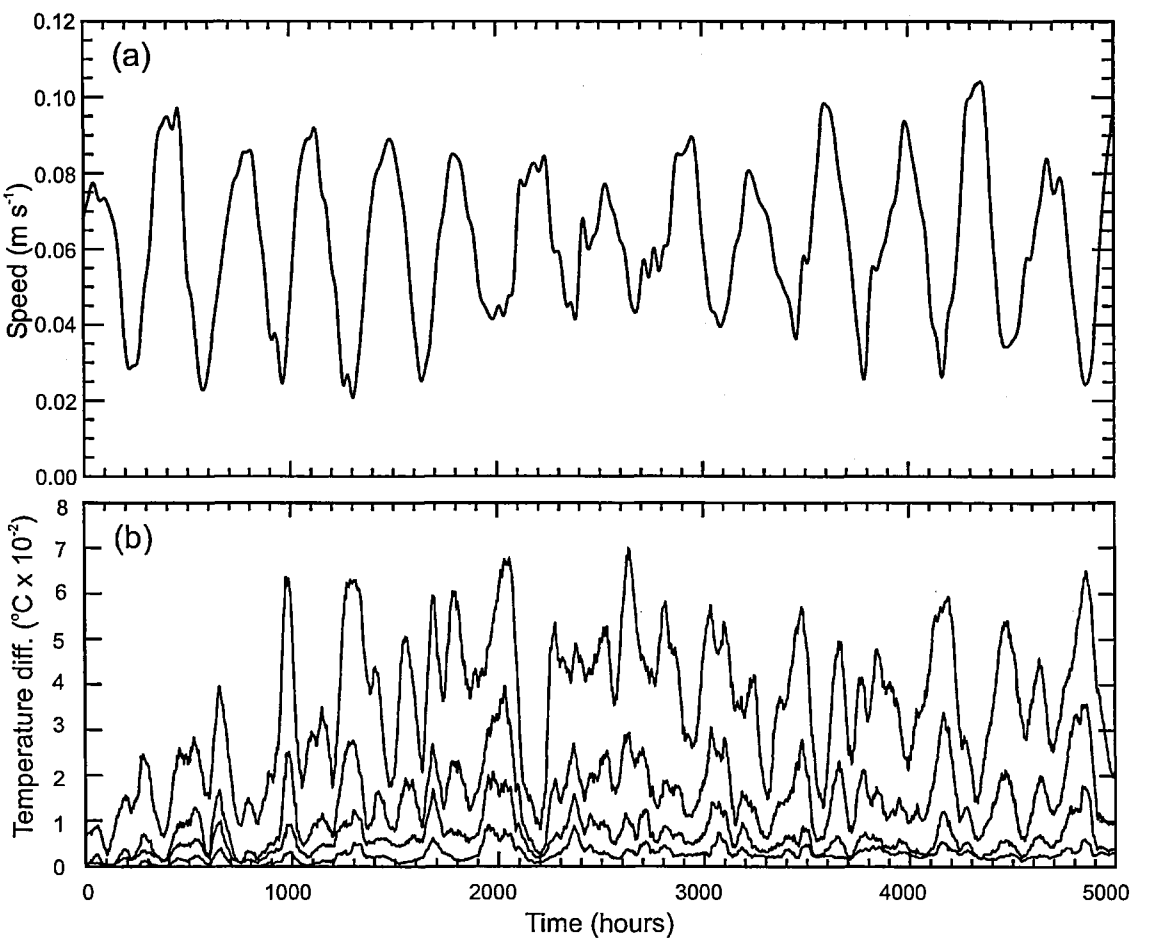

Figure 7.8 (a) Site 3 current speed record, smoothed with a 48-hour low pass filter over a seven month period. The peak speeds occur at spring tides with the weakest currents at neap tides. **(b)** Plot of the smoothed temperature difference between the thermistor located at the ice shelf base and thermistors 3 m, 6 m, 11 m and 21 m below the ice shelf base.

7.2.3 Site 4

At Site 4 (S4 in Figure 4.3) the mean flow of 0.15 m s^{-1} is about double the mean tidal currents. During the CTD measurements the water adjacent to the ice shelf base was close to the in situ freezing point (within the limits of the CTD instrument of ±0.003°C) giving a summer basal melt rate of between 0 and 0.2 m a^{-1} [*Nicholls et al.*, 2001]. However, close to the ice shelf base much of the mean velocity may have been lost to vertical shear, with only the average tidal speed remaining, giving a reduced summer maximum melt rate of about 0.1 m a^{-1}. Through the winter, the temperature measured by the uppermost sensor increased by approximately 0.05°C. Assuming this temperature increase occurs at the ice shelf base during winter and applying the same velocity arguments, a melt rate of between 0.9 and 2 m a^{-1} was predicted [*Nicholls et al.*, 2001].

Applying the mixing model to the 621-m summer water column, with mean flow of 0.15 m s^{-1}, the amount of mean flow lost to vertical shear near the ice shelf base is small. At 1 m from the ice shelf base the velocity is 0.12 m s^{-1}, giving a revised calculated melt rate of up to 0.07 m a^{-1} at the time of the CTD observations and 1.0 m a^{-1} during the winter. Forcing the vertical mixing model with the 8 largest tidal constituents and allowing the water column to evolve, an equilibrium melt rate of 0.005 m a^{-1} was determined. By including the parameterization for internal waves and shear instability, the melt rate increased two fold as additional heat is brought up from the pycnocline, approximately 40 m below the ice shelf base (Figure 7.9). The influence of vertical shear associated with the boundaries does not extend more than a few tens of metres into the water column and internal wave activity appears limited to the pycnocline near the ice shelf base. Clearly, as the deepest of the three sub-ice shelf sites, the local vertical heat flux resulting from tidal activity makes only a small contribution to the basal melt rate.

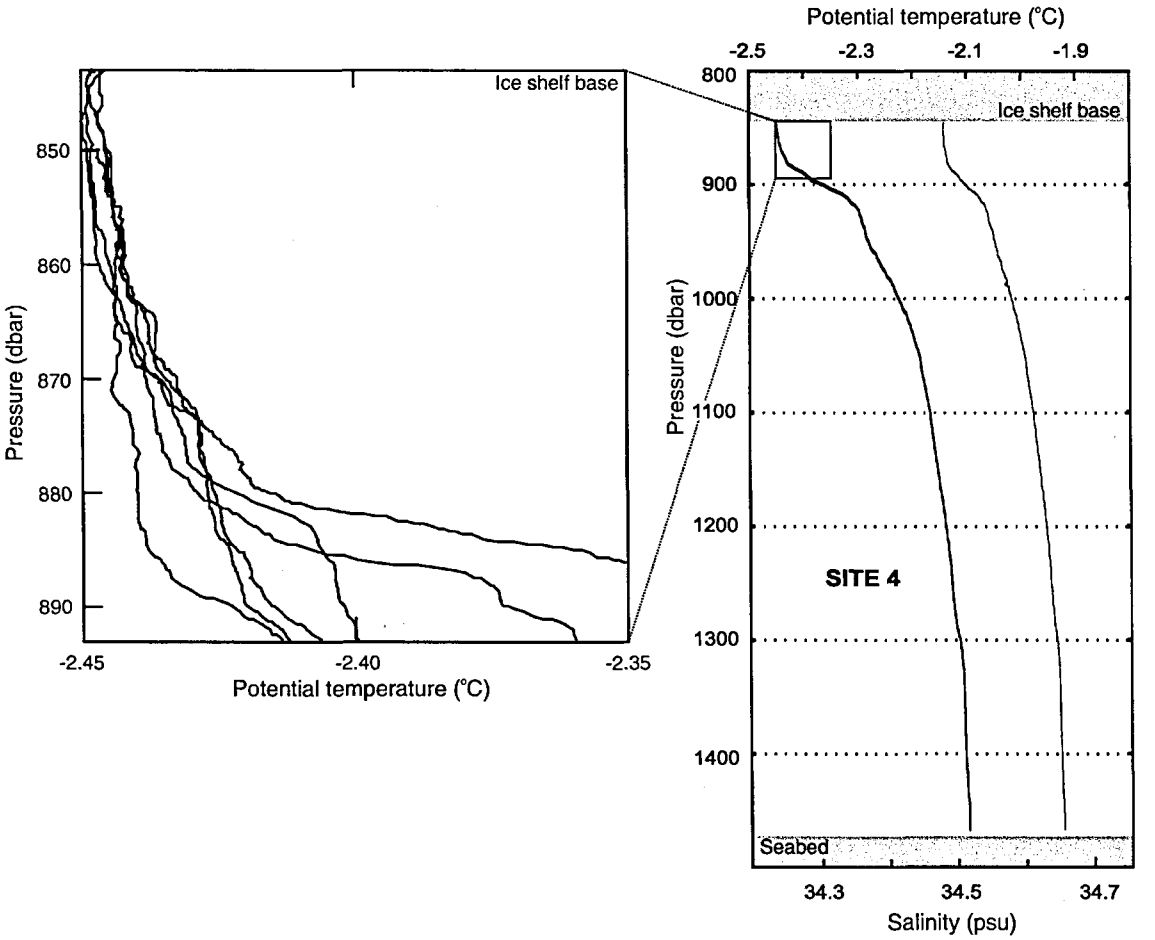

Figure 7.9 A detailed plot of the observed potential temperature in the upper 50 m of the water column at Site 4 and a plot of the mean potential temperature ans salinity for the whole water column. The upper 30 m constitutes the mixed layer adjacent to the ice shelf base. The temperature variability during the observations is approximately 0.005°C and the temperature increase over the mixed layer is approximately 0.01°C.

7.2.4 Site 5

At the time of the CTD measurements at Site 5 (S5 in Figure 4.3), the water adjacent to the ice shelf base was approximately 0.07°C above the in situ freezing point with a mean speed of 0.5 m s^{-1}, suggesting a summer melt rate of 6 m a^{-1} [*Nicholls et al.*, 2001]. As at Site 4, much of the mean velocity close to the ice shelf base may have been lost to vertical shear. With only the average tidal speed remaining, a lower melt rate of about 1 m a^{-1} is obtained [*Nicholls et al.*, 2001]. During winter the mean speed at the upper current meter decreased to 0.25 m s^{-1} and the temperature at the upper temperature sensor, which is below the warm intrusion (Figure 7.10), increased by ~0.05°C. It is however unlikely that this warming will

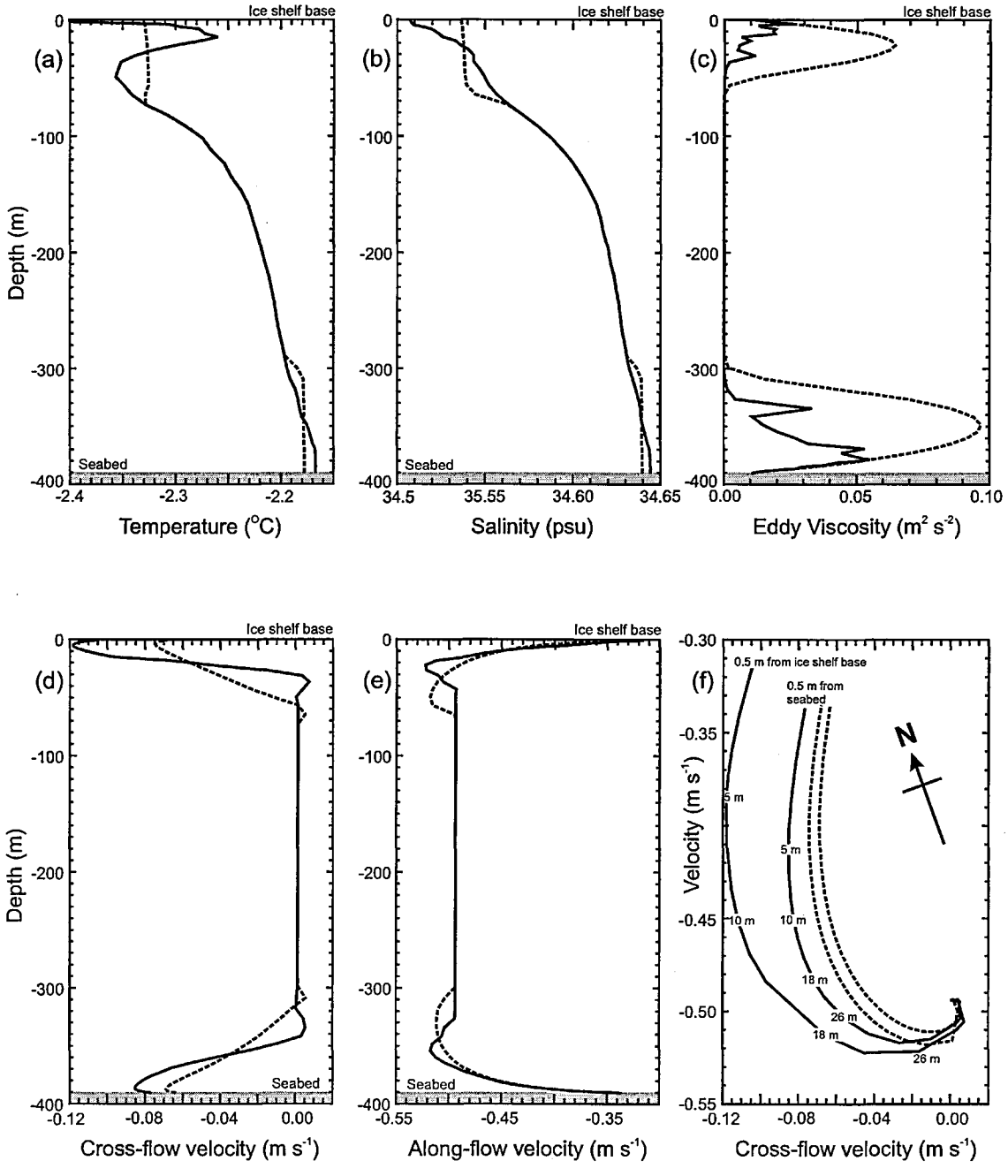

Figure 7.10 Property profiles of the water column at Site 5. The solid lines indicate the observed **(a, b)** or modelled profiles **(c-f)** at the time of the initial observations. The dashed lines indicate the modelled profiles after the water column has evolved over a period of 6 hours through mixing and melting. The observed mixed layers at the ice shelf base and seabed extend over only a few metres but rapidly develop to thicknesses of 60 m and 80 m respectively in the 0.5 m s^{-1} southerly flow as shown by the profiles of **(a)** temperature, **(b)** salinity and **(c)** eddy viscosity. The modelled current velocity profiles in **(d)** and **(e)** show an Ekman layer at both boundaries with cross-flow velocities of almost 0.12 m s^{-1} close to the ice shelf base bringing warmer water from the east, and 0.09 m s^{-1} at the seabed. A westerly flow of 0.015 m s^{-1} is required throughout the mid-water column to balance the Ekman transport close to the boundaries. **(f)** shows the along and cross-flow velocities from above, with the Ekman spirals generated at both boundaries. Also, the distance from the boundary is indicated.

occur at the ice shelf base as the intrusion is thought to be controlled by the Ekman transport of warmer water from the coast of Berkner Island [*Nicholls et al.*, 2001].

Applying the mixing model to the 402-m summer water column (Figure 7.10) and forcing a mean southerly flow of 0.5 m s^{-1}, the extent of the Ekman transport can be determined. The modelled current profiles along and across the mean flow together with their Ekman spirals are also shown in Figure 7.10. The Ekman layer at the ice shelf base occupies the upper 30 m of the water column with the highest westerly velocities (>0.1 m s^{-1}) in the top 15 m, corresponding to the position of the observed warm intrusion. In the bottom 40 m of the water column, the lower Ekman layer has a peak westerly velocity of over 0.08 m s^{-1}. To balance the flux in the two Ekman layers, an easterly flow of 0.015 m s^{-1} would be required in the mid-water column. The question of the amount of mean flow lost to vertical shear near the ice shelf base can also be evaluated. The mixing model gives a velocity of 0.35 m s^{-1} at 1 m from the ice shelf base, giving a calculated melt rate of 4.2 m a^{-1} at the time of the CTD observations. Tidal currents have been ignored in the above mixing model simulations as they are much weaker than the mean flow. However, in isolation the weak mean tidal currents (~0.07 m s^{-1}) would result in less than 0.01 m a^{-1} of basal melting, even with the inclusion of internal waves. To highlight the dynamic nature of the water column at Site 5, it was allowed to evolve through mixing and melting over a period of 6 hours, equivalent to the water column travelling a distance of almost 11 km. Without any restoring of the water column, the upper and lower mixed layers develop rapidly to depths of 60 and 80 m, respectively (Figure 7.10).

7.3 Model results for a sub-ice shelf cavity

7.3.1 Model configuration

In this section, the mixing model simulations are for a 200-m water column beneath an ice shelf with a surface temperature of -27°C, similar to the more tidally active regions close

to Ronne Ice Front, around Korff and Henry Ice Rises and close to grounding lines. The surface forcing is ramped up over approximately 16 tidal cycles and the model allowed to stabilise. The wintertime conditions found on Berkner Shelf are used to provide the initial water column temperature and salinity of -1.9°C and 34.65 psu, and the ice shelf draft of 250 m is similar to that found along Ronne Ice Front. Although these initial oceanographic conditions and ice shelf draft represent a particular region, the temperature and salinity range is relatively small beneath FRIS (approximately -1.90 to -2.55°C and 34.48 to 34.77 psu) [*Nicholls and Makinson*, 1998; *Nicholls et al.*, 2001] and the results will provide an insight into the broad pattern of tidal mixing regimes within the sub-ice shelf cavity.

7.3.2 Tidal current profiles in a homogeneous sea

To maintain the initial homogeneous water column conditions throughout this simulation the model is thermodynamically decoupled from the ice shelf to prevent melting and subsequent stratification of the water column. However, the ice shelf base remains a second frictional surface, doubling the amount of water column occupied by boundary layers. In some regions the high water velocity or proximity to the critical latitude, or a combination of the two, will lead to the combined boundary layer thickness exceeding that of the water column. Therefore as the two boundary layers interact, the amplitude of R_+ throughout the water column is below its 'free stream' velocity. Keeping the M_2 surface forcing parameters constant (for example $U = 0.3$ m s^{-1} and $P = 0.0$) and allowing the model to stabilise, the resulting tidal currents are analysed to obtain the rotary current profiles. Figure 7.11 illustrates the retarding effect of the two interacting boundary layers on R_+ as the M_2 critical latitude is approached from the south.

Observations from the southern Weddell Sea [*Foldvik et al.*, 1990; *Foldvik et al.*, 2001] support the prediction that for semi-diurnal tides the amplitude of R_- is largely depth independent while the amplitude of R_+ is strongly depth-dependent. The net water column

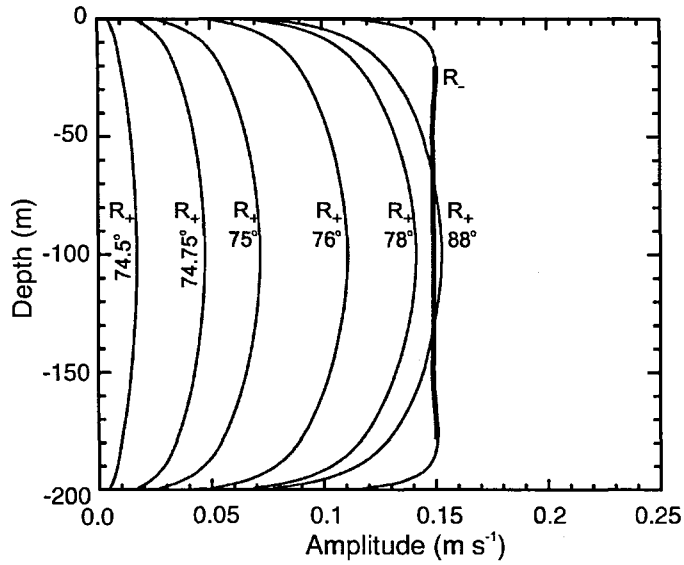

Figure 7.11 The vertical structure of the M_2 rotary components in a 200 m homogeneous water column beneath an ice shelf. The clockwise component (R_-) has small boundary layers, while the boundary layers of the anticlockwise component (R_+) occupy the whole water column. As the M_2 critical latitude at 74°28'18"S is approached from the south the anticlockwise component (R_+) of the flow is retarded while (R_-) remains unchanged. The free stream region of R_- is highlighted in bold.

velocity structure results from the addition of the two components and their associated boundary layers. The tidal current ellipse polarization is therefore depth dependent, becoming increasingly negative towards the boundaries (Figure 7.11).

To examine the latitudinal extent of the combined effects of critical latitude and velocity on water column structure, a range of surface forcing values for U are applied at different latitudes while maintaining $P = 0.0$. The resulting M_2 amplitude of R_+ at the midpoint in the water column is shown in Figure 7.12a. Here, the greatest impact is at the critical latitude where all R_+ amplitudes are affected. The range of influence is dependent on the water velocity, with higher velocities affected the most because of their larger boundary layers. It follows that shallower water would also extend the latitudinal range of influence. By reducing the water column thickness to 100 m and maintaining the same forcing, the dashed line in Figure 7.12a shows the greater latitudinal range over which the two boundary layers occupy the entire water column and retard the flow. Conversely, in deeper water the

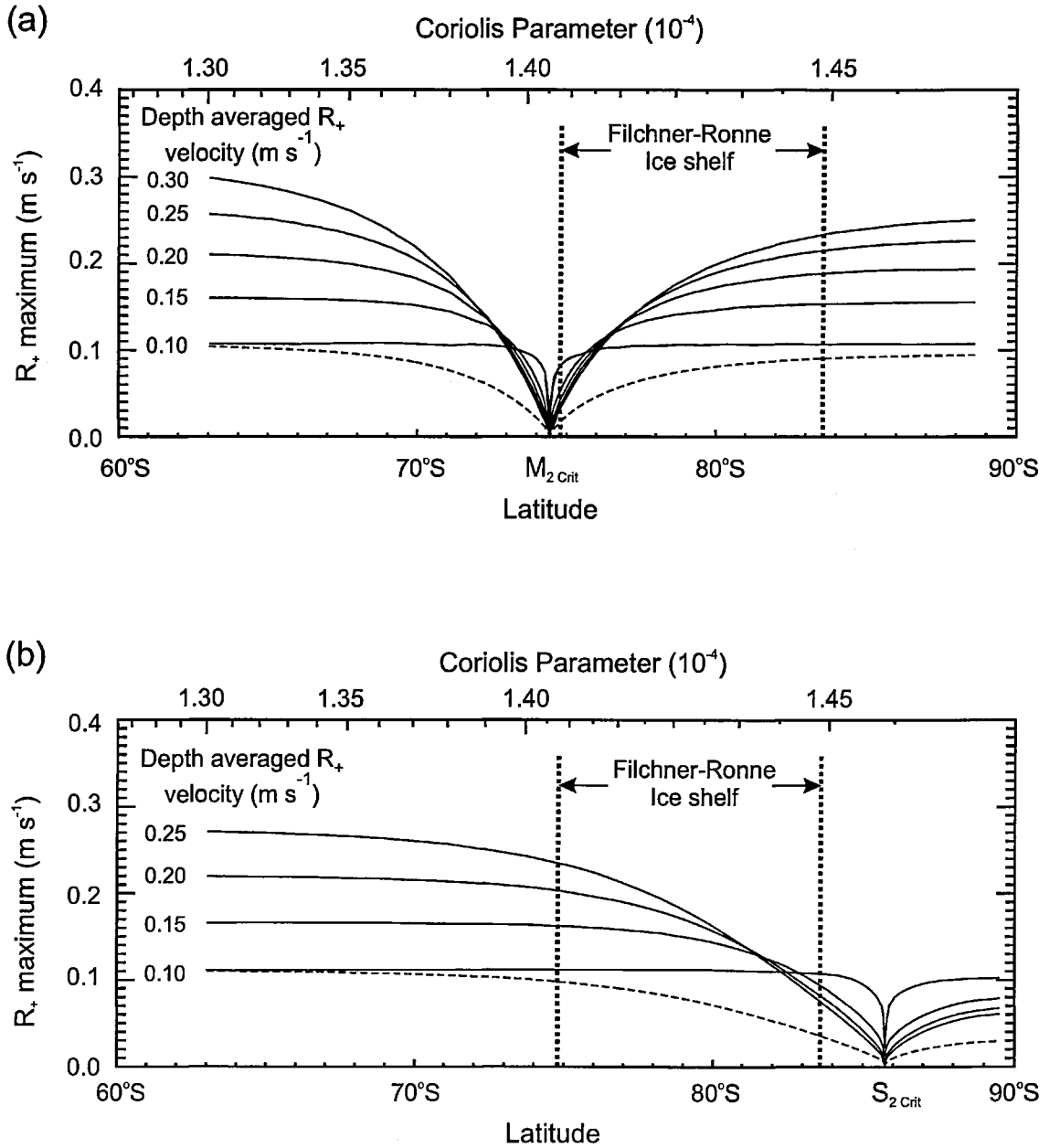

Figure 7.12 The amplitude of **(a)** the M_2 and **(b)** the S_2 anticlockwise component (R_+) at the mid-water column along a transect spanning the critical latitude. Several free stream amplitudes were used to illustrate the combined effect of critical latitude and water velocity in the 200 m homogeneous water column. The dashed line represents R_+ in a 100 m water column. The region where the two boundary layers interact and retard the flow is greatest at highest velocities or in shallower water. The position of FRIS lies between the dotted lines and the asymmetry in the plots results from the non-linear variation of the Coriolis parameter with latitude..

latitudinal range will decrease. While the northern part of FRIS lies close to the M_2 critical latitude, the southernmost areas of the ice shelf are closest to the S_2 critical latitude. The amplitude pattern of the S_2 tidal currents mirror those of M_2 beneath FRIS, though they are approximately 40% smaller (Chapter 4). Applying the model in the same way, the resulting S_2 amplitude of R_+ at the midpoint in the water column is shown in Figure 7.12b to illustrate the range of influence of the S_2 boundary layers. The remainder of the modelling will now focus on M_2 tidal currents, but the characteristics of M_2 tidal currents will also be representative of the S_2 tidal currents.

7.3.3 Tidal current profiles in a stratified sea

To simulate the effects of stratification the model is thermodynamically coupled to the ice shelf allowing melting to take place. The model is initially allowed to stabilise over 80 M_2 tidal cycles using an unstratified water column and constant surface forcing parameters ($U = 0.3$ m s^{-1} and $P = 0.0$). Over a further 200 cycles (about 103 days) melting is enabled and a pycnocline is quickly established in the upper half of the water column. To represent a well mixed inflowing water mass, the deepest 20 m of the water column is held at its initial temperature and salinity conditions throughout the model run. However, vertical mixing creates a lower mixed layer that extends through most of the lower 100 m. As the water column structure is modified by melting and mixing the development of the tidal current structure beneath the ice shelf is shown in Figure 7.13. Here the reference latitude is 75°S but other latitudes close to the critical latitude would give a similar pattern of results. Initially the two R_+ boundary layers occupy the entire water column and the flow associated with the R_+ component is retarded below its free stream velocity. As melting progresses the water column stratifies and the maximum R_+ velocity tracks the deepening pycnocline. In this example, R_+ shows a two to three fold increase over the non-stratified case as it attains its free stream velocity in the vicinity of the pycnocline, though farther away from the critical latitude this increase would be smaller. The final M_2 tidal current

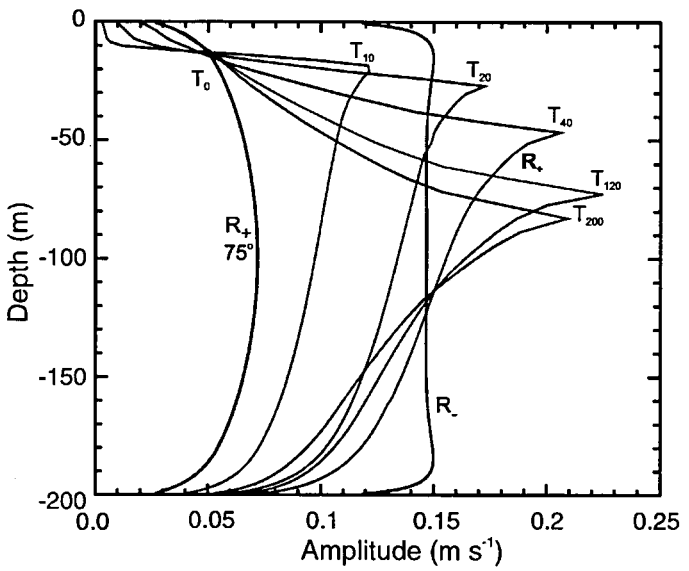

Figure 7.13 The vertical structure of the M_2 rotary components beneath an ice shelf during the onset of melting and development of a deepening pycnocline. In this example, T_0 represents R_+ at 75°S before melting is initiated and T_{10} through to T_{200} indicate the number of tidal cycles over which melting has taken place. Initially the flow is retarded, but attains its free stream velocity in the part of the water column association with the pycnocline. After 200 tidal cycles there is no significant change in R_+ or the depth of the pycnocline.

structure in Figure 7.13 is almost identical to the observations beneath fast-ice in the Canadian Arctic (Figure 7.5), confirming that the M_2 tidal current close to the critical latitude reaches a maximum at the depth of the pycnocline [*Prinsenberg and Bennett*, 1989].

The effect of the stratification on R_+ depends both on the strength of the building pycnocline and on the initial level of retardation compared with the free stream velocity. These effects increase for increasing free stream velocities and as the critical latitude is approached (Figure 7.13). In areas subject to changes in stratification, either on daily, spring-neap or seasonal time scales, the R_+ component can exhibit substantial fluctuations in amplitude. Similar conditions arise in the North Sea where the bottom boundary layer outcrops at the surface: observations show significant differences in the vertical tidal current structure between the well mixed winter conditions, where the flow remains retarded, and stratified

summer conditions where the flow attains its free stream value above the pycnocline [*Howarth*, 1998]. *Simpson and Souza* [1995] found similar changes in tidal current structure on a semi-diurnal time scale near the Dutch coast in the freshwater region of the Rhine outflow.

7.3.4 Southern Weddell Sea current profiles

Lying between the M_2 and S_2 critical latitudes, current meters close to FRIS should show the impacts of critical latitude and changes in stratification. To show these impacts, a harmonic analysis was applied to the initial 662-hour section of a current meter record to separate six tidal constituents (Q_1, O_1, K_1, N_2, M_2, and S_2). The analysis was repeated by moving the 662-hour window forward in steps of 24 hours until the end of the record was reached. A time series of the amplitudes of R_+ and R_- was then generated for each constituent. Beneath the ice shelf however, the combination of small changes in stratification, deep water column, weak tidal currents and large distance from the critical latitudes result in no significant changes in R_+ for semi-diurnal tidal currents.

Elsewhere in the southern Weddell Sea and closer to the M_2 critical latitude, current meters situated offshore of Ronne Ice Front show the impacts of critical latitude and changes in stratification. The moorings (FR6, FR5, R2 and FR3) were deployed within 5 to 10 km of the ice front and their positions are shown in Figure 4.3. Most of the records are more than two years in length [*Woodgate et al.*, 1998; *Foldvik et al.*, 2001]. Closest to the M_2 critical latitude is FR6, 26 km to the south and close to the northern most part of Ronne Ice Shelf. Figure 7.14 shows the amplitudes of both rotary components for M_2, and of R_+ for constituents S_2 and N_2 at a depth of 442 m. Temperature data from the mooring was also smoothed over a 662-hour period to show the corresponding changes in temperature. During winter, the formation of WSW results in a mixed water column and in summer the water column is stratified because of outflowing ISW. Because of the proximity of the M_2

critical latitude and the changes in stratification, the amplitude of R_+ (M_2) exhibits a two-fold increase during summer months. Despite the remoteness of the other semi-diurnal critical latitudes the changes in stratification during the summer also result in small increases in the amplitudes of R_+ (S_2) and R_+ (N_2). It should be noted that in this analysis, K_2 is not seperated from S_2 and there is an underlying six month signal with an amplitude of 0.013 m s^{-1} remaining even in R_- (S_2). Nevertheless, a significantly stronger signal associated with summer stratification is visible within R_+ (S_2).

Two other current meter records at FR6 have also been analysed to provide a profile of the two M_2 rotary tidal current components (Figure 7.15). During wintertime, the R_+ boundary layer appears to occupy the entire water column because of the nearby critical latitude, with R_- having an almost uniform profile. However, through summer and despite FR6 being offshore, the lower portion of the R_+ profile is similar to modelled (Figure 7.13) and observed (Figure 7.5) current profiles found beneath fixed ice cover. Clearly, during summer stratification the presence of the ice shelf base influences currents several kilometres offshore with the amplitude of R_+ decreasing in the mid-water column because of friction from the ice shelf base, while R_- remains unaffected.

Applying the same method of analysis to the other ice front moorings farther from the M_2 critical latitude, possible profiles of R_+ and R_- for M_2 are shown in Figure 7.16. FR5 was located on the eastern side of Ronne Depression with a pattern of stratification equivalent to that at FR6 [*Woodgate et al.*, 1998]. For a stratified water column the tidal current profile is similar to FR6, with the amplitude of R_+ decreasing towards the depth equivalent to that of the ice shelf base. In contrast to FR6, R_+ exhibits no large boundary layer in the fully mixed water column of winter, despite the close proximity of the critical latitude.

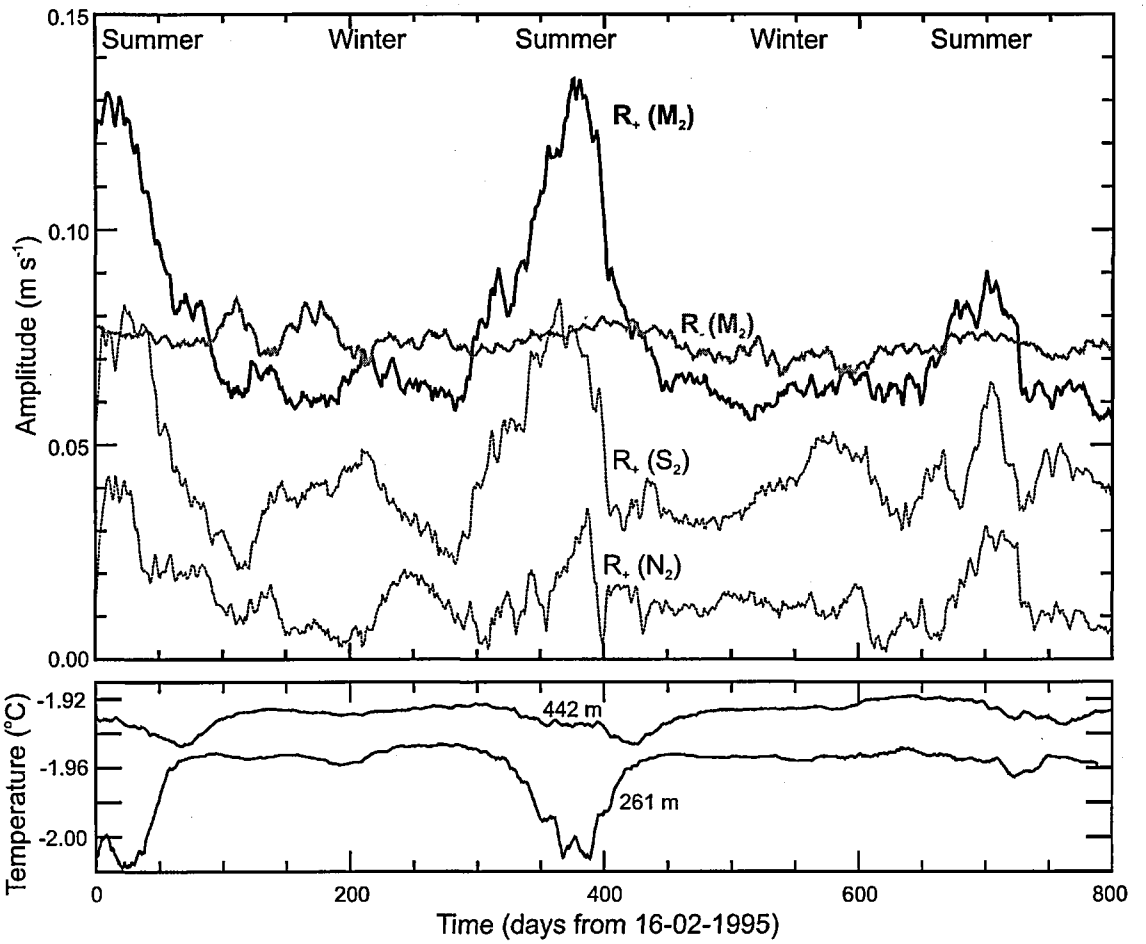

Figure 7.14 The seasonal variability of the clockwise and anticlockwise rotary tidal current components for M_2 at mooring FR6 at a depth of 442 m. The anticlockwise component of S_2 and N_2 are indicated by the dotted lines. The water temperature at 442 m and 261 m is shown in the lower panel.

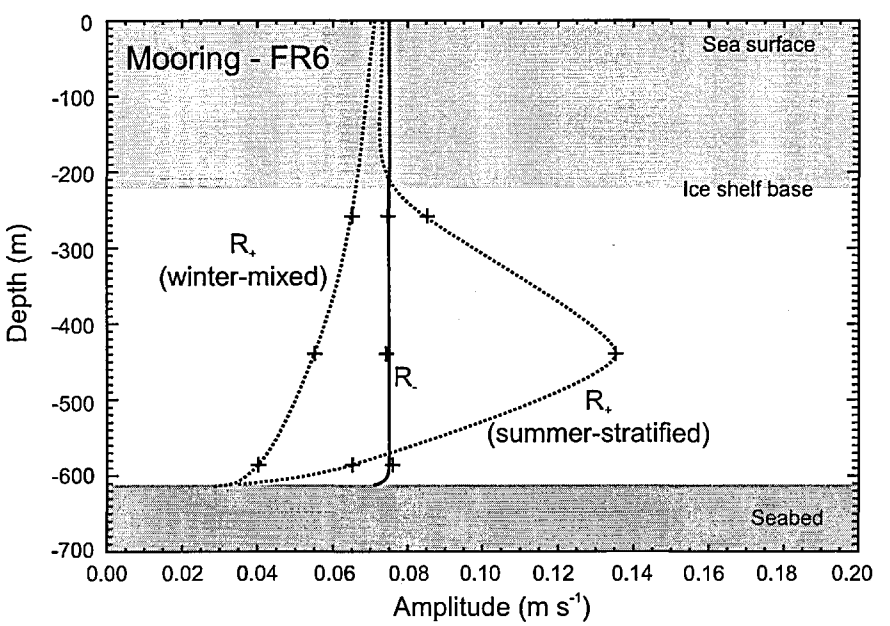

Figure 7.15 The clockwise and anticlockwise tidal current components for M_2 at mooring FR6. The portion of water column occupied by the nearby ice shelf is indicated by the light shading and the seabed is indicated with the darkest shading. The crosses are current meter measurements and the lines indicate the extrapolated vertical current profiles for a well mixed and stratified water column.

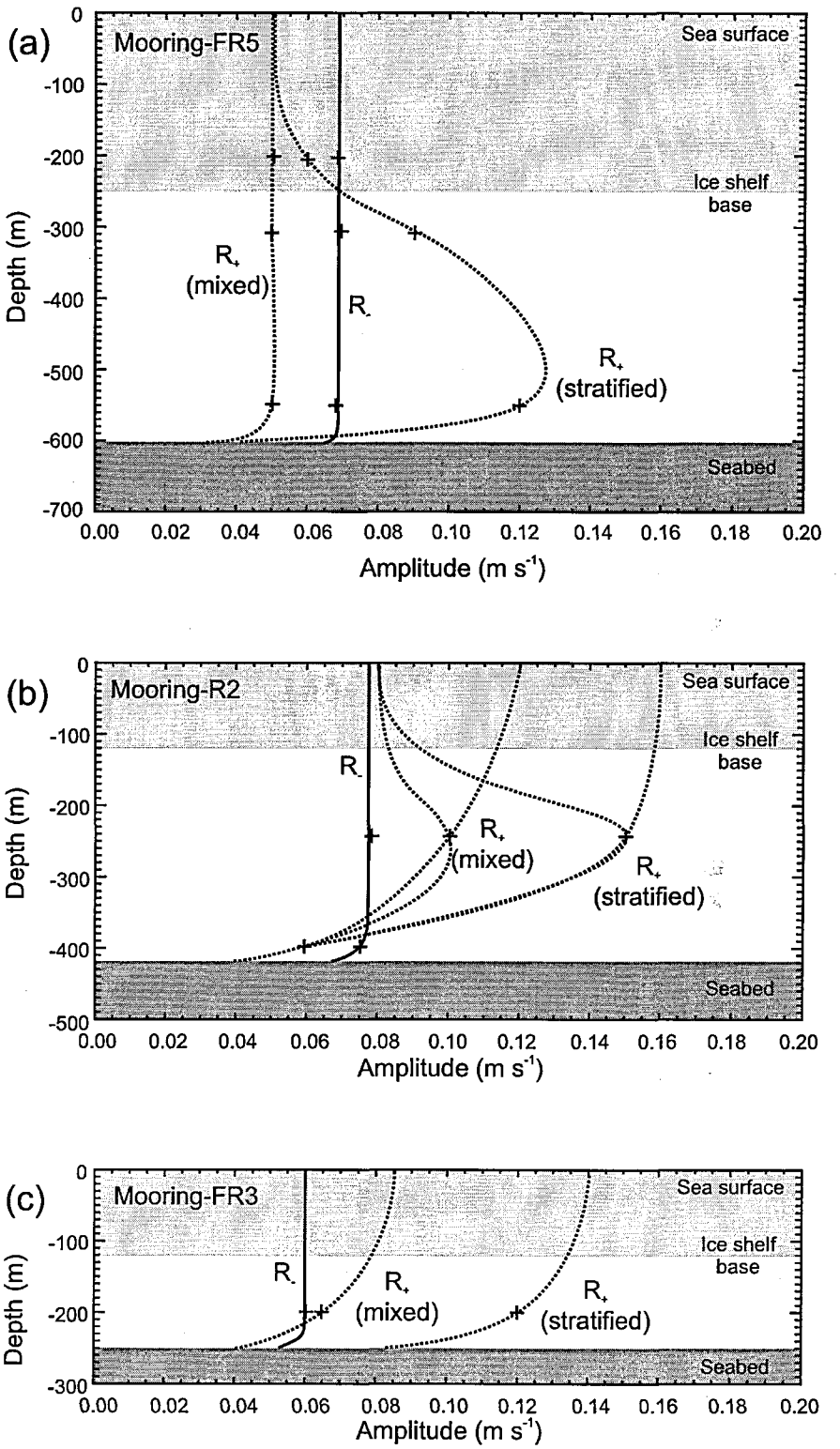

Figure 7.16 The clockwise and anticlockwise tidal current components for M_2 at **(a)** mooring FR5, **(b)** mooring R2 and **(c)** mooring FR3. The portion of water column occupied by the nearby ice shelf is indicated by the light shading and the seabed is indicated with the darkest shading. The crosses are current meter measurements and the lines indicate possible vertical current profiles for a well mixed and stratified water column.

Located midway along Ronne Ice Front, R2 is clearly influenced by the effects of critical latitude and stratification [*Foldvik et al.*, 2001]. During late winter and early spring the water column is well mixed as the temperature at both levels is close to the surface freezing point. An intrusion of MWDW in the mid-water column [*Foldvik et al.*, 2001] results in the summer stratification. Without a current meter at a depth equivalent to the nearby ice shelf base, it is not possible to determine if the profile of the R_+ amplitude in Figure 7.16b decreases as at FR5 and FR6 or increases towards the surface.

Of the four ice front moorings, FR3 is farthest from the M_2 critical latitude (2.5° or 280 km to the south). As at the other mooring sites the water column is at the surface freezing point in winter with ISW providing the stratification in the late summer/autumn [*Woodgate et al.*, 1998]. R_+ is still strongly influenced by the critical latitude and changes in stratification with the amplitude of R_+ doubling during summer while R_- remains unchanged (Figure 7.16c). With only one current meter however, it is not known whether the amplitude of R_+ is reduced higher in the water column as at FR5 and FR6.

7.3.5 Effects of ellipse polarization

The one-dimensional vertical mixing model has been used to simulate a wide range of different current amplitudes and ellipse polarizations for the M_2 tidal constituent at 79°S, the mean position of FRIS. Once the model has stabilised after 80 tidal cycles using an unstratified 200-m water column, melting is initiated. The surface forcing parameters remain unchanged while the stratification evolves over a further 120 cycles (about 62 days) with the lowest 20 m of the water column held at constant temperature and salinity throughout. The melt rates, which are initially high for all polarizations, decrease as the mixed layer next to the ice shelf base cools towards the in-situ freezing point. Tidal currents with a more positive polarization however, continue to deepen the mixed layer and pycnocline towards the middle of the water column, maintaining a strong vertical heat flux

and higher rates of melting. This dependence of vertical mixing on ellipse polarization was highlighted by *Simpson and Sharples* [1994] for northern mid-latitudes.

To illustrate the extent of mixing the melt water from the ice shelf base down through the upper half of the water column, the dependence of the pycnocline depth after 10 tidal cycles on mean polarization is plotted in Figure 7.17 for a range of tidal current strengths. After only 10 tidal cycles the vigorous mixing, associated with strong tidal currents and positive polarizations, has deepened the pycnocline almost to the middle of the water column. While the temperature and salinity within the model are fixed in the lower part of the water column, the pycnocline depth cannot exceed 100 m or half the water column thickness. Clearly there is asymmetry in the resulting thickness of the mixed layers, which is dependent on the ratio and magnitude of the two rotary currents and, therefore, on the magnitude and polarization of the tidal current ellipse. For predominantly clockwise tidal currents ($P < -0.5$) the depth of the pycnocline is constrained by the depth of the R_- boundary layer. As the polarization becomes more positive, the boundary layer of R_+

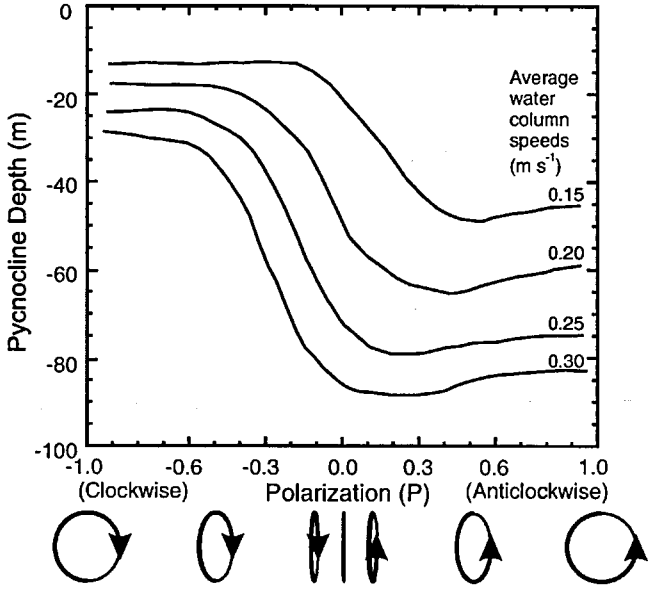

Figure 7.17 Pycnocline depth in the upper half of the water column after 10 M_2 tidal cycles at 79°S over which melting has taken place for different average water column speeds versus the mean polarisation of the M_2 tidal current ellipse.

becomes increasingly influential, producing more mixing in the mid-water column and rapidly deepening the pycnocline over the region $-0.3 < P < 0.3$. With no significant increase in mid-water column mixing as the polarization increases, there is no further deepening of the pycnocline for the predominantly anticlockwise tidal currents ($P > 0.5$).

Applying a broader range of surface forcings, the dependence after 10 tidal cycles of pycnocline depth on the resulting mean rotary components of the tidal current ellipse is contoured in Figure 7.18. Here strong tidal currents and positive polarizations result in the pycnocline depth almost reaching its maximum of 100 m, whereas negative polarizations give a much shallower pycnocline. Given sufficient time, the middle of the pycnocline would lie close to the middle of the water column for all forcings as the water column structure, vertical heat flux, and melt rate reached an equilibrium state. Assuming the water column structure is approaching equilibrium after 120 tidal cycles for all but the weakest tidal currents, the melt rate is contoured in Figure 7.19. There is a strong dependence of both the pycnocline depth and the melt rate on polarization of the tidal current ellipse, with both parameters showing a similar pattern. For both parameters, the deepest pycnocline and highest melt rates are associated with the more positive polarizations. The greatest changes in melt rate occur over the range $-1.0 < P < 0.2$, as the R_+ boundary layers introduce increasing levels of mixing into the mid-water column, bringing warmer water up to the ice shelf base. Beyond this polarization range the longer term melt rate shows a slight decrease for given average water speeds. This decrease can be attributed to no significant change in the mid-water column mixing combined with a decreasing boundary velocity as the shear from R_- diminishes with increasing polarization.

7.4 Application to FRIS

The broad range of surface forcings applied to the model generate a wide range of tidal currents that are analysed to obtain the mean rotary components. Therefore, the effects of

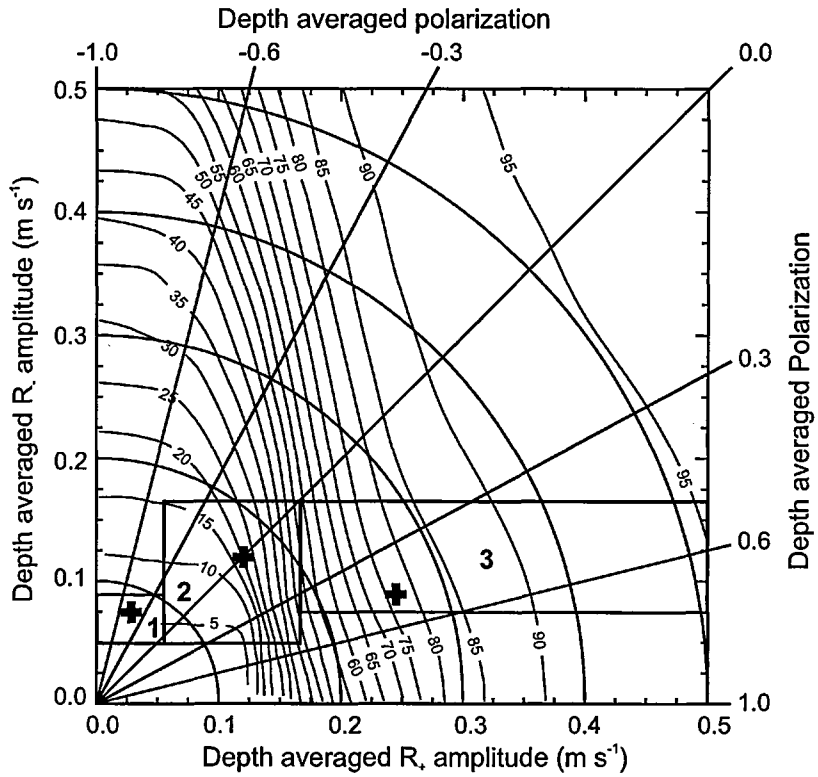

Figure 7.18 The dependence of the pycnocline depth (m) after 10 M_2 tidal cycles at 79°S on the depth averaged rotary components of the M_2 tidal current ellipse. The contours are every 5 m and the total water column thickness was 200 m. The lines radiating from the origin connect points of equal polarisation and the arcs connect points of equal mean water column speed. The boxes indicate the tidal current characteristics for : 1) eastern most part of Filchner Ice Shelf and north of Doake Ice Rumples ; 2) south of Korff and Henry Ice Rises ; and 3) Ronne Ice Front. The crosses mark the positions from which the water column property profiles in Figure 7.20 where obtained.

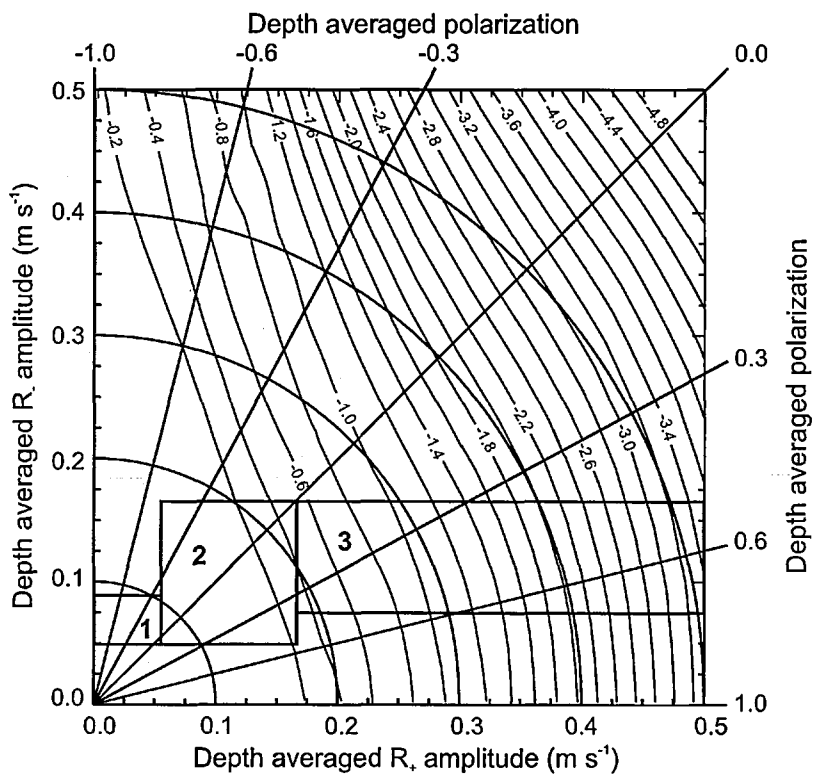

Figure 7.19 Same as for Figure 7.18 but with the dependence of the melt rate (m a^{-1}) after 120 tidal cycles on the depth averaged rotary components of the tidal current ellipse. The contours are every 0.2 m a^{-1}.

latitude on the tidal current structure will be embedded within the mean R_+ and R_- components. Since FRIS occupies a narrow band of latitudes (79°S ±4°) the dependence of pycnocline depth and melt rate on mean R_+ and R_- should vary little with position on the ice shelf. However, the influence of proximity to the critical latitude on the R_+ component results in some differences from the results for 79°S shown in Figures 7.18 and 7.19. The greatest differences of up to 20% occur for positive polarizations and speeds below 0.25 m s^{-1}, where the contribution of turbulence from R_+ dominates the vertical mixing. Here, the critical latitude strongly influences the R_+ current component (Figure 7.12a) with additional turbulence being generated from the increased shear as R_+ attains its free stream velocity around the developing pycnocline (Figure 7.13). This results in higher melt rates and slightly shallower pycnocline depths as the critical latitude is approached. For negative polarizations and higher current speeds there is little or no latitudinal influence. Consequently, the model results from 79°S are broadly representative of the range of latitudes occupied by FRIS.

Beneath the ice shelf, the modelled M_2 and S_2 tidal velocities can reach 0.5 m s^{-1} and 0.3 m s^{-1}, respectively, typically three to six times higher than for the diurnal tides. The M_2 ellipse polarization ranges from -0.95 to +0.7 (Figure 7.3a) with predominantly anticlockwise rotation associated with the shallow water close to Ronne Ice Front. In the central part of Ronne Ice Shelf and at the mouths of the ice stream and glacier inlets predominantly clockwise rotation occurs, which results from the interaction of a semi-diurnal Kelvin wave with basins or inlets of different scales [*Carbajal*, 1997].

The almost complete range of possible polarizations present beneath FRIS suggests that, in light of the model results, a wide range of vertical mixing regimes will exist. The boxes in Figures 7.18 and 7.19 broadly divide the tidal current characteristics beneath FRIS into three main regions. However, the melt rates in Figure 7.19 are not predictions of basal melt

rates beneath FRIS, only the contribution that tidal vertical mixing makes to the heat supply at the ice shelf base. Taking a representative point from each of these three tidal current regions beneath FRIS (indicated by the crosses in Figure 7.18), profiles from the model of mixing length, turbulent kinetic energy, eddy viscosity, dissipation and density change are plotted in Figure 7.20. The model was spun up and allowed to stabilise over 80 tidal cycles. The profiles are plotted at hourly intervals over the final M_2 tidal cycle prior to melting and also after a further 10 tidal cycles, with melting, to show the effects of stratification.

7.4.1 Polarization -1.0 to -0.3

Regions where $P < -0.3$ in water approximately 200 m deep are confined to a few small areas such as the easternmost part of Filchner Ice Shelf and just to north of Doake Ice Rumples. The combination of weak tidal currents and negative polarization (region 1 in Figures 7.18 and 7.19) produce low levels of TKE (Figure 7.20a). The turbulent dissipation is greatest close to the boundaries followed by an almost linear decrease on a $\log_{10}$ scale with distance away from the boundaries, characteristic of all the dissipation profiles in Figure 7.20. The effect of stratification on the water column is to suppress turbulence, inhibiting the transfer of momentum and reducing the eddy viscosity, particularly in the vicinity of the pycnocline. The pycnocline effectively separates the water column into two parts with TKE generated at the upper boundary being confined to a small upper mixed layer. This small mixed layer cools rapidly towards the in-situ freezing point, creating a large density contrast across the pycnocline. The remainder of the water column comes under the influence of the lower boundary with the pycnocline acting effectively as a free surface. Consequently, TKE and dissipation increase in the mid-water column, increasing both the eddy viscosity and mixing length over a large portion of the lower water column (Figure 7.20a).

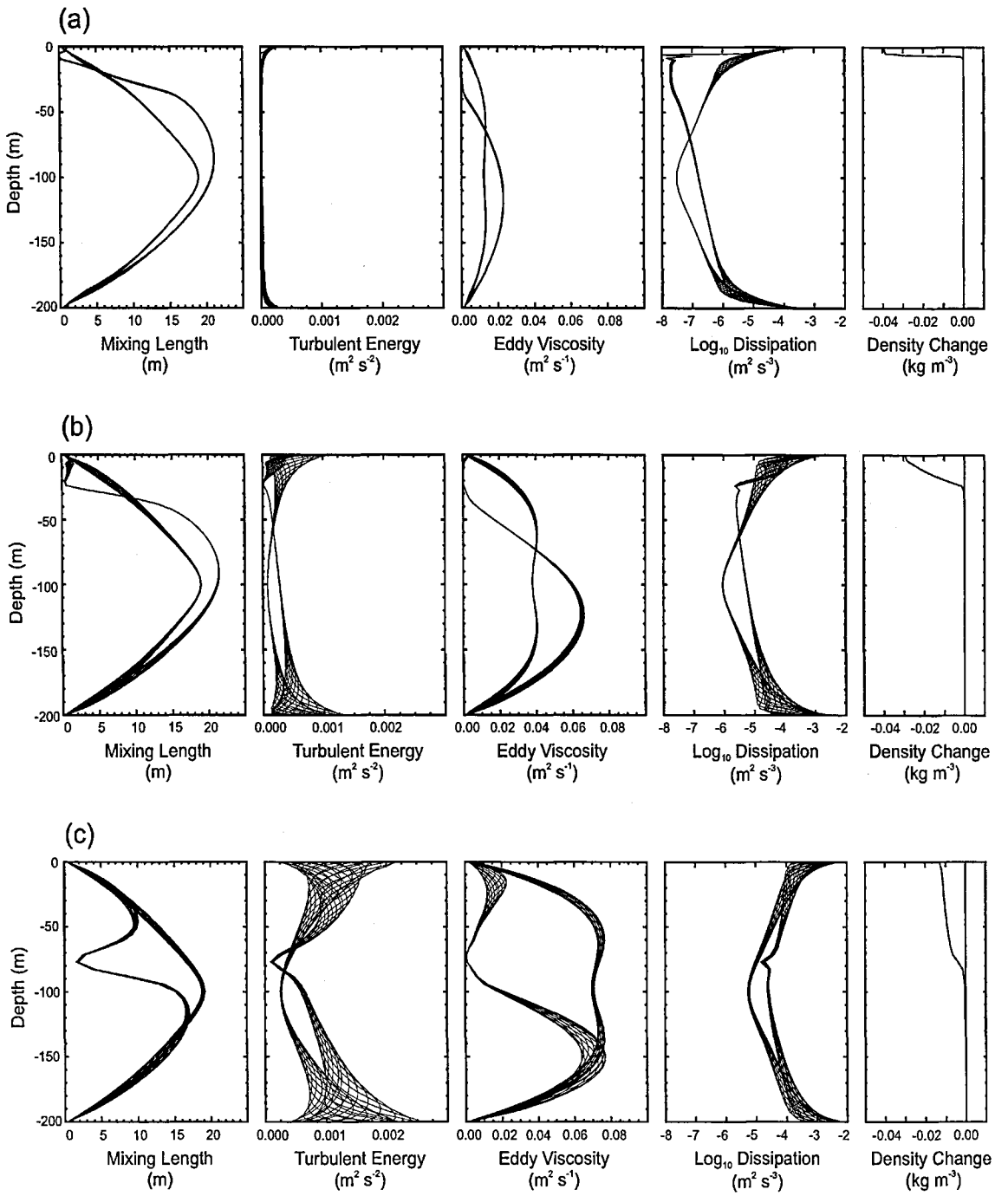

Figure 7.20 Profiles through a 200-m water column of: mixing length; turbulent kinetic energy; eddy viscosity; dissipation; and density change. The profiles are at hourly intervals over a M_2 tidal cycle for a homogeneous water column (symmetrical profiles) and after melting takes place over 10 M_2 tidal cycles (non-symmetrical profiles). The resultant stratification and pycnocline depth are shown by the change in density from the initial homogeneous conditions. The three locations are indicated by crosses in Figure 7.18 and are representative of the three regions beneath FRIS **(a)** eastern most part of Filchner Ice Shelf and north of Doake Ice Rumples (Box 1); **(b)** south of Korff and Henry Ice Rises (Box 2); and **(c)** Ronne Ice Front (Box 3).

In other regions where $P < -0.3$ such as the central Ronne Ice Shelf and mouths of ice stream inlets, the water column thickness can be up to 600 m, with low speed tidal currents compounding the effects of low polarization. Although in this polarization study the model does not cover these water thicknesses, it can be inferred that vertical mixing will be confined to the small boundary layers of R_- and the upper and lower boundary layers will be isolated from each other. In this situation, turbulence generated from tidal currents will not contribute to mid-water column mixing, and melt resulting from tidal vertical mixing will be close to zero. But where heat is available from horizontal advection in the upper mixed layer, tidal currents will enhance the basal melting.

7.4.2 Polarization -0.3 to 0.3

Most of FRIS lies between $P = \pm 0.3$, similar to the region south of Korff and Henry ice rises. This region is characterised by moderate tidal currents and a water column around 200 m thick. Its M_2 polarization and velocity range occupies region 2 in Figures 7.18 and 7.19, with representative water column properties shown in Figure 7.20b. When compared with region 1, the moderate tidal currents provide increased TKE, enhancing the eddy viscosity and leading to a deeper penetration of the pycnocline into the water column. Other water column characteristics develop in the same way as in region 1 (Figure 7.20a). The initial development and penetration into the water column of the pycnocline is sensitive to changes in polarization over this range ($P = \pm 0.3$) and the increasing polarization can lead to a three to four-fold increase in the pycnocline depth (Figure 7.17). The longer term melt rate is less sensitive where the polarization is positive, but once the polarization is below $P = 0$ the melt rate begins to decline rapidly (Figure 7.19). In areas where tidal currents are constrained to flow approximately parallel to grounding lines ($R_+ \approx R_-$), such as the Orville Coast and south of the ice rises, modification of the ellipse polarization is not possible, therefore the transverse pressure gradient must balance the Coriolis force to maintain flow

parallel to the coast. Here, there will be regions extending from grounding lines that are dominated by the interacting R_+ boundary layers and therefore exhibit high levels of mixing.

7.4.3 Polarization 0.3 to 1.0

The Ronne Ice Front region is characterised by shallow water (< 200 m), strong tidal currents, positive ellipse polarizations ($0.3 < P < 0.7$) and occupies region 3 in Figures 7.18 and 7.19. In this high current regime intense mixing takes place, with rapid deepening of the pycnocline and strong melting sustained for as long as the water column remains above the in-situ freezing point. These features are shown in Figure 7.20c, with high levels of TKE extending into the mid-water column, forming a deep pycnocline with the smallest density contrast of the three regions. This small density contrast after 10 tidal cycles is the result of the rapid mixing of melt water down into the mid-water column while maintaining a strong vertical heat flux, keeping the upper water column above the in-situ freezing point and maintaining further melting.

Extending the model time over a 100-day period, the evolution of water masses advected through the shallow Ronne Ice Front region can be followed. Conditions similar to those found in the ice front region are reproduced by three water columns of 100, 150, and 200 m with average water speeds of 0.4, 0.35 and 0.3 m s^{-1}, respectively. The initial water column is assumed to be homogeneous, with properties typical of winter offshore conditions in this region (-1.9°C, 34.65 psu). As the entire water column is advected beneath the ice shelf with a draft of 250 m, a pycnocline develops that is ultimately eroded (Figure 7.21). Initially the melt rates are high (3-5 m a^{-1}) but as the water column approaches the in situ freezing conditions, melting approaches zero (Figure 7.21d). To simulate spring tides, water speeds were doubled for six days and during this time a weak pycnocline develops in the deepest water column only (dashed lines in Figure 7.21c). Elsewhere, in shallower water,

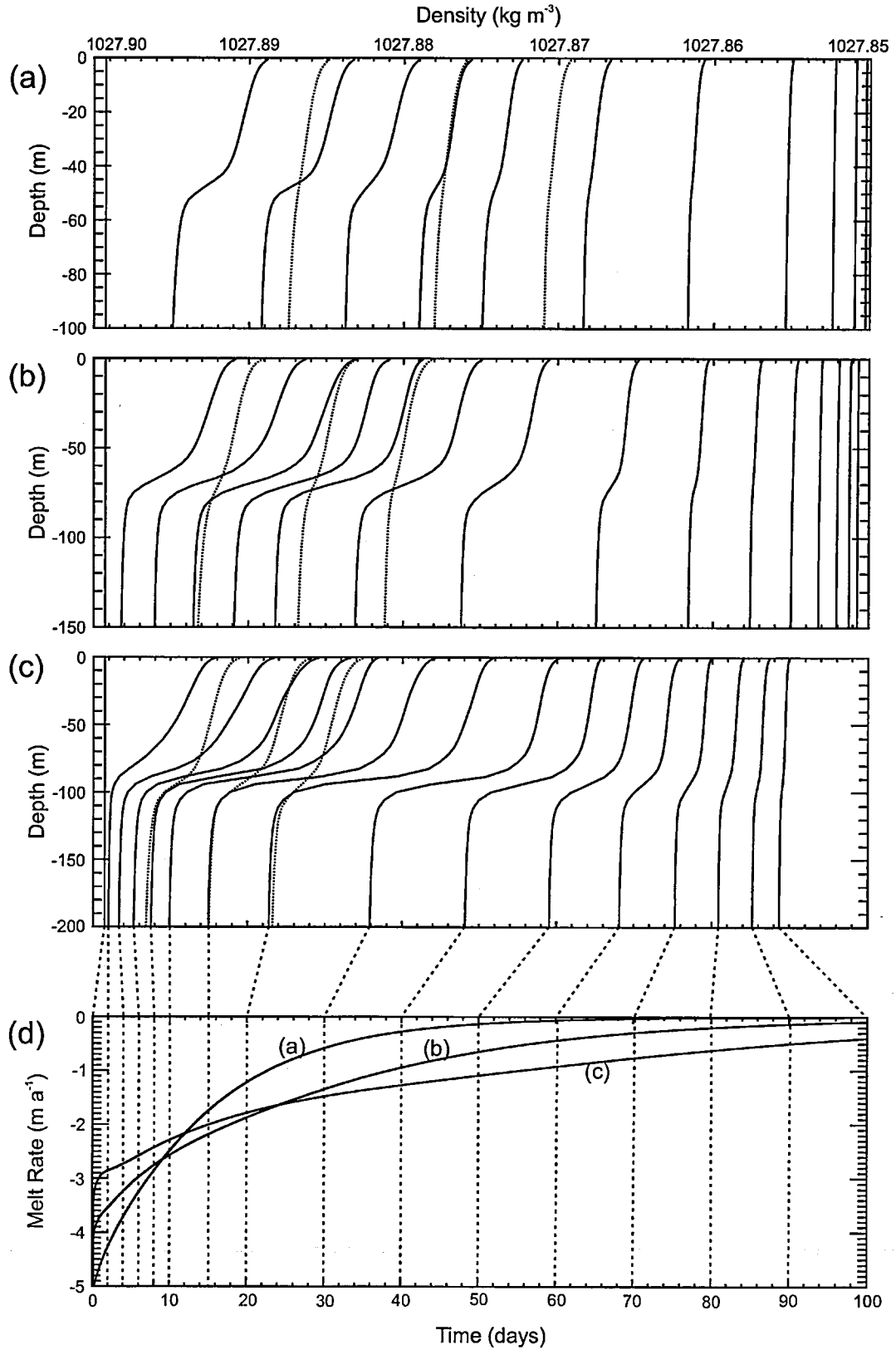

Figure 7.21 Pycnocline formation and erosion for conditions similar to those found close to Ronne Ice Front. The development of the density profile (solid line) with time is shown at t = 0, 2, 4, 6, 8, 10, 15 ,20 days and every 10 days thereafter (Note : the density axis is reversed). The average M_2 water column speeds are **(a)** 0.3 m s^{-1} , **(b)** 0.35 m s^{-1} and **(c)** 0.4 m s^{-1} and linked to **(d)** the corresponding melt rate. The dashed lines show the development of the density profile at t = 2, 4 and 6 days for double the average M_2 water column speeds, equivalent to spring tides. The ice shelf draft was set at 250 m and the water column was initially set to -1.9°C, 34.65 psu (1027.899kg m^{-3}) with an end state of -2.09°C, 34.58 psu (1027.847 kg m^{-3}).

the water column is essentially fully mixed with initial melt rates double the rates shown in Figure 7.21d.

Because of the strong mixing and melting in the 80-100 km wide ice front region, water masses passing through it will emerge as ISW, possibly close to the in situ freezing point. Only if advection were to exceed 0.15 m s^{-1} in the deeper parts of the water column around 52-54°W the lower half of the water column may remain unchanged. However, both observations [*Foldvik et al.*, 2001] and numerical modelling of tidal residual currents (Chapter 5) and thermohaline circulation [*Gerdes et al.*, 1999; *Jenkins and Holland*, In press] suggest typical velocities of up to 0.05 m s^{-1}. Clearly, it is unlikely that any water mass within the shallow ice front region will remain unmodified. Consequently, only the deeper Ronne and Filchner Depressions provide a route for unmodified WSW to enter the sub-ice shelf cavity and penetrate towards the deep grounding lines.

7.5 Summary and conclusions

The application of a 1-D vertical mixing model, thermodynamically coupled to an ice shelf, has shown the role played by tidal currents under the influence of the earth's rotation in vertical mixing. At deep water sites where observations exist, the model shows that local tidal mixing is a minor contributor to the vertical heat flux. At most it supports only a few centimetres of melt per year as opposed to the observed melt rates, one to two orders of magnitude higher. The model and observations show that vertical tidal current structure under ice shelves can be dramatically modified by the proximity of critical latitudes and changes in stratification, particularly in shallow water. Furthermore, the model shows that both the pycnocline development and the tidal contribution to basal melt rate are sensitive to tidal current ellipse polarization. Beneath FRIS, which is bounded by the critical latitudes of the M_2 and S_2 semi-diurnal tides, several key areas experience the extremes of the

polarization range, creating regions of widely differing levels of tidally induced vertical mixing and basal melting. The key results from the vertical mixing model are:

1. In deep water regions with low tidal currents, tidal mixing is not expected to be the dominant provider of vertical heat flux.
2. For predominantly clockwise ellipse rotation the model predicts mixing restricted by the small boundary layer of the R_- rotary component.
3. As the polarization becomes increasingly positive, the thickening boundary layer and associated shear of R_+ causes the mixing to rapidly penetrate deeper into the mid-water column.
4. The resultant melting gives over an order of magnitude difference between the lowest melt rates for purely clockwise tidal currents and the highest for purely anticlockwise tidal currents.
5. Changes in stratification can dramatically modify the vertical tidal current structure, particularly near semi-diurnal critical latitudes.
6. Unmodified WSW cannot reach the deeper parts of the sub-ice shelf cavity through the shallow region of Ronne Ice Front except via the much deeper Ronne and Filchner depressions.

As a consequence of these points, simple parameterizations of tidally-induced vertical mixing for use in sub-ice shelf circulation models are unlikely to represent the combined effects of semi-diurnal critical latitudes, stratification and ellipse polarization. Also, by omitting tides from circulation models beneath FRIS, key features such as the intense mixing along Ronne Ice Front and the influence of ellipse polarizations are neglected. Ultimately, a more comprehensive representation of tides and their associated mixing processes will be needed within circulation models to determine their contribution to and influence on sub-ice shelf circulation.

7.6 References

Carbajal, N., Two applications of Taylor's problem solution for finite rectangular semi-enclosed basins, *Continental Shelf Research, 17* (7), 803-817, 1997.

Foldvik, A., T. Gammelsrød, E. Nygaard, and S. Østerhus, Current meter measurements near Ronne Ice Shelf, Weddell Sea: Implications for circulation and melting underneath the Filchner-Ronne ice shelves, *Journal of Geophysical Research*, 2001.

Foldvik, A., J.H. Middleton, and T.D. Foster, The Tides of the Southern Weddell Sea, *Deep-Sea Research, 37* (8), 1345-1362, 1990.

Furevik, T., and A. Foldvik, Stability at M(2) critical latitude in the Barents Sea, *Journal of Geophysical Research, 101* (C4), 8823-8837, 1996.

Gerdes, R., J. Determann, and K. Grosfeld, Ocean circulation beneath Filchner-Ronne Ice Shelf from three-dimensional model results, *Journal of Geophysical Research, 104* (C7), 15827-15842, 1999.

Howarth, M.J., The effect of stratification on tidal current profiles, *Continental Shelf Research, 18* (11), 1235-1254, 1998.

Jenkins, A., and D.M. Holland, A model study of ocean circulation beneath Filchner-Ronne Ice Shelf, Antarctica: implications for bottom water formation., *Geophysical Research Letters*, In press.

Kraus, E.B., and J.S. Turner, A one-dimensional model of the seasonal thermocline II. The general theory and its consequences, *Tellus, 19*, 98-105, 1967.

MacAyeal, D.R., Numerical Simulations of the Ross Sea Tides, *Journal of Geophysical Research, 89* (C1), 607-615, 1984a.

MacAyeal, D.R., Thermohaline Circulation Below the Ross Ice Shelf - a Consequence of Tidally Induced Vertical Mixing and Basal Melting, *Journal of Geophysical Research, 89* (C1), 597-606, 1984b.

Morris, E.M., and D.G. Vaughan, Snow Surface Temperatures in West Antarctica, *Antarctic Science, 6* (4), 529-535, 1994.

Nicholls, K.W., and K. Makinson, Ocean circulation beneath the western Ronne Ice Shelf, as derived from in situ measurements of water currents and properties, in *Ocean, Ice, and Atmosphere: Interactions at the Antarctic Continental Margin*, edited by S.S. Jacobs, and R.F. Weiss, pp. 301-318, American Geophysical Union, Washington DC, 1998.

Nicholls, K.W., S. Østerhus, K. Makinson, and M.R. Johnson, Oceanographic conditions south of Berkner Island, beneath Filchner-Ronne Ice Shelf, Antarctica, *Journal of Geophysical Research, 106* (C6), 11481-11492, 2001.

Nøst, E., Calculating Tidal Current Profiles from Vertically Integrated Models near the Critical Latitude in the Barents Sea, *Journal of Geophysical Research, 99* (C4), 7885-7901, 1994.

Prandle, D., The Vertical Structure of Tidal Currents, *Geophysical and Astrophysical Fluid Dynamics, 22* (1-2), 29-49, 1982.

Prinsenberg, S.J., and E.B. Bennett, Vertical Variations of Tidal Currents in Shallow Land Fast Ice- Covered Regions, *Journal of Physical Oceanography, 19* (9), 1268-1278, 1989.

Robertson, R., L. Padman, and G.D. Egbert, Tidal currents in the Weddell Sea, in *Ocean, Ice and Atmosphere: Interactions at the Antarctic Continental Margin, Antarct. Res. Ser.*, edited by S.S. Jacobs, and R. Weiss, pp. 341-369, AGU, 1998.

Scheduikat, M., and D.J. Olbers, A one-dimensional mixed layer model beneath the Ross Ice Shelf with tidally induced vertical mixing, *Antarctic Science, 2*, 29-42, 1990.

Shirasawa, K., and R.G. Ingram, Characteristics of the turbulent oceanic boundary layer under sea ice. Part 1: A review of the ice-ocean boundary layer, *J. Marine Systems, 2*, 153-160, 1991.

Siddall, M., K. Nicholls, G.F. Lane-Serff, and K. Makinson, Warm core eddies beneath Ronne Ice Shelf, Antarctica, *Journal of Geophysical Research*, inprep.

Simpson, J.H., and J. Sharples, Does the Earths Rotation Influence the Location of the Shelf Sea Fronts, *Journal of Geophysical Research, 99* (C2), 3315-3319, 1994.

Simpson, J.H., and A.J. Souza, Semidiurnal Switching of Stratification in the Region of Fresh- Water Influence of the Rhine, *Journal of Geophysical Research, 100* (C4), 7037-7044, 1995.

Soulsby, R.L., The bottom boundary layer of the shelf sea, in *Physical oceanography of Coastal and Shelf Seas*, edited by B. Johns, pp. 189-226, New York, 1983.

Souza, A.J., and J.H. Simpson, The modification of tidal ellipses by stratification in the Rhine ROFI, *Continental Shelf Research, 16* (8), 997-1007, 1996.

Woodgate, R.A., M. Schröder, and S. Østerhus, Moorings from the Filchner Trough and the Ronne Ice Shelf Front: Preliminary Results, in *Filchner Ronne Ice Shelf Programme Report No 12*, edited by H. Oerter, pp. 85-90, Alfred-Wegener-Institue for Polar and Marine Research, Bremerhaven, Germany, 1998.

CHAPTER 8

General summary

8.1 Summary of described work

The preceding chapters of this thesis have presented an observational and modelling study of tidal currents and associated vertical mixing processes beneath Filchner-Ronne Ice Shelf. The described work may be separated into two stages.

The first phase involved the enhancement of the hot water drilling system, providing a capability to penetrate up to 1000 m of ice shelf and access the ocean beneath. Work from two field seasons which successfully penetrated ice up to 941 m thick is described in Chapter 2. This chapter includes the drilling techniques used and presents data from the measurements of water column properties and current measurements. These unique sub-ice shelf data sets provide the first insight into the oceanographic regime in the deeper parts of the FRIS cavity up to 500 km from the ice front.

In order to better understand the oceanographic regime beneath FRIS, numerical models are used to fill in the large gaps between sparse observations and point to key areas where observations can be made to test their validity. Here, the modelling of the tides initially used a two-dimensional depth-averaged barotropic tidal model applied to the southern Weddell Sea (Chapter 3). The bathymetry and ice shelf thickness data sets that are used to form the model domain were discussed. These data sets suffer from sparse data coverage in many areas, thus reducing the accuracy of the model. Another source of error may also arise from the open boundary forcing although a very recent circum-Antarctic tidal model

is likely to offer improved boundary conditions. Using the limited number of available tidal data, the tidal model which included the sub-ice shelf cavity, was shown in Chapter 4 to be capable of broadly simulating the pattern of tidal currents in the southern Weddell Sea and beneath FRIS. Figure 8.1a shows the spacial variability of the M_2 tidal ellipses over the region and Figure 8.1b shows the range of M_2 ellipse polarizations determined from the model. The model results also show the pattern of tidal energy flux and dissipation over the region. In addition, the model was used to indicate the magnitude of tidal residual currents (Chapter 5) over the continental shelf, along the ice front and within the cavity beneath FRIS (Figure 8.2). The strongest residual currents were associated with the main topographic feature in the water column thickness, Ronne Ice Front, where current speeds of up to 10 cm s^{-1} were predicted by the model. Observations show that tidal residuals contribute to a mean north-westward flow along the ice front but that other process can modify or dominate the along ice front flow. However, one key effect of ice front residuals is ability their to transfer a significant flux of water (350,000 m^3s^{-1}) across this topographic barrier between the sub-ice shelf cavity and the adjacent continental shelf.

In addition to the depth averaged tidal model, a one-dimensional vertical mixing model was constructed based on theories of turbulent mixing developed from laboratory and geophysical flows (Chapter 6). Results from laboratory studies of heat and mass transfer in turbulent flows were also used at the ice-ocean interface at the ice shelf base. This model was used in Chapter 7 to assess the impact of semi-diurnal critical latitude, changes in stratification, tidal current magnitude and polarization on the vertical heat flux and subsequent basal melt rate and also tidal current profiles. Using the small number of observations from beneath the ice shelf, the results from the mixing model clearly show that local tidal mixing at these deep water sites is a minor contributor to the vertical heat flux and the high rates of melting must be the result of a larger scale circulation. In regions of shallow water (<200 m) beneath the ice shelf such as grounding lines, south of Korff and

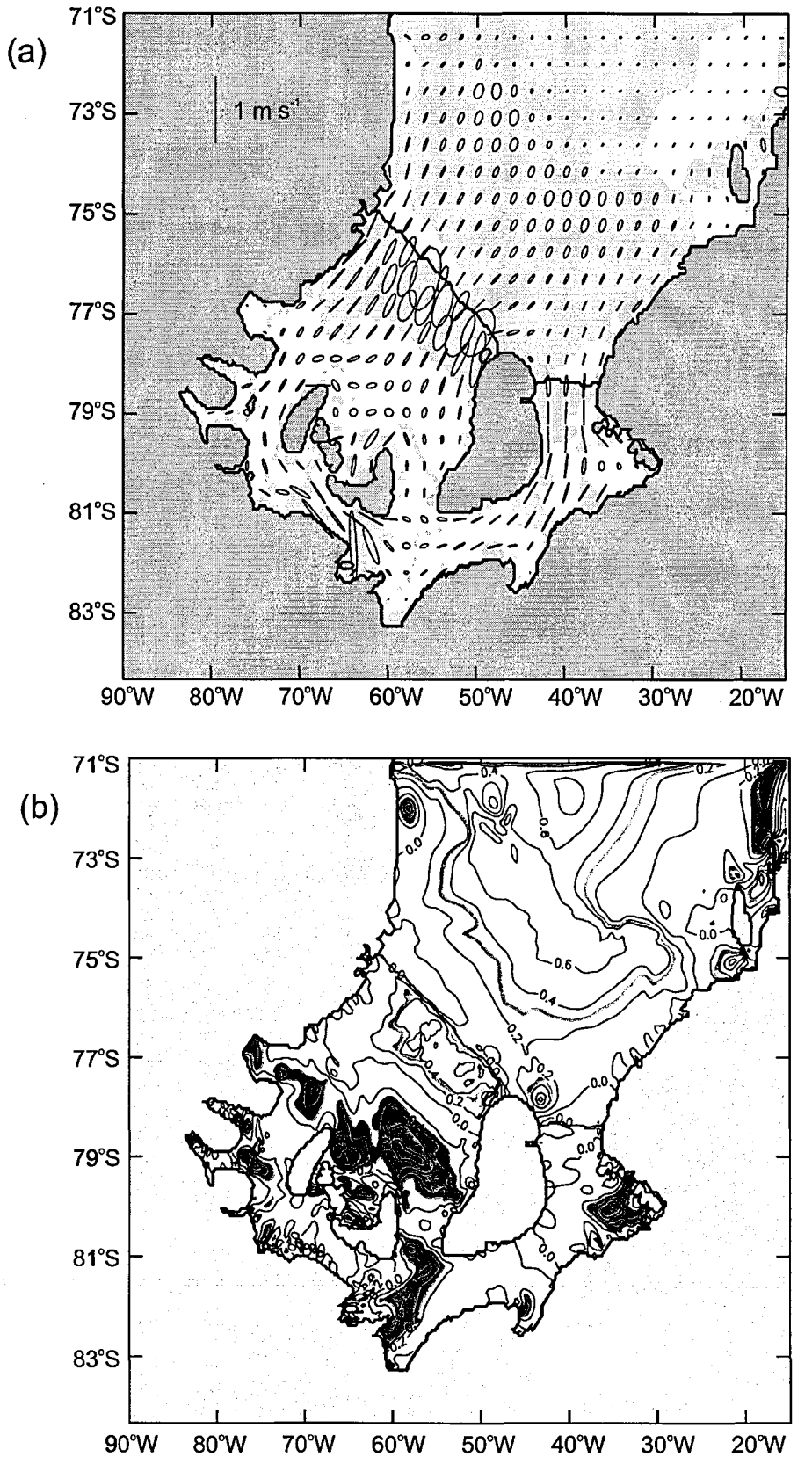

Figures 8.1 (a) Modelled tidal current ellipses plotted at every eighth grid point for the M_2 tidal constituent. The lightly shaded regions indicate anticlockwise rotation of the currents vectors. **(b)** The M_2 tidal ellipse polarization (P) with a contour spacing of 0.2. The blue shading shows regions of strong clockwise rotation ($P < -0.3$), red shading shows regions of strong anticlockwise rotation ($P > 0.3$).

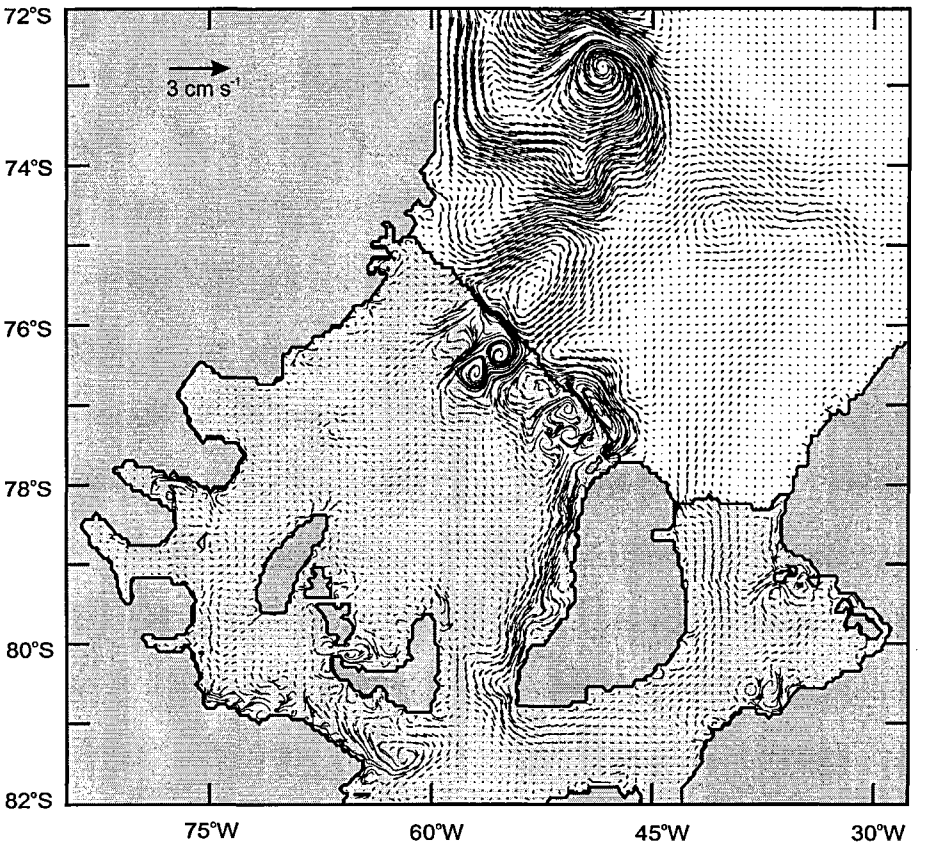

Figure 8.2 The Lagrangian residual tidal currents (tracer paths) obtained by removing the oscillatory components from the time series of water current. These mean currents are strongest over the western continental shelf, along Ronne Ice Front and the western coast of Berkner Island, and south of Henry and Korff Ice Rises.

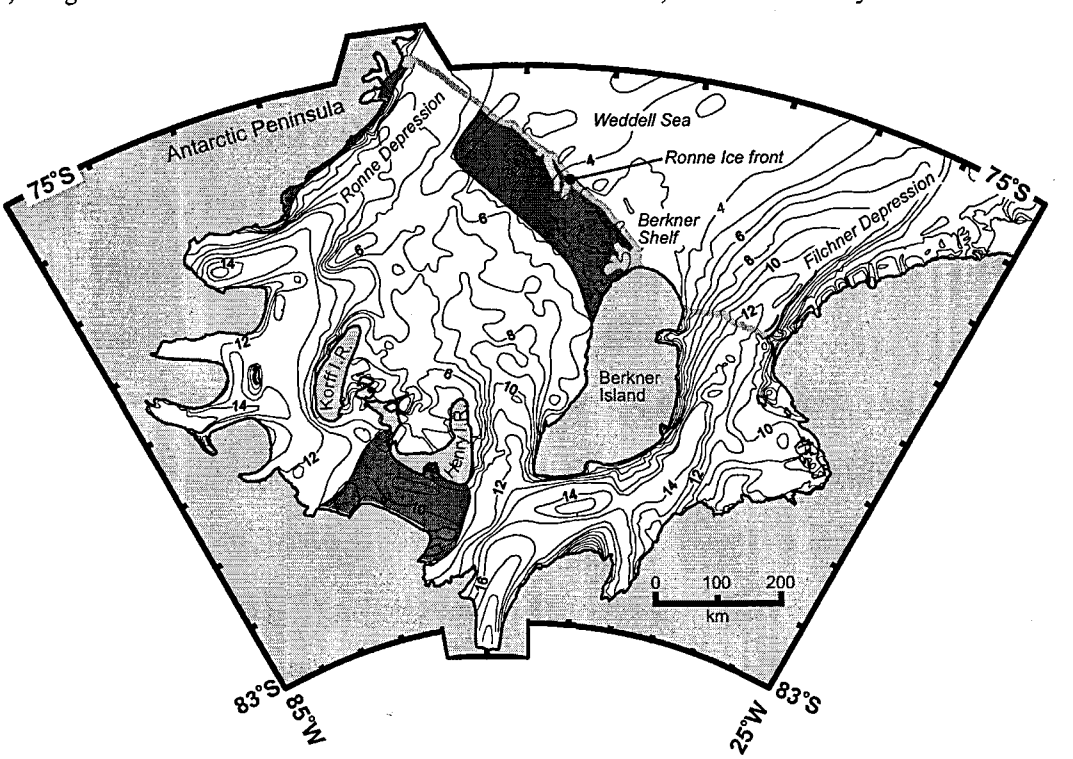

Figure 8.3 Map showing areas beneath Filchner-Ronne Ice Shelf where of vigorous tidal mixing is likely to occur (dark shading). In addition there will be regions varying in width from a few hundred metres to a few kilometres at grounding lines where vigorous tidal mixing is likely to occur. The contours give bathymetry in 100's of metres below sea level.

Henry ice rises and close to Ronne Ice Front, the model indicated high levels of mixing and melting. Therefore, water masses passing through these vigorous mixing regions (Figure 8.3) are likely to be modified (cooled and freshened) through interaction with the ice shelf base.

Due to the proximity of the semi-diurnal critical latitude, where the tidal frequency equals the frequency of the Coriolis parameter, large boundary layers form for the positive (anticlockwise) rotating component of the semi-diurnal tidal ellipse. The mixing model has shown that these large boundary layers aid vertical mixing particularly for more positive tidal ellipse polarizations (Figure 8.4) where the anticlockwise component dominates. The mixing model indicates that for a given average water column speed the basal melt rate can vary by an order of magnitude over the range of ellipse polarizations. In figure 8.1b, the highlighted areas with negative polarizations will have tidal boundary layers of only a few metres, whereas areas with positive polarizations will have large boundary layers that may occupy the entire water column resulting in vigorous mixing and melting. Current meter moorings close to Ronne Ice Front show the presence of these large semi-diurnal boundary layers which can be modified by seasonal stratification (Figure 8.5). The vertical mixing model also shows both the presence of large boundary layers that extend through the whole water column and the effects of stratification on the anticlockwise rotating tidal component of the semi-diurnal tides. Hence, beneath FRIS, tidal current profiles and basal melt rates are strongly influenced by the presence of the critical latitude and the tidal ellipse polarization.

8.2 What has been learnt from this study?

The key conclusion to be drawn from this work is that the previously unmodelled tidal currents of the southern Weddell Sea have a significant impact within the cavity beneath FRIS and over the adjacent continental shelf. Tidal currents exert their greatest influence

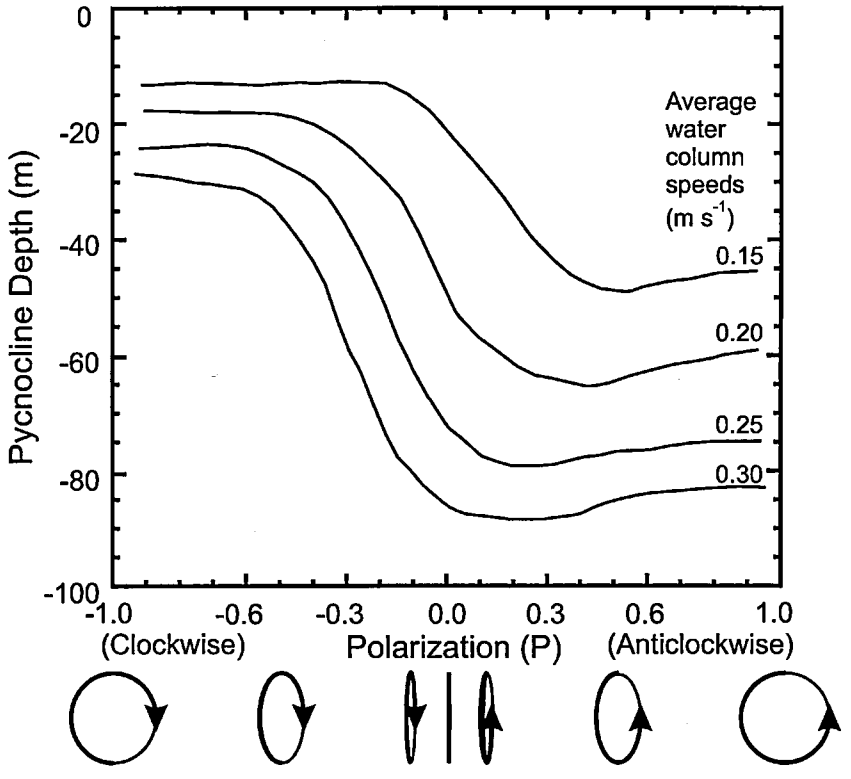

Figure 8.4 Pycnocline depth in the upper half of the water column after 10 M_2 tidal cycles at 79°S over which melting has taken place for different average water column speeds versus the mean polarisation of the M_2 tidal current ellipse.

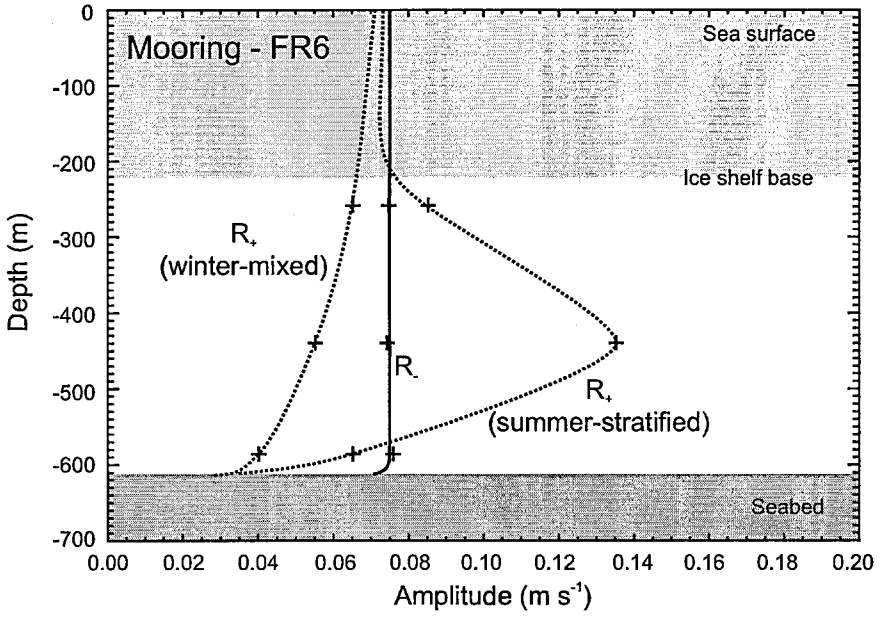

Figure 8.5 The clockwise and anticlockwise tidal current components for M_2 at mooring FR6. The portion of water column occupied by the nearby ice shelf is indicated by the light shading and the seabed is indicated with the darkest shading. The crosses are current meter measurements and the lines indicate the extrapolated vertical current profiles for a well mixed and stratified water column.

in shallow water regions by driving mean flows and providing strong vertical mixing to sustain basal melting. These processes therefore influence the ice shelf morphology, the underlying ocean and the oceanography of the southern Weddell Sea.

Using a two-dimensional barotropic tidal model, this study presents the first analysis of tidal energy flux and dissipation that results from friction at the seabed and ice shelf base. The resulting vertical mixing is shown to be highly significant and capable of sustaining melt rates of several metres per year and influencing the ice shelf morphology, particularly along much of Ronne Ice Front. In addition, the model quantified the magnitude and pattern of tidally generated mean flows within the cavity beneath FRIS and over the adjacent continental shelf. These mean flows especially in the region of Ronne Ice Front, help ventilate the sub-ice shelf cavity. Inflowing waters carry heat into the cavity while outflowing waters export Ice Shelf Water onto the continental shelf.

To look in greater detail at the vertical structure of the water column a sub-ice shelf one-dimensional mixing model was developed. Influenced by semi-diurnal critical latitude and stratification, the model highlighted for the first time, the effects of tidal ellipse polarization on vertical mixing and basal melt rates beneath an ice shelf. Positive polarizations are shown to enhance vertical mixing through the development of thick boundary layers with stratification capable of producing large increases in the tidal current amplitude. Additionally, Ronne and Filchner depressions have been identified as the only areas where unmodified Western Shelf Water can penetrate deep into the ice shelf cavity, ultimately providing heat to drive basal melting close to grounding lines.

Away from FRIS, Ice Shelf Water crosses the continental shelf within Filchner Depression. At the continental shelf break it descends the slope and contributes to the formation of AABW and the global thermohaline circulation. This work has shown that the tidal

processing of water masses beneath FRIS is an element that links the ice shelf to the world's deep oceans.

8.3 Future work

Understanding the processes controlling the sub-ice shelf oceanographic environment is key to the development of circulation models that can predict ocean circulation, the production of Ice Shelf Water and the influence of a changing climate. This study has clearly demonstrated through observational and numerical modelling work that tidal currents, residual tidal currents and tidal vertical mixing play a significant role in the sub-ice shelf oceanographic environment beneath Filchner-Ronne Ice Shelf.

To date, no sub-ice shelf circulation model has included tides or any parameterizations of tides. By fully incorporating tides within these models a clearer description will emerge of their role in vertical mixing, basal melting and thermohaline circulation within the entire sub-ice shelf cavity. However, one area that is not well understood outside laboratory conditions and unique to this environment is the upper ocean boundary layer adjacent to the ice shelf base in a region bounded by the semi-diurnal critical latitudes. Presently no detailed field observations exist in the upper boundary layer that is essential to the understanding of ice-ocean interaction beneath ice shelves. Future fieldwork is necessary to test and possibly modify the parameterization of the transfer of heat, salt and momentum in this upper ocean boundary layer in areas with high and low melt rates. This is crucial to the development of superior predictive sub-ice shelf models that can be used to investigate the impact of climate change on thermohaline circulation and ice sheet extent.

Over recent years there has been growing interest in melt rates at deep grounding lines that may be sensitive to climate change. Further fieldwork could be used to determine water mass modification by tidal processes as it descends towards deep grounding lines but more

importantly at the grounding line itself where tides are believed aid some of the highest basal melt rates beneath the ice shelves that are important to the sub-ice shelf oceanographic regime.

Any further fieldwork and numerical modelling of sub-ice shelf processes will provide a better understanding of the interaction between the ocean and Filchner-Ronne Ice Shelf and its response to changes in ocean circulation and climate. It would also offer a clearer indication of Ice Shelf Water production beneath FRIS, its contribution to Weddell Sea Bottom Water and ultimately Antarctic Bottom Water formation which can exert a long-term influence on global climate.

Appendix

A.1 Surface forcing functions

To derive a surface forcing function in terms of the resulting tidal ellipse polarization and its semi-major axis, the complex form of the momentum equations are required. For details of their derivation the reader is referred to either *Soulsby* [1983] or *Carbajal* [2000] where both the velocity and sea surface slope are divided into two counter rotating components

$$i(\omega + f)R_+ = \frac{\partial}{\partial z}\left(K_M \frac{\partial R_+}{\partial z}\right) - gS_+ \qquad \text{(A1)}$$

$$-i(\omega - f)R_- = \frac{\partial}{\partial z}\left(K_M \frac{\partial R_-}{\partial z}\right) - gS_- \,, \qquad \text{(A2)}$$

where ω is the tidal frequency, f is the Coriolis parameter, K_M is the vertical eddy viscosity, g the gravitational acceleration and z is vertical distance. R_- and R_+ represent the purely clockwise and anticlockwise constant magnitude velocity vectors that rotate at the tidal frequency and S_- and S_+ are the rotary components of the sea surface elevation gradients. Outside the boundary layer away from the influence of bottom friction, the first terms on the right-hand side of (A1) and (A2) are small and the free stream tidal current is given by

$$R_{\infty+} = \frac{igS_+}{\omega + f} \quad \text{and} \qquad \text{(A3)}$$

$$R_{\infty-} = \frac{-igS_-}{\omega - f} \quad . \tag{A4}$$

Assuming the maximum tidal current corresponds to the maximum surface slope aligned along the x-axis (S_x) and the minimum tidal current corresponds to the minimum surface slope aligned along the y-axis (S_y)

$$S_x = |S_+| + |S_-| \tag{A5}$$

$$S_y = |S_+| - |S_-| \quad , \tag{A6}$$

rearranging (A3) and (A4) and substituting into (A5) and (A6) gives S_x and S_y in terms R_+ and R_-. Rearranging and grouping R_+ and R_- in terms of the maximum tidal current or semi-major axis ($U = R_+ + R_-$) and polarization ($P = [R_+ - R_-]/[R_+ + R_-]$) gives

$$S_y = \frac{U(f + P\omega)}{g} \tag{A7}$$

$$S_x = \frac{U(\omega + Pf)}{g} \tag{A8}$$

the surface forcing functions along the x-axis and y-axis.

A.2 References

Carbajal, N., A criterion to locate regions with anticyclonic tidal current rotation, *Continental Shelf Research*, *20* (3), 281-292, 2000.

Soulsby, R.L., The bottom boundary layer of the shelf sea, in *Physical oceanography of Coastal and Shelf Seas*, edited by B. Johns, pp. 189-226, New York, 1983.

JOURNAL OF GEOPHYSICAL RESEARCH, VOL. 104, NO. C6, PAGES 13,449–13,465, JUNE 15, 1999

Modeling tidal currents beneath Filchner-Ronne Ice Shelf and on the adjacent continental shelf: their effect on mixing and transport

Keith Makinson and Keith W. Nicholls
British Antarctic Survey, Natural Environment Research Council, Cambridge, England

Abstract. A depth–averaged tidal model has been applied to the southern Weddell Sea. The model domain covers the southern continental shelf, including the ocean cavity beneath Filchner-Ronne Ice Shelf. Reasonable agreement with the available current meter data has been achieved. Our results confirm that in areas with shallow water and large topographic gradients, tidal oscillations with peak velocities up to 1 m s^{-1} play a significant role in the vertical mixing and transport of water masses. The estimated energy dissipation beneath Filchner-Ronne Ice Shelf due to surface friction is 25 GW, approximately 1% of the world's total tidal dissipation. Tidally induced Lagrangian residual currents converging at the ice front, an area of strong mixing, draw together water masses from the continental shelf and sub–ice shelf cavity. The model indicates that Lagrangian residual currents have fluxes of up to 250,000 m^3 s^{-1}, and speeds of over 5 cm s^{-1} along the ice front, with over 350,000 m^3 s^{-1} being exchanged between the sub–ice shelf cavity and adjacent continental shelf. These currents are particularly efficient in ventilating the sub–ice shelf cavity within 150 km of Ronne Ice Front. Such strong tidal mixing will significantly modify the properties of water masses that flow through this region, particularly to the west of Berkner Island. The model predictions indicate that tidal processes strongly influence the oceanographic conditions in the vicinity of Ronne Ice Front. Shipborne observations along the ice front support many of the model predictions concerning the effect of tides on the hydrography.

1. Introduction

The continent of Antarctica is fringed by ice shelves, the floating portion of the Antarctic Ice Sheet. Their presence affects both the flow of ice from the continental interior and the hydrography of the adjacent continental shelf. The two largest ice shelves, the Ross and Filchner-Ronne, together form a large part of the West Antarctic Ice Sheet. Located in the southern Weddell Sea, Filchner-Ronne Ice Shelf (FRIS) covers an area of almost 450,000 km^2 [*Fox and Cooper*, 1994] and is by volume the largest ice shelf, draining 24% of the area of the continent's grounded ice. Ronne Ice Shelf's thickness ranges from around 300 m at the ice front to a maximum of 2000 m at its deep grounding lines. The southern Weddell Sea is of considerable oceanographic interest as Ice Shelf Water (ISW) formed beneath FRIS is ultimately transformed into Antarctic Bottom Water (AABW) in the deep ocean. About 80% of AABW has its origin in this region [*Foldvik and Gammelsrød*, 1988].

Close to Filchner-Ronne Ice Front the oscillatory action of the tides, the tidal divergence, and the offshore winds act to export sea ice out of the region. Throughout much of the year they maintain a strip of open water, usually called a shorelead, along the ice front [*Foldvik et al.*, 1985; *Foldvik and Gammelsrød*, 1988]. In this shore lead there is a concentrated production of High Salinity Shelf Water (HSSW) [*Gill*, 1973], a dense water mass formed by salt rejection during the production of sea ice. In general, the seafloor slopes down toward the continental interior, and so the HSSW flows beneath the ice shelf.

Once beneath FRIS the HSSW enters an unusual oceanographic environment. Within the sub–ice shelf cavity, water masses are isolated from atmospheric forcing, and tidal and thermohaline processes dominate the circulation. Once the HSSW has descended to the grounding line regions it has an in situ temperature up to 1°C higher than the pressure freezing point of seawater [*Jenkins and Bombosch*, 1995]. Occupying the lower portion of the water column, the HSSW is separated from the ice shelf base by ISW which has a temperature close to the in situ freezing point. *MacAyeal* [1984a] suggests tidal stirring as a probable mechanism for mixing the HSSW up through the water column into the overlying ISW, thereby sustaining strong melting where the HSSW comes into contact with the base of the ice shelf. Thus tides may play a crucial role in the thermohaline circulation beneath the ice shelf. In addition to their contribution to vertical mixing, tidal oscillations over topographic features drive steady barotropic circulations, or residual currents, that contribute to the large-scale transport of heat, salt, and other tracers. Probably the most significant topographic feature affecting the water column in the southern Weddell Sea is the ice front of FRIS. Across some portions of the ice front, there is a step change of more than 50% in the water column thickness. Strong residual currents are likely to be associated with this step.

To determine the contribution of tidal processes to the oceanographic regime in the vicinity of the ice shelf, we apply a high-resolution, depth-averaged tidal model to the southern Weddell Sea. The domain covers the southern continental shelf, including the ice shelf–covered region. The model is driven at its boundary by a larger-scale application of the same code [*Smithson*

Paper number 1999JC900008.
0148-0227/99/1999JC900008$09.00

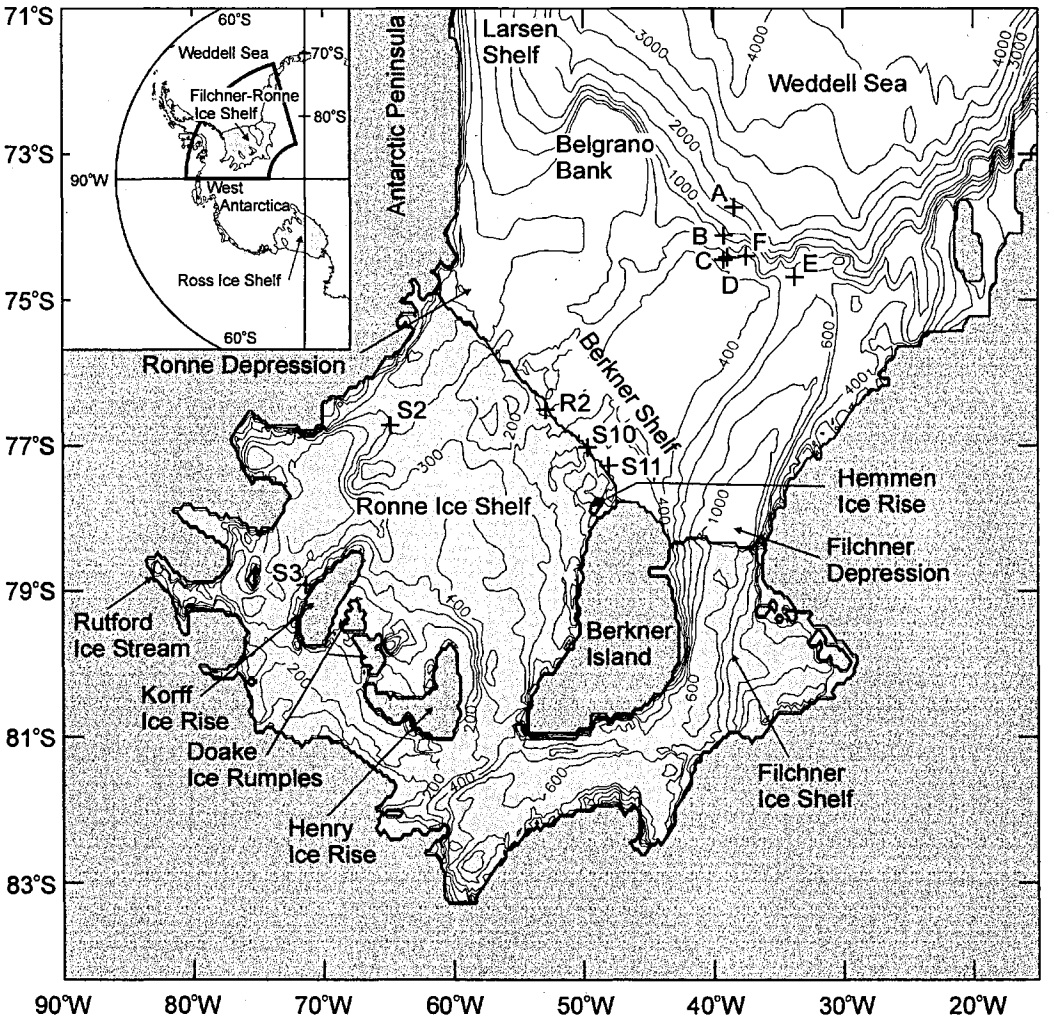

Figure 1. Map showing the model domain. The darkest shading indicates areas of grounded ice, and the lighter shading indicates the floating ice shelf. The contours give the water column thickness in meters. The location and name of current measurement sites used for comparison with the model are marked. The inset indicates the position of Filchner-Ronne Ice Shelf (FRIS) in the southern Weddell Sea, and the box shows the region covered by the model domain.

et al., 1996], which in turn is driven at its boundary by the global tidal model of *Schwiderski* [1980]. In this study we are not concerned with the precise prediction of tides for the region. Rather, we seek to estimate the likely effects of tidal processes on the oceanography of the ice shelf environs. We show that oceanographic observations from along a large section of Ronne Ice Front can be explained by tidal effects and that the oceanographic conditions in some areas of the sub–ice shelf cavity itself are likely to be dominated by tidal, rather than purely thermohaline, processes.

First, we present the barotropic tidal model used for this study, including a description of the domain. The output from the model includes tidal elevations and currents, of which this paper addresses only the latter. Other authors have already considered tidal elevations in this region [*Genco et al.*, 1994; *Robertson et al.*, 1998; *Robinson*, 1996; *Smithson et al.*, 1996]. A comparison with the available tidal current measurements is given in section 3. Section 4 presents average tidal currents and mixing energies and discusses how the pattern of basal melting is influenced by tidally induced vertical heat fluxes. The Eulerian and Lagrangian residual currents that result from tidally generated residual vorticity and Stokes drift are presented in section 5. The estimates of tidal mixing and Lagrangian residual currents are used in section 6 to explain some of the features found in hydrographic observations from the shore lead.

2. Numerical Model, Bathymetry, and Results

The model used in this study is a finite difference barotropic tidal model in spherical polar coordinates [*Smithson et al.*, 1996] based on depth-averaged equations of continuity and motion discretized onto the model grid. The grid used is the Arakawa "C grid." The domain, shown in Figure 1, lies between latitudes 71°S and 84°S, and longitudes 15°W and 90°W. This encompasses the entire southern Weddell Sea continental shelf, including the region covered by FRIS. The model grid has a regular spacing of 4′ latitude by 15′ longitude, corresponding to 7.4 km north-south and ranging from 9 km to 3.4 km east-west. The seabed stress is related to the depth mean current using a quadratic friction law and the coefficient of bottom friction was set to 0.0025. However, beneath

the ice shelf area the value was doubled to account for the additional drag at the ice-ocean interface. Apart from providing a second frictional surface and reducing the water column thickness, the ice shelf has no influence on the tides in this model. The horizontal eddy viscosity was taken to be 5.0 $m^2 s^{-1}$ over the whole domain. The time step Δt for the integration was set at 15 s to ensure the Courant-Friedrichs-Lewy (CFL) condition, $\Delta t < \Delta s(2gD)^{-0.5}$, was satisfied throughout the domain. Δs is the grid spacing, g is the gravitational acceleration, and D is the water column thickness.

In this application the model is forced with a time series of sea surface heights along its open boundary. Data for the boundary were obtained by interpolation of results from a regional model [*Smithson et al.*, 1996] that was itself forced by the *Schwiderski* [1980] model. The time series of sea surface elevation for each node along the boundary were computed using the amplitude and phase of six tidal constituents (Q_1, O_1, K_1, N_2, M_2, S_2). The equations of motion and continuity were solved using an explicit finite difference method.

North of 75°S the bathymetry for the model was taken from the U.S. Naval Oceanographic Office Digital Bathymetric Data Base 5 (DBDB5) data set [*Van Wyckhouse,* 1973]. In that data set a shallow region known as the Belgrano Bank (73°S, 50°W), which lies near the continental shelf break, has a minimum water depth of 10 m. The General Bathymetric Chart of the Oceans (GEBCO) data set of *Johnson et al.* [1983], which includes ship data from Belgrano Bank and recent cruise data from this area (K. W. Nicholls, personal communication, 1998), suggests a minimum of no less than 400 m in this area. In our domain we increased the minimum depth to 400 m, similar to the depth of the surrounding continental shelf. Recent geophysical airborne data from the western Weddell Basin [*Labrecque and Ghidella,* 1997] suggest that the correct position of the southern section of Larsen continental shelf edge lies as much as 100 km to the east of the DBDB5 position. A correction has not been included in the present model bathymetry. South of 75°S bathymetry and ice shelf thickness data were from the digital data set prepared by *Vaughan et al.* [1994], updated with more recent seismic data from the areas south of Berkner Island, and Korff and Henry Ice Rises [*Johnson and Smith,* 1997; *Mayer et al.*, 1995].

In areas not covered by ice shelf, bathymetry and water column thickness are the same. Over these areas the water column thickness ranges from 4000 m in the Weddell Sea basin to less than 250 m on the continental shelf, the shallowest being the Berkner Shelf, north of Berkner Island (Figure 1). Beneath FRIS, however, the model uses the water column thickness, defined as the difference between seabed depth and ice shelf draft [*Vaughan et al.*, 1995]. Here the water column thickness is 100 m or less near Ronne Ice Front, increasing to more than 600 m near some sections of the southern grounding line.

Initial model conditions consisted of no currents and an undisturbed sea surface. The model was run for 41.5 days with the elevations and currents being recorded hourly over the final 27.6 days. The recorded time series is long enough for the harmonic analysis method to be used to separate the six constituents that drive the model [*Foreman,* 1977]. The analysis provided tidal amplitude and phase information for elevations and currents at each grid point in the domain. Tidal elevations obtained using the same model but applied to the entire western Weddell Sea have been discussed by *Smithson et al.* [1996] and *Robinson* [1996] and are not discussed further here.

Amplitudes and phases of the eastward and northward components of each tidal current constituent predicted by the model were used to construct current ellipses. The current ellipses

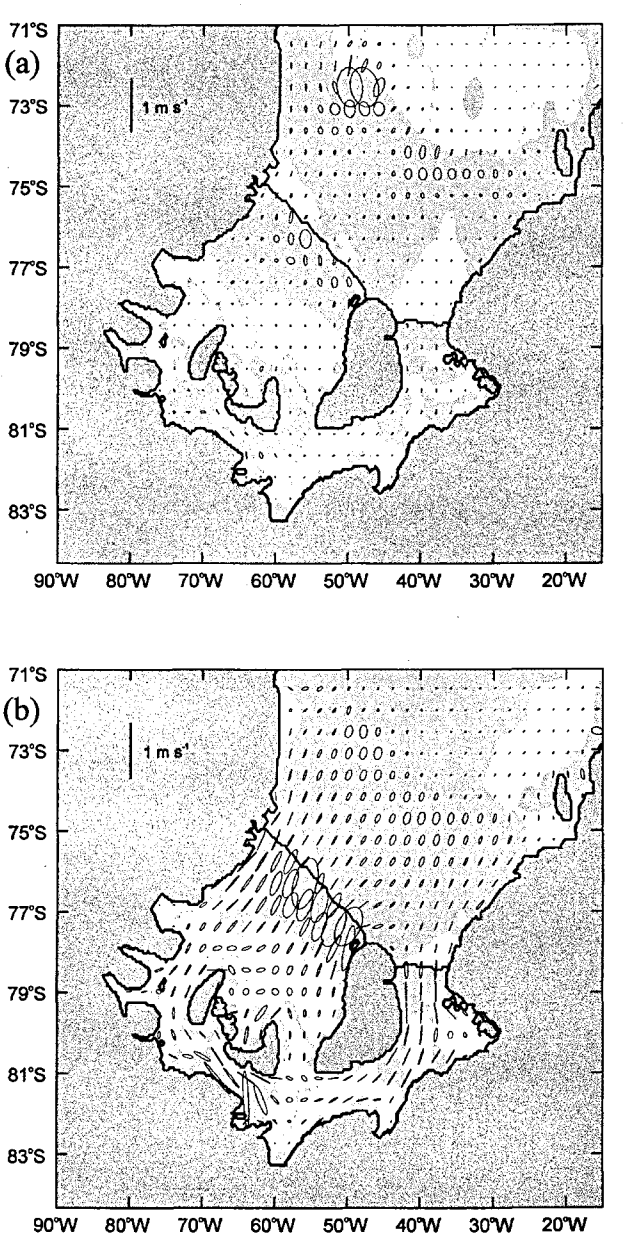

Figure 2. Modeled tidal current ellipses plotted at every eighth grid point for the (a) K_1 and (b) M_2 tidal constituents, which are representative of other constituents in the diurnal and semi-diurnal bands, respectively. The lightly shaded regions indicate anticlockwise rotation of the currents.

for the main diurnal tide K_1 and the main semidiurnal tide M_2 are representative of other constituents in their band and are plotted every eighth grid point over the model domain in Figures 2a and 2b. Shaded and unshaded areas show anticlockwise and clockwise rotation of current vectors.

In the deep Weddell Sea all current constituents are weak, with amplitudes less than 0.02 m s^{-1}. At the continental shelf break, diurnal currents are up to 5 times larger than on the continental shelf. *Middleton et al.* [1982] observed similar amplification in this region, and attributed it to the presence of diurnal barotropic shelf waves. Over the continental shelf the highest velocities (>0.5 m s^{-1} for M_2) are found in shallow areas, particularly the region south of Ronne Ice Front, close to Berkner Island. There the draft of the ice

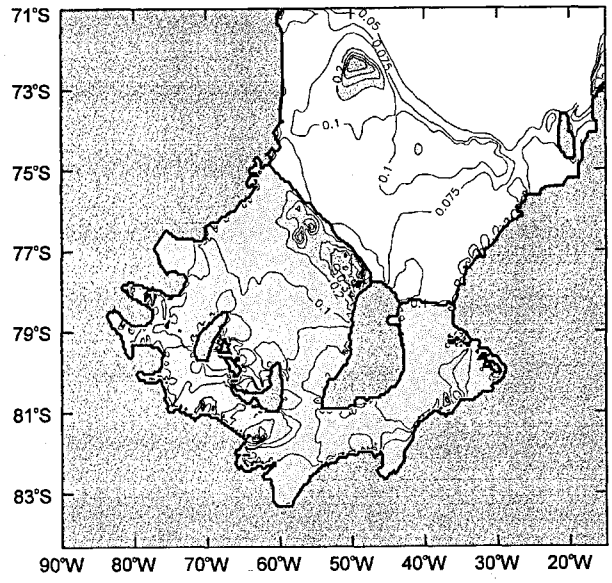

Figure 3. A contour plot of the average RMS water speeds over the model domain, with speeds greater than 0.2 m s^{-1} heavily shaded. The highest speeds are found in the shallow region south of Ronne Ice Front and Belgrano Bank.

shelf combines with shallow bathymetry to create a water column less than 100 m thick. In shallow areas the ellipses become more open, indicating a tidal current of nearly constant strength throughout the tidal cycle. Over the continental shelf close to the coast the ellipses are greatly flattened, particularly for the semi-diurnal tides, and the major axes are aligned parallel to the nearest coastline. These characteristics are consistent with a Kelvin wave propagating around the embayment. *MacAyeal* [1984b] similarly interpreted the semidiurnal tides in the southern Ross Sea.

The modeled tidal constituents were combined and averaged over a spring-neap cycle to calculate the average root mean square (RMS) water speed over the domain (Figure 3). Average RMS speeds greater than 0.2 m s^{-1} are highlighted, and average RMS spring speeds are typically double the values shown in Figure 3. Of the three regions where the average currents are high, two correspond to areas of relatively shallow water (<200 m): the area south of Ronne Ice Front and south of Henry Ice Rise. The third region, where the water column is 400 m, is centered on Belgrano Bank. This area is subject to tidal amplification in the diurnal band (Figures 2a and 2b) resulting in high RMS speeds.

The tidal energy flux vectors were computed over the model domain using $\mathbf{u}(g\rho D\eta+\rho D½|\mathbf{u}|^2)$, where $\mathbf{u}$ is the depth-averaged tidal velocity, D is the water column thickness, η is the displacement of the sea surface from the equilibrium level, g is the gravitational acceleration, and ρ is the seawater density in this region (1028 kg m^{-3}). The first term representing the work done against gravity during the tidal cycle dominates over the kinematic energy term. Figure 4 is a map of the energy flux vectors and shows a proportion of the main energy flux from the Weddell Sea crossing the continental shelf via the Filchner Depression, before propagating beneath Filchner Ice Shelf. Once beneath the ice shelf most of the flux circulates clockwise south of the ice rises. A small portion branches to the north, between Henry Ice Rise and Berkner Island. Most of the energy beneath the ice shelf is associated with the semidiurnal Kelvin wave that propagates around the embayment.

3. Available Data and Comparison With Model Results

Ice shelves and year-round sea ice cover greatly limit the number of current meter observations from the Weddell Sea. A total of 11 current measurement sites that lie within the model domain are used to validate the model. The current meter sites, shown in Figure 1, fall into three main groups: six continental shelf break sites lying mostly within a concentrated area around 74°S 39°W; three ice front sites positioned close to or up against the eastern section of Ronne Ice Front; and two sub–ice shelf sites, of which one is a thermistor cable site. The accuracy of the derived ellipses is chiefly dependent on the lengths of the time series, which are given in Table 1. The table also shows the instrument depth and the tidal species that were extracted. The observed and modeled current ellipses for the constituents extracted from the observed time series are shown in Figure 5. The modeled tidal velocities have been adjusted to account for the difference between the water column thickness measured at the sites and that used in the model domain.

At the continental shelf break, moorings were deployed and recovered by several different groups over the period 1968 to 1980 [*Elder and Seabrooke*, 1970; *Foldvik and Kvinge*, 1974; *Middleton et al.*, 1982; 1987]. Taking site C (Figure 5), which is representative of the six sites in the area, the modeled diurnal currents reproduce the observed amplification seen for K_1 and Q_1. Unlike the observed data set, the model shows amplification in O_1, most probably the result of incorrect bathymetry along the continental shelf break and adjacent sea. The absence of O_1 amplification in the observations has been attributed to the interaction of diurnal barotropic shelf waves that results from variations in the temporal mean velocity field interacting with the irregular shelf topography [*Foldvik et al.*, 1990]. The phase of the diurnal components are rather poorly reproduced by the model. For the semidiurnal currents the model overestimates the amplitudes, particularly for M_2 and N_2, though there is reasonable agreement in the phases.

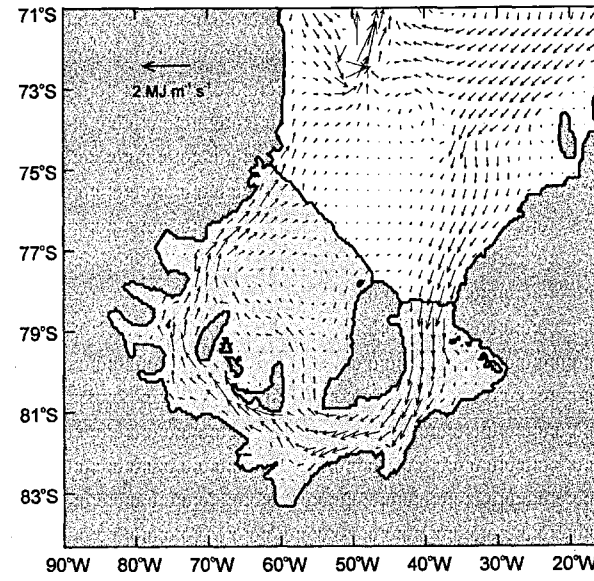

Figure 4. Average tidal energy flux vectors are plotted for every eighth grid point of the model domain. The majority of the energy flux enters the sub–ice shelf cavity via the Filchner Depression.

Table 1. Summary of Current Meter Sites Used for Comparison with the Model Results

Site	Location Type	Instrument Depth, m	Record length, days	Constituents	Reference
A	Shelf break	1815 *	419	Q_1, O_1, P_1, K_1, N_2, M_2, S_2, K_2	*Foldvik et al.* [1990]
B	Shelf break	620 *	257	Q_1, O_1, P_1, K_1, N_2, M_2, S_2, K_2	*Foldvik et al.* [1990]
C	Shelf break	375 *	631	Q_1, O_1, P_1, K_1, N_2, M_2, S_2, K_2	*Foldvik et al.* [1990]
D	Shelf break	400 *	504	Q_1, O_1, P_1, K_1, N_2, M_2, S_2, K_2	*Foldvik et al.* [1990]
E	Shelf break	375 *	257	Q_1, O_1, P_1, K_1, N_2, M_2, S_2, K_2	*Foldvik et al.* [1990]
F	Shelf break	445 *	31	O_1, K_1, N_2, M_2, S_2	*Foldvik et al.* [1990]
S10	Ice front	100 & 224	4.5	K_1, M_2	*Foldvik et al.* [1985]
S11	Ice front	25 & 75 †	11	K_1, M_2	*Foldvik et al.* [1985]
R2	Ice front	258 & 411	435	O_1, P_1, K_1, N_2, M_2, S_2, K_2	*E. Nygaard* (unpublished report, 1995)
S2	Sub–ice shelf	-‡	660	O_1, K_1, M_2, S_2	*Makinson and Nicholls* [1996]
S3	Sub–ice shelf	1125	+565	Q_1, O_1, P_1, K_1, N_2, M_2, S_2, K_2	*Makinson and Nicholls* [1996]

* More than one current meter was present at the site; details of the instrument with greatest height above bottom are given, typically 100 m above bottom.

† The shallowest instrument was believed to be above the draft of the ice shelf.

‡ Constituents estimated from thermistor cable data (see Appendix).

The three ice front mooring locations used in the model have been moved by up to 8 km perpendicular to the ice front to take account of the 1300 m yr^{-1} advance rate [*Vaughan and Jonas*, 1996]. Using the 1986/1987 ice front position, mooring locations were moved so as to maintain their relative distance from the ice front. The change in water depth is minimal as the bathymetry is relatively flat at these locations. Two of the three ice front sites, S10 and R2, were located a few kilometers offshore of the ice front. At these sites the modeled constituents are in reasonable agreement with the observations both in phase and amplitude. Poor agreement between the model and the third ice front site (S11) is illustrated in Figure 5, particularly for M_2. This probably results from either the inability of the model to reproduce the tides accurately in close proximity to an abrupt change in the water column depth or from the limited length of the record. In addition to the ice front moorings, *Foldvik et al.* [1985] used a Braystoke meter close to the ice front to obtain further current data at 20 m and 50 m depths. There are differences in the direction of flow between the model and the data but the ebb and flow of the tide correspond well both in time and magnitude.

Beneath the ice shelf, 17 km from the west coast of Korff Ice Rise, Site 3 (S3 in Figure 1) represents the only direct measurement of the sub–ice shelf currents [*Nicholls et al.*, 1997]. The orientations of the modeled ellipses agree with the observations, and the phases differ by no more than 15°. However, the major axes of the modeled currents are 30% larger than observed. During conductivity-temperature-depth (CTD) profiling at the site a bottom sensor suggested the presence of small-scale topography that might be responsible for these differences. Currents at Site 2 (S2 in Figure 1) have been estimated from a thermistor cable suspended beneath the ice shelf. The analysis yielded the lengths of the major axes of the O_1, K_1, M_2 and S_2 ellipses and also the phase for each constituent. The method of analysis is described in the Appendix. Modeled and inferred major axes amplitudes and phases generally agree to within 0.2 cm s^{-1} and 20°, the only exception being the M_2 amplitude, which was 25% (7 cm s^{-1}) lower than the value derived from the observations.

Indirect observational evidence is available to support the relative current strengths along Ronne Ice Front. *Haase* [1986] obtained a transect of surface sediment samples along Ronne Ice Front within 3.5 km of the barrier that showed a broad diversity of sediments, suggesting a wide range of current environments (Figure 3). Over Berkner Shelf the sediments consisted purely of sand. They contained structures typical of a high-energy current regime, that is, velocities over 20 cm s^{-1}, 1 m above the seafloor over the shallowest areas of Berkner Shelf. Observations by *Foldvik et al.* [1985], like the model results, reveal RMS water velocities of 26-30 cm s^{-1}, with peak spring velocities reaching 1 m s^{-1}. In the area of intermediate water depth (400-500 m) along the central ice front silt, and clay fractions were found to be high. The high clay content suggests very low velocities of 0-2 cm s^{-1}. Over the central ice front section, mean velocities from the model are 10 cm s^{-1}, with current measurements within 20 m of the seafloor giving essentially the same value (E. Nygaard, Preliminary results from current measurements in position R2 (76°29'S, 53°00'W) outside the Ronne Ice Shelf in the southern Weddell Sea 1993-1994, unpublished report, Geophysical Institute, Bërgen, Norway, 1995) (hereinafter referred to as E. Nygaard (unpublished report, 1995)). , both higher than suggested by the sediments. On the ridge, further to the northwest, the sediments contain mainly fine sands, with current ripples indicating water velocities of at least several centimeters per second. RMS model velocities were 18-20 cm s^{-1} over the ridge. Finally, over Ronne Depression and close to the Antarctic Peninsula the gravel and mud content increases. The gravel and drop stones are of glacial origin with the muds indicating a low current regime. As with the central ice front section, modeled velocities are higher (13 cm s^{-1}) than suggested by the sediments. Two additional sample sites, 10-15 km from the ice front, exhibit an increase in silt and clay, suggesting weaker currents in the deeper waters away from the influence of the ice shelf. Modeled RMS velocities offshore from Ronne Ice Front are generally lower than the ice front currents, and in this way consistent with the sediment content.

There are several potential sources of error in the model. The

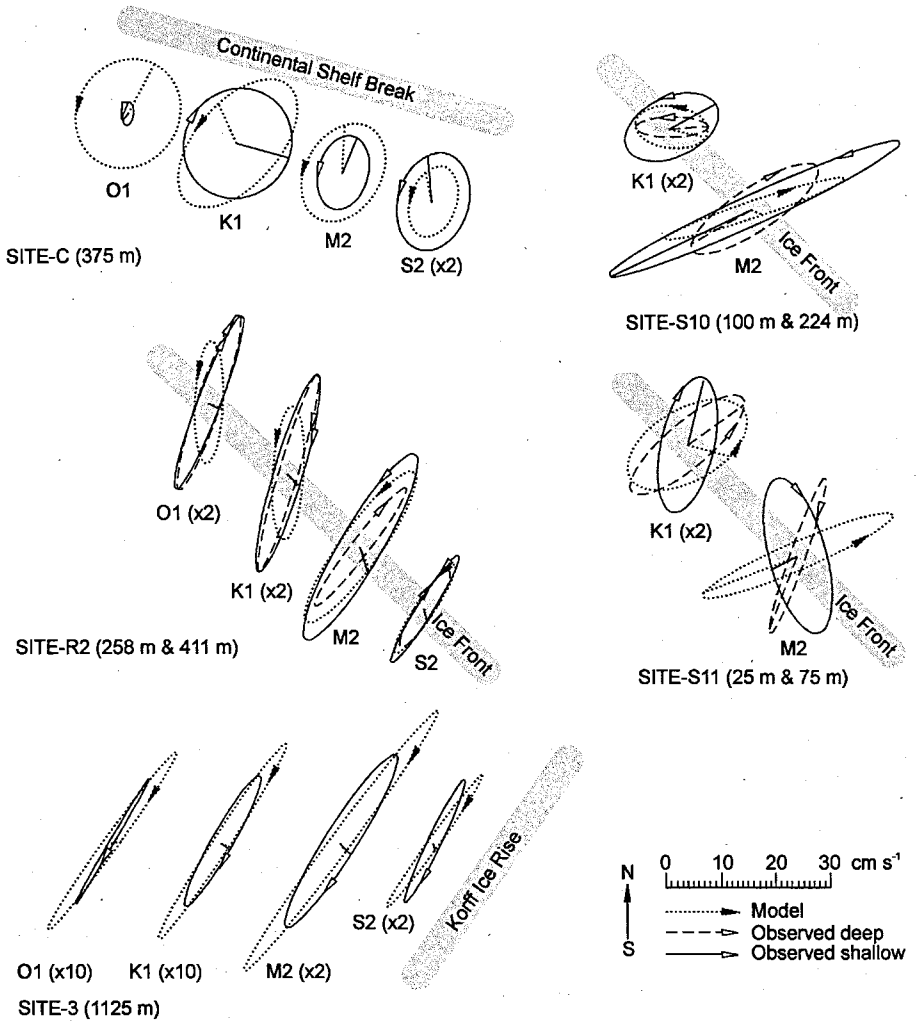

Figure 5. Tidal ellipses from the available current meter sites overlain with results from the model. Where the constituent is small a multiplying factor is applied and indicated. The current vector's sense of rotation is indicated by an arrow, and its phase by line from the ellipse center. The orientation of any significant nearby topography and the depth of the instrument are indicated. The ellipses from site C are shown to represent the continental shelf break sites.

forcing at the open boundary was provided by a larger area model which used a poorly known bathymetry. In particular, the location of the edge of the Larsen continental shelf was wrong by up to 100 km. The Schwiderski global tidal data set used to force the larger scale model is also likely to be less accurate in this region [*Le Provost et al.*, 1995]. In the present application of the model, the water column thickness over the ice shelf area is subject to errors both in the seabed depth and ice thickness, neither of which are well known at the model resolution. The location of some of the current meter sites is not ideal for testing modeled currents. Examples are sites at the ice front where the water column has a step change in thickness of hundreds of meters leading to significant errors in current phase, amplitude, and rotation. Overall, however, the model has achieved a reasonable fit to the known data, successfully reproducing the general features of the tidal flow.

4. Tidal Energy and Vertical Mixing Beneath the Ice Shelf

Tidal currents are likely to be the principal source of energy for mixing in those areas of the southern Weddell Sea isolated from atmospheric forcing by the presence of ice shelves and fast ice. Frictional drag from the seafloor and ice shelf base produces vertical shear, the resultant turbulence causing vertical mixing through the water column. Assuming a quadratic drag law, the rate of dissipation of energy by surface friction E is proportional to the cube of the depth-averaged velocity $\mathbf{u}$ and is given by $E=\rho k|\mathbf{u}|\mathbf{u}\cdot\mathbf{u}$. Variables ρ and k are the density of seawater and the bottom friction coefficient which are assigned the values used in the model run (1028 kg m^{-3} and 0.0025). As in the model run, to account for the presence of the ice shelf base as a second frictional surface, the bottom friction coefficient was doubled for grid points covered by ice shelves. As energy dissipation is proportional to the cube of the water speed, areas of high dissipation are spatially similar to those with high currents, that is, areas of shallow water.

The potential for ice shelf flexure at the grounding lines to act as a sink for tidal energy was first discussed by *Doake* [1978]. Such an energy sink is not present in the model used in this study. Although *Smithson et al.* [1996] found evidence that higher friction coefficients beneath the ice shelf may improve the fit between modeled and observed tidal elevations, predicted tidal elevations and currents modeled by *Robertson et al.* [1998] and in this study agree reasonably well with observations, suggesting that

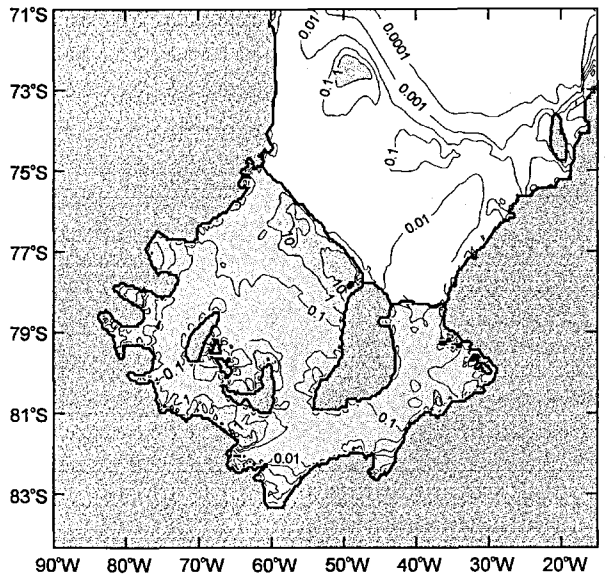

Figure 6. The minimum basal melt rate required to maintain stratification of the water column contoured using a $\log_{10}$ scale. Areas where basal melt rate to maintain stratification is above 1 m yr^{-1} are highlighted.

energy dissipation can be adequately modeled without resorting to additional sinks at grounding lines. These results agree with *Vaughan* [1995], who also suggests that the tidal flexure of ice shelf margins does not dissipate much energy.

From this study the total dissipation over FRIS is 25 GW, nearly an order of magnitude greater than the 3.5 GW dissipated beneath Ross Ice Shelf [*MacAyeal*, 1984a] and accounting for approximately 1% of the world's total tidal dissipation budget [*Tsimplis et al.*, 1995]. Almost three quarters of the energy is lost in the shallow region south of Ronne Ice Front, with most of the remainder being dissipated south of Henry Ice Rise. The highest dissipations beneath the ice shelf (> 1 W m^{-2}) are near to the eastern end of Ronne Ice Front. Over the adjacent continental shelf, which has a thicker water column and therefore lower water velocities, the dissipation is significantly less: a total of 8 GW, half of which is lost in a small area around 73°S, 50°W.

It has been estimated that 1-2% of the tidal energy dissipated at frictional surfaces is available for vertical mixing of the water column [*Fearnhead*, 1975; *Schumacher et al.*, 1979]. The power required to mix the water column is the power needed to distribute fresh water melted from the ice shelf base through the water column and is therefore dependent on the melt rate F. The power required is given by $2F\rho\beta gSD$ where $\beta = 1/\rho\,(\partial\rho/\partial S) = 0.8 \times 10^{-3}$ $(‰)^{-1}$, S is the salinity of HSSW (34.75 ‰) in the lower half of the water column, and D is the water column thickness. The power available from tidal dissipation is $\alpha\rho k|\mathbf{u}|\mathbf{u}\cdot\mathbf{u}$, where α (0.015) is the fraction of total energy estimated to be available for vertical mixing. Therefore for a water column to be well mixed, the melt rate F must be less than $F_m = \alpha\rho(k|\mathbf{u}|\mathbf{u}\cdot\mathbf{u})/(1/2\rho\beta gSD)$ [*MacAyeal*, 1984a]. Conversely, in areas where melt rates are greater than F_m, stratification will prevail. Figure 6 shows the pattern of distribution of F_m, rather than definative values, based on best estimates of the parameters which can be varied, for example, the fraction and composition of HSSW in the lower portion of the water column [*Nicholls and Makinson*, 1998]. Direct verification of the extent of a stratified or well-mixed water column is limited by scarcity of observations. Likewise, basal melt rates are poorly known and are normally determined using indirect approaches such as glaciological measurements [*Jenkins and Doake*, 1991], ice shelf temperature profiles [*Grosfeld et al.*, 1992] and oceanographic data [*Nicholls and Makinson*, 1998].

Near Ronne Ice Front melt rates of 1.5-6 m yr^{-1} have been determined by a number of different methods [*Kohnen*, 1982; *Jenkins and Doake*, 1991; *Grosfeld et al.*, 1992]. Here tidal oscillations force warm surface waters beneath the ice shelf, causing rapid melting [*Gammelsrød and Slotsvik*, 1981], particularly during summer months when there is an additional heat input into the offshore ocean water. Despite the high melt rates, the model results predict that the water column will be well mixed, for F_m in these areas is over 10 m yr^{-1} (Figure 6).

In areas of the ice shelf cavity where ice crystals form in the water column [*Bombosch and Jenkins*, 1995], such as the central Ronne Ice Shelf [*Robin et al.*, 1983; *Nicholls et al.*, 1991], the basal melt rate is negative. The rate of negative melt depends on whether the ice crystals are held in suspension, or whether they are deposited on the ice shelf base. Ice crystals suspended in the water column provide additional buoyancy, and consequently contribute to the stratification [*Jenkins and Bombosch*, 1995]. Tidal stirring, when F_m<0, therefore has the effect of enhancing stratification but also of reducing the deposition of ice at the ice shelf base and mixing warmer water up through the water column.

Closer to the grounding lines, where the ice shelf is thickest, the pressure freezing point of seawater is depressed by up to 1°C, and relatively high basal melt rates are possible if HSSW is mixed up through the water column. Indeed, melt rates of between 3.5 and 7 m yr^{-1} have been calculated within 20 km of the grounding line of Rutford Ice Stream [*Jenkins and Doake*, 1991; *Smith*, 1996; *Corr et al.*, 1996]. Here, however, the model predicts that the water column is stratified, as $F>F_m$ (Figure 6). In these areas, the high vertical heat fluxes necessary to maintain such basal melt rates are probably induced by shear between the deeper, warmer water and plumes of ISW rapidly ascending the steep basal slope [*MacAyeal*, 1984a; *Jenkins*, 1991]. Such ISW plumes could be initiated very near the grounding line where the water column finally pinches out, and where tidal mixing is likely to be locally high. The pinching out of the water column is not properly represented at the resolution of this model. An extended region of thin cavity south of Henry Ice Rise leads to F_m exceeding 10 m yr^{-1} (Figure 6), and a well-mixed water column is therefore likely. In this area the basal melt rate is expected to be high compared with nearby stratified areas.

Beneath FRIS, vertical mixing competes with the stratifying influence of basal melting. Tidal fronts separate the abrupt changes in water properties caused by variations in the level of vertical mixing between well-mixed and stratified regions [*Simpson*, 1981]. The balance between tidal mixing and buoyancy input from basal melting therefore determines frontal positions. A tidal front causes an inclination of isopycnals which leads to along-front geostrophic currents. The model predicts tidal fronts near the ice front where the direction of any induced flow would be along the front towards the southeast (Figure 6). Beneath the ice shelf, however, the small density contrasts that are possible across a mixing front (0.2 kg m^{-3}) are likely to be too weak for the development of frontal flows.

5. Residual Current Generation and Model Results

5.1. Eulerian Residual Currents

Unlike the oscillatory component of the tides, tidal rectification causes a net displacement of water parcels over the tidal cycle.

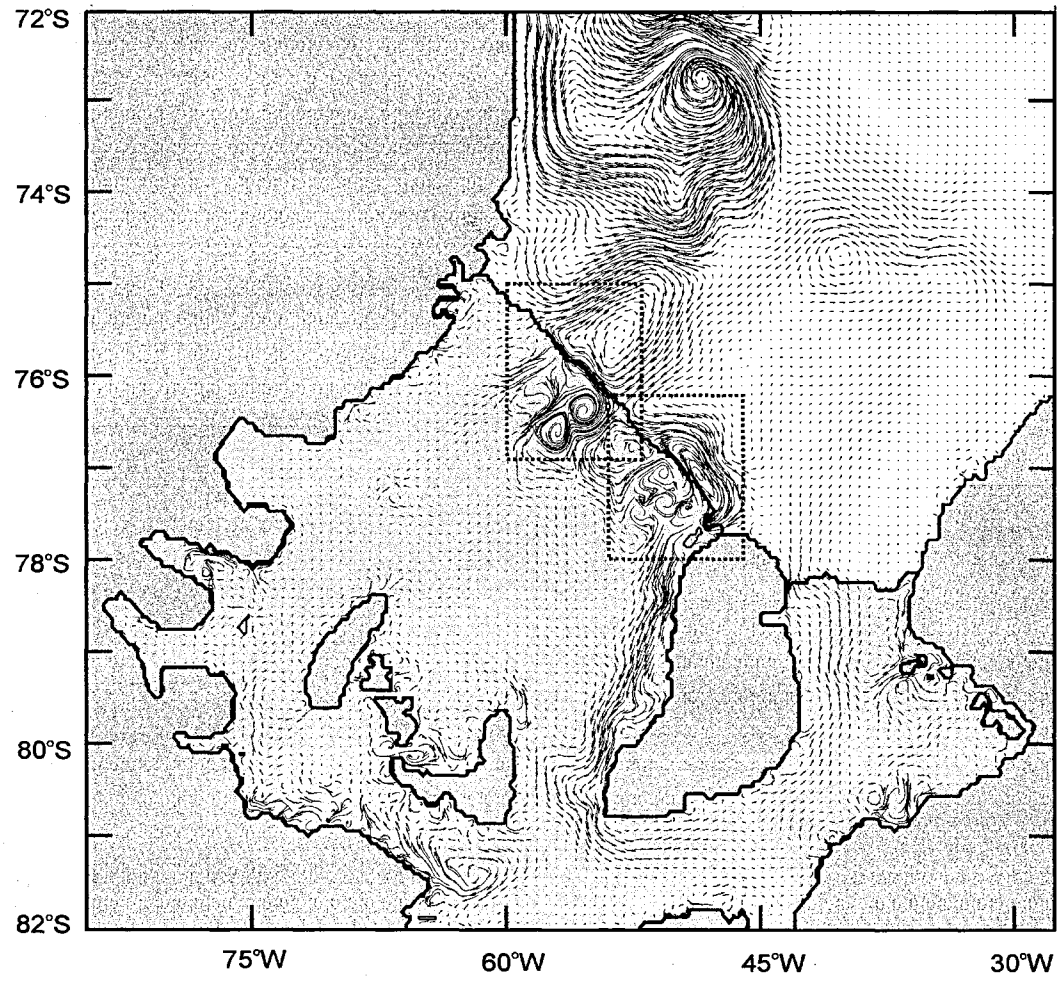

Figure 7. The Lagrangian residual tidal currents obtained by removing the oscillatory components from the time series of water current. These mean currents are strongest over the western continental shelf, along Ronne Ice Front and the western coast of Berkner Island, and south of Henry and Korff Ice Rises. The boxes indicate the regions shown in Figures 10 and 11.

Robinson [1981] identified three mechanisms for the generation of tidally rectified flows. He showed that the strength of the flows depends on the horizontal and vertical length scales of topography, and the magnitude of the tidal current constituents. Tidal currents flowing across the step change in water column thickness present at an ice front will generate a residual flow along the barrier with the ice shelf on the left. This current is the Eulerian residual current and can be detected using moored current meters.

Robinson [1981] noted that a model will underestimate residual currents if the grid spacing underestimates the topographic gradients. Even if the topographic features are well resolved, the residual currents will be underestimated in areas where the tidal excursion is small compared with the grid size. To improve the estimation of residual currents in the model we increased the node density from 15 to 35 nodes per degree of latitude and from 4 to 8 nodes per degree of longitude. For the area of the ice front this yields a grid spacing of less than 3.5 km. To comply with the CFL condition, the time step was reduced from 15 to 8 s. All other parameters remained the same. As before, harmonic analysis was used to find the phase and amplitude of the principal tidal constituents, giving the same results as the lower resolution model. These oscillatory components were then removed from the modeled currents to reveal the Eulerian residuals.

Robinson [1981] found that an adequate approximation for the maximum residual flow at a sharp topographic step such as occurs at the ice front is given by $V_a = 0.15\times10^{-4}(\Delta h/h)E$. V_a is the maximum speed in the flow and is found at the step itself. $\Delta h/h$ is the depth change ratio of the topographic feature, provided its spatial extent is less than the tidal excursion E, perpendicular to the feature. As an example, water column thickness changes of 300 to 100 m in the ice front region of Berkner Shelf, coupled with 8 km average tidal excursions perpendicular to the ice front, will induce a residual Eulerian velocity of 8 cm s^{-1} parallel to the ice front. The agreement between this value and the model prediction (7-8 cm s^{-1}) gives confidence that the model resolution in this area is adequate to represent the tidal residuals fully. The only direct determination of the mean Eulerian flow in this region is from current meter deployments close to the ice front on the Berkner Shelf at S11 and S10. S11 was at the ice front itself, and the record showed a mean surface current of 8 cm s^{-1} directed northwest along the ice front. Below the ice shelf draft, however, at a depth of 75 m, the measured mean current was 4 cm s^{-1} to the west. S10 was located 10 km offshore, close to the center of an offshore gyre in the modeled residuals. The current meter record showed a mean current of approximately 2 cm s^{-1}, directed to the northwest at 100 m depth and to the northeast at 224 m depth. For this location

the model predicted a residual of 1.5 cm s^{-1} to the northwest. In both cases the model is in closest agreement with the near surface measurements. In deep water areas with less tidal activity and large topographic gradients, such as Filchner Ice Front, the residuals will be underestimated due to insufficient model resolution. At Filchner Ice Front the average tidal excursion is approximately 1.1 km and the water column thickness changes from 1100 to 600 m. This gives an expected residual current, V_a, of 0.75 cm s^{-1}, compared with the model prediction of 0.25 cm s^{-1}. At the continental shelf break a similar effect is seen where steep gradients and small tidal excursions lead to an underestimation of residual currents by up to 50%. The Filchner Ice Front and the steep continental slope represent an extreme; in most areas the residual currents are adequately resolved.

5.2. Lagrangian Residual Currents

In addition to the Eulerian residual currents a water parcel may experience Stokes Drift resulting from the spatial variations in the characteristics of the oscillatory tidal current. This means that the paths actually followed by a water parcel, which are needed when investigating net fluxes, cannot be determined from Eulerian residuals alone. Stokes Drift is typically one third the size and in the opposite direction to the Eulerian residual flow [*Loder*, 1980]. It is greatest where the rotation of the tidal ellipse reverses across the ice front. The net water parcel motion due to tidal activity is the sum of the Eulerian residual current and Stokes Drift and is the Lagrangian residual current (Figure 7).

The Lagrangian motion of water parcels, or tracers, was determined from the hourly Eulerian velocity data from the model by trilinear interpolation onto 2 min intervals. A tricubic spline interpolation gave no significant improvement in the results. Examples of the Lagrangian motion of three tracers over a 35 day period are shown in Figure 8a, illustrating the combination of oscillatory and residual currents. Using a 49 hour low-pass filter, the tracer trajectories were smoothed and are indicated by the heavy lines. In Figure 8b the 44 smoothed tracer trajectories show a particular point near the ice front, indicated by a cross, north of which they continue along the ice front, and south of which the tracers are drawn under the ice shelf. This example illustrates the capacity of the residual tidal currents to transport water into and out of the ice shelf cavity. Unlike the purely oscillatory tidal motion, this mechanism is capable of ventilating the cavity well beyond one tidal excursion. Such exchange across the ice front is not seen by *Grosfeld et al.* [1997] in their thermohaline circulation model, in which the ice front acts as a barrier.

In order to determine mean Lagrangian velocities, tracer trajectories must be averaged over a sufficiently long time period. For each grid node a tracer was introduced every hour for 709 hours, the period of almost exactly two spring neap cycles. The Lagrangian trajectory of each tracer was determined using the interpolation method described above and recorded over a 100 hour period. Each trajectory was low-pass filtered with a 49 hour cutoff to remove the oscillatory part of the tide. The displacement of the tracer was calculated over the central 50 hour period. Finally, the mean of all 709 tracer displacements yielded a representation of the mean Lagrangian velocity at the position where the tracers were originally introduced. Volume fluxes could then be determined by integrating the product of the mean Lagrangian velocities and water column thickness across sections. To test the consistancy of the mean Lagrangian circulation, the net volume flux over sections bounded by coastlines were calculated. Several sections, including the front of FRIS, gave net flows close to zero (< 1000 m^3 s^{-1}). Figure 9 shows a cross section of water

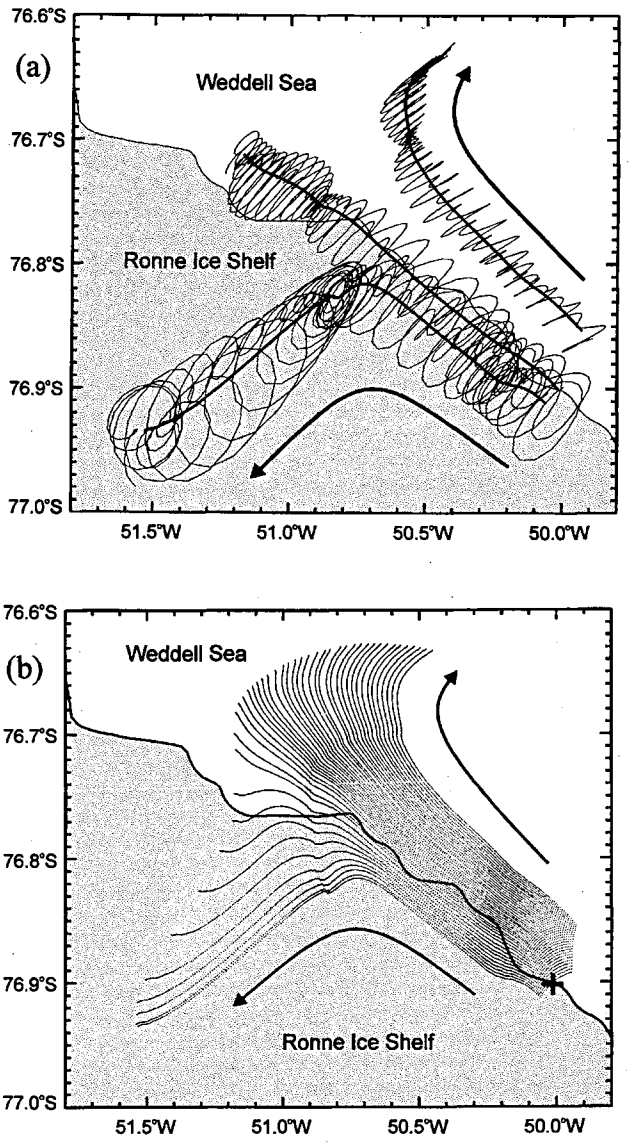

Figure 8. Examples of Lagrangian tracer trajectories over a 35 day period in the area of the ice front shown by the box in Figure 10. The arrows indicate the direction of flow. (a) Three Lagrangian tracer trajectories with smoothed trajectories indicated by the heavy lines. (b) Smoothed trajectories of 44 tracers with an initial spacing of approximately 200 m. The plus indicates where tracers either remain in open water or enter the sub–ice shelf as the flow bifurcates.

depth, water speed, and water flux perpendicular to the western section of Ronne Ice Front at 55°W. The finite model resolution makes the step in water column thickness appear as a steep slope, with the peak flux centered on the ice front. Over the model domain strong residual Lagrangian currents are present in three main areas (Figure 7):, the ice front region of Ronne Ice Shelf, the western continental shelf, and the western coast of Berkner Island.

5.3. Eastern Ronne Ice Front

The greatest depth changes and highest tidal velocities are found along the ice front northwest of Berkner Island (Figure 10) and cause the highest residual velocities of 5.6 cm s^{-1}. This flow (A, in Figure 10) is northwest, parallel to the ice front, with

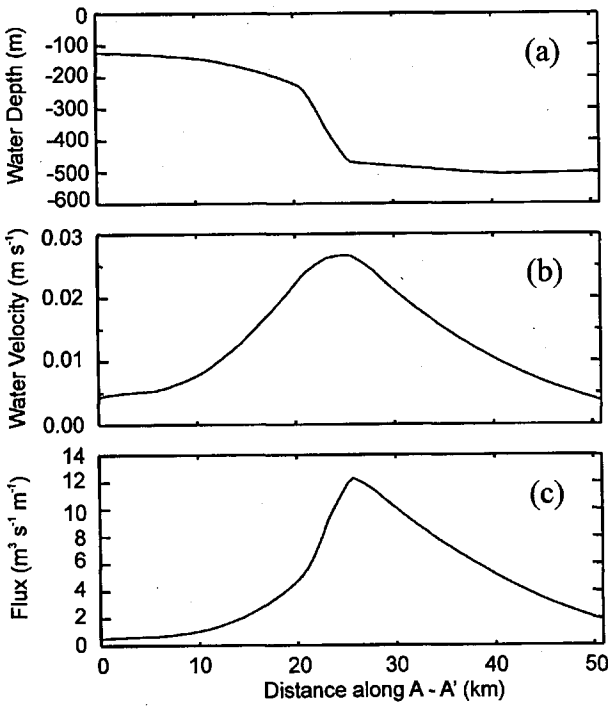

Figure 9. A section perpendicular to Ronne Ice Front at 55°W (A-A' in Figure 11) showing (a) the step change in the water column thickness at the ice front as represented by the model, (b) the mean residual water velocity parallel to the ice front with the peak velocity centered on the ice front, and (c) the mean volume flux across A-A', which totals 250,000 m^3 s^{-1}.

volume transports of up to 135,000 m^3 s^{-1} at 50°W. North of the ice front there is an elongated clockwise gyre (G1) parallel to and centered 10-15 km from the ice front. The gyre extends up to 50 km northeast from its center and has a circulation time of about 1 year. The return Lagrangian volume flux (B) associated with this Berkner Shelf gyre is 175,000 m^3 s^{-1} at up to 2 cm s^{-1}. Beneath the ice shelf, complicated topography results in several eddies that transport water into and out of the sub–ice shelf cavity. The only outflow (C) in this region lies between 49° and 49.5°W (20,000 m^3 s^{-1}). At two locations, water flows from the shore lead into the cavity. Between 50.8°W and 51.8°W the flow along ice front diverges, with one branch forming a diffuse inflow (D) of 80,000 m^3 s^{-1}. Further to the east the second inflow (E) of 55,000 m^3 s^{-1} is concentrated along the western coast of Hemmen Ice Rise before it is joined from the west by a 35,000 m^3 s^{-1} flow. This combined flow then continues southwards along the Berkner Island coast.

5.4. Western Ronne Ice Front

The largest along-ice front flux (F in Figure 11) is situated between the center of Ronne Ice Front and the submarine ridge to the east of Ronne Depression. There between 150,000 and 300,000 m^3 s^{-1} flows parallel to a 100 km length of the ice front. The overall structure consists of anticlockwise and clockwise gyres either side of the barrier. Centered 40-50 km from the ice front, the offshore gyre (G2 in Figure 11) is relatively diffuse, extending more than 100 km to the northeast from its center. Typically, velocities of 0.5 to 1 cm s^{-1} give a circulation time of 2.5 years. The total flow northeast towards the continental slope from the ice front (G) is 330,000 m^3 s^{-1}. The corresponding inflow (H) is 280,000 m^3 s^{-1} at 0.6 cm s^{-1}. Beneath the ice shelf two large circulations, each 40-50 km in diameter, merge to form a larger anticlockwise circulation. To their west residual currents are associated with the submarine ridge. Two inflows (K and M) are located at 55.4°W (50,000 m^3 s^{-1}) and at 57.3°W (70,000 m^3 s^{-1}), with two outflows (J and L) located at 54.3°W (175,000 m^3 s^{-1}) and at 56.8°W (20,000 m^3 s^{-1}). There is a point of convergence of residuals at the ice front, centered on 53.5°W. West of this point, water masses flow parallel to the ice front toward Ronne Depression. To the east, between 52°W and 53°W, there is a broad outflow (N, 20,000 m^3 s^{-1}) which becomes incorporated into the Berkner Shelf offshore gyre (G1, Figure 10).

5.5. Continental Shelf

Over the continental shelf, close to the peninsula, a substantial southerly flow (1.4 cm s^{-1} and 500,000 m^3 s^{-1}) extends from 71°S (the model boundary) to 74°S (Figure 7) where the majority turns to the east and joins the northern tip of the gyre from the western Ronne (G2, Figure 11). In a similar model that extends to the northern tip of the Antarctic Peninsula, the flow appears to originate as far north as 69°S [*Robinson*, 1996]. The region around Belgrano Bank is part of the continental slope where there is significant diurnal amplification, and steep topographic gradients, resulting in strong residual currents. A large anticlockwise circulation dominates the residual current pattern over the western continental shelf north of FRIS (Figure 7). Reducing the gradient of the continental slope in this region by 50% has the effect of reducing both the diurnal amplification and residual currents by a similar proportion, though the overall flow regime remains similar. The only other location where residual currents flow south on to the continental shelf is at 74°S 43°W. There the velocities are lower, 0.3-0.4 cm s^{-1}. Over the open ocean no account is taken of any thermohaline or wind-driven circulation which are poorly known. Estimates by *Gill* [1973] suggest velocities of the order of centimeters per second; consequently, residual currents will be modulated with currents driven by other processes.

During 1986 three huge icebergs broke away from Filchner Ice Shelf [*Ferrigno and Gould*, 1987], two of which became grounded on Berkner Shelf between 40-45°W and 76-77°S. The model was used to determine their effect on the residual currents, assuming that the icebergs were grounded over their entire area. Without the grounded icebergs, the residual currents in this area are not significant. With them, weak residual currents form an anticlockwise flow around the bergs. Ungrounded parts of the bergs would effectively form ice front type features and have strong associated residual flows.

5.6. Ice Shelf Cavity

The flow around Berkner Island (Figure 7), is the largest residual flow entirely beneath the ice shelf. At 78°S the peak velocity is 3 cm s^{-1} with a flux of 90,000 m^3 s^{-1}. As the water column thickness increases, velocities decrease but the volume flux increases to over 100,000 m^3 s^{-1}. The increased flux results from the addition of weak easterly residual flows set up along the water column contours in the central Ronne Ice Shelf. At the southern tip of Berkner Island peak velocities are only 0.5 cm s^{-1} in the 500 m water column. Beyond this point the flow turns to the east and north following the coast at velocities of between 0.2-0.4 cm s^{-1}, until eventually crossing the Filchner Ice Front with a flux of 125,000 m^3 s^{-1} and continuing northward. The time taken for a water parcel to travel to the southern tip of Berkner Island is approximately 2 years, with another 8 years needed for it to arrive at the Filchner Ice Front.

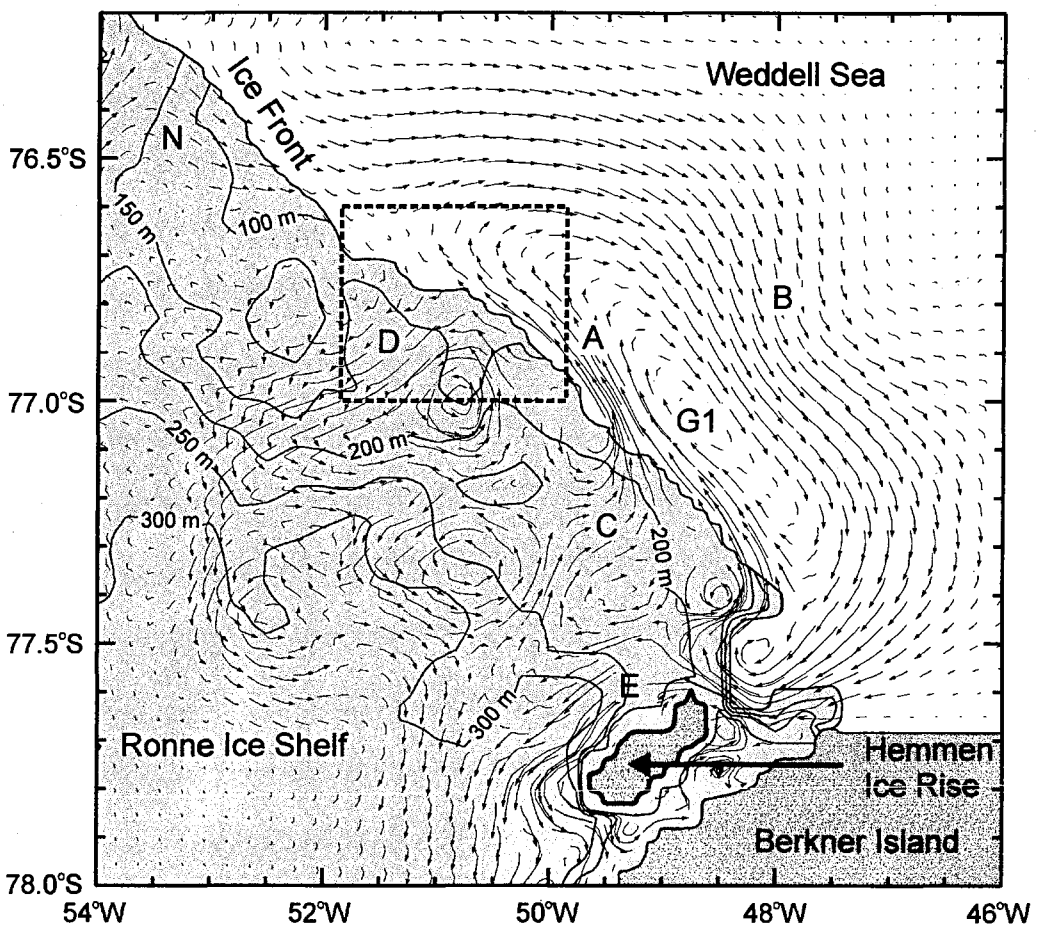

Figure 10. Smoothed Lagrangian residual trajectories over a 7 day period in the region of Berkner Shelf. Grounded ice is represented by the darkest shading, and floating ice shelf is represented by the lighter shading. The contours are of ice shelf draft at intervals of 50 m. The box marks the region shown in Figure 8.

Korff Ice Rise, Doake Ice Rumples, and Henry Ice Rise make up the areas of grounded ice that occupy the southern central region of Ronne Ice Shelf (Figure 1). Between these areas of grounded ice there are three channels, 5-20 km wide with a water column of approximately 50 m, connecting the central and southern Ronne Ice Shelf cavity. These channels have high residual currents of up to 6 cm s^{-1} with associated flows of between 3 and 6000 m^3 s^{-1} yielding a total flux of 10-15,000 m^3 s^{-1} from the southern trough to the central Ronne Ice Shelf. Either side of the channels and around the ice rises the residual currents mainly constitute a series of headland eddies. To the south of the ice rises there is a weak westerly flow (0.5-3 cm s^{-1} and 30-60,000 m^3 s^{-1}) found principally along the southern coast of the trough and comprising several eddies. There are also many vigorous gyres that are restricted to small coastal features and which do not contribute to the larger scale transport.

Over the southern Weddell Sea continental shelf and FRIS, only sparse bathymetric data are available because of the inaccessibility of the region. In the western Weddell Sea, heavy sea ice conditions persist throughout the year, greatly limiting shipborne observations. Beneath FRIS itself the geometry of the sub–ice shelf cavity can be determined only by a combination of seismic surveys and ice thickness data. The most tidally active regions beneath the ice shelf also have the shallowest water column, particularly in the region of the eastern Ronne Ice Front. Seismic data coverage is most dense over this area [*Vaughan et al.*, 1995], typically every 5-10 km providing increased confidence in the model results. Elsewhere, uncertainties in the water column thickness greatly reduce confidence in the detailed model predictions. Nevertheless, the types of structure in the modeled residual current field, and strength of the flows, are expected to be representative of the actual residual currents.

6. Impact of Tidal Processes on Hydrography and Ice Shelf Morphology

Filchner-Ronne Ice Front encompasses a wide range of current environments with different oceanographic processes, such as thermohaline circulation, residual currents and mixing, dominating certain sections of the ice front hydrography. We now consider how mixing and the residual currents predicted by the barotropic model would be expected to affect the distribution of tracers (temperature and salinity) observed at Filchner-Ronne Ice Front, and the topography of the ice shelf itself in the vicinity of the ice front. CTD data have been collected along the ice front during several cruises over the last 30 years: USCGC *Glacier* in 1968 [*Elder and Seabrooke*, 1970] and in 1973 [*Carmack and Foster*, 1975]; R/V *Polarsirkel* in 1980 [*Foldvik et al.*, 1985]; *Polarstern* in 1984 [*Rohardt*, 1984]; and R/V *Lance* in 1993 [*Gammelsrød et*

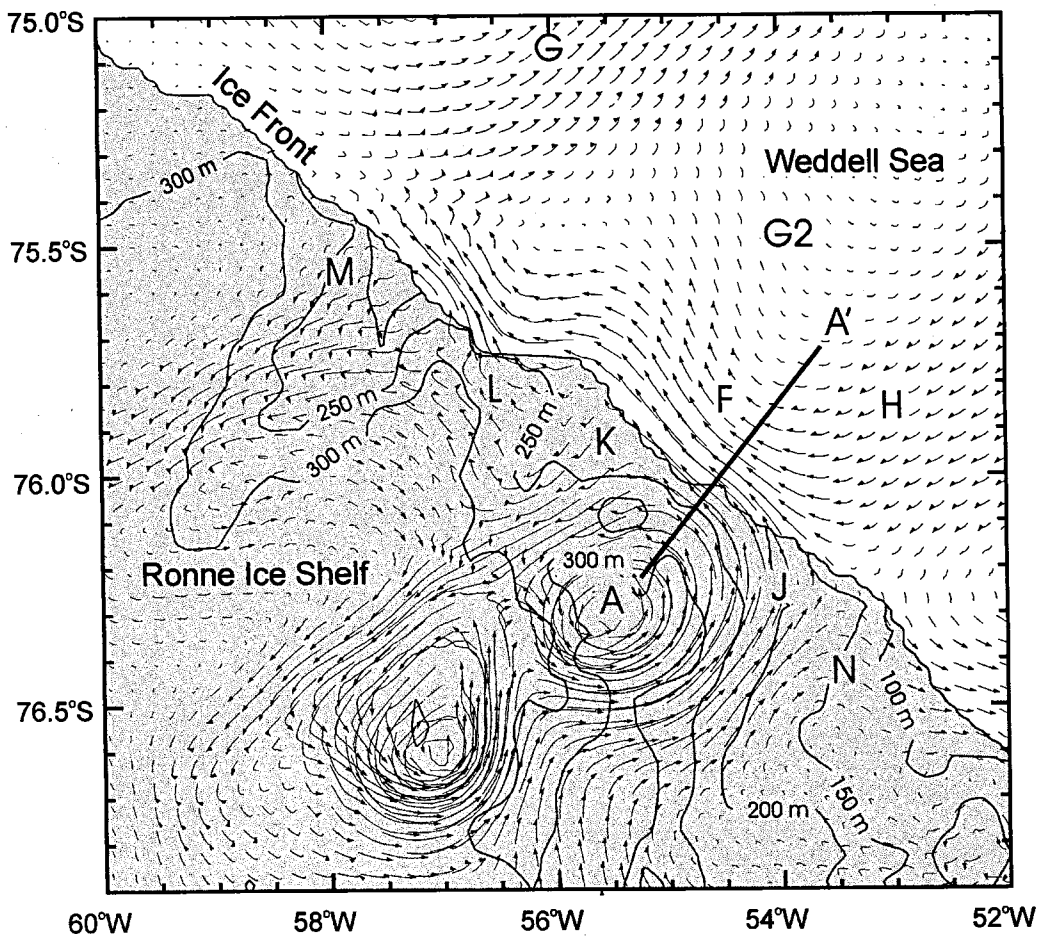

Figure 11. Smoothed Lagrangian residual trajectories over a 7 day period in the region of the western Ronne Ice Front. The ice shelf is represented by the shaded region and the contours give the ice shelf draft.

al., 1994]. All the hydrographic surveys were conducted during the austral summer months with the last three spanning the majority of the Filchner-Ronne Ice Front.

6.1. Tidal Oscillations and Mixing

CTD measurements in tidally active regions are often affected by the tidal state during the measurement. One cause of this is the presence of horizontal gradients in the measured properties over the extent of the tidal excursion. Such gradients are likely near the ice front: the sudden change in water column thickness gives strong gradients in tidal energy available for vertical mixing, introducing the possibility of tidal fronts. The difference in the temperature of the water being mixed down from the upper boundary on either side of the ice front, especially during the austral summer, will also compound the effect. The motion of mixing fronts back and forth across the ice front means that the results of CTD measurements made in the shore lead will be strongly influenced by the state of the tide. As an example, during spring tides on Berkner Shelf, measurements made at the ice front toward the end of a period of inflow would be sampling water that was previously 5 km offshore. Conversely, at the end of an outflow, the water being sampled will have originated up to 15 km beneath the ice shelf. Yo-yo CTD stations close to the ice front occupied on Berkner Shelf at 50° 07'W [*Foldvik et al.*, 1985] and 50° 40'W [*Rohardt*, 1984] show that during periods of outflow there is a cooling throughout the water column, typically by a few tenths of a degree, but in extreme cases by up to 1°C in near surface waters. An additional effect influencing ice front CTD measurements results from the combination of strong mixing beneath the ice shelf and the purely periodic advection of water back and forth across the ice front. As the flow field is not completely reversible due to mixing, this is likely to result in an efficient horizontal transfer of tracers into and out of the cavity, but with no net water flow [*Wunsch*, 1996].

6.2. Residual Currents

In the remainder of this section we consider the effects of the transfer of water itself by the residual tidal currents described in the last section. Away from the ice front the tidal residuals are much weaker, and in the absence of knowledge of the wind or buoyancy-forced flow over the continental shelf it is not clear whether they are significant. We therefore concentrate on the ice front region, where most of the CTD stations have been located. The salinity and potential temperature sections compiled by *Foldvik et al.* [1985] are shown in Figures 12a and 12b and will be used for reference, together with smoothed Lagrangian trajectories over a 6 week period along the whole Filchner-Ronne Ice Front region (Figure 12c).

6.3. Ice Shelf Cavity Outflows

Between 48°W and 51°W, the modeled residual flow at the ice front is almost parallel to the barrier (Figure 10), though there is a net outflow from beneath the ice shelf. Outflowing water would

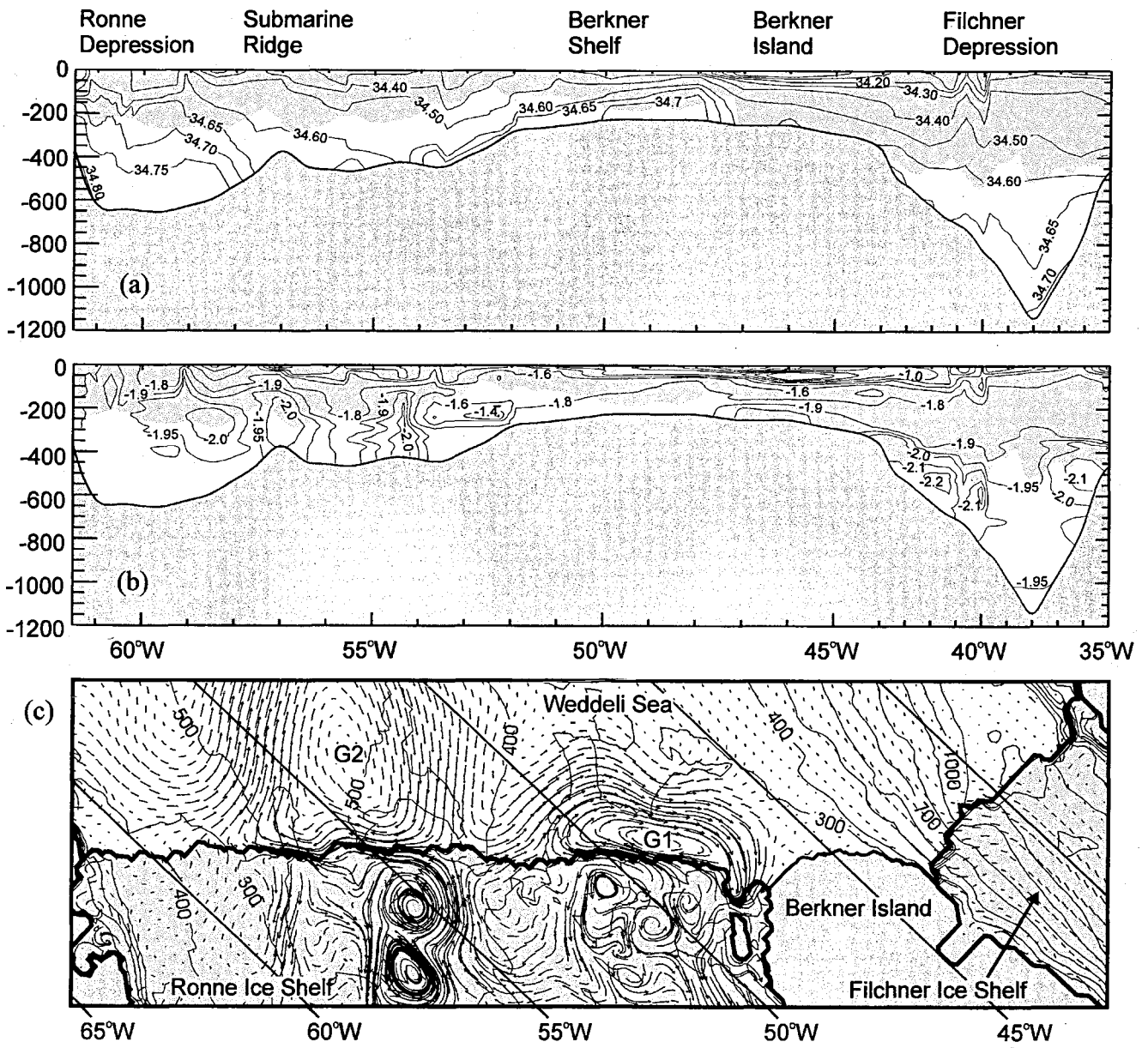

Figure 12. Sections of (a) salinity and (b) potential temperature along the ice front from Ronne Depression to the Filchner Depression [after *Foldvik et al.*, 1985]. The bathymetry is represented by the darkest shading, and the ice shelf draft is indicated by the lighter shading. (c) Lagrangian trajectories over a 6 week period in the region of Filchner-Ronne Ice Front. The contours are of water column thickness at intervals of 100 m.

normally be expected to show signs of glacial melt in the potential temperature-salinity (θ-S) signature, and it is surprising that only one of the yo-yo sites located at the ice front revealed ISW in the water column during the outflow part of the tidal cycle [*Foldvik et al.*, 1985]. The S and θ sections presented in Figure 12 show no evidence of a steady ISW presence in this region, and it is unclear whether there are indeed no tidally driven outflows, or whether they simply do not contain ISW. The offshore gyre (G1) in this region would be expected to increase the residence time of water on the Berkner Shelf, thereby increasing the water's salinity through sea ice formation.

West of 54°W, *Foldvik et al.* [1985] and *Rohardt* [1984] observed three ISW plumes emerging from beneath the ice shelf at 54.2°W and 56.8°W on the submarine ridge and at 58.5-59.7°W in Ronne Depression. *Gammelsrød et al.* [1994] observed ISW in the same locations but did not differentiate between the two western plumes, possibly because of the lower density of CTD stations in that area. At 53.25°W, modeled residual currents converge on the ice front, before diverging along the ice front to the east and west (Figure 11). West of this point any ISW emerging from beneath the ice shelf will remain close to the ice front, trapped by the flow parallel to the barrier. The modeled Lagrangian residuals predict a strong outflow between 53.9°W and 54.5°W (J) and weaker outflow associated with the submarine ridge between 56.7°W and 57°W (L). These predicted outflow locations agree with the positions of the ISW plumes observed by *Foldvik et al.* [1985], *Rohardt* [1984], and *Gammelsrød et al.* [1994]. Using the model to predict the tidal state when CTD measurements were made along the western Ronne Ice Front, the observed hydrographic features do not appear to be the result of periodic

tidal excursions. Residual current outflows might therefore explain the two eastern ISW plumes observed by *Foldvik et al.* [1985] (Figure 12). The westernmost ISW plume (58°W) appears unlikely to be primarily the result of residual tidal currents: the residual outflow at this location is weak, at about 0.3 cm s^{-1}. The section in Figure 12b shows that unlike the two eastern plumes which have their temperature minima at, or close to, the seafloor, the western outflow is centered around 250 m with Western Shelf Water (WSW) below it. This structure suggests an outflow underlain by an inflow, which is not consistent with a tidally forced barotropic current. We therefore suggest that the western plume is driven primarily by thermohaline processes.

6.4. Ice Shelf Cavity Inflows

In areas where inflows are anticipated, CTD sections at the ice front will give few indications. The maximum in the water temperature between the two eastern ISW plumes around 55.2°W (Figure 12b) [*Foldvik et al.*, 1985; *Rohardt*, 1984] is consistent with warmer offshore waters being drawn beneath the ice shelf. Figure 11 shows the residual currents in the ice front region overlaid with contours of ice shelf draft, indicating a good correlation between thinner ice shelf and the route of the inflows K and M. Further to the east on Berkner Shelf, the model predicts inflows between 50.8°W and 51.8°W (D in Figure 10) and along the western side of Hemmen Ice Rise (E in Figure 10). The western inflow (D) appears to be associated with a thinning of the ice shelf. We believe that the thinning in the ice shelf is a result of preferential melting associated with relatively warm, tidally driven inflows. As residual currents are topographically steered, ice shelf thinning will, to some extent, influence the route of the residual flows, but the primary control on the water column thickness in these areas is the bathymetry.

6.5. Modified Weddell Deep Water Intrusion

Foldvik et al. [1985] and *Gammelsrød et al.* [1994] interpreted the temperature maximum on the western slope of Berkner Shelf as an intrusion of Modified Weddell Deep Water (MWDW) formed by mixing Winter Water (WW) and Weddell Deep Water (WDW). *Foster and Carmack* [1976] observed the intrusion of MWDW on the continental shelf at 40°W, up to 100 km from the shelf break. *Gammelsrød et al.* [1994] suggested that from the continental shelf break, a distance of about 450 km from the ice front, a geostrophically balanced flow of MWDW followed the 400 m isobath to the ice front, before appearing to flow beneath the ice shelf. Associated with the 400 m isobath the model gives a very weak southwesterly residual current (0.2-0.4 cm s^{-1}) (Figure 12c) that might contribute to the transport of MWDW across the continental shelf. The sloping isopycnals associated with the MWDW between 52°W and 53.7°W, which can be seen as sloping isohalines in Figure 12a, suggest a southward flow beneath the ice shelf. Predicted residual currents in the area, however, range from zero up to 0.8 cm s^{-1} parallel to and slightly away from the ice front. In the vicinity of the intrusion, the ice shelf thins significantly, probably as the result of melting by the MWDW combined with the effects of the western inflow (D) on Berkner Shelf.

Offshore from the ice front region, the width of the MWDW intrusion has not been measured. The residual currents at the ice front on Berkner Shelf will force water northwest along the barrier, restricting the easterly extent of the MWDW intrusion at the ice front to approximately 51.5°W. From the model results (Figure 12c) MWDW joins the two dominant offshore gyres (G1 and G2). In CTD sections perpendicular to the ice front at 49°W and 51°W, *Foldvik et al.* [1985] observed MWDW warmer than −1.4°C at 20-60 km from the ice front, suggesting that the MWDW is directed away from the ice front, consistent with the modeled residual gyre G1. Evidence for MWDW entrainment into the western gyre (G2) can be found in data from a station at 54°W as a small warm core (−1.51°C) 10 km from the ice front [*Foldvik et al.*, 1985].

6.6. Contribution of Residual Currents to Mass Transport

Along the entire Ronne Ice Front, the contribution of residual currents to water mass transport appears to be comparable to thermohaline driven flows. Observations by *Nicholls et al.* [1997] indicate a 200,000 m^3 s^{-1} thermohaline inflow of WSW that enters the deep sub–ice shelf cavity via the Ronne Depression. After transformation to ISW, this water mass is presumed to emerge from beneath the ice shelf as the plume in the Ronne Depression. Away from the Ronne Depression, in the tidally active regions of Ronne Ice Front, modeled residual currents exchange approximately 250,000 m^3 s^{-1} across the ice front, between the sub–ice shelf cavity and open sea.

Along Filchner Ice Front the model predicts a weak northward current (0.2-0.4 cm s^{-1}, 125,000 m^3 s^{-1}) at the western side of the depression. Observations by *Foldvik et al.* [1985] show corresponding ISW cores emerging at a similar locations. However, modelling of thermohaline circulations in this region by *Grosfeld et al.* [1996] and geostrophic calculations by *Carmack and Foster* [1975] gave fluxes of approximatly 400,000 m^3 s^{-1} entering and leaving the ice shelf cavity. Also, *Foldvik et al.* [1985] derived an ISW flow of about 10^6 m^3 s^{-1} at the shelf break associated with Filchner Depression. As in the case of the Ronne Depression, we suggest that the hydrography along Filchner Depression is dominated by thermohaline processes, tidal residuals playing a minor or insignificant role.

7. Summary and Conclusions

A depth-averaged barotropic tidal model has been used to simulate the tidal currents of the southern Weddell Sea with no account taken of thermohaline or wind-driven processes. In total, six tidal constituents (Q_1, O_1, K_1, N_2, M_2, S_2) were modeled. There is reasonable agreement between the results from the model and the limited number of available current meter records, given the potentially large errors in bathymetric and ice shelf thickness data used to determine the water column thickness, particularly away from the Filchner-Ronne Ice Front region where only sparse data coverage is available. The largest deviations between measurements and model are found in the diurnal band. However, the model results demonstrate that both oscillatory and residual tidal currents play an important role in the oceanic processes beneath and in the vicinity of Filchner-Ronne Ice Shelf.

The strongest tidal currents are found on Berkner Shelf along Ronne Ice Front. Where the ice shelf significantly reduces the water column thickness, tidal currents peak at over 1 m s^{-1} during spring tides. In this area, tidal excursions of up to 15 km beneath the ice shelf, and up to 5 km in the open sea, help maintain a shore lead and therefore the production of HSSW. Energy dissipation by bottom friction is highest in shallow water regions, particularly beneath the ice shelf where the total energy dissipation, approximately 25 GW, accounts for almost 1% of the global energy budget [*Tsimplis et al.*, 1995]. A consequence of the energy dissipation is vertical mixing through the water column, close to the ice front this sustains observed melt rates of up to 6 m yr^{-1}. In the deeper regions of the ice shelf cavity where energy dissipation

is low, vertical mixing is likely to play only a small role in modifying the water column structure.

The application of this depth-averaged model has also yielded a description of the tidally generated residual currents which have been supported by the available ice front observations. These appear to play an important role in the transfer of water between the sub–ice shelf cavity and the adjacent continental shelf. Along the eastern section of Ronne Ice Front the water column thickness reduces from 250 m to less than 100 m. Modeled Lagrangian residual currents reach mean velocities of 5 cm s^{-1} in this area. Further to the west these currents transport up to 250,000 m^3 s^{-1} along the ice front. In addition to the along ice front flows there are a number of specific locations where Lagrangian residual currents transport water masses into and out of the sub–ice cavity of FRIS. The rate of exchange totalling approximately 350,000 m^3 s^{-1} is less than estimates attributed to thermohaline circulation but are of the same order. Shipborne hydrographic observations along the ice front support many of the model predictions. Lagrangian residual flows from the cavity coincide with observations of ISW plumes, and ice shelf thinning coincides with flows entering the cavity, consistent with warmer offshore water being imported and causing preferential melting. Along 350 km of Ronne Ice Front the combination of strong residual currents, large tidal excursions and vigorous mixing give rise to a region where strong melting is both predicted by the model and seen in observations. Along this section of ice front and up to 70 km inshore, melting averages 2-3 m yr^{-1} [*Kohnen*, 1982; *Jenkins and Doake*, 1991; *Grosfeld et al.*, 1992], giving a net loss of 50-75 km^3 yr^{-1}, equivalent to 11-16 cm yr^{-1} over the whole FRIS.

Away from the ice front, where residual currents are weaker, it is unclear to what extent they influence the hydrography. Over the open ocean the effect of tidal residuals will combine with the wind and thermohaline forcing; it is not clear which affect will dominate. In the deep water areas beneath FRIS, particularly the Filchner and Ronne Depressions, residual currents are weak, and we assume thermohaline flows dominate. The largest residual flow that penetrates deep beneath the ice shelf transports approximately 100,000 m^3 s^{-1} of water anticlockwise around Berkner Island. The flow originates on the Berkner Shelf, west of Berkner Island, and finally emerges from beneath the western end of Filchner Ice Front. Direct confirmation of this current is not yet available.

Probably the most important result from this study has been to show that tidal processes strongly influence the oceanographic conditions in the vicinity of Ronne Ice Front and can explain many of the observations made in the shorelead. The combination of vigorous mixing, large tidal excursions, and strong Lagrangian residual currents has a dominant effect on the hydrography beneath about 60% of Ronne Ice Front.

Appendix: Extraction of Tidal Constituents From Site 2 Thermistor Cable Data

An example portion of the 22-month thermistor cable record is shown in Figure A1. The amplitude of the signal at twice tidal frequency increases down the water column. Assuming the signal is due to the cable swinging in the tidal flow, the most accurate temperature profile through the water column will be given when the temperatures reach a local maximum, that is, when the cable is hanging vertically (we expect the temperature to increase monotonically with increasing depth [*Nicholls*, 1996]). A "demodulated" record of temperature profiles was therefore obtained by selecting those profiles for which the deepest thermistor showed a local maximum value. After appropriate filtering, a 22-month record of water column temperatures was obtained [*Nicholls*, 1996]. It was then possible to determine the depth of each thermistor at each of the samples between those times the cable was assumed to be vertical.The way a cable hangs in a vertically uniform current can be described by

$$\frac{dT^*}{dl^*} = (c^* + \sin(\theta))\cos(\theta)$$

$$\frac{d(\theta)}{dl^*} = \frac{\cos^2(\theta) - c^*\sin(\theta)}{T^*}$$

where $T^*(l)$, c^*, and l^* are the nondimensional tension in the cable, the cable's weight per unit length, and the distance along the cable from the bottom end, respectively. They are nondimensionalized by using the length of the cable L and the force per unit length F exerted on the vertically hanging cable by the water flowing at a speed U. Here $\theta(l)$ is the angle between the cable and the downward vertical. F is given by $F = C_d \rho U^2 a$. Here C_d is the drag coefficient for a cylinder, taken to be 1.0 [see, e.g., *Batchelor*, 1967], ρ is the density of seawater, and a is the radius of the cable. By using the value of the weight suspended at the bottom of the cable as an initial value for the tension, and zero as the initial value for θ, the equations were integrated from the bottom up to the ice

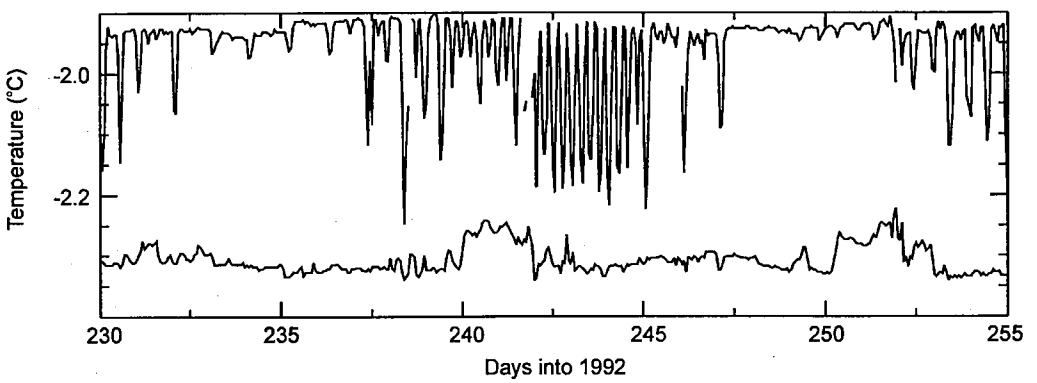

Figure A1. Excerpt from the 22-month time series from the shallowest thermistor (bottom trace) and the deepest thermistor (top trace) from the thermistor cable at Site 2 (S2 in Figure 1). Four-times-daily oscillations in the upper trace indicate that the cable is swinging in a primarily semi-diurnal tidal current. Spring-neap variability is visible in the record.

shelf base using a Runge-Kutta algorithm. For a given water speed U the vertical position of each thermistor could then be predicted.

Using the record of thermistor depths, the results of the simple model of the way the cable hangs yields 10 records of water speed. As the vertical motion was the greatest for the deepest thermistor, this speed record was used for the extraction of tidal constituents. A synthetic speed record was created by making initial guesses for the phase and magnitude of the four tidal constituents that are largest in the Weddell Sea region: O_1, K_1, M_2, and S_2. The mean square deviation between the synthetic speed record and the record obtained from the cable was then calculated. This error was minimized using a minimization routine to explore the eight-dimensional space formed by the phase and amplitude of the four constituents. Several different initial guesses were made to locate all the likely minima in the error field, and the solution with the smallest minimum error was finally selected. As the cable is able only to give speed information, the phase of the entire set of constituents contains a 180° ambiguity. The principal assumptions inherent in this method are that the tidal velocity is constant throughout the water column, the size of the minor axes of the tidal ellipses for each constituent is small compared with the major axes, and that the tidal ellipses are all oriented in the same direction.

Acknowledgments. The authors would like to thank Adrian Jenkins and Laurie Padman for many useful discussions and two anonymous reviewers for their constructive comments.

References

Batchelor, G.K., *An Introduction to Fluid Mechanics*, Cambridge Univ. Press, New York, 1967.

Bombosch, A., and A. Jenkins, Modeling the formation and deposition of frazil ice beneath Filchner-Ronne Ice Shelf, *J. Geophys. Res., 100*(C4), 6983-6992, 1995.

Carmack, E.C., and T.D. Foster, Circulation and distribution of oceanographic properties near the Filchner Ice Shelf, *Deep Sea Res., 22*, 77-90, 1975.

Corr, H., M. Walden, D.G. Vaughan, C.S.M. Doake, A. Bombosch, A. Jenkins and R.M. Frolich, Basal melt rates along the Rutford Ice Stream, in *Filchner Ronne Ice Shelf Programme, Rep. 10*, pp. 11-15, Alfred-Wegener Inst., Bremerhaven, Germany, 1996.

Doake, C.S.M., Dissipation of tidal energy by Antarctic ice shelves, *Nature, 275*, 304-305, 1978.

Elder, R.B., and J.M. Seabrooke, Oceanography of the Weddell Sea, *U.S. Coast Guard Oceanogr. Rep., 30*, 1970.

Fearnhead, P.G., On the formation of fronts by tidal mixing around the British Isles, *Deep Sea Res., 22*, 311-321, 1975.

Ferrigno, J.G. and W.G. Gould, Substantial changes in the coastline of Antarctica revealed by satellite imagery, *Polar Rec., 23*, 577-583, 1987.

Foldvik, A., and T. Gammelsrød, Notes on southern ocean hydrography, sea-ice and bottom water formation, *Palaeogeogr. Palaeoclimatol. Palaeoecol., 67*, 3-17, 1988.

Foldvik, A., T. Gammelsrød, N. Slotsvik, and T. Tørresen, Oceanographic conditions on the Weddell Sea Shelf during the German Antarctic Expedition 1979/80, *Polar Res., 3*, 209-226, 1985.

Foldvik, A. and T. Kvinge, Bottom currents in the Weddell Sea, *Rep. 37*, Univ. of Bergen, Bergen, Norway, 1974.

Foldvik, A., J.H. Middleton, and T.D. Foster, The tides of the southern Weddell Sea, *Deep Sea Res., 37*, 1345-1362, 1990.

Foreman, M.G.G., *Manual for Tidal Currents Analysis and Prediction*, Inst. of Ocean Sci., Patricia Bay, Sidney, B.C., 1977.

Foster, T.D., and E.C. Carmack, Frontal zone mixing and Antarctic Bottom Water formation in the southern Weddell Sea, *Deep Sea Res., 23*, 301-317, 1976.

Fox, A.J., and A.P.R. Cooper, Measured properties of the Antarctic ice sheet derived from the SCAR Antarctic digital database, *Polar Rec., 30*, 201-206, 1994.

Gammelsrød, T., A. Foldvik, O.A. Nøst, Ø. Skagseth, L.G. Anderson, E. Fogelqvist, K. Olsson, T. Tanhua, E.P. Jones, and S. Østerhus, Distribution of water masses on the continental shelf in the southern Weddell Sea, In: *the Polar Oceans and Their Role in Shaping the Global Environment, The Nansen Centennial Volume, Geophys. Monogr. Ser.*, vol. 85, edited by O.M. Johannessen et al. pp 159-176, AGU, Washington, D. C., 1994.

Gammelsrød, T., and N. Slotsvik, Hydrographic and current measurements in the southern Weddell Sea 1979/80, *Polarforschung, 51*(1), 101-111, 1981.

Genco, M.L., F. Lyard, and C. Le Provost, The oceanic tides in the South Atlantic Ocean, *Ann. Geophys., 12*, 868-886, 1994.

Gill, A.E., Circulation and bottom water production in the Weddell Sea, *Deep Sea Res., 20*, 111-140, 1973.

Grosfeld, K., N. Blindow, and F. Thyssen, Bottom melting on Filchner-Ronne Ice Shelf, Antarctica, using different measuring techniques, *Polarforschung, 62*(2/3), 71-76, 1992.

Grosfeld, G., R. Gerdes, and J. Determann, Thermohaline circulation beneath and in front of Filchner Schelfeis, in *Filchner Ronne Ice Shelf Programme, Rep. 10*, pp. 32-37, Alfred-Wegener Inst., Bremerhaven, Germany, 1996.

Grosfeld, G., R. Gerdes, and J. Determann, Thermohaline circulation and interaction between ice shelf cavities and the adjacent open ocean, *J. Geophys. Res., 102*(C7), 15,595-15,610, 1997.

Haase, G.M., Glaciomarine sediments along the Filchner/Ronne Ice Shelf, southern Weddell Sea: First results of the 1983/84 Antarktis-II/4 Expedition, *Mar. Geol.,, 72*, 241-258, 1986.

Jenkins, A., A one-dimensional model of ice shelf-ocean interaction, *J. Geophys. Res., 96*(C11), 20,671-20,677, 1991.

Jenkins, A., and A. Bombosch, Modelling the effects of frazil ice crystals on the dynamics and thermodynamics of ice shelf water plumes, *J. Geophys. Res., 100*(C4), 6967-6981, 1995.

Jenkins, A., and C.S.M. Doake, Ice-ocean interaction on Ronne Ice Shelf, Antarctica, *J. Geophys. Res., 96*(C1), 791-813, 1991.

Johnson, M.R., and A.M. Smith, Seabed topography under the southern and western Ronne Ice Shelf from seismic surveys, *Antarct. Sci., 9*(2), 201-208, 1997.

Johnson, G.L., J.R. Vanney, D.J. Drewry, and G. Robin, General bathymetric chart of the oceans (GEBCO), Can. Hydrogr. Serv., Ottawa, Ont., 1983.

Kohnen, H., Glaciological investigations in the frontal zone of the Filchner and Ronne Ice Shelves, *Ann. Glaciol., 3*, 160-165, 1982.

LaBrecque, J.L., and M.E. Ghidella, Bathymetry, depth to magnetic basement, and sediment thickness estimates from aerogeophysical data over the western Weddell Basin, *J. Geophys. Res., 102*(B4), 7929-7945, 1997.

Le Provost, C., A.F. Bennett, and D.E. Cartwright, Ocean tides for and from TOPEX/POSEIDON, *Science, 267*, 639-642, 1995.

Loder, J.W., Topographic rectification of tidal currents on the sides of Georges Bank, *J. Phys. Oceanogr., 10*, 1399-1416, 1980.

MacAyeal, D.R., Thermohaline circulation below the Ross Ice Shelf: A consequence of tidally induced vertical mixing and basal melting, *J. Geophys. Res., 89*(C1), 597-606, 1984a.

MacAyeal, D.R., Simulation of Ross Sea tides, *J. Geophys. Res., 89*(C1), 607-615, 1984b.

Makinson, K., and K.W. Nicholls, Modelling tidal currents beneath Filchner-Ronne Ice Shelf, in *Filchner Ronne Ice Shelf Rep.* 10, pp. 58-67, Alfred-Wegener Inst., Bremerhaven, Germany, 1996.

Mayer, C., A. Lambrecht and H. Oerter, Glaciological investigations on the Foundation Ice Stream, in *Filchner Ronne Ice Shelf Programme, Rep 9.*, pp. 57-63, Alfred-Wegener Inst., Bremerhaven, Germany, 1995.

Middleton, J.H., T.D. Foster, and A. Foldvik, Low-frequency currents and continental shelf waves in the southern Weddell Sea, *J. Phys. Oceanogr., 12*, 618-634, 1982.

Middleton, J.H., Foster T.D., and A. Foldvik, Diurnal shelf waves in the southern Weddell Sea, *J. Phys. Oceanogr., 17*, 784-791, 1987.

Nicholls, K.W., Temperature variability beneath Ronne Ice Shelf, Antarctica, from thermistor cables, *J. Geophys. Res., 101*(C1), 1199-1210, 1996.

Nicholls, K.W. and K. Makinson, Ocean circulation beneath the western Ronne ice shelf, as derived from in situ measurements of water currents and properties, in *Ocean, Ice, and Atmosphere: Interactions at the Antarctic Continental Margin, Antarct. Res. Ser.* vol. 75, edited by S.S. Jacobs and R.F. Weiss, pp. 301-318, AGU, Washington, D. C., 1998.

Nicholls, K.W., K. Makinson, and M.R. Johnson, New oceanographic data from beneath Ronne Ice Shelf, Antarctica, *Geophys. Res. Lett., 24*(2), 167-170, 1997.

Nicholls, K.W., K. Makinson, and A.V. Robinson, Ocean circulation beneath Ronne Ice Shelf, *Nature, 354*, 221-223, 1991.

Robertson, R., L. Padman, and G.D. Egbert, Tides in the Weddell Sea, in *Ocean, Ice, and Atmosphere: Interactions at the Antarctic Continental Margin, Antarct. Res. Ser.*, vol. 75, edited by S.S. Jacobs and R.F. Weiss, pp. 341-369, AGU, Washington, D. C., 1998.

Robin, G. de Q., C.S.M. Doake, H. Kohnen, R.D. Crabtree, S.R. Jordan, and D. Möller, Regime of the Filchner-Ronne ice shelves, Antarctica, *Nature, 302*, 582-586, 1983.

Robinson, A. V. Modelling the tides of the southern Weddell Sea, M. Phil. thesis, 84 pp., British Antarctic Survey, Cambridge, England, February, 1996.

Robinson, I. S., Tidal vorticity and residual circulation, *Deep Sea Res., 28A*, 195-212, 1981.

Rohardt, G., Hydrographische untersichungen am rand des Filchner Schelfeises, *Ber. Zur Polarforschung, 19*, 137-143, 1984.

Schumacher, J.D., T.H. Kinder, D.J. Pashinski, and R.L. Charnell, A structural front over the continental shelf of the eastern Bering Sea, *J. Phys. Oceanogr., 9*, 79-87, 1979.

Schwiderski, E. W., On charting global ocean tides, *Rev. Geophys., 18*, 243-268, 1980.

Simpson, J.H., The shelf-sea fronts: Implications of their existence and behaviour, *Philos. Trans. R. Soc. London, Ser. A 302*, 531-546, 1981.

Smith, A.M., Ice shelf basal melting at the grounding line, measured from seismic observations, *J. Geophys. Res., 101*(C10), 22,749-22,755, 1996.

Smithson, M.J., A.V. Robinson, and R.A. Flather, Ocean tides under the Filchner-Ronne Ice Shelf, Antarctica, *Ann. Glaciol., 23*, 217-225, 1996.

Tsimplis, M. N., R. Procter, and R.A. Flather, A two-dimensional tidal model for the Mediterranean Sea, *J. Geophys. Res., 100*(C8), 16,223-16,239, 1995.

Van Wyckhouse, R., Digital bathymetric database 5, *Tech. Rep. TR-233*, U.S. Naval Oceanogr. Off., Bay St. Louis, Miss., 1973

Vaughan, D.G., Tidal flexure at ice shelf margins, *J. Geophys. Res., 100*(B4), 6213-6224, 1995.

Vaughan, D.G., and M. Jonas, Measurement of velocity of Filchner-Ronne Ice Shelf in *Filchner Ronne Ice Shelf Programme, Rep. 10*, pp. 111-116, Alfred-Wegener Inst., Bremerhaven, Germany, 1996.

Vaughan, D.G., J. Sievers, C.S.M. Doake, G. Grikurov, H. Hinze, V.S. Pozdeev, H. Sandhäger, H.W. Schenke, A. Solheim, and F. Thyssen, Map of the subglacial and seabed topography 1:2000000 Filchner-Ronne Schelfeis/Weddell Sea, Antarktis, Inst. für Angew. Geod., Frankfurt-am-Main, Germany, 1994.

Vaughan, D.G., J. Sievers, C.S.M. Doake, H. Hinze, D.R. Mantripp, V.S. Pozdeev, H. Sandhäger, H.W. Shenke, A. Solheim, and F. Thyssen, Subglacial and seabed topography, ice thickness and water column thickness in the vicinity of Filchner-Ronne-Schelfeis, Antarctica, *Polarforschung, 64(2)*, 75-88, 1995.

Wunsch, C., *The Ocean Circulation Inverse Problem*, pp. 78-80, Cambridge Univ. Press, New York, 1996.

K. Makinson and K.W. Nicholls, British Antarctic Survey, Natural Environment Research Council, High Cross, Madingley Road, Cambridge, CB3 0ET, England. (k.makinson@bas.ac.uk)

(Received March 27, 1998; revised October 16, 1998; accepted December 31, 1998.)

Modeling Tidal Current Profiles and Vertical Mixing beneath Filchner–Ronne Ice Shelf, Antarctica

KEITH MAKINSON

British Antarctic Survey, Natural Environment Research Council, Cambridge, United Kingdom

(Manuscript received 8 January 2001, in final form 6 July 2001)

ABSTRACT

One of the warmest water masses beneath Filchner–Ronne Ice Shelf (FRIS) is dense, high salinity shelf water (HSSW) that flows into the sub-ice-shelf cavity from the ice front and occupies the lower portion of the water column. A one-dimensional turbulence closure ocean model has been applied to this high latitude sub-ice-shelf environment to demonstrate that tidal currents mix HSSW vertically through the water column and cause melting at the bottom of the ice shelf. Significantly FRIS lies near the critical latitude for the semidiurnal tide, where the Coriolis frequency equals the tidal frequency, resulting in a strongly depth-dependent tidal current and thick boundary layers. Using the model, the effect of the critical latitude, stratification, and the polarization of the tidal current ellipse on boundary layer structure and subsequent vertical mixing are examined. The model shows that stratification significantly affects how the shape of the tidal current ellipse varies with depth and that both the depth to which the pycnocline initially develops and the longer term melt rates are highly dependent on tidal current ellipse polarization. The sensitivity to both the stratification and the polarization are due, in large part, to the proximity of the critical latitude. Positive polarizations (anticlockwise rotating current vectors) quickly develop deeper pycnoclines and maintain higher melt rates than negative polarizations (clockwise rotating current vectors). For many areas beneath FRIS the polarization ranges from -0.3 to $+0.3$; here the modeled pycnocline development is sensitive to polarization, though the effect on the time-averaged melt rate is suppressed for positive polarizations. However, in key areas where the polarization exceeds ± 0.3 and the ellipses are more open and circular, the effects of polarization are significant. Levels of tidal mixing and associated melting vary by more than an order of magnitude over the whole tidal ellipse polarization range, showing that very different mixing and melting regimes are present beneath FRIS.

1. Introduction

The largest mass of floating ice on earth is located in the southern Weddell Sea at the margin of the Antarctic ice sheet. The Filchner–Ronne system of ice shelves (FRIS) (Fig. 1) is a floating extension of the Antarctic Ice Sheet, draining 24% of the area of the continent's grounded ice and covering an area slightly less than that of France (Fox and Cooper 1994). Direct oceanographic measurements from beneath FRIS confirm that high salinity shelf water (HSSW), a product of sea ice formation north of the ice shelf, flows into the sub-ice-shelf cavity (Nicholls and Makinson 1998; Nicholls et al. 2001). This relatively warm, dense water occupies the lower portion of the water column in an environment isolated from atmospheric forcing, in which tidal and thermohaline processes are thought to dominate the circulation. MacAyeal (1984) suggested *tidal stirring* as a probable mechanism for mixing HSSW up through the sub-ice-shelf water column to be transformed, through melting at the underside of the ice shelf, into ice shelf water (ISW). Since ISW is a precursor of Antarctic Bottom Water (Foldvik and Gammelsrød 1988) and Southern Ocean bottom water formation takes place mostly in the Weddell Sea (Ganachaud and Wunsch 2000), mixing processes beneath FRIS are potentially significant for global ocean circulation.

In the cavity beneath an ice shelf frictional stress at both the seabed and the ice shelf base influences the vertical structure of tidal currents, induces vertical mixing, and enables the development of two well-defined mixed boundary layers. These frictional boundary layers are made up of a thin region of high shear and a thicker region of low shear. Beyond this boundary layer is the free stream region where there is no shear and where the current is independent of depth (Soulsby 1983). Where fixed ice cover is present and tidal currents in deep water are weak, the frictional boundary layers occupy a small fraction of the water column. However, in shallow water with strong tidal currents, they can occupy the entire water column, dominating the tidal current structure and associated vertical mixing (Prinsenberg and Bennett 1989). Tidal simulations for

Corresponding author address: Keith Makinson, British Antarctic Survey, Natural Environment Research Council, High Cross, Madingley Road, Cambridge CB3 0ET, United Kingdom.
E-mail: kmak@bas.ac.uk

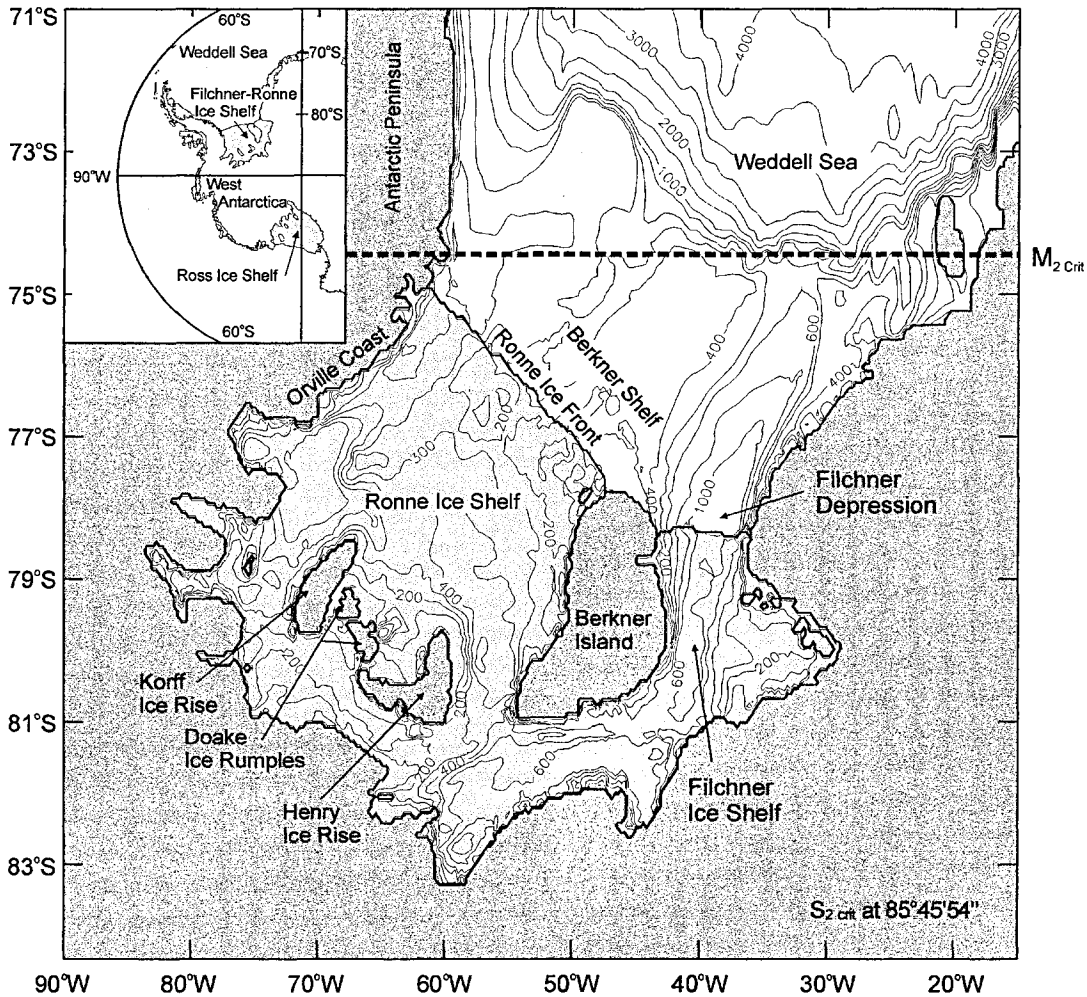

FIG. 1. Map showing the water column thickness in the area of Filchner–Ronne Ice Shelf and extending over the continental shelf. The contours give water column thickness in meters. The darkest shading indicates areas of grounded ice, and the lighter shading indicates the floating ice shelf. The critical latitude for the semidiurnal tidal constituent M_2 is indicated by the dashed line and the inset indicates the position of FRIS in the southern Weddell Sea.

the southern Weddell Sea show that the mean barotropic tidal currents beneath FRIS attain speeds of up to 0.2–0.5 m s^{-1}, with peak velocities reaching 1 m s^{-1} (Makinson and Nicholls 1999; Robertson et al. 1998). Close to the Ronne Ice Front, and along grounding lines of FRIS where the ice first comes afloat, these tidal currents are thought to result in significant levels of vertical mixing, and high basal melt rates.

To determine the influence of vertical tidal mixing on melting beneath Ross Ice Shelf, Scheduikat and Olbers (1990) developed two one-dimensional mixed layer models, thermodynamically coupled to an ice shelf, one with two layers and one with three layers. Both were Kraus and Turner type models (Kraus and Turner 1967), which were forced by a barotropic tidal current. In the two-layer model, the horizontally homogeneous upper mixed layer interacted with the ice shelf while the lower layer remained passive and represented an infinite heat and salt reservoir. In the three-layer model, the bottom layer was treated as a mixed layer and included the advection of heat and salt, while a third layer was introduced between the two mixed layers. With the two-layer model it was found that basal melting or freezing was strongly dependent on the ratio of the major and minor axes of the tidal current ellipse. Flat or degenerate ellipses yielded cyclic currents with the top layer entraining and then detraining water from the layer below. When the current was at its maximum during the tidal cycle, entrainment and melting would occur. With open, circular ellipses there was little or no entrainment from the layer below and heat lost from the upper layer to the ice shelf gave a small amount of freezing, irrespective of the tidal current amplitude. The three-layer model gave similar results, but with reduced melt rates resulting from a better representation of the thermocline. Scheduikat and Olbers (1990), however, did not include the effects of the earth's rotation.

Using a one-dimensional turbulence closure model

that included the earth's rotation, Simpson and Sharples (1994) considered the effects of tidal current ellipse polarization on tidal front behavior. Polarization (P) is used to define the shape and sense of rotation of a tidal current ellipse

$$P = \pm V/U, \tag{1}$$

where U and V are the semimajor and semiminor axes of the tidal current ellipse, respectively. The polarization ranges from a purely circular clockwise current ($P = -1$), through a flat or degenerate ellipse ($P = 0$), to a purely circular anticlockwise current ($P = +1$). With the inclusion of rotation, Simpson and Sharples (1994) found that predominantly clockwise tidal currents (in the Northern Hemisphere) produced substantial differences in the predicted positions of fronts over previous nonrotational models, with fronts extending into deeper waters where the polarization was increasingly negative.

The rotational effect on vertical mixing is accounted for by decomposing the elliptical tidal current into purely anticlockwise (R_+) and clockwise (R_-) components and considering their respective frictional boundary layers. The two constant magnitude rotary velocity components rotate at the tidal frequency, and each has a characteristic frictional boundary layer thickness, δ_+ and δ_-, given by (Prandle 1982):

$$\delta_+ \approx \left(\frac{2K_M}{|\omega + f|}\right)^{1/2} \quad \text{and} \tag{2}$$

$$\delta_- \approx \left(\frac{2K_M}{|\omega - f|}\right)^{1/2}, \tag{3}$$

where K_M is the eddy viscosity, f is the Coriolis parameter, and ω the frequency of the tidal oscillation. Assuming a constant eddy viscosity for semidiurnal tides at northern midlatitudes the thickness of the clockwise frictional boundary layer will be about three times greater than for the anticlockwise frictional boundary layer. An effective combined boundary layer thickness (δ) is suggested by Soulsby (1983)

$$\delta = \frac{(R_+\delta_+ + R_-\delta_-)}{(R_+ + R_-)}. \tag{4}$$

Consequently, tidal currents with more negative polarizations in the Northern Hemisphere have larger boundary layers, allowing mixing to penetrate farther into the water column interior and tidal fronts to advance into deeper water.

The spatial variability of the tidal currents beneath FRIS was determined by Makinson and Nicholls (1999) using a two-dimensional depth-averaged barotropic tidal model of the southern Weddell Sea. The M_2 tidal ellipse polarization over this region is shown in Fig. 2. All the semidiurnal tidal constituents exhibit an almost identical pattern of polarization with regions of strongly positive and negative polarization present beneath FRIS, suggesting a wide range of boundary layer depths.

At higher northern latitudes the boundary layer of R_- is much larger than the R_+ component as $|\omega - f|$ tends to zero at the critical latitude (φ_{crit}). At this latitude the tidal frequency equals the Coriolis or inertial frequency, $\omega = |f| = 2\Omega \sin \varphi_{crit}$, where the earth's angular velocity $\Omega = 7.2921151 \times 10^{-5}$ rad s^{-1}. Furevik and Foldvik (1996) showed that a thick benthic boundary layer develops as the critical latitude is approached. A thicker boundary layer produces less intense shear near boundaries but extends the shear over a larger thickness of the water column, and is likely to enhance vertical mixing near the critical latitude.

In the Southern Hemisphere, the northwest corner of FRIS lies near the critical latitude of the M_2 tidal constituent at 74°28′18″S, while the southernmost areas of the ice shelf are closest to the S_2 critical latitude at 85°45′54″S. In the shallow regions close to the Ronne Ice Front, south of Henry Ice Rise and along grounding lines, the combined effects of strong tidal currents and the proximity of the critical latitude will further thicken the boundary layers. This produces extensive areas over which the boundary layers may occupy the entire water column, and here the free stream region of the tidal current will be absent. At high latitudes the diurnal tides do not exhibit these large differences between the thickness of the boundary layers of R_+ and R_- as, for these frequencies; $|f|$ is almost twice as large as ω.

Boundary layer thickness is further complicated by the stratifying effect of any buoyancy input. The only source of buoyancy beneath FRIS is the net production of an estimated 1500–3000 m^3 s^{-1} of meltwater (Nicholls and Makinson 1998), which is critical for driving the circulation over large areas of the region and has important implications for water column structure. Buoyancy effects caused by freezing or melting under sea ice have been found to play an important role in modifying turbulent processes (Shirasawa and Ingram 1991). During melting the water column becomes stratified while the tidal forcing remains unchanged. The effect of stratification is to suppress turbulence, inhibiting the transfer of momentum and reducing the eddy viscosity, hence reducing the boundary layer thickness from the homogenous case (Souza and Simpson 1996). Further modification of the vertical tidal current structure occurs in the vicinity of the pycnocline, which becomes decoupled from the mixed layers at the seabed and ice base (Prinsenberg and Bennett 1989). Near the critical latitude, the influence of eddy viscosity on the vertical tidal current profiles is significant (Nøst 1994): a small change results in a large variation in the anticlockwise component in the Southern Hemisphere, while the clockwise component remains unaffected.

Effects of tides are usually ignored within sub-ice-shelf circulation models. For FRIS, this means that the estimated 25 GW of tidal energy dissipation associated with surface friction are also ignored (Makinson and Nicholls 1999; Robertson et al. 1998). Vertical mixing resulting from tidal currents has been parameterized

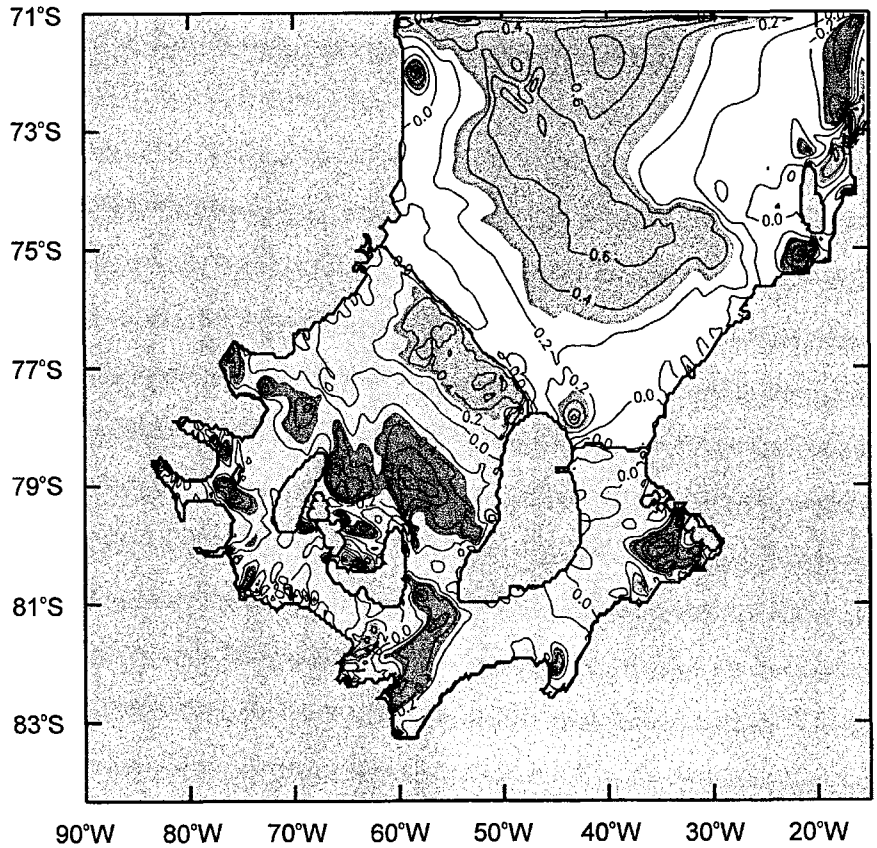

FIG. 2. The M_2 tidal current ellipse polarization of the depth-averaged velocity predicted by Makinson and Nicholls (1999) for the southern Weddell Sea. The contours have a 0.2 spacing. The darkest shading shows regions of strong clockwise rotation ($P < -0.3$), the lighter shading shows regions of strong anticlockwise rotation ($P > 0.3$).

only as a function of average water column speeds derived from two-dimensional barotropic tidal models (Makinson and Nicholls 1999; MacAyeal 1984). This parameterization is poor for high-latitude regions dominated by semidiurnal tides with a wide range of tidal current ellipse polarizations.

In this paper a one-dimensional ocean model, coupled thermodynamically to the ice shelf, is applied to a sub-ice-shelf water column to study vertical profiles of tidal currents, vertical mixing, and basal melting beneath Filchner–Ronne Ice Shelf. The model is described in the next section, together with the parameters used to define the model properties and the initial conditions. Results from the model in section 3 show the proximity to the M_2 and S_2 critical latitudes affects the vertical tidal current structure and how this is further affected by the presence of stratification. Also described are the effects of depth-averaged tidal current ellipse polarization on vertical mixing and basal melting over a wide range of polarizations and current amplitudes. The implications for FRIS of the results from the mixing model are then discussed.

2. Model description

The one-dimensional model uses an implicit finite difference scheme to integrate the horizontal velocity components (u, v) of the momentum equations

$$\frac{\partial u}{\partial t} = -S_x g \sin(\omega t - \phi_x) + fv + \frac{\partial}{\partial z}\left(K_M \frac{\partial u}{\partial z}\right) \quad \text{and} \quad (5)$$

$$\frac{\partial v}{\partial t} = -S_y g \sin(\omega t - \phi_y) - fu + \frac{\partial}{\partial z}\left(K_M \frac{\partial v}{\partial z}\right) \quad (6)$$

with x and y positive in the east and north directions and z increasing positively upward, with $z = 0$ at the ice–ocean boundary and $z = -h$ at the seabed. Here, K_M is the vertical eddy viscosity, f is the Coriolis parameter, g the gravitational acceleration, and ω is the tidal frequency; S_x, S_y and ϕ_x, ϕ_y are the prescribed tidal surface slope amplitudes and phases. A phase difference of $\pi/2$ is maintained between ϕ_x and ϕ_y, while the amplitude of the tidal slopes are determined from

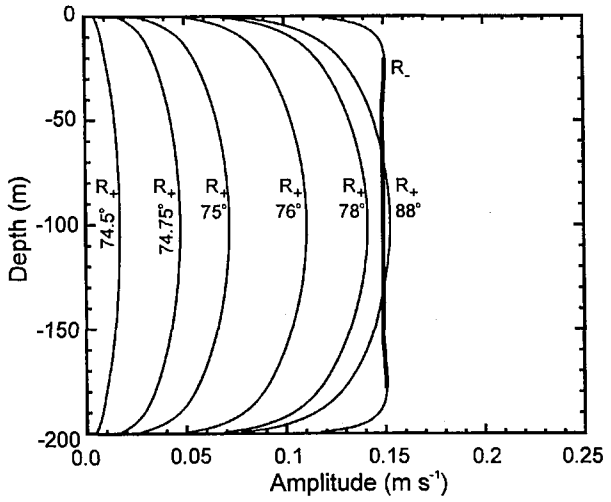

FIG. 3. The vertical structure of the M_2 rotary components in a 200-m homogeneous water column beneath an ice shelf. The clockwise component (R_-) has small boundary layers, while the boundary layers of the anticlockwise component (R_+) occupy the whole water column. As the M_2 critical latitude at 74°28′18″S is approached from the south the anticlockwise component (R_+) of the flow is retarded while (R_-) remains unchanged. The free stream region of R_- is highlighted in bold.

$$S_x = \frac{U(\omega + Pf)}{g} \tag{7}$$

$$S_y = \frac{U(f + P\omega)}{g}, \tag{8}$$

where U determines the maximum speed of the tidal current (semimajor axis) and P, which ranges between ± 1.0, controls the polarization of the tidal current ellipse. More details on the derivation of (7) and (8) are given in the appendix. At both the ice–ocean interface and the seabed, a quadratic drag law is applied with a drag coefficient of $C_{d100} = 0.0025$. A smoothly graded vertical mesh is used to give the highest resolution at the boundaries. The thickness of the two layers adjacent to each of the boundaries are set to 1.0 m. The node depth at the center of each layer of the remaining water column (z_{rem}) is determined from Lynch et al. (1996)

$$Z_{\text{node}} = -z_{\text{rem}} + \varepsilon(z_{\text{rem}}) - \beta \sin(2\pi\varepsilon), \tag{9}$$

where ε increases linearly with node number from 0 at the bottom to 1 at the top. For a total water column thickness of 200 m with 61 nodes, the constant β is set to give the desired layer resolution of 1.0 m near the boundaries and approximately 6 m in the mid-water column.

Both heat and salt are conserved in the model and their vertical diffusion within the water column are governed in the model by

$$\frac{\partial(T, S)}{\partial t} = \frac{\partial}{\partial z}\left(K_H \frac{\partial(T, S)}{\partial z}\right), \tag{10}$$

where K_H is the vertical eddy diffusivity, T is the water temperature, and S the water salinity. There is no flux of heat or salt through the seabed. At the ice–ocean interface, phase changes during melting or freezing produce heat and freshwater fluxes, which will be considered later in this section.

The effects of turbulence in transferring momentum and mixing heat and salt are determined by the widely used, level 2.5 turbulence closure scheme of Mellor and Yamada (1982) incorporating the modifications of Galperin et al. (1988). This provides vertical viscosity and diffusivity coefficients that depend on the interaction of flow and stratification, which are provided by the relation

$$K_M, K_H = q\, l\, (S_M, S_H), \tag{11}$$

where $q^2/2$ is the turbulent kinetic energy (TKE), l is turbulence mixing length scale, and S_M and S_H are stability functions related to the Richardson number. The local evolution of both q and l are given by

$$\frac{\partial q^2}{\partial t} = \frac{\partial}{\partial z}\left(K_q \frac{\partial q^2}{\partial z}\right) + K_M\left[\left(\frac{\partial u}{\partial z}\right)^2 + \left(\frac{\partial v}{\partial z}\right)^2\right] + \frac{2g}{\rho_0} K_H \frac{\partial \rho}{\partial z} - \frac{2q^3}{B_1 l} \tag{12}$$

$$\frac{\partial q^2 l}{\partial t} = \frac{\partial}{\partial z}\left(K_q \frac{\partial q^2 l}{\partial z}\right) + lE_1 K_M\left[\left(\frac{\partial u}{\partial z}\right)^2 + \left(\frac{\partial v}{\partial z}\right)^2\right] + \frac{lE_1 g}{\rho_0} K_H \frac{\partial \rho}{\partial z} - lw\frac{q^3}{B_1 l}. \tag{13}$$

The terms on the right-hand side are, respectively, the vertical turbulent diffusion, shear production, buoyancy production, and dissipation of turbulent kinetic energy; B_1 and E_1 are empirical constants, ρ_0 is the seawater reference density, and K_q is the vertical turbulent diffusivity for q^2 and $q^2 l$. A wall proximity function (w) is used to maintain a log-law near the boundaries. The seawater density (ρ) is related to temperature and salinity by the equation of state (Gill 1982).

At the ice–ocean interface melting is a function of temperature, salinity, and speed of the water adjacent to the interface. As the interface is approached eddies are suppressed and the eddy diffusivity decreases to a point where molecular diffusion becomes the principal transfer mechanism for heat and salt. The parameterization of transfer coefficients for heat (γ_t) and salt (γ_s) follow Kader and Yaglom (1972)

$$\gamma_t = \frac{u_*}{2.12 \ln(u_* D/\nu) + 12.5\text{Pr}^{2/3} - 9} \tag{14}$$

$$\gamma_s = \frac{u_*}{2.12 \ln(u_* D/\nu) + 12.5\text{Sc}^{2/3} - 9}, \tag{15}$$

where Pr and Sc are the molecular Prandtl and Schmidt numbers for seawater, ν is the kinematic viscosity, u_*

is the friction velocity, and D is the layer thickness adjacent to the ice shelf.

Basal melt rate, m (negative for melting) is determined from Nicholls et al. (2001)

$$m = [\gamma_t(T_b - T_f)] \Big/ \left[aS_b \frac{\gamma_t}{\gamma_s} - \frac{L}{c_w} - (T_i - T_f)\frac{c_i}{c_w} \right], \quad (16)$$

where T_b and S_b are the temperature and salinity of the seawater adjacent to the ice–ocean interface; c_w and c_i are the specific heat capacities of seawater and ice; L and T_i are the latent heat of ice fusion and ice shelf surface temperature; T_f is the pressure freezing point for seawater of salinity S_f at the ice–ocean interface and is determined from the linear form of pressure freezing point relationship (Millero 1978)

$$T_f = aS_f + b + cp_{io}, \quad (17)$$

where a, b, and c are physical constants (-0.0573°C psu^{-1}, 0.0832°C, and 7.61×10^{-4}°C dbar^{-1}), and p_{io} is the pressure at the ice–ocean interface in dbar.

During the production of melt water, heat is required to warm the ice to the in situ melting point and melt the ice prior to mixing. Assuming the salinity of the ice is zero, the bulk change in temperature (ΔT) and salinity (ΔS) for the 1-m thick layer adjacent to the ice shelf base over the time step (Δt) is prescribed by

$$\Delta T = \frac{\Delta M}{M_b + \Delta M}\left\{\left[T_f - \frac{L}{c_w} - \frac{c_i}{c_w}(T_f - T_i)\right] - T_b\right\} \quad (18)$$

and

$$\Delta S = -\frac{\Delta M}{M_b + \Delta M} S_b, \quad (19)$$

where ΔM is the meltwater mass determined from (16) and M_b is the layer water mass.

To examine the vertical structure of the M_2 tidal currents, the resulting u and v model velocity data from (5) and (6) are analyzed to determine the amplitude (A_u, A_v) and phase (ϕ_u, ϕ_v) of the velocity components. These data are used to construct clockwise and anticlockwise rotary components (Souza and Simpson 1996):

$$R_+ = |0.5[A_u^2 + A_v^2 + 2uv\sin(\phi_v - \phi_u)]^{1/2}| \quad (20)$$

$$R_- = |0.5[A_u^2 + A_v^2 - 2uv\sin(\phi_v - \phi_u)]^{1/2}|. \quad (21)$$

When viewed from above, R_- and R_+ are the purely clockwise and anticlockwise constant magnitude velocity vectors that rotate at the tidal frequency. These two components combine to give the time-varying velocity vector that results in the tidal current ellipse (Prandle 1982) and are used to determine the semimajor (U) and semiminor (V) axes and polarization, from (1), of the tidal ellipse:

$$U = |R_+| + |R_-| \quad (22)$$

$$V = |R_+| - |R_-|. \quad (23)$$

In this study, the one-dimensional model simulations are for a 200-m water column beneath an ice shelf with a surface temperature of -27°C, similar to the more tidally active regions close to the Ronne Ice Front, around Korff and Henry Ice Rises, and close to grounding lines. The surface forcing is ramped up over approximately 16 tidal cycles and the model allowed to stabilize. The wintertime conditions found on Berkner Shelf are used to provide the initial water column temperature and salinity of -1.9°C and 34.65 psu and the ice shelf draft of 250 m is similar to that found along the Ronne Ice Front. Although these initial oceanographic conditions and ice shelf draft represent a particular region, the temperature and salinity range is relatively small beneath FRIS (approximately -1.90° to -2.55°C and 34.77 to 34.48 psu) (Nicholls et al. 2001; Nicholls and Makinson 1998) and the model results will provide an insight into the broad pattern of tidal mixing regimes within the sub-ice-shelf cavity.

3. Model result

a. *Tidal current profiles in a homogeneous sea*

To maintain the initial homogeneous water column conditions throughout this simulation the model is thermodynamically decoupled from the ice shelf to prevent melting and subsequent stratification of the water column. However, the ice shelf base remains a second frictional surface, doubling the amount of water column occupied by boundary layers. In some regions the high water velocity or proximity to the critical latitude, or a combination of the two, will lead to the combined boundary layer thickness exceeding that of the water column. Therefore as the two boundary layers interact, the amplitude of R_+ throughout the water column is below its "free stream" velocity. Keeping the M_2 surface forcing parameters constant (e.g., $U = 0.3$ m s^{-1} and $P = 0.0$) and allowing the model to stabilize, the resulting tidal currents are analyzed to obtain the rotary current profiles. Figure 3 illustrates the retarding effect of the two interacting boundary layers on R_+ as the M_2 critical latitude is approached from the south.

Observations from the southern Weddell Sea (Foldvik et al. 1990; Foldvik et al. 2001) support the prediction that for semidiurnal tides the amplitude of R_- is largely depth independent while the amplitude of R_+ is strongly depth dependent. The net water column velocity structure results from the addition of the two components and their associated boundary layers, and so the tidal current ellipse polarization is depth dependent, becoming increasingly negative toward the boundaries (Fig. 3).

To examine the latitudinal extent of the combined effects of critical latitude and velocity on water column structure, a range of surface forcing values for U are applied at different latitudes while maintaining $P = 0.0$. The resulting M_2 amplitude of R_+ at the midpoint in the

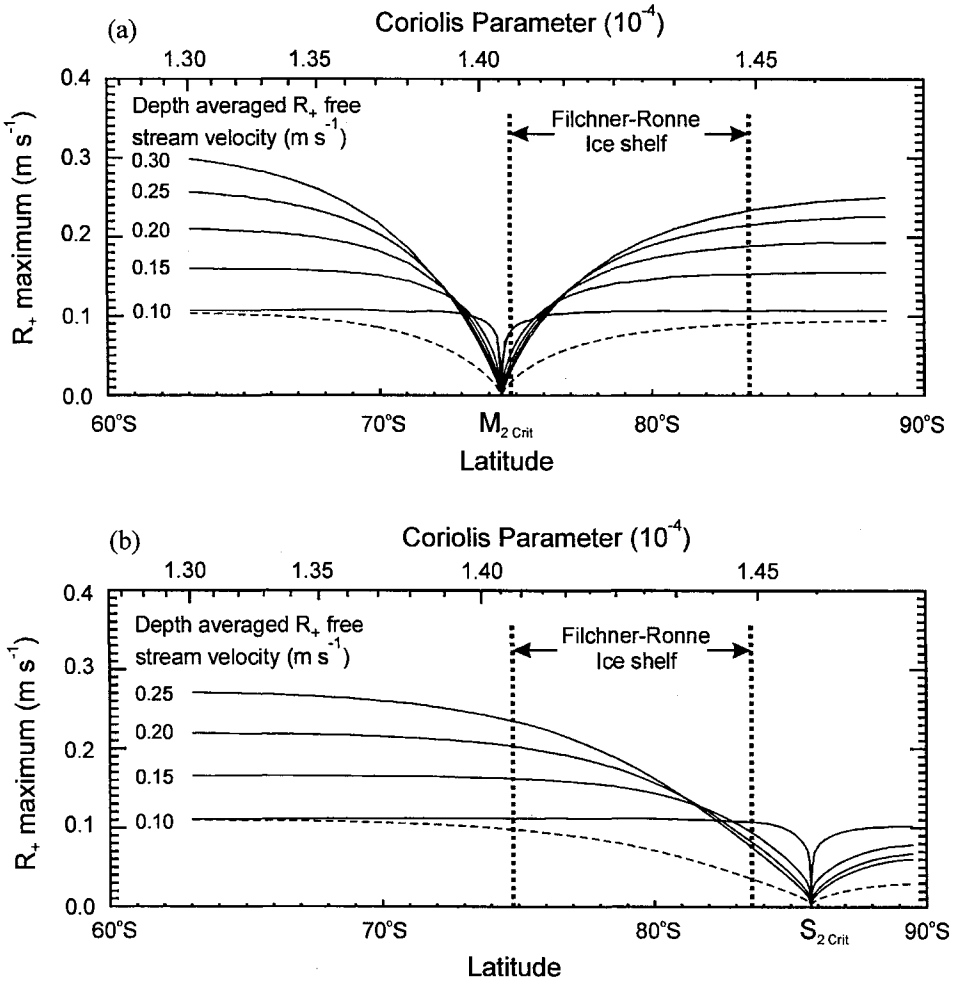

FIG. 4. The amplitude of (a) the M_2 and (b) the S_2 anticlockwise component (R_+) at the mid-water column along a transect spanning the critical latitude. Several free stream amplitudes were used to illustrate the combined effect of critical latitude and water velocity in the 200-m homogeneous water column. The dashed line represents R_+ in a 100-m water column. The region where the two boundary layers interact and retard the flow is greatest at highest velocities or in shallower water. The position of FRIS lies between the dotted lines and the asymmetry in the plots results from the nonlinear variation of the Coriolis parameter with latitude.

water column is shown in Fig. 4a. Here, the greatest impact is at the critical latitude where all R_+ amplitudes are affected. The range of influence is dependent on the water velocity, with higher velocities affected the most because of their larger boundary layers. It follows that shallower water would also extend the latitudinal range of influence. By reducing the water column thickness to 100 m and maintaining the same forcing, the dashed line in Fig. 4a shows the greater latitudinal range over which the two boundary layers occupy the entire water column and retard the flow. Conversely, in deeper water the latitudinal range will decrease. While the northern part of FRIS lies close to the M_2 critical latitude, the southernmost areas of the ice shelf are closest to the S_2 critical latitude. The amplitude pattern of the S_2 tidal currents mirror those of M_2 beneath FRIS, though they are approximately 40% smaller (Makinson and Nicholls 1999). Applying the model in the same way, the resulting S_2 amplitude of R_+ at the midpoint in the water column is shown in Fig. 4b to illustrate the range of influence of the S_2 boundary layers. The remainder of the modeling will now focus on M_2 tidal currents only; however, the characteristics of M_2 tidal currents will also be representative of the S_2 tidal currents.

b. Tidal current profiles in a stratified sea

To simulate the effects of stratification the model is thermodynamically coupled to the ice shelf allowing melting to take place. The model is initially allowed to stabilize over 80 M_2 tidal cycles using an unstratified water column and constant surface-forcing parameters ($U = 0.3$ m s^{-1} and $P = 0.0$). Over a further 200 cycles (about 103 days) melting is enabled and a pycnocline

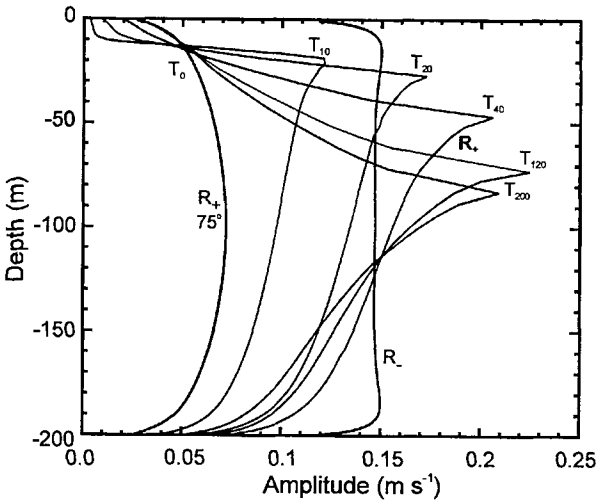

FIG. 5. The vertical structure of the M_2 rotary components beneath an ice shelf during the onset of melting and development of a deepening pycnocline. In this example, T_0 represents R_+ at 75°S before melting is initiated and T_{10} through to T_{200} indicate the number of tidal cycles over which melting has taken place. Initially the flow is retarded, but attains its free stream velocity in the part of the water column association with the pycnocline. After 200 tidal cycles there is no significant change in R_+ or the depth of the pycnocline.

is quickly established in the upper half of the water column. To represent a well-mixed inflowing water mass, the deepest 20 m of the water column are held at their initial temperature and salinity conditions throughout the model run. However, vertical mixing creates a lower mixed layer that extends through most of the lower 100 m. As the water column structure is modified by melting and mixing the development of the tidal current structure beneath the ice shelf is shown in Fig. 5. Here the reference latitude is 75°S but other latitudes close to the critical latitude would give a similar pattern of results. Initially the two R_+ boundary layers occupy the entire water column and the flow associated with the R_+ component is retarded below its free stream velocity. As melting progresses, the water column stratifies and the maximum R_+ velocity tracks the deepening pycnocline. In this example, R_+ shows a two- to threefold increase over the nonstratified case as it attains its free stream velocity in the vicinity of the pycnocline, though farther away from the critical latitude this increase would be smaller. The final M_2 tidal current structure in Fig. 5 is almost identical to the observations beneath fast-ice in the Canadian Arctic, confirming that the M_2 tidal current close to the critical latitude reaches a maximum at the depth of the pycnocline (Prinsenberg and Bennett 1989).

The effect of the stratification on R_+ depends both on the strength of the building pycnocline and on the initial level of retardation compared with the free stream velocity. This increases for increasing free stream velocities and as the critical latitude is approached (Fig. 4). In areas subject to changes in stratification, either on daily, spring–neap or seasonal time scales, the R_+ component can exhibit substantial fluctuations in amplitude. Similar conditions arise in the North Sea where the bottom boundary layer outcrops at the surface: observations show significant differences in the vertical tidal current structure between the well-mixed winter conditions, where the flow remains retarded, and stratified summer conditions where the flow attains its free stream value above the pycnocline (Howarth 1998). Simpson and Souza (1995) found similar changes in tidal current structure on a semidiurnal timescale near the Dutch coast in the freshwater region of the Rhine outflow.

c. *Polarization effects*

The one-dimensional vertical mixing model has been used to simulate a wide range of different current amplitudes and ellipse polarizations for the M_2 tidal constituent at 79°S, the mean position of FRIS. Once the model has stabilized after 80 tidal cycles using an unstratified water column, melting is initiated. The surface forcing parameters remain unchanged while the stratification evolves over a further 120 cycles (about 62 days) with the lowest 20 m of the water column held at constant temperature and salinity throughout. The melt rates, which are initially high for all polarizations, decrease as the mixed layer next to the ice shelf base cools toward the in situ freezing point. Tidal currents with a more positive polarization however, continue to deepen the mixed layer and pycnocline toward the middle of the water column, maintaining a strong vertical heat flux and higher rates of melting. This dependence of vertical mixing on ellipse polarization was highlighted by Simpson and Sharples (1994) for northern midlatitudes.

To illustrate the extent of mixing meltwater from the ice shelf base down through the upper half of the water column, the dependence of the pycnocline depth after 10 tidal cycles on mean polarization is plotted in Fig. 6 for a range of tidal current strengths. After only 10 tidal cycles the vigorous mixing, associated with strong tidal currents and positive polarizations, has deepened the pycnocline almost to the middle of the water column. While the temperature and salinity remain fixed in the lower part of the water column the pycnocline depth will not exceed 100 m or half the water column thickness. Clearly there is asymmetry in the resulting thickness of the mixed layers, which is dependent on the ratio and magnitude of the two rotary currents and, therefore, on the magnitude and polarization of the tidal current ellipse. For predominantly clockwise tidal currents ($P < -0.5$) the depth of the pycnocline is constrained by the depth of the R_- boundary layer. As the polarization becomes more positive, the boundary layer of R_+ becomes increasingly influential producing more mixing in the midwater column and rapidly deepening the pycnocline over the region $-0.3 < P < 0.3$. With

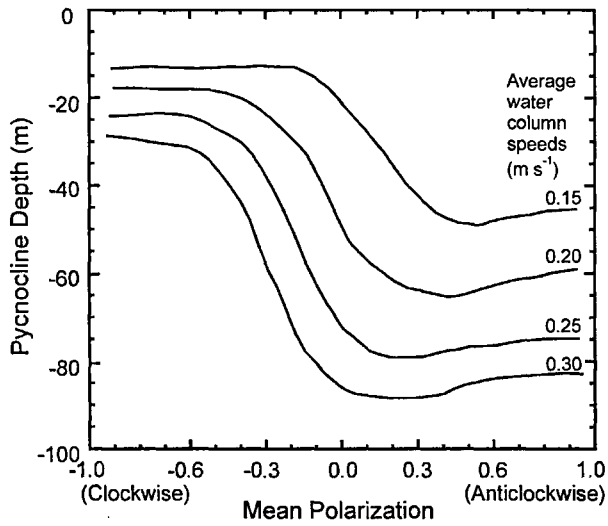

FIG. 6. Pycnocline depth in the upper half of the water column after 10 M_2 tidal cycles at 79°S over which melting has taken place for different average water column speeds vs the mean polarization of the M_2 tidal current ellipse.

no significant increase in midwater column mixing as the polarization increases, there is no further deepening of the pycnocline for the predominantly anticlockwise tidal currents ($P > 0.5$).

Applying a broader range of surface forcings, the dependence after 10 tidal cycles of pycnocline depth on the resulting mean rotary components of the tidal current ellipse is contoured in Fig. 7. Here strong tidal currents and positive polarizations result in the pycnocline depth almost reaching its maximum of 100 m, whereas negative polarizations give a much shallower pycnocline. Given sufficient time, the middle of the pycnocline would lie close to the middle of the water column for all forcings as the water column structure, vertical heat flux, and melt rate reached an equilibrium state. Assuming the water column structure is approaching equilibrium after 120 tidal cycles for all but the weakest tidal currents, the melt rate is contoured in Fig. 8. There is a strong dependence of both the pycnocline depth and the melt rate on polarization of the tidal current ellipse, with both parameters showing a similar pattern. For both parameters, the deepest pycnocline and highest melt rates are associated with the more positive polarizations. The greatest changes in melt rate occur over the range $-1.0 < P < 0.2$, as the R_+ boundary layers introduce increasing levels of mixing into the mid–water column, bringing warmer water up to the ice shelf base. Beyond this polarization range the longer-term melt rate shows a slight decrease for given average water speeds. This decrease can be attributed to no significant change in the mid–water column mixing combined with a decreasing boundary velocity as the shear from R_- diminishes with increasing polarization.

4. Application to FRIS

The broad range of surface forcings applied to the model generate a wide range of tidal currents that are analyzed to obtain the mean rotary components. Therefore, the effects of latitude on the tidal current structure will be embedded within the mean R_+ and R_- components. Since FRIS occupies a narrow band of latitudes (79°S ± 4°) the dependence of pycnocline depth and melt rate on mean R_+ and R_- should vary little with position on the ice shelf. However, the influence of proximity to the critical latitude on the R_+ component results in some differences from the data at 79°S in Figs. 7 and 8. The greatest differences of up to 20% occur for positive polarizations and speeds below 0.25 m s^{-1}, where the contribution of turbulence from R_+ dominates the vertical mixing. Here, the critical latitude strongly influences the R_+ current component (Fig. 4a) with additional turbulence being generated from the increased shear as R_+ attains its free stream velocity around the developing pycnocline (Fig. 5). This results in higher melt rates and slightly shallower pycnocline depths as the critical latitude is approached. For negative polarizations and higher current speeds there is little or no latitudinal influence. Consequently, the model results from 79°S are broadly representative of the range of latitudes occupied by FRIS.

Beneath the ice shelf, the modeled M_2 and S_2 tidal velocities can reach 0.5 m s^{-1} and 0.3 m s^{-1}, respectively, typically three to six times higher than for the diurnal tides (Makinson and Nicholls 1999). The M_2 ellipse polarization ranges from −0.95 to +0.7 (Fig. 2) with predominantly anticlockwise rotation associated with the shallow water close to the Ronne Ice Front. In the central part of Ronne Ice Shelf and at the mouths of the ice stream and glacier inlets predominantly clockwise rotation occurs, which results from the interaction of a semidiurnal Kelvin wave with basins or inlets of different scales (Carbajal 1997).

The almost complete range of possible polarizations present beneath FRIS suggests that, in light of the model results, a wide range of vertical mixing regimes will exist. The boxes in Figs. 7 and 8 broadly divide the tidal current characteristics beneath FRIS into three main regions. However, the melt rates in Fig. 8 are not predicting basal melt rates beneath FRIS, only the contribution that tidal vertical mixing makes to the heat supply at the ice shelf base. Taking a representative point from each of these three tidal current regions beneath FRIS (indicated by the crosses in Fig. 7), profiles from the model of mixing length, turbulent kinetic energy, eddy viscosity, dissipation, and density change are plotted in Fig. 9. The model was spun up and allowed to stabilize over 80 tidal cycles. The profiles are plotted at hourly intervals over the final M_2 tidal cycle prior to melting and then after a further 10 tidal cycles, with melting, to show the effects of stratification.

Regions where $P < -0.3$ in water approximately 200

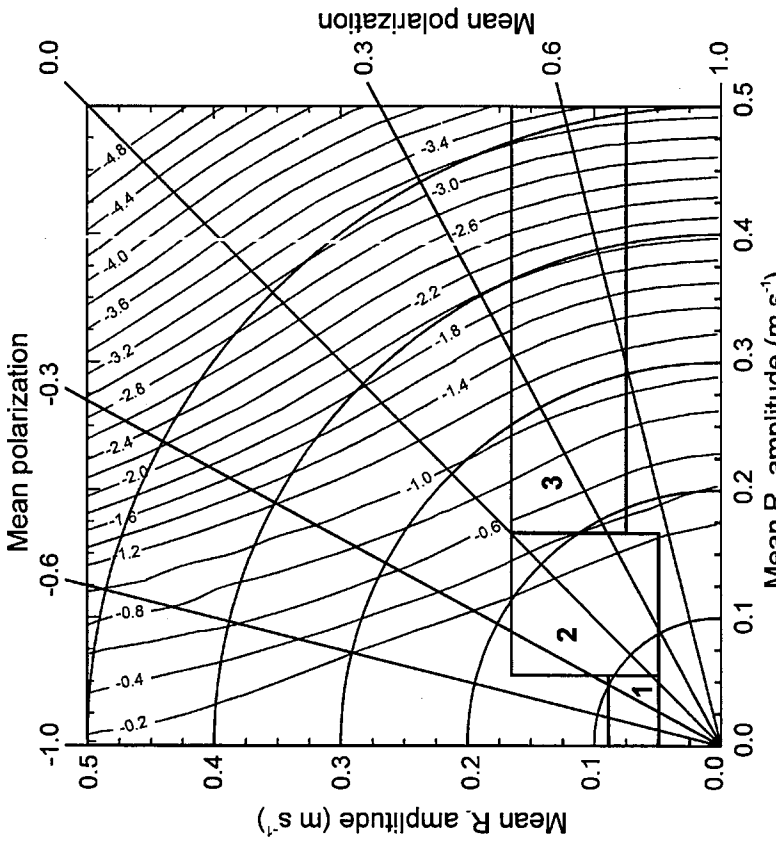

FIG. 8. Same as for Fig. 7 but with the dependence of the melt rate (m yr^{-1}) after 120 tidal cycles on the mean rotary components of the tidal current ellipse. The contours are every 0.2 m yr^{-1}.

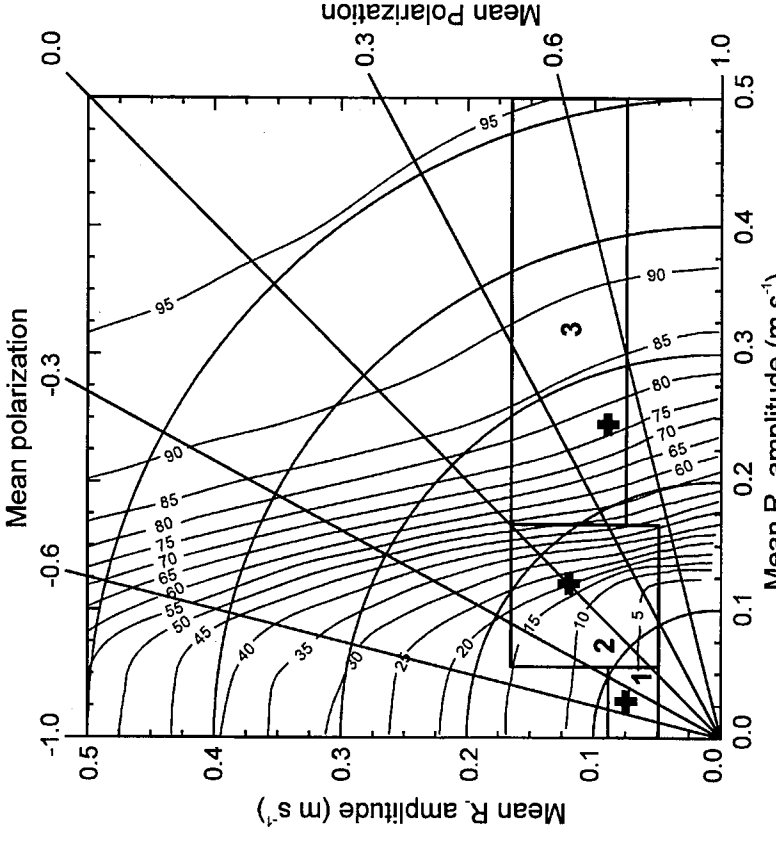

FIG. 7. The dependence of the pycnocline depth (m) after 10 M_2 tidal cycles at 79°S on the mean rotary components of the M_2 tidal current ellipse. The contours are every 5 m and the total water column thickness was 200 m. The lines radiating from the origin connect points of equal polarization and the arcs connect points of equal mean water column speed. The boxes indicate the tidal current characteristics for: 1) eastern most part of Filchner Ice Shelf and north of Doake Ice Rumples; 2) south of Korff and Henry Ice Rises; and 3) Ronne Ice Front. The crosses mark the positions from which the water column property profiles in Fig. 9 were obtained.

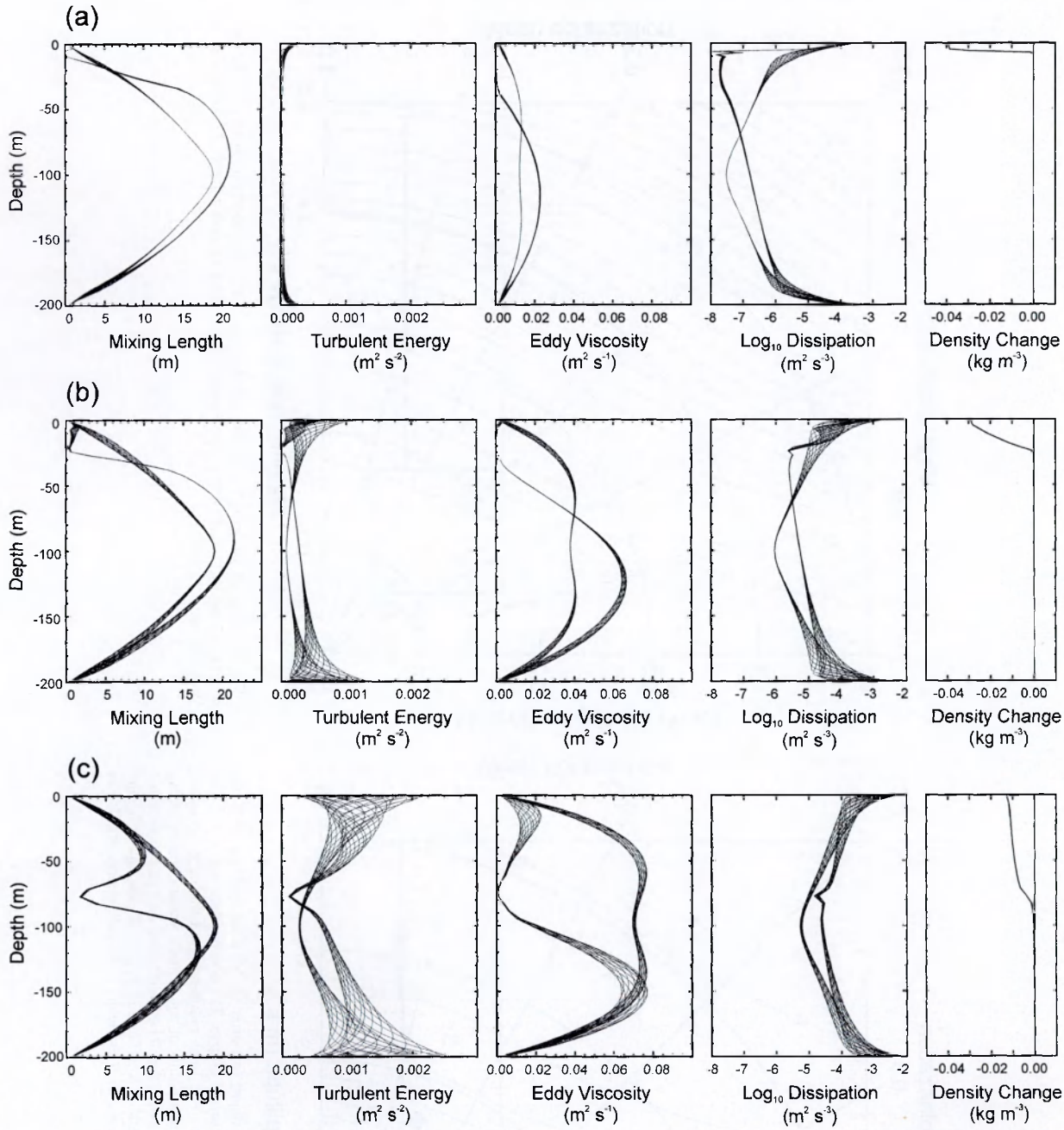

FIG. 9. Profiles through a 200-m water column of mixing length, turbulent kinetic energy, eddy viscosity, dissipation, and density change. The profiles are at hourly intervals over a M_2 tidal cycle for a homogeneous water column (symmetrical profiles) and after melting takes place over 10 M_2 tidal cycles (nonsymmetrical profiles). The resultant stratification and pycnocline depth are shown by the change in density from the initial homogeneous conditions. The three locations are indicated by crosses in Fig. 7 and are representative of the three regions beneath FRIS (a) easternmost part of Filchner Ice Shelf and north of Doake Ice Rumples (box 1); (b) south of Korff and Henry Ice Rises (box 2); and (c) Ronne Ice Front (box 3).

m deep are confined to a few small areas such as the easternmost part of Filchner Ice Shelf and just to north of Doake Ice Rumples. The combination of weak tidal currents and negative polarization (region 1 in Figs. 6 and 7) produce low levels of TKE (Fig. 9a). The turbulent dissipation is greatest close to the boundaries followed by an almost linear decrease on a $\log_{10}$ scale with distance away from the boundaries, characteristic of all the dissipation profiles in Fig. 9. The effect of stratification on the water column is to suppress turbulence, inhibiting the transfer of momentum and reducing the eddy viscosity, particularly in the vicinity of the pycnocline. The pycnocline effectively separates the water column into two parts with TKE generated at the

upper boundary being confined to a small upper mixed layer. This small mixed layer cools rapidly toward the in situ freezing point, creating a large density contrast across the pycnocline. The remainder of the water column comes under the influence of the lower boundary with the pycnocline acting effectively as a free surface. Consequently, TKE and dissipation increase in the mid–water column, increasing both the eddy viscosity and mixing length over a large portion of the lower water column (Fig. 9a).

Other regions where $P < -0.3$ such as the central Ronne Ice Shelf and mouths of ice stream inlets, the water column thickness can be up to 600 m with low speed tidal currents, compounding the effects of low polarization. Although the model does not specifically cover these water thicknesses, it can be inferred that vertical mixing will be confined to the small boundary layers of R_- and the upper and lower boundary layers will be isolated from each other. In this situation, turbulence generated from tidal currents will not contribute to mid-water-column mixing, and melt resulting from tidal vertical mixing will be close to zero. However, where heat is available from horizontal advection in the upper mixed layer tidal currents will enhance the basal melting.

Most of FRIS lies between $P = \pm 0.3$, similar to the region south of Korff and Henry ice rises. This region is characterized by moderate tidal currents and a water column around 200 m thick (Fig. 1). Its M_2 polarization and velocity range occupies region 2 in Figs. 6 and 7, with representative water column properties shown in Fig. 9b. When compared with region 1, the moderate tidal currents provide increased TKE, enhancing the eddy viscosity and leading to a deeper penetration of the pycnocline into the water column. Other water column characteristics develop in the same way as in region 1 (Fig. 9a). The initial development and penetration into the water column of the pycnocline is sensitive to changes in polarization over this range ($P = \pm 0.3$) and the increasing polarization can lead to a three- to fourfold increase in the pycnocline depth (Fig. 6). The longer term melt rate is less sensitive where the polarization is positive, however, once the polarization falls below $P = 0$ the melt rate begins to decline rapidly (Fig. 8). In areas where tidal currents are constrained to flow approximately parallel to grounding lines ($R_+ \approx R_-$), such as the Orville coast and south of the ice rises, modification of the ellipse polarization is not possible, therefore the transverse pressure gradient must balance the Coriolis force to maintain flow parallel to the coast. Here, there will be regions extending from grounding lines that are dominated by the interacting R_+ boundary layers and therefore exhibit high levels of mixing.

The Ronne Ice Front region is characterized by shallow water (<200 m), strong tidal currents, positive ellipse polarizations ($0.3 < P < 0.7$) and occupies region 3 in Figs. 6 and 7. In this high current regime intense mixing takes place, with rapid deepening of the pycnocline and strong melting sustained for as long as the water column remains above the in situ freezing point. These features are shown in Fig. 9c, with high levels of TKE extending into the midwater column, forming a deep pycnocline with the smallest density contrast of the three regions. This small density contrast after 10 tidal cycles is the result of the rapid mixing of meltwater down into the midwater column while maintaining a strong vertical heat flux, keeping the upper water column above the in situ freezing point and maintaining further melting.

5. Conclusions

The application of a 1D turbulent closure model, thermodynamically coupled to an ice shelf, has shown the role played by tidal currents under the influence of the earth's rotation in vertical mixing. The model shows that vertical tidal current structure under ice shelves is dramatically modified by the proximity of critical latitudes and changes in stratification; and both the pycnocline development and basal melt rate are sensitive to tidal current ellipse polarization. Beneath Filchner–Ronne Ice Shelf, which is bounded by the critical latitudes of the M_2 and S_2 semidiurnal tides, several key areas experience the extremes of the polarization range, creating regions of widely differing levels of tidally induced vertical mixing and basal melting. The key results from this study are

1) For predominantly clockwise rotation the model predicts mixing restricted by the small boundary layer of the R_- rotary component.
2) As the polarization becomes increasingly positive, the thickening boundary layer and associated shear of R_+ causes the mixing to rapidly penetrate deeper into the midwater column.
3) The resultant melting gives over an order of magnitude difference between the lowest melt rates for purely clockwise tidal currents and the highest for purely anticlockwise tidal currents.
4) Changes in stratification can dramatically modify the vertical tidal current structure, particularly near semidiurnal critical latitudes.

As a consequence of these points, simple parameterizations of tidally induced vertical mixing for use in sub-ice-shelf circulation models are unlikely to represent the combined effects of semidiurnal critical latitudes, stratification, and ellipse polarization. Ultimately, a more comprehensive representation of tides and their associated mixing processes will be needed to determine their contribution to sub-ice-shelf circulation.

Acknowledgments. The author wishes to thank Keith Nicholls and two anonymous reviewers for many valuable comments that significantly improved the manuscript.

APPENDIX

Surface Forcing Functions

To derive a surface forcing function in terms of the resulting tidal ellipse polarization and its semimajor axis, the complex form of the momentum equations are required. For details of their derivation the reader is referred to either Soulsby (1983) or Carbajal (2000), where both the velocity and sea surface slope are divided into two counterrotating components

$$i(\omega + f)R_+ = \frac{\partial}{\partial z}\left(K_M \frac{\partial R_+}{\partial z}\right) - gS_+ \qquad \text{(A1)}$$

$$-i(\omega - f)R_- = \frac{\partial}{\partial z}\left(K_M \frac{\partial R_-}{\partial z}\right) - gS_-, \qquad \text{(A2)}$$

where ω is the tidal frequency, f is the Coriolis parameter, K_M is the vertical eddy viscosity, g the gravitational acceleration, and z is vertical distance; R_- and R_+ represent the purely clockwise and anticlockwise constant magnitude velocity vectors that rotate at the tidal frequency, and S_- and S_+ are the rotary components of the sea surface elevation gradients. Outside the boundary layer away from the influence of bottom friction, the first terms on the right-hand side of (A1) and (A2) are small and the free stream tidal current is given by

$$R_{\infty+} = \frac{igS_+}{\omega + f} \quad \text{and} \qquad \text{(A3)}$$

$$R_{\infty-} = \frac{-igS_-}{\omega - f}. \qquad \text{(A4)}$$

Assuming the maximum tidal current corresponds to the maximum surface slope aligned along the x axis (S_x) and the minimum tidal current corresponds to the minimum surface slope aligned along the y axis (S_y)

$$S_x = |S_+| + |S_-| \qquad \text{(A5)}$$

$$S_y = |S_+| - |S_-|, \qquad \text{(A6)}$$

rearranging (A3) and (A4) and substituting into (A5) and (A6) gives S_x and S_y in terms R_+ and R_-. Rearranging and grouping R_+ and R_- in terms of the maximum tidal current or semimajor axis ($U = R_+ + R_-$) and polarization ($P = [R_+ - R_-]/[R_+ + R_-]$) gives

$$S_x = \frac{U(\omega + Pf)}{g} \qquad \text{(A7)}$$

$$S_y = \frac{U(f + P\omega)}{g} \qquad \text{(A8)}$$

the surface forcing functions along the x and y axes.

REFERENCES

Carbajal, N., 1997: Two applications of Taylor's problem solution for finite rectangular semi-enclosed basis. *Cont. Shelf Res.*, **17,** 803–817.

——, 2000: A criterion to locate regions with anticyclonic tidal current rotation. *Cont. Shelf Res.*, **20,** 281–292.

Foldvik, A., and T. Gammelsrød, 1988: Notes on Southern Ocean hydrography, sea-ice and bottom water formation. *Palaeogeogr. Palaeoclimatol. Palaeoecol.*, **67,** 3–17.

——, J. H. Middleton, and T. D. Foster, 1990: The tides of the southern Weddell Sea. *Deep-Sea Res.*, **37,** 1345–1362.

——, T. Gammelsrød, E. Nygaard, and S. Østerhus, 2001: Current meter measurements near Ronne Ice Shelf, Weddell Sea: Implications for circulation and melting underneath the Filchner–Ronne Ice Shelves. *J. Geophys. Res.*, **106,** 4463–4477.

Fox, A. J., and A. P. R. Cooper, 1994: Measured properties of the Antarctic ice sheet derived from SCAR Antarctic digital database. *Polar Rec.*, **30,** 201–206.

Furevik, T., and A. Foldvik, 1996: Stability at M_2 critical latitude in the Barents Sea. *J. Geophys. Res.*, **101,** 8823–8837.

Galperin, B., L. H. Kantha, S. Hassid, and A. Rosati, 1988: A quasi-equilibrium turbulent energy-model for geophysical flows. *J. Atmos. Sci.*, **45,** 55–62.

Ganachaud, A., and C. Wunsch, 2000: Improved estimates of global ocean circulation, heat transport and mixing from hydrographic data. *Nature,* **408,** 453–456.

Gill, A. E., 1982: *Atmosphere–Ocean Dynamics.* International Geophysical Research Series, Vol. 30, Academic Press, 662 pp.

Howarth, M. J., 1998: The effect of stratification on tidal current profiles. *Cont. Shelf Res.*, **18,** 1235–1254.

Kader, B. A., and A. M. Yaglom, 1972: Heat and mass transfer laws for fully turbulent wall flows. *Int. J. Heat Mass Transfer,* **15,** 2329–2351.

Kraus, E. B., and J. S. Turner, 1967: A one-dimensional model of the seasonal thermocline II. The general theory and its consequences. *Tellus,* **19,** 98–105.

Lynch, D. R., J. T. C. Ip, C. E. Naimie, and F. E. Werner, 1996: Comprehensive coastal circulation model with application to the Gulf of Maine. *Cont. Shelf Res.*, **16,** 875–906.

MacAyeal, D. R., 1984: Thermohaline circulation below the Ross Ice Shelf: A consequence of tidally induced vertical mixing and basal melting. *J. Geophys. Res.*, **89,** 597–606.

Makinson, K., and K. W. Nicholls, 1999: Modeling tidal currents beneath Filchner–Ronne Ice Shelf and on the adjacent continental shelf: Their effect on mixing and transport. *J. Geophys. Res.*, **104,** 13 449–13 465.

Mellor, G., and T. Yamada, 1982: Development of a turbulence closure-model for geophysical fluid problems. *Rev. Geophys.*, **20,** 851–875.

Millero, F. J., 1978: Annex 6: Freezing point of seawater. Eighth report of the Joint Panel of Oceanographic Tables and Standards. *UNESCO Tech. Pap. Mar. Sci.*, **28,** 29–31.

Nicholls, K. W., and K. Makinson, 1998: Ocean circulation beneath the western Ronne Ice Shelf, as derived from in situ measurements of water currents and properties. *Ocean, Ice, and Atmosphere: Interactions at the Antarctic Continental Margin.* S. S. Jacobs and R. F. Weiss, Eds., Antarctic Research Series, Vol. 75, Amer. Geophys. Union, 301–318.

——, S. Østerhus, K. Makinson, and M. R. Johnson, 2001: Oceanographic conditions south of Berkner Island, beneath Filchner–Ronne Ice Shelf. Antarctica. *J. Geophys. Res.*, **106,** 11 481–11 492.

Nøst, E., 1994: Calculating tidal current profiles from vertically integrated models near the critical latitude in the Barents Sea. *J. Geophys. Res.*, **99,** 7885–7901.

Prandle, D., 1982: The vertical structure of tidal currents and other oscillatory flows. *Geophys. Astrophys. Fluid Dyn.*, **22,** 29–49.

Prinsenberg, S. J., and E. B. Bennett, 1989: Vertical variations of tidal currents in shallow land fast ice-covered regions. *J. Phys. Oceanogr.*, **19,** 1268–1278.

Robertson, R., L. Padman, and G. D. Egbert, 1998: Tidal currents in the Weddell Sea. *Ocean, Ice, and Atmosphere: Interactions at the Antarctic Continental Margin.* S. S. Jacobs and R. F. Weiss, Eds., Antarctic Research Series, Vol. 75, Amer. Geophys. Union, 341–369.

Scheduikat, M., and D. J. Olbers, 1990: A one-dimensional mixed layer model beneath the Ross Ice Shelf with tidally induced vertical mixing. *Antarct. Sci.,* **2,** 29–42.

Shirasawa, K., and R. G. Ingram, 1991: Characteristics of the turbulent oceanic boundary layer under sea ice. Part 1: A review of the ice–ocean boundary layer. *J. Mar. Syst.,* **2,** 153–160.

Simpson, J. H., and J. Sharples, 1994: Does the Earth's rotation influence the location of shelf sea fronts. *J. Geophys. Res.,* **99,** 3315–3319.

——, and A. J. Souza, 1995: Semidiurnal switching in the region of freshwater influence of the Rhine. *J. Geophys. Res.,* **100,** 7037–7044.

Soulsby, R. L., 1983: The bottom boundary layer of the shelf sea. *Physical Oceanography of Coastal and Shelf Seas,* B. Johns, Ed., Elsevier, 189–226.

Souza, A. J., and J. H. Simpson, 1996: The modification of tidal ellipses by stratification in the Rhine ROFI. *Cont. Shelf Res.,* **16,** 397–414.